

DOCTORAL THESIS

Modelling and Simulation of Arterial Blood Pulsation via Bioimpedance

Ksenija Pesti

TALLINN UNIVERSITY OF TECHNOLOGY
DOCTORAL THESIS
34/2021

Modelling and Simulation of Arterial Blood Pulsation via Bioimpedance

KSENIJA PESTI



TALLINN UNIVERSITY OF TECHNOLOGY

School of Information Technologies

Thomas Johann Seebeck Department of Electronics

This dissertation was accepted for the defence of the degree 28/05/2021

Supervisor:

Prof Emeritus Mart Min
Thomas Johann Seebeck Department of Electronics
Tallinn University of Technology
Tallinn, Estonia

Co-supervisor:

PhD Margus Metshein
Thomas Johann Seebeck Department of Electronics
Tallinn University of Technology
Tallinn, Estonia

Opponents:

Prof Assoc. Dr.-Ing. Daniel Teichmann
Center for Health Informatics and Technology
The Maersk Mc-Kinney Moller Institute
University of Southern Denmark

Prof PhD Vahur Zadin
Institute of Technology
Faculty of Science and Technology
University of Tartu

Defence of the thesis: 21/06/2021, Tallinn

Declaration:

Hereby I declare that this doctoral thesis, my original investigation and achievement, submitted for the doctoral degree at Tallinn University of Technology has not been submitted for doctoral or equivalent academic degree.

Ksenija Pesti

signature



European Union
European Regional
Development Fund



Investing
in your future

Copyright: Ksenija Pesti, 2021

ISSN 2585-6898 (publication)

ISBN 978-9949-83-716-8 (publication)

ISSN 2585-6901 (PDF)

ISBN 978-9949-83-717-5 (PDF)

Printed by Koopia Niini & Rauam

TALLINNA TEHNIKAÜLIKOO
DOKTORITÖÖ
34/2021

Arteriaalse verepulsatsiooni modelleerimine ja simuleerimine bioimpedantsi kaudu

KSENIJA PESTI



To my family

Contents

List of Publications	10
Author's Contribution to the Publications	12
Acronyms	13
Introduction	14
Motivation and study	14
Overview of the thesis.....	15
Methodology used in the thesis	16
Objectives of the thesis and research questions.....	17
Contributions of the thesis	18
1 Background	21
1.1 Electrical bioimpedance	22
1.1.1 Electrical impedance	22
1.1.2 Electrical model of cell and tissue.....	23
1.1.3 Electrical properties of biological tissue	25
1.2 Principles of the induced current approach	27
1.2.1 Frequency and skin effect	28
1.3 Monitoring of central aortic pressure of blood	29
1.3.1 Blood pressure wave curve.....	29
1.3.2 State of the art of continuous CAP estimation	31
1.4 Modelling and Simulation.....	32
1.4.1 Finite element method	33
1.4.2 Maxwell's equations	33
2 Eddy Current Bioimpedance Measurement on a Tissue Mimicking Phantom Materials.....	35
2.1 Introduction.....	36
2.1.1 Dielectric properties of the tissue mimicking phantom material	36
2.1.2 Tissue-mimicking phantoms for bioimpedance analysis	36
2.1.3 Study and motivation.....	37
2.2 Manufacturing and Calibration of Gelatine Tissue-Mimicking Phantoms.....	38
2.2.1 Composition and manufacturing of gelatine tissue mimicking phantoms.....	38
2.2.2 Measurement of electrical conductivity of the unique gelatin phantom sample	39
2.2.3 Calibration of the gelatine phantom material	40
2.2.4 Results.....	41
2.3 Validation of Simulations by Eddy Current Methods with Real Measurements on Phantom Materials.....	42
2.3.1 Eddy current impedance measurements.....	42
2.3.2 Modelling and simulation of eddy current impedance measurement	43
2.3.3 Simulation results	45
2.4 Chapter Summary	47

3 Electrode Placement Strategies for the Measurement of Radial Artery Bioimpedance	48
3.1 Introduction.....	49
3.1.1 Bioimpedance-based sensing of blood pulse wave in radial artery.....	49
3.1.2 Sensitivity distribution	50
3.1.3 Study and motivation.....	51
3.2 Electrode Configuration and Placement Strategies.....	52
3.2.1 In-line four-electrode impedance sensing on radial artery: distal and circular electrode placements	53
3.2.2 Impedance sensing on radial artery: various four-electrode placements and FIM electrode placements.....	54
3.3 Simulation of Sensitivity Distribution for Radial Artery EBI Measurements	56
3.3.1 Building a geometry	56
3.3.2 Defining the material properties	57
3.3.3 Adding a physics and defining physics boundary conditions.....	58
3.3.4 Creating the mesh.....	58
3.3.5 Simulation study steps and solving the model.	59
3.3.6 Post-processing the results.....	59
3.4 Measurement	60
3.4.1 Instrumentation.....	60
3.4.2 Measurement Method and Setup	61
3.5 Results	62
3.5.1 Simulation results: in-line distal and circular four-electrode placements	62
3.5.2 Simulation results: various four-electrode placements and FIM electrode placements	64
3.5.3 Experimental results: various four-electrode and focused (FIM) electrode placements	66
3.5.4 Comparative evaluation of the simulation and experimental results	68
3.6 Chapter Summary.....	69
4 Eddy Current Sensing of Radial Artery Bioimpedance.....	70
4.1 Introduction.....	71
4.1.1 Inductive sensors	71
4.1.2 Study and motivation.....	72
4.2 Simulation Study of Radial Artery Bioimpedance Sensing with Different Coil Types	72
4.2.1 Simplified forearm model description	73
4.2.2 Types of coils used in FEM simulation	74
4.2.3 FEM simulation results.....	76
4.3 Simulation Study of Radial Artery Bioimpedance Sensing by Using Toroidal Core Coil with Concentrated to Radial Artery Winding Position	80
4.3.1 Determination of the effect of capacitive electrodes adding on the simulation results.....	80
4.3.2 Determination of the magnetic core permeability effect on the simulation results of induced current sensing on radial artery	83
4.3.3 Determination of the frequency effect on the simulation results of induced current sensing on radial artery.....	85

4.4 Experimentation and Simulation Study for Detecting Pulse Wave in Radial Artery by Using Air Gapped Toroidal Magnetic Cores.....	86
4.4.1 Experimental measurement setup	86
4.4.2 Simulations of magnetic flux density distribution	88
4.4.3 Results and discussion	88
4.5 Chapter Summary.....	90
Conclusions	91
List of Figures	94
List of Tables	97
References	98
Acknowledgements.....	104
Abstract	105
Lühikokkuvõte	107
Appendix 1	109
Publication I.....	109
Publication II.....	119
Publication III.....	127
Publication IV.....	139
Publication V.....	147
Appendix 2.....	155
Experimental results.....	155
Curriculum vitae.....	160
Elulookirjeldus	161

List of Publications

The list of author's publications, on the basis of which the thesis has been prepared:

- I. Pesti, Ksenija; Kõiv, Hip; Gordon, Rauno (2015). Validation of simulations of eddy current methods with measurements on phantom materials for biomedical engineering R&D. *International Journal of Bioelectromagnetism*, 17 (2), 57–63.
- II. Pesti, Ksenija; Kõiv, Hip; Min, Mart (2019). Simulation of the Sensitivity Distribution of Four-Electrode Impedance Sensing on Radial Artery. *IEEE Sensors Applications Symposium (SAS) Proceedings, Sophia Antipolis, France*, 279–285.
- III. Pesti, Ksenija; Metshein, Margus; Annus, Paul; Kõiv, Hip; Min, Mart (2021). Electrode Placement Strategies for the Measurement of Radial Artery Bioimpedance: Simulations and Experiments. *IEEE Transactions on Instrumentation and Measurement*, 70, 1–10.
- IV. Metshein, Margus; Pesti, Ksenija; Min, Mart; Annus, Paul; Märten, Olev (2020). Feasibility of Utilizing Air Gapped Toroidal Magnetic Cores for Detecting Pulse Wave in Radial Artery. *2020 17th Biennial Baltic Electronics Conference (BEC), Tallinn, Estonia, IEEE*, 1–5.
- V. Priidel, Eiko; Pesti, Ksenija; Min, Mart; Ojarand, Jaan; Märten, Olev (2021). FPGA-based 16-bit 20MHz device for the inductive measurement of electrical bio-impedance. *International Instrumentation and Measurement Technology Conference (IEEE I2MTC2021), Glasgow, Scotland, May 17-20, 2021 (accepted, paper 4374)*, 1–5.

In addition, author's other publications listed below are related to the current thesis. They cover some part of research, contributing in frames of preliminary or supportive activities:

1. Gordon, Rauno; Pesti, Ksenija (2014). System for bioimpedance signal simulation from pulsating blood flow in tissues. In: Kanoun, O. (Ed.). Lecture Notes on Impedance Spectroscopy: Measurement, Modelling and Applications, 51–58.
2. Kõiv, Hip; Pesti, Ksenija; Gordon, Rauno (2016). Electric impedance measurement of tissue phantom materials for development of medical diagnostic systems. In: O. Kanoun (Ed.). Progress reports on impedance spectroscopy: Measurements, Modelling and Applications, 131–137.
3. Min, Mart; Kõiv, Hip; Priidel, Eiko; Pesti, Ksenija; Annus, Paul (2019). Noninvasive Acquisition of the Aortic Blood Pressure Waveform. In: N. Nasiri (Ed.), Wearable Devices. London: IntechOpen, 19 pages.
4. Kõiv, Hip; Pesti, Ksenija; Min, Mart; Land, Raul (2019). Investigation of cost-effective carbon nanofiber/carbon fiber and silicone polymer composite material for wearable bioimpedance device. 2019 IEEE Sensors Applications Symposium (SAS) Proceedings, Sophia Antipolis, France, 2019. IEEE, 1–6.
5. Kõiv, Hip; Pesti, Ksenija; Min, Mart; Land, Raul; Must, Indrek (2020). Comparison of the Carbon Nanofiber-/Fiber- and Silicone-Based Electrodes for Bioimpedance Measurements. IEEE Transactions on Instrumentation and Measurement, 69, 1455–1463.

Author's Contribution to the Publications

Contribution to the papers in this thesis are:

- I. The author planned and performed the experiments. The author performed the computer simulations, processed and compared the obtained results. The author wrote the paper.
- II. The author defined the research problems. The author performed the computer simulations, processed and compared the results. The author wrote the paper.
- III. The author defined the research problem. The author performed the computer simulations, processed and compared simulation results. The author wrote the paper.
- IV. The author performed the computer simulations, processed and compared simulation results.
- V. The author performed the computer simulations, processed and compared simulation results.

Acronyms

2D	Two-dimensional
3D	Three-dimensional
AC	Alternating Current
BIA	Bioimpedance Analysis
BP	Blood Pressure
CAP	Central Aortic Pressure
CC	Current-carrying
CVD	Cardiovascular Disease
DAQ	Data Acquisition
DC	Direct Current
DICOM	Digital Imaging and Communications in Medicine
DP	Diastolic Pressure
EBI	Electrical Bioimpedance
ECG	Electrocardiography
EIT	Electrical Impedance Tomography
EIS	Electrical Impedance Spectroscopy
FE	Finite Element
FEM	Finite Element Method
FIM	Focused Impedance Measurement
GTF	Generalized Transfer Function
ICG	Impedance Cardiography
IPG	Impedance Plethysmography
MRI	Magnetic Resonance Imaging
NDT	Nondestructive
PCB	Printed Circuit Board
PP	Pulse Pressure
PPG	Photoplethysmogram
PU	Pick-up
SP	Systolic Pressure
TF	Transfer Function
vdP	van der Pauw
VID	Volume Impedance Density

Introduction

Motivation and study

According to the World Health Organization, cardiovascular diseases (CVDs) are the leading cause of death [1]. Heart rate and blood pressure are two common physiological vital signs to monitor. The measure of vital signs indicates the physical health of a person and provides an indication of diseases and disorders. Monitoring these signs is of the interest of individuals, medical personnel and, at the very top, of the government because it provides the basic data for predicting and improving public health.

Heart rate and blood pressure can be indicative of a pathophysiological state in individual. Therefore, heart rate and blood pressure are important physiological vital signs for continuous monitoring. Healthcare institutes use this information to monitor the health condition of their patients. This is of particular importance for patients with predicted cardiac disease where heart rate and blood pressure need to be monitored closely for early detection of cardiac complications. Furthermore, cardiac activity output of individuals under mentally or physically stressful conditions may be used to trigger alert of potentially fatal events such as heart stroke, cardiac disorder and mental break down [2].

With the progress in biomedical engineering, wearable health monitoring devices that provide ease of use and comfort are becoming a popular way to continuously monitor an individual's health condition. Wearable health monitoring devices are employed at places such as the home, an ambulance and a hospital, the military and space coalitions, training, sports etc. The first documented wearable device for monitoring cardiac activity in the form of arterial pulse, called the sphygmometer, was constructed by Étienne-Jules Marey in 1860 [3]. The principle of the device included the application of a needle onto artery and recording its movement. The electrocardiogram (ECG) was discovered in 1872 by Alexander Birmick Muirhead. A special medical device was developed by Einthoven in 1901 and used for getting ECG. After that, many methods of heart rate measurements and cardiorespiratory activity monitoring have been developed. To date, methods of cardiorespiratory activity monitoring can be classified into electrical, electromagnetic, optical, microwave, acoustic or mechanical means. Each of the methods for hemodynamic monitoring has its advantages and limitations. The advantages and disadvantages for each these methods are well reported and discussed in literature. Typical challenges of the existing techniques are related to a need of direct contact with body surface, impact of movement artefacts, invasiveness, and ability of real-time monitoring and analysis of blood pulse waveform. Through these discussions, it was found that a novel, non-invasive method is required to support the continuous monitoring of blood pulse waveform through a wearable device. Such a solution must be small enough to fit the wearable device, capable of operating at low electrical power and be movement-artefacts proof. In addition, in order to support prolonged usage, this method must also be able to operate without the need of a direct contact with body surface.

Overview of the thesis

This thesis introduces and analyzes a non-invasive method for continuous monitoring of central aortic blood (CAP) pressure curve by using electrical bioimpedance (EBI) sensing on the human forearm. This method is based on measuring the change of blood volume by EBI applying AC current into the forearm and sensing the voltage. Using the measurement of current and voltage, it is possible to calculate the impedance of the segment of the body. Measured EBI variations $\Delta Z(t)$ correspond to variations of blood volume due to the heart's activity in each cardiac cycle. It was expected that the volume variations correspond to changes in the blood pressure curve.

The following steps were taken to carry out the research. First, a phantom for mimicking a human forearm was developed [4]. The phantoms can be used to calibrate, compare and evaluate sensing systems before applying them on the real object. In the thesis, a method to produce a gelatin-based tissue-mimicking phantom material is presented as essential part of following development of modelling and simulation. Sodium chloride (NaCl) was used to adjust the electric properties of the phantoms. The results obtained from experiments showed that conductivity of the material increased linearly with NaCl concentration and reliable forearm tissue mimicking samples were produced. The impedance of planar coil placed on the phantoms were measured experimentally in order to compare results to outcomes of simulation with the aim of evaluating FEM simulation accuracy of the eddy current measurement in biomedical applications.

Second, the non-invasive method of central aortic pressure (CAP) evaluating by measuring the electrical bioimpedance (EBI) of radial artery with resistive coupling is introduced. The resistive coupling approach is based on the use of direct contact electrodes that constitute the galvanic contact with tissue. Because EBI measurement instrumentation is sensitive to noise, different electrode placement and configuration strategies were compared to find the most suitable ones by using experimentations and finite element method (FEM) simulations. Significantly novel version of focused impedance method (FIM) was proposed: a five-electrode FIM strategy, namely.

However, the galvanic contact with tissue in resistive coupling method could become an obstacle in prolonged periods of continuous monitoring of cardiac activity: the solution could reduce comfort. The alternative solution in the form of inductive coupling provides the opportunity to overcome the direct contact problems and even acquire cardiac activity through fabric by contact-free monitoring and remote controlling. Another advantage provided by electromagnetic field-based technology is that it allows to capture different electrophysiological parameters instead of using just mechanical movements [5].

As the presence of galvanic contact in EBI measuring is not essential, the object may be excited by eddy currents induced due to time varying magnetic fields. Similarly, as for resistive coupling, the response is measured by registering the eddy currents that are the products of secondary magnetic fields, generated in the excited object. In the thesis, the potentiality of monitoring pulse wave by positioning different induction sensors onto the location of radial artery in the forearm was investigated. The simulations in Comsol Multiphysics (The COMSOL® Software Product) were implemented by using the finite element method on the models of several coil types of different shapes and properties. In addition, the feasibility study of utilization of air-gapped toroidal magnetic cores for monitoring changing volume of pulsating blood in arteries is presented. The results of experimental measurements were validated with simulation of magnetic flux density distribution.

Methodology used in the thesis

Under the alternating electrical excitation, biological tissues expose a complex electrical impedance, which depends on tissue compositions and structures, health status, and applied signal frequency [6]. Over past few decades, a number of impedance based non-invasive tissue characterization and disease diagnosis techniques have been proposed: (1) – bioelectrical impedance analysis (BIA) [7], [8], [9], [10]; (2) – electrical impedance spectroscopy (EIS) [11], [12], [13]; (3) – electrical impedance plethysmography (IPG) [14], [15], [16]; (4) – impedance cardiography (ICG) [17], [18], [19]; and (5) – electrical impedance tomography (EIT) [20], [21], [22].

ICG has been researched since the 1940s. ICG is a technology that calculates the changes of blood volume in transthoracic region over time in terms of variations in the transthoracic electrical bioimpedance. Body impedance is changed due to the blood circulation caused by heart rhythms. Therefore, analysing the transthoracic electrical bioimpedance, the health of the heart along with a number of hemodynamic parameters can be evaluated. The ICG procedure represents the impedance measurement, which is conducted by injecting a low amplitude constant value alternating electric current $i(t)$ (frequency range of 20 kHz to 100 kHz) according to IEC 60601-1 into the volume conductor and measuring the corresponding voltage [23]. The frequency dependent impedance $Z(t)$ is calculated using the ratio of voltage $v(t)$ to current $i(t)$ applied, and the impedance variation $\Delta Z(t)$ is examined.

A promising bioimpedance technique to derive a blood pressure-related waveform from the radial artery is presented in the thesis. A low amplitude current is injected into the forearm on top of radial artery through current electrodes, and the difference on voltage electrodes is measured. Evaluated bioimpedance gives the change of the impedance during the cardiac cycle. With each heartbeat, the volume of the blood in the radial artery changes, and it reflects in an impedance curve, which corresponds to a blood pressure waveform.

Two methods of bioimpedance measurement on radial artery were utilized in the study: (1) – bioimpedance measurement based on resistive coupling, and (2) – bioimpedance measurement based on magnetic induction coupling. Model buildings, simulations and experimental studies were performed for both of these methods with the goal to find the most suitable electrode set-ups for the bioimpedance measurement on the radial artery.

On-body measurement of electrical bioimpedance requires little equipment and simple units [24]. This gives a possibility to make it low cost. These are desirable properties in a biomedical setting. Since the electrical bioimpedance in tissues is a function of such variables as ion concentrations, cell geometry, extracellular fluids, intracellular fluids, organ geometry, etc., changes in these variables could be detectable. However, it is challenging to establish a link between measured impedance change and a change in one or even more of the input variables. This means that electrical bioimpedance measurements, in general, have good sensitivity but poor specificity [24].

For that reason, it may be challenging to create measurement setups of clinical value. When using bioimpedance measurements to diagnose a condition, the chosen setup should detect the particular condition. One way to check this is to test a number of setups on a number of individuals with and without the given condition. However, this is obviously time consuming, and there may be medical reasons to avoid such tests unless they are absolutely necessary. In addition, it could be still unclear how much each tissue or organ has contributed to the final measurement result.

To bypass the problem, phantoms or computer models and simulations could be used, so the specific contribution from tissue and organ can be seen and even quantified. Modelling and simulations become more attractive as computers and software become increasingly capable. Simulations help to understand what is actually measured, and to gain insight in volume impedance experimental measurements. Modelling and simulation tools such as COMSOL Multiphysics® allow to gain understanding of the bioimpedance measurements method without actually doing the measurements.



Figure 0.1 Flow diagrams showing the sequence of activities within the research made.

A 3D geometrical input data from MRI scan of a human forearm was set to a model used to simulate a bioimpedance measurement in the thesis (Figure 0.1). The mesh of the model was merged with electrical properties for the relevant tissues, and a simulation was done in COMSOL Multiphysics®. Available volume output data are sensitivity, current density and magnetic flux density. Available numerical output data is electromagnetic coil impedance. The output data are presented in both, numbers and graphs.

Objectives of the thesis and research questions

The overall goal of the thesis is to give simulation and modelling based suggestions for the design and evaluation of sensors for wearable devices to monitor cardiac activity on radial artery of humans.

The main tasks of the thesis to solve by using are the following:

- A. To investigate the possibilities and precision of bioimpedance method for non-invasive acquisition of the aortic blood pressure waveform by using resistive and inductive coupling.
- B. To develop gelatine phantoms, the electrical conductivity of which could be manipulated with NaCl for mimicking non-invasive acquisition of the aortic blood pressure waveform by using of bio-impedance measurement.
- C. To determine the most suitable configurations and placements of resistive coupling electrodes on the forearm for non-invasive acquisition of the aortic blood pressure waveform.
- D. To investigate induction coils of different shapes and parameters with the goal of determining the most suitable coil features and parameters for non-invasive acquisition of the aortic blood pressure waveform by using inductive coupling.

The research questions raised in the thesis and answered on the bases of simulation and modelling results, are the following:

1. Is the gelatin-based tissue mimicking phantom material manipulated with NaCl sufficiently reliable for bioimpedance measurement?
2. Which resistive coupling electrode configuration and placement strategy has the highest EBI measurement sensitivity in the region of the radial artery?
3. What kind of resistive coupling electrode placements and configurations on the forearm provide the highest extent of changes in measured impedance $Z(t)$, caused by the pulsating volume of blood in the radial artery?
4. Which coils provide the highest response to the changes in measured impedance caused by the pulse in radial artery?
5. Is it possible to increase the extent of changes in measured impedance, caused by the pulse in radial artery in case of the toroidal magnetic coil with a winding concentrated to radial artery position? We applied: (1) – changing relative permeability of the core material, (2) – changing of measurement frequency, and (3) – adding capacitive electrodes for the directing of current density lines.
6. Is it possible to utilize air-gapped toroidal magnetic cores for monitoring volume changes of pulsating blood in radial artery?

Contributions of the thesis

The focus of present work is directed on the development of non-invasive sensors for a wearable device intended to monitor the blood pressure curves (waveforms) from the data acquired from the results of electrical bioimpedance (EBI) measurements on human radial artery. The most interesting is to obtain a central aortic pressure (CAP) curve from the radial EBI variations. The main contributions of thesis work can be summarized as follows:

1. Developing a low-cost, easily obtainable, reliable and stable over time tissue-mimicking phantom material for the research and development of bioimpedance applications, including EBI measurements on phantom material and validations by FEM simulations.
2. The determination of placement and configuration of resistive-coupled electrodes on the forearm that provide the best access to the EBI changes due to the blood volume change, representing the pulsating blood. Simulation study of sensitivity distribution of EBI measurement on forearm model with different placements and configurations of resistively coupled electrodes. A novel method of focused measurement approach was proposed: the five-electrode FIM.

3. The simulation study to determine the inductive coil sensor that proposes the best access to the EBI change due to blood volume variations representing the pulsating blood. The effects of relative permeability of core and frequency selection on the response of impedance change was determined. In addition, it was demonstrated that it is possible to close the eddy current lines through the capacitive electrodes to increase current density in the radial artery region.

This thesis is based on Publications I to V. The outline of the Publications is presented below:

Publication I: Validation of simulations of eddy current methods with measurements on phantom materials for biomedical engineering R&D

Simulations of eddy current measurements were validated with comparison to real measurements on gelatine-based tissue-mimicking phantom materials. The electric conductivity of the phantom materials was adjusted by changing its composition and using van der Pauw method for conductivity validation. Then, COMSOL Multiphysics® FEM simulations of electric impedance of a planar coil on the tissue model were compared to impedance measurements of the planar coil on real phantom material with the same properties. From the results, it was evident that the finite element method can be used for eddy currents in biomedical engineering R&D up to 12 MHz frequency.

Pesti, Ksenija; Kõiv, Hip; Gordon, Rauno (2015). Validation of simulations of eddy current methods with measurements on phantom materials for biomedical engineering R&D. International Journal of Bioelectromagnetism, 17 (2), 57–63.

Publication II: Simulation of the Sensitivity Distribution of Four-Electrode Impedance Sensing on Radial Artery. IEEE Sensors Applications Symposium (SAS) Proceedings

Simulation of non-invasive sensing to evaluate the physical condition of patient through measuring continuous cardiac output on radial artery of human was presented. In order to optimize the signal acquisition, the measurement should possess highest sensitivity in the region. Finite element modelling and simulation of the arterial network of human forearm was described. The spatial sensitivity of four-electrode system for bioimpedance measurements was estimated for different in-line electrode setups and the sensitivity field was described graphically based on FEM simulation.

Pesti, Ksenija; Kõiv, Hip; Min, Mart (2018). Simulation of the Sensitivity Distribution of Four-Electrode Impedance Sensing on Radial Artery. IEEE Sensors Applications Symposium (SAS) Proceedings, Sophia Antipolis, France, 279–285.

Publication III: Electrode Placement Strategies for the Measurement of Radial Artery Bioimpedance: Simulations and Experiments

A non-invasive sensing system that is based on measuring EBI variations of radial artery is proposed to evaluate the physical condition of patient. To optimize the signal acquisition, different electrode placement strategies were compared with the goal of finding the most suitable ones. The finite element method (FEM) simulation of sensitivity distribution and experimental measurements on radial artery were performed for experimenting circular and distal electrode placements. Importantly, also the modified

electrode placement strategies, guided by the idea of focused impedance method (FIM), were investigated. A novel version of FIM based simulation was proposed: a five-electrode FIM strategy.

Pesti, Ksenija; Metshein, Margus; Annus, Paul; Kõiv, Hip; Min, Mart (2021). Electrode Placement Strategies for the Measurement of Radial Artery Bioimpedance: Simulations and Experiments. IEEE Transactions on Instrumentation and Measurement, 70, 1–10.

Publication IV: Feasibility of utilizing air gapped toroidal magnetic cores for detecting pulse wave in radial artery

The feasibility study of utilization of air gapped toroidal magnetic cores for monitoring changing volume of pulsating blood in artery was presented. The changing impedance of conductive path of blood is represented by a single solid core copper wire, connected to a closed circuit with potentiometer. Commercially available toroidal magnetic cores with two different shapes of custom implemented air gaps and desired number of windings were used to induce current in copper wire. The theoretical expectation of the possibility to focus most of the reluctance of emerging magnetic field into the air gap was experimented. The results of on-desk measurements were validated with finite element method simulation of magnetic flux density distribution.

Metshein, Margus; Pesti, Ksenija; Min, Mart; Annus, Paul; Märten, Olev (2020). Feasibility of utilizing air gapped toroidal magnetic cores for detecting pulse wave in radial artery. 17th Biennial Baltic Electronics Conference (BEC) Proceedings (BEC), Tallinn, Estonia, IEEE, 1–5.

Publication V: FPGA-based 16-bit 20MHz device for the inductive measurement of electrical bio-impedance

A novel FPGA based 16-bit 20MHz device has been developed for the measurement of electrical impedance variation in real time. The paper discloses an implementation of the device for monitoring the human cardiorespiratory activity by measuring the bio-impedance variations due to blood pulsation using the magnetic induction method. The device was tested in the frequency range of analogue signals up to 20 MHz, getting 4000 measurement results during every second.

Priidel, Eiko; Pesti, Ksenija; Min, Mart; Ojarand, Jaan; Märten, Olev (2021). FPGA-based 16-bit 20MHz device for the inductive measurement of electrical bio-impedance. International Instrumentation and Measurement Technology Conference (IEEE I2MTC2021), Glasgow, Scotland, May 17-20, 2021 (accepted), 1–6.

1 Background

Bioimpedance analysis requires understanding of the impedance response of human body to externally applied electrical stimulus. The principle of measuring electrical bioimpedance (EBI) gains great attention. This chapter targets to provide the overview of electrical bioimpedance measurement of cardiac activity monitoring, which supports understanding the research described in this thesis.

When electrical properties of the material are known, the questions regarding the distribution of current or electric field in material can be solved with Maxwell's equations. Simulation and modelling is an important part of the scientific research. Finite element simulations of electrical bioimpedance measurement were carried out in the thesis to demonstrate and develop the EBI sensing for monitoring the CAP of blood.

Overview of approaches for continuous central aortic pressure (CAP) estimation based on literature review is presented in this Chapter.

Section 1.1 introduces the principles in characterization of biological tissues in frames of measuring the EBI. Electrical model of tissue is described in the Section. Section 1.2 presents the principles of eddy current approach, which uses electromagnetic induction of excitation current in tissues. Section 1.3 gives an overview of methods for arterial blood pulsation monitoring and explains blood pressure wave curves Section 1.4 introduces the principles of finite element method (FEM) and Maxwell's equations used for modelling and simulation.

1.1 Electrical bioimpedance

Bioimpedance describes the passive electrical properties of biological materials and refers to measuring the corresponding voltage drop in the sample at the applied current. Bioimpedance is a frequency-dependent complex quantity. Due to capacitive effect, it has a voltage phase-shifts with respect to the current in the time-domain.

Bioimpedance measurement technique requires minimally two or more electrodes for applying alternating current, which affects as ion moving in the tissue: namely the ions, not electrons, are the charge carriers in biological tissues. According to [25], the impedance between the electrodes may reflect “seasonal variations, blood flow, cardiac activity, respired volume, bladder, blood and kidney volumes, uterine contractions, nervous activity, the galvanic skin reflex, the volume of blood cells, clotting, blood pressure and salivation [26]. Impedance spectroscopy gives important information about tissues and membrane structures and extracellular liquid distributions [26]. In the medical applications, bioimpedance provides high sensitivity, is invasive, and gives real-time measurements. Unfortunately, since bioimpedance depends on several phenomena, selection of this, which is of interest requires specific filtering and other parameter extraction methods.

1.1.1 Electrical impedance

Impedance is a general term related to the ability to oppose alternating current (AC) flow, expressed as the ratio between an AC sinusoidal voltage and an AC sinusoidal current in an electric circuit [26] or electrically conductive environment. In practice, two possibilities exist: (1) – a voltage is applied to an object and the current passing through the object is measured, or (2) – a small constant value current at a fixed frequency is passed through electrodes and the voltage drop between electrodes shows a measure of impedance. Impedance is a complex quantity, where the real part is the resistance R and the imaginary part is reactance X :

$$X_C = -\frac{1}{2\pi f C} \quad (1)$$

$$X_L = 2\pi f L \quad (2)$$

$$Z = R + jX \quad (3)$$

where X_C is capacitive and X_L inductive reactance, f is the frequency, Z is impedance, C is capacitance, R is resistance and j is an imaginary unit. Remark: the inductive reactance X_L is absent in biological tissues. When capacitive element is involved in high frequency AC circuit, the reactance of it has a negative value (1), and also a negative phase shift appears between current and voltage, which can be expressed in degrees. AC voltage that appears across the ideal capacitive element is -90° out of phase as a result to current flowing through capacitive element. Ideal resistive element exhibits in-phase properties (zero phase shift). In a circuit with both elements present, the phase difference lays somewhere in between 0° and -90° , depending on the actual values of elements.

The impedance Z could be divided into real (ReZ) and imaginary part (ImZ):

$$Z = ReZ + jImZ \quad (4)$$

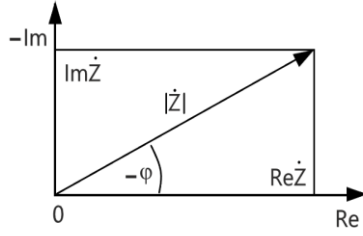


Figure 1.1 Impedance vector $|Z|$ with real (ReZ) and imaginary (ImZ) parts. Remark: imaginary axis represents negative values here.

The impedance vector $|Z|$ in Cartesian coordinate system can be seen in Figure 1.1 with the length $|Z|$ as magnitude and the phase angle φ , which are represented as follows:

$$|Z| = \sqrt{ReZ^2 + ImZ^2} \quad (5)$$

$$\varphi = \arctan(ImZ/ReZ) \quad (6)$$

1.1.2 Electrical model of cell and tissue

Tissue electrical parameters depend fundamentally on its physiology and various phenomena. Tissue is composed of cells with poorly conducting thin cell membranes and well conductive fluids inside and outside of cell [26].

The electrical model of cell and its environment (Figure 1.2a) describes the cell membrane as dielectric layer and extracellular and intracellular media are modelled as resistances. Variations of cell's electrical model are presented in Figure 1.2. The circuit in the Figure 1.2b is equivalent to the model shown in Figure 1.2a after performing some simplifications. Moreover, the membrane conductance is very low and usually resistance representing membrane (R_m) is ignored, therefore (Figure 1.3c). This electrical model of cell employed by [27] is considered to be a good approximation of the passive electrical properties of a single cell for frequencies up to several MHz [28]. The Fricke-Morse model has been widely used in EBI analysis due to its simplicity for direct physical interpretation and its ability to describe the main dispersion in the frequency range of 1 kHz to 10 MHz (β -dispersion) [27]. With the model (Figure 1.2c), cells are modelled with just three elements.

In a tissue, the impedance contribution from all cells is combined so that the same electrical model (obviously with different values) can characterize the impedance behavior: a resistance representing the extracellular medium (R_e) in parallel with the series combination of a capacitance (C_m) representing the membranes, and resistance which represents the intracellular medium (R_i). The resistive behavior of the extracellular and intracellular media is basically due to their contents of ions: most abundant ions in the extracellular medium are Na^+ and Cl^- and the most abundant ion is K^+ in the intracellular media [28].

Similarly to capacitive behavior in the frequency domain, the low frequency currents will not penetrate into the cell, meaning that $Z = R_e$, whereas high frequency currents will flow freely through the cell membrane, which results as a voltage phase-shift in respect to the current in the time-domain. The impedance value Z results at higher frequencies as $Z = R_i R_e / (R_i + R_e)$.

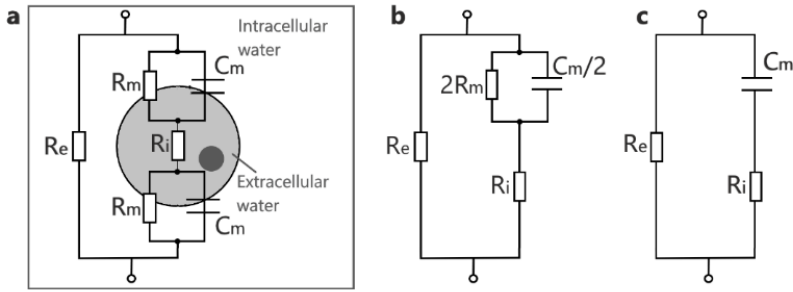


Figure 1.2 Single cell with equivalent circuit (a), its simplified mode (b) and Fricke-Morse model (c).

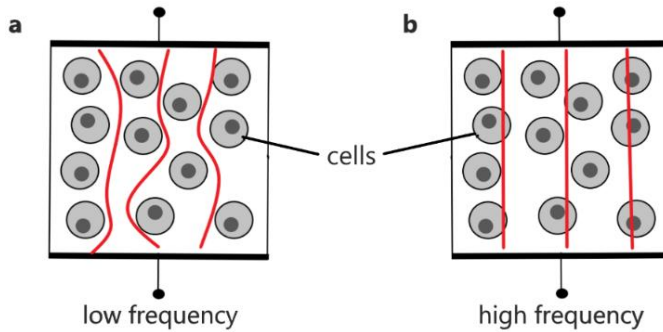


Figure 1.3 Graphical representation of current flow through a tissue at low frequency (a) and high frequency (b).

Graphical representation of current flow through a tissue at low and high frequencies is shown on Figure 1.3. Idealized graph of the impedance magnitude is presented in Figure 1.4.

Described model is reasonable for dilute cell suspensions. However, the tissue bioimpedance tends to be more complex and it is necessary to substitute the capacitance in the previous models. The solution proposed by Fricke [29] includes adding an additional parameter α supposed to depict the effective non-ideal capacitor instead of ideal capacitor (in the case of $\alpha = 1$). Parameter α obtains values in the range $0 \leq \alpha \leq 1$ and expresses the displacement of a center of the circular line below the real axis in impedance phasor diagram (see Figure 2.1b). The Cole-Cole equation represents mathematically the dielectric parameters of biological tissues and can be defined in terms of complex permittivity, complex conductivity, and the overall impedance [10].

The dependence of impedance on frequency ω (due to the capacitive effects of cell membranes) is presented in Cole-Cole equation:

$$Z(\omega) = R_{\infty} + \frac{R_0 - R_{\infty}}{1 + (j\omega\tau)^{1-\alpha}} \quad (7)$$

where $Z(\omega)$ is the impedance, R_{∞} is the resistance at very high frequency, R_0 is the resistance at very low frequency, ω is an angular frequency ($\omega = 2\pi f$) and τ is the relaxation time of the system or time constant.

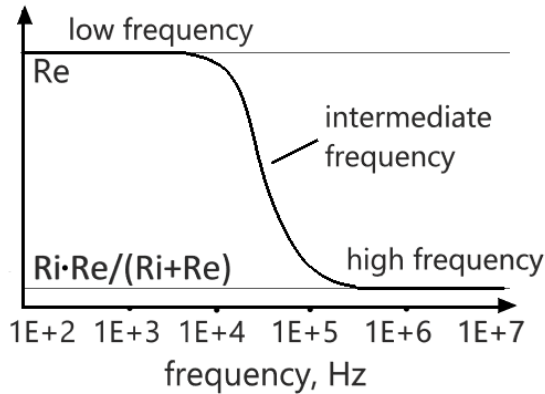


Figure 1.4 Idealized graph of magnitude of the tissue's impedance.

1.1.3 Electrical properties of biological tissue

The electrical properties of biological tissues have been of interest over a century, starting when electrical resistance and capacitance measurement instruments became available [30]. Determining of electrical properties of body tissues includes many methods, such as impedance techniques, electrocardiography, nerve transmission etc. It offers attractive prospective technologies for biomedical applications, such as functional electrical stimulation and the diagnosis and treatment of various physiological conditions with weak electric currents, radio-frequency hyperthermia, electrocardiography, and body composition. In general, a tissue is defined as a group of similar cells and their intercellular substance joined together to perform a specific function [31]. Tissues make up organs and various parts of the body. For example, tissues of the body are skin, muscle, fat, tendon, nerve, blood, marrow and cortical bone etc. Fluids produced by living organism like blood, lymph, saliva, urine, gastric juice etc. are termed as biological fluids.

Biological tissues may be regarded in two ways: (1) as a volume conductor, or (2) a dielectric. At frequencies lower than 100 kHz, the most tissues are dominantly electrolytic conductors with ionic charge carriers [32]. At higher frequencies, the dielectric properties of tissue may dominate [32]. When electric field is applied in the tissue the free ions start migrating according to electrolytic characteristics of the tissue.

Electrical conductivity σ is a fundamental property of a material that quantifies a measure of a material's ability to conduct electrical current. It is defined as the ratio of the current density to the electric field strength:

$$\sigma = \frac{J}{E} \quad (8)$$

where J is current density, E is electric field strength and σ is electrical conductivity. Conductivity is inverse of electrical resistivity ρ :

$$\sigma = \frac{1}{\rho} \quad (9)$$

Static relative permittivity ϵ_r of a material describes the ability to permit storage of electric energy [32]. It is defined as the ratio of the amount of stored electrical energy when a potential is applied, relative to the permittivity of a vacuum.

The relative permittivity ϵ_r is complex and frequency-dependent:

$$\epsilon_r = \frac{\epsilon(\omega)}{\epsilon_0} \quad (10)$$

where $\epsilon(\omega)$ is permittivity evaluated for the frequency, ϵ_0 is the electric constant and ϵ_r is relative permittivity. The static relative permittivity ϵ_r is the relative permittivity for a frequency of zero.

A key concept in understanding the electrical properties of tissues is polarization. Generally, polarization is the disturbance of the charge distribution in a region, induced by electric field [32]. Living cells are polarizable and their membranes could be polarized. An electric field displaces the charges, positive and negative charges move to opposite directions, dipoles are formed, and material is polarized. Dipole is an electric doublet, which consists of two equal but opposite sign charges, kept at a small distance and thus hindered to recombine [32]. Polarization and permittivity are related closely. High polarization means high permittivity. Permittivity is a measure of the amount of dipole moment density induced by an electric field:

$$D = \epsilon E = \epsilon_0 E + P \quad (11)$$

where D is a dipole moment density and P is polarization.

The dielectric permittivity represents a combined macroscopic effect of various molecular phenomena causing electrical polarization. Schwan (1957) introduced α -, β - and γ -dispersion regions in the dielectric permittivity graph to characterize the anomalous electric properties of biomaterials [33]. The contribution of each of the phenomena varies with frequency (Table 1.1). The permittivity usually has a frequency-dependent part and frequency-independent part. First is due to ionic conduction and the second is due to dielectric relaxation [30]. The frequency dependence of permittivity will determine the frequency dependence of conductivity and conversely [30]. When conductivity increases with frequency, then the permittivity decreases.

Figure 1.5 shows how permittivity in biological materials typically decreases with increasing frequency. Such clearly separated dispersions can be found with cell suspensions [32]. When dealing with a highly non-uniform structure, like most tissues are, more than one specific interaction mechanism to dispersion is presented at specific frequency range. The dispersion regions are much broader and overlapping [32].

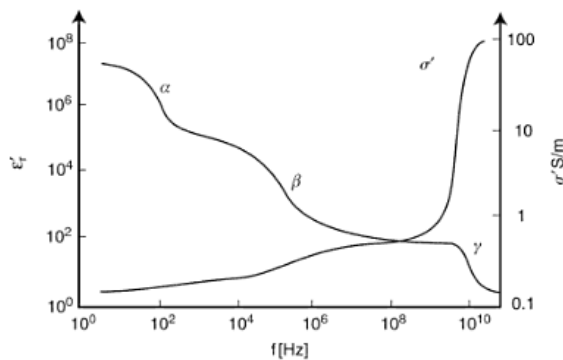


Figure 1.5 Dispersion regions for a tissue, idealized. Modified from Schwan (1988) [32].

Table 1.1 Dielectric dispersion regions [32].

Dispersion type	Characteristic frequency	Mechanism
α	mHz - kHz	Counterion effects (perpendicular or lateral) near the membrane surfaces, active cell membrane effects and gated channels, intracellular structures (e.g. sarcotubular system), ionic diffusion, dielectric losses (at lower frequencies the lower the conductivity)
β	0.1 – 100 MHz	Maxwell-Wagner effects, passive cell membrane capacitance, intracellular organelle membranes, protein molecule response
γ	0.1 – 100 GHz	Dipolar mechanisms in polar media such as water, salts and proteins

1.2 Principles of the induced current approach

Magnetically induced currents, known as eddy current in practice (also called Foucault current according to Jean Bernard Leon Foucault (1819–1868)), are created through a process called electromagnetic induction discovered by Michael Faraday (1791–1867). The eddy current method is used in many different industrial applications, such as non-destructive testing (NDT) etc. and in different biomedical application such as recognizing pathological tissue from healthy tissue, monitoring cardio-respiratory activity etc.

In its most basic form, the eddy current measurement model consists of a primary coil excited by an alternating voltage at a fixed frequency, and a detecting secondary coil. Every coil is characterized by the impedance Z_0 which is a complex number defined as:

$$Z_0 = \frac{V_0}{I_0} = R_0 + jX_0 = \sqrt{R_0^2 + X_0^2} = |Z|_{\varphi} \quad (12)$$

$$\tan\varphi = \frac{X_0}{R_0} \quad (13)$$

where $|Z|$ is impedance magnitude and φ is a phase angle.

When an AC excites a coil, it creates a time-varying magnetic field with magnetic flux lines concentrated at the centre of the coil. A time-varying magnetic induction flux density induces currents in an electrical conductor.

The electromotive force E is proportional to the time-rate change of the magnetic flux density Φ_B :

$$E = -\frac{d\Phi_B}{dt} \quad (14)$$

When the primary coil approaches an electrically conductive material, eddy current induced in the material and alter the induced voltage and phase on the detecting coil. The induced currents flowing within the test material and generate a secondary magnetic field. This magnetic field contributes to oppose the primary magnetic field and has a weakening effect on the primary magnetic field (Figure 1.6).

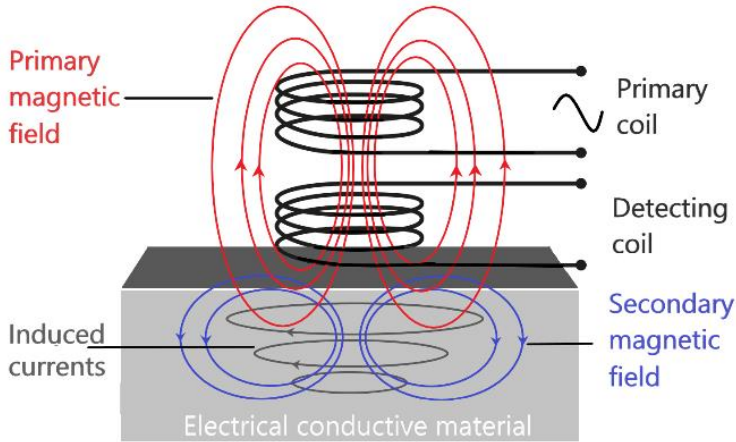


Figure 1.6 Basic model of eddy current measurement.

Variations in the electrical conductivity and magnetic permeability of the different test materials causes a change in eddy current and a corresponding change in phase and amplitude that can be detected by measuring the impedance changes in the detecting coil.

1.2.1 Frequency and skin effect

Eddy current flow is not constantly distributed throughout the entire volume of test material: it is stronger at the surface decreasing with the distance from the surface. This phenomenon is known as the skin effect. The skin effect appears when eddy currents at any depth produce magnetic fields which oppose the primary field. These magnetic fields cause the net magnetic flux reduction and decrease in current flow when depth increases.

The depth of penetration decreases with increasing frequency and increasing conductivity and magnetic permeability. The standard depth of penetration δ is defined as the depth, at which eddy current intensity drops to $1/e$ (about 37%) of their surface density.

$$\delta \approx \frac{1}{\sqrt{\pi f \mu \sigma}} \quad (15)$$

where δ is standard depth of penetration, f is test frequency, μ is magnetic permeability and σ is electrical conductivity. Figure 1.7 illustrates the electromagnetic field penetration inside a material at two different frequencies.

The sensitivity of eddy current measurements depends on the density of induced currents at the object. So, it is important to consider the strength of eddy current at the location of interest. The estimation of depth of penetration for each of the tissues of forearm shows that the eddy current EBI measurement on forearm is not limited by the skin depth at frequency used in the research presented in the thesis (Section 4). For inductive sensing it is preferable to use higher frequencies (e.g. 10 MHz instead of 100 kHz, which is widely used in resistive coupling measurement) [34]. Human tissues have low electrical conductivity in comparison with metals, therefore measurements at higher frequencies have more reasonable penetration depth of the generated electromagnetic field in the body [34].

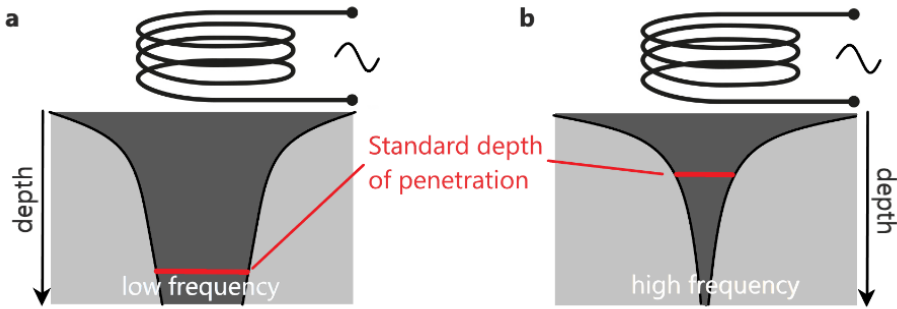


Figure 1.7 Illustration of the electromagnetic field penetration inside a material at low frequency (a) and high frequency (b).

1.3 Monitoring of central aortic pressure of blood

Cardiovascular diseases (CVDs) is a frequent cause of death globally. Evaluation of CVDs involves continuous measurement of patient's blood pressure (BP) showing the real load on the heart. Arterial blood pressure is a fundamental cardiovascular variable and it is routinely measured in perioperative and intensive care medicine. BP monitoring is mandatory in patients having surgery with anaesthesia and patients with circulatory shock [35]. BP measurements have a significant impact on patient management in intensive care and perioperative medicine, especially for the timely identification and correct treatment of hypotension [36]. In addition, BP waveform commits insights into the diagnosis of many disease states like coronary artery disease, obstructive sleep apnea, diabetes etc. [37].

At the moment, the most accurate and preferable method of continuous monitoring of BP is the direct invasive measurement, using intra-arterial catheter, which is inserted into the aorta through radial or femoral artery. However, this invasive procedure could cause several complications to the patient: infections, haemorrhages, hematomas, and arterial embolization [38]. Alternative non-invasive sensing methods for continuous BP estimation are presented in this section.

1.3.1 Blood pressure wave curve

Central aortic pressure (CAP) of blood is the pressure in the ascending aorta, just after the left ventricle. CAP of blood is the pressure that the target organs of body are exposed [36]. When the left ventricle ejects blood into the aorta, the CAP of blood rises and maximal following ejection is termed the systolic pressure (SP). When the left ventricle is relaxing and refilling, the CAP of blood decreases until its lowest value, which occurs just before the ventricle ejects blood into the aorta (diastolic pressure (DP)).

When BP is measured using a sphygmomanometer, the upper value is the systolic pressure (SP) and the lower value is the diastolic pressure (DP). The difference between the SP and DP is called aortic pulse pressure (PP).

The pulse limited by the upper and lower value of BP, consists of a series of harmonics moving along the arterial tree. The pulse pressure wave is formed from the combination of the pressure wave generated by the left ventricle in systole and waves reflected back from the peripheral vascular system at the interface between large arteries, arteries and arterioles (Figure 1.8).

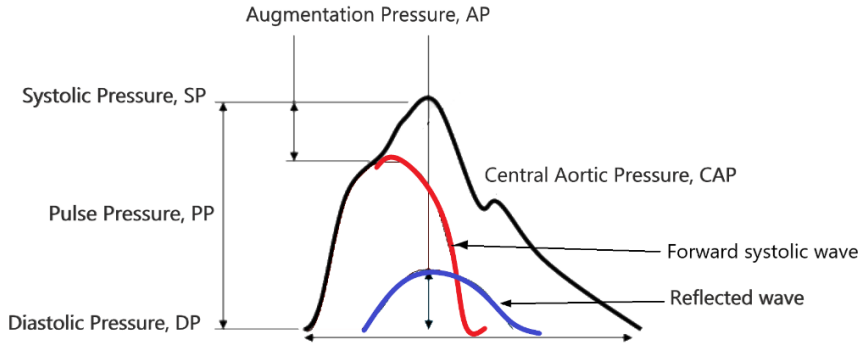


Figure 1.8 Central aortic pressure waveform as a sum of forward and reflected waves.

When arterial pressure is measured, the SP and DP are slightly different than the pressure found in the aorta (CAP) or the pressure found in other distributing arteries. As the PP travels down the aorta and into distributing arteries, there are characteristic changes in the SP and DP. The SP increases and the DP decreases, therefore the PP rises, as the pressure pulse travels away from the aorta (Figure 1.9). This occurs because of reflective waves from vessel branching.

Pressure wave recorded anywhere in the arterial network depends on the pattern of left ventricular ejection, viscoelastic properties of the artery, the viscosity of the blood, wave reflection and wave dispersion. These key parameters are directly influenced by the state of health and fitness of the patient and depend on hemodynamic and pathophysiological characteristics of each subject. Among all these characteristics, age, heart rate, aortic stiffening, body height, sex, and increased BP are the most important factors that account for influencing of the difference between CAP of blood and arterial BP. The clinical importance of measuring CAP of blood instead of arterial BP is based on the evidence of a strong prediction of adverse events in both general population samples and in large groups of patients with similar cardiovascular risk factors or diseases.

By using mathematical transformation (transfer functions (TF)), it is possible to evaluate the central aortic pressure and wave form from the arterial blood pressure waveform, calibrated by peripheral BP. Applying a valid transfer function allows derivation of an aortic pressure waveform (Figure 1.10). A TF encodes the alterations introduced by the arterial tree on the original signal, which generates the aortic waveform, and assumes that the properties of the upper limb arteries are virtually identical between individuals [39].

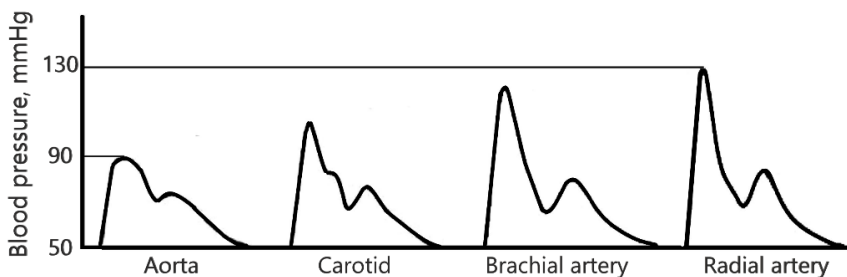


Figure 1.9 Amplification of blood pressure (BP) curve from aorta to peripheral arteries.

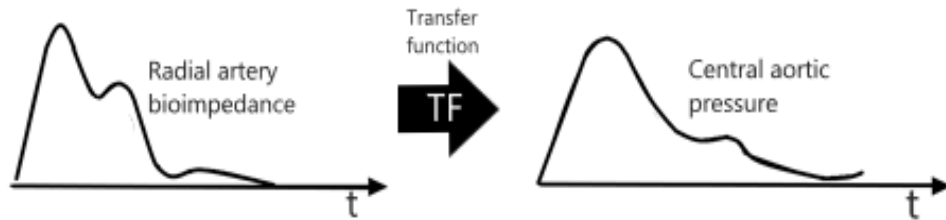


Figure 1.10 CAP waveform reconstruction from measured cycle of EBI waveform by the aid of transfer function TF.

1.3.2 State of the art of continuous CAP estimation

Currently the most accurate and common method for CAP estimation in medical practice is an invasive approach, when a pressure transducer is connected to the tube catheter inserted into the aorta or artery. In addition to the CAP monitoring, intra-arterial catheters are used as an intravascular access for blood sampling in high-risk surgical and critically ill patients. The risks of the method include: (1) pain and discomfort during placement of the catheter, (2) possible infections, (3) danger of blood clots formation, and (4) bleeding [40]. Also, invasive measurement of CAP cannot be routinely applied in asymptomatic patients. Therefore, noninvasive methods must be relied on.

The noninvasive measurement of CAP is based on the analysis of an arterial waveform estimated by different methods, usually calibrated with brachial BP [39]. One of the most attractive non-invasive approaches to detect the central aortic pressure CAP is the carotid or radial artery applanation tonometry, which has the widest application in devices performing pulse wave analysis [41]. In applanation tonometry, a pressure sensor is placed manually onto the radial artery, and a constant applanation is applied against the blood vessel for the waveform reading. The measured pressure signal is then translated into the aortic pressure waveforms using TF. Applanation tonometry, performed directly with a hand-held tonometer, requires skills and training for pressure waveform recordings, therefore the recordings are operator-dependent. However, more recently, new devices have been developed allowing an operator-independent recording of the arterial pressure waveform (Omron HEM-9000AI) [39]. Table 1.2 compares available applanation tonometry devices for estimation of the CAP of blood.

Another method of non-invasive continuous BP monitoring is oscillometric approach (Arteriograph™; TensioMed Kft) using a brachial BP cuff. When the pressure in the cuff is higher than the BP inside the artery, the artery is squeezed. As the pressure in the cuff decreases and drops below SP, blood starts to flow in the artery. These spurts of blood flow cause the artery in the cuffed region to expand with each pulse. With each pulse the characteristic so called Korotkoff sounds could be detected. Cuff pressure oscillations could be recorded to detect pulsatile blood: cuff pressure is high pass filtered to extract the small oscillations at the cardiac frequency and the envelope of these oscillations is computed [42]. The challenges of the method include: (1) sensitivity to differences in pulse pressure and artery stiffness, (2) accurate extraction of systolic and diastolic pressures from the envelope of cuff pressure oscillations [42], and (3) the need to use instrumentation properly validated for specific population groups and subject characteristics [43].

A further promising technique to evaluate a BP wave form from radial artery is bioimpedance [44], [45], [46]. This approach involves EBI measurement on the radial

artery on the wrist, so the changes of artery impedance are translated into the central aortic pressure curve using transfer function (TF). A low amplitude current is directed to the forearm on top of radial artery through electrodes, and a voltage difference between electrodes is measured. The bioimpedance variations (ΔZ) correspond to variations of blood volume due to the heart's activity in each cardiac cycle. The thesis focuses on the research concerning EBI sensing method for measurements on pulsating radial artery to evaluate central aortic pressure waveform. Detailed specifications of the method are presented further in this thesis.

Table 1.2 Comparison of different devices using tonometry method to measure CAP, modified from [4].

Device	Company	Method of estimation	Advantages (+) and disadvantages (-)
SphygmoCor	AltCorMedical	GTF (radial-aortic)	(+): industrial standard for non-invasive CAP estimation, opportunity to select the best possible reading to minimize artefacts (-): compression of artery, handheld, operator dependent, poor reproducibility
BPro	HealthSTATS	GTF (N-point average)	(+): 24 h measuring at home environment, FDA and CE approved (-): compression of artery, inconsistent pressure
TL-300	Tensys Medical	GTF (radial-aortic)	(+): wrist bracelet (-): moving artefacts, measurement only by clinical personnel.
HEM-9000AI	Omron Healthcare	Linear regression algorithm	(+): array of sensors (-): inconsistent pressure

1.4 Modelling and Simulation

Simulation and modelling is an important part of engineering, manufacturing and scientific research used to simulate designs, devices and processes. These could be utilized to mimic the behaviour of a system or phenomena and to analyse different theoretical models. Using simulations have many advantages, for example: (1) different levels of abstractions help us to understand behaviour of the system and its parts at all levels, (2) minimizing costs, (3) decreasing design time, and (4) finding effective methods for demonstrating processes in time and frequency domain, etc. However, computation is limited and due to simplifying the model some mismatches could appear in simulated outcomes compared to later real results.

Finite element (FE) simulations of EBI measurement were carried out using COMSOL Multiphysics® in the thesis to demonstrate and develop the EBI sensing for monitoring the CAP of blood. Modelling workflow consists of the following main steps:

1. Set up the model environment;
2. Creating definitions;
3. Building a geometry of forearm and electrodes;
4. Defining the material properties for each boundary and domain;
5. Defining physics boundary conditions;
6. Creating the mesh;
7. Setting up study steps and solver configurations and computing with the model;
8. Post-processing the results.

1.4.1 Finite element method

When electrical properties of the material are known, the questions regarding the distribution of current or electric field in a homogeneous or composite material can be solved with Maxwell's equations. Generally, there are two types of problems to be solved in differential equations: (1) initial value problems (differential equation with an initial condition to specify the value of unknown at some particular point in the domain, and (2) boundary value problems (computing of the values of interior, when the values on the material boundary are known). An example of boundary value problem in bioimpedance research is evaluation of the current distribution in tissue from excitation with electrodes placed on the surface of the material.

As the Maxwell's equations basically describe an infinite-dimensional object, finite-dimensional approximation should be used to represent the solution. One form of such approximation is the finite element method (FEM). This method involves dividing the geometry into small elements and the solution is expressed as the weighted sum of basic functions in each element [32]. In the thesis, the finite element method is used to solve the model.

When solving complex three-dimensional models with frequency dependent tissue parameters, it is important to define the problem in the simplest way to reduce the computing time. The results are more easily obtained, if three-dimensional problem may be reduced by symmetry to two dimensions.

1.4.2 Maxwell's equations

A mathematical equation is an idealized model to describe real phenomena. The problem of electromagnetic analysis is of solving Maxwell's equations of certain boundary conditions [47]. Maxwell's equations are a set of equations, stating the relationships between the fundamental electromagnetic quantities:

- Electric field strength E , $[V/m]$;
- Electric displacement or electric flux density D , $[C/m^2]$;
- Magnetic field strength H , $[A/m]$;
- Magnetic flux density B , $[T]$;
- Current density J , $[A/m^2]$;
- Electric charge density ρ , $[C/m^3]$; [47].

The FEM handles differential equations and for this reason, the differential form of equations is used in the thesis. Maxwell equations, written in differential form, relate to a point in space. For general time-varying electromagnetic fields, Maxwell's equations can be written as:

$$\nabla \times H = J + \frac{\partial D}{\partial t} \quad (16)$$

$$\nabla \times E = -\frac{\partial B}{\partial t} \quad (17)$$

$$\nabla \cdot D = \rho \quad (18)$$

$$\nabla \cdot B = 0 \quad (19)$$

where ∇ is the differential vector operator $\nabla = \frac{i\partial}{\partial x} + \frac{j\partial}{\partial y} + \frac{k\partial}{\partial z}$, and i , j and k are the unity vectors in a Cartesian coordinate system, and P is electric polarization. Equation 16 refers Maxwell-Ampère's law. Equation 17 refers Faraday's law. Equation 18 and 19 are two forms of Gauss' law: the electric and magnetic form, respectively. The equations 15 and 16 are extremely robust and also valid under nonhomogeneous, nonlinear, and anisotropic conditions and relate the time and space derivatives at a point to the current density in the point [48]. Another basic equation is the equation of continuity:

$$\nabla \cdot J = -\frac{\partial \rho}{\partial t} \quad (20)$$

The equations that describe the relations of macroscopic properties of the medium are given as:

$$D = \varepsilon_0 E + P \quad (21)$$

$$B = \mu_0 (H + M) \quad (22)$$

$$J = E \cdot \sigma \quad (23)$$

where ε_0 is the permittivity of vacuum, μ_0 is the permeability of vacuum, and σ is the electrical conductivity. The electric polarization vector P describes material polarization when an electric field E is present. It can be interpreted as the volume density of electric dipole moments [47]. Similarly, the magnetization vector M describes how the material is magnetized when a magnetic field H is present. It can be interpreted as the volume density of magnetic dipole moments [47].

2 Eddy Current Bioimpedance Measurement on a Tissue Mimicking Phantom Materials

With the increased use of bioimpedance analysis in biomedical engineering applications, the ability to provide phantoms that are capable of mimicking desired properties of body tissues is important. On this account, gelatine-based phantom materials with realistic electrical properties were produced. This chapter focuses on the considerations for developing phantom materials, specifically to exhibit the dielectric properties of a human forearm tissues for bioimpedance analysis. Sodium chloride (NaCl, 99+%) was utilized to achieve different electrical constants typical to several tissues. Electrical conductivity of each phantom material sample was then obtained using van der Pauw (vdP) method [49]. Based on outcomes of the research, it was demonstrated that a reasonably accurate tissue mimicking phantom samples could be produced using a gelatine base with additives. Hence, it is possible to construct phantoms that mimics electrical properties of specific tissue for the purpose of biomedical engineering studies. Those phantoms could be used in the development of medical diagnostic systems that use bioimpedance measurement with: either conductive electrodes or eddy currents to estimate the physiological state and processes in the patient [50].

In addition, simulations of eddy current measurements were validated with comparison to real measurements on phantom materials. The results of COMSOL Multiphysics® FEM simulations of electric impedance of a planar coil placed on the tissue model were compared to impedance measurements of the planar coil on real phantom material with the same properties.

This chapter is based on the author's publications I and [50], and is organized as follows. In Section 2.1 the basics and directions concerning tissue-mimicking phantoms developing for bioimpedance analyses are introduced. Section 2.2 describes developing, implementation and calibration of gelatine tissue mimicking phantom. Section 2.3 focuses on the validation of simulations of eddy current methods with actual measurements on phantom materials. Section 2.4 summarizes the chapter.

2.1 Introduction

Concerns about tissue-mimicking phantoms for bioimpedance analyses are introduced. The aim of the research is set up and the study features are presented in the section.

2.1.1 Dielectric properties of the tissue mimicking phantom material

Dielectric properties of tissues are complex and heterogeneous and the electrical response of tissues varies significantly for each individual and physiological condition. Also, the frequency response of tissues is different for each tissue type. The studies of the dielectric parameters of human body tissues have been compiled by Gabriel [51] in terms of conductivity and relative permittivity. The dielectric response of tissues derives from the complex dielectric relaxation dispersion over their frequency range response [10]. In 1941 Cole and Cole proposed a theory to represent mathematically the dielectric parameters of biological tissues [29]. The Cole equation defined in terms of impedance is shown below [10]:

$$Z(\omega) = R_{\infty} + \frac{R_0 - R_{\infty}}{1 + (j\omega\tau)^{1-\alpha}} \quad (24)$$

The equation can be visualized as a Nyquist plot where the real and imaginary parts of the impedance are presented as a function of frequency (Figure 2.1b). Also, the impedance can be geometrically interpreted with Bode plot where the abscissa is a logarithmic scale of the frequency and one ordinate is the logarithm of the impedance Z while the second ordinate is the phase shift Φ (Figure 2.1a).

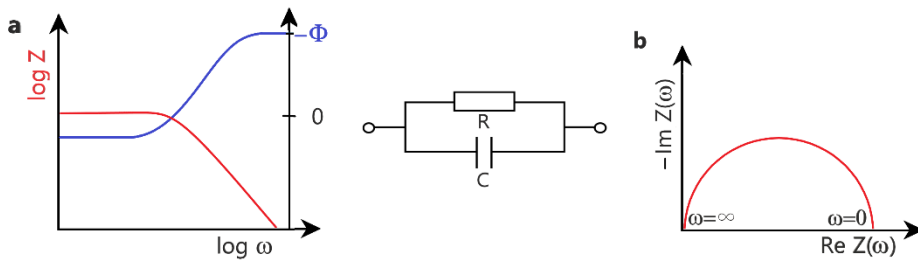


Figure 2.1 Bode plot (a) and Nyquist (Cole) plot (b) for representing the impedance of parallel RC circuit.

2.1.2 Tissue-mimicking phantoms for bioimpedance analysis

In medical imaging applications, phantoms with known geometry and material composition are frequently used in the development of measuring and imaging systems or algorithms [52]. The tissue-mimicking phantoms imitate essential properties of biological tissues with the aim of providing clinically realistic measurement and imaging environment. In comparison to real tissues, phantoms provide repeatable and adaptable materials with needed mechanical, structural and other properties with the goal to accurately mimic human tissues [53].

Certain properties of tissue, like in case of BIA dielectric properties, are of critical importance when constructing a tissue-mimicking phantom and must be mimicked within a tissue-imitating geometry. Several studies [53], [54] introduced materials for imitating human soft tissues and organs with specified dielectric properties. Phantom materials were introduced to simulate electrical properties of the human torso [55]. A gel phantom to mimic different muscle tissues was developed [53].

Due to tissue complexity and heterogeneity, it is challenging to estimate their dielectric properties. The electrical response varies significantly for each tissue type and physiological condition. Therefore, the development of a phantom becomes application specific [10].

Many phantom materials are available for mimicking human tissues. These could be classified as hydrogels, organogels, and flexible elastomer materials for radiological tissue parameters [56]. Agar, agarose, and gelatine gels, manipulated by varying NaCl concentration from 0–1 mg/ml are often utilized for mimicking tissue electrical properties [57].

2.1.3 Study and motivation

The purpose of this work is to test and develop tissue phantom materials to mimic the electrical response of human forearm tissue for the continued development of hemodynamic monitoring by using EBI. Phantoms are useful for research and development as these are reproducible and stable with controlled properties. Also, human experiments could be reduced when proper tissue-similar sample is available [58]. Phantoms help to gain insight in volume impedance experimental measurements.

In this study, gelatine was utilized as the phantom base. The development of such phantom material was continued by the research group and phantom of forearm with radial artery for EBI measurement was presented in 2018 [4] (see Figure 2.2). However, the study presented in the thesis focuses only on determining the dielectric parameters of the phantom material and does not consider the mechanical and geometrical properties of forearm tissues. The tissues have been considered to be isotropic and homogenous.

The impedance of the material, measured with eddy current sensors, and the results of respective eddy current measurement simulation were compared and discussed in order to evaluate FEM simulation accuracy for biomedical applications. Accurate computer simulation with valid results is a valuable research tool in biomedical engineering.



Figure 2.2 Forearm phantom prepared for EBI measurement [4].

2.2 Manufacturing and Calibration of Gelatine Tissue-Mimicking Phantoms

The samples of gelatine tissue mimicking phantoms with defined electric conductivities were produced and reported in [50]. This involves preparing the phantom material, designing PCB-s for impedance measurements and measuring impedance of the sample with Van der Pauw (VdP) method. Different electrical conductivities of phantom materials were achieved by adjusting different amounts of sodium chloride. To develop tissue mimicking phantoms with realistic electrical properties, the respective electric conductivities were obtained from [51] and used as guidelines in phantom development. The mixture was placed into Plexiglas enclosure with two double-sided printed circuit boards (PCB) for measurements. Measurements within frequency range from 100 Hz to 100 MHz were held using impedance analyser. Conductivity of phantom material was calculated at a single frequency of 10 kHz.

2.2.1 Composition and manufacturing of gelatine tissue mimicking phantoms

Phantoms made of solidifying liquid materials with gelatine were produced due to simplicity of manufacturing and acquisition of ingredients, also ease to simulate electrical properties of many different biological tissues. Gelatine was used in this study as it is commercially available, cheap, and it melts at 35°C (when agar needs more heating (85°C)). The composition of phantom material included: (1) distilled water and (2) gelatin to form the phantom body, (3) formaldehyde solution (37 wt.%) to rise melting temperature of material, so it could be used later in room temperature (22°C – 25°C), (4) Ethyl 4-hydroxybenzoate (99+%) and (5) Germall® Plus. Germall® to prevent bacterial invasion, and (6) Sodium chloride (NaCl, 99+%) to adjust different electrical constants of phantom materials. Table 2.1 shows an example of a phantom mixture used in the study.

The phantom material manufacturing (Figure 2.3) procedure included following steps:

1. Gelatine was added to distilled water for dilation.
2. The diluted mixture was placed on hot water bath till it became clear and homogeneous.
3. After the temperature of mixture has dropped to 30°C – 35°C the rest of distilled water, Formaldehyde solution (37 wt.%), Germall® Plus, Sodium chloride (NaCl, 99+%) were added to the mixture and mixed.
4. The phantom mixture was placed into designed Plexiglas enclosure with inner dimensions of 50mm x 50mm x 50mm. A rotation machine was used during solidifying to obtain more homogeneous phantom.
5. The phantom is later placed in the refrigerator for storage.

Table 2.1 Gelatin tissue mimicking phantom mixture ingredients [50].

Ingredient	Amount
Distilled water	250 ml for dilation 333 ml added later
Gelatine powder	40 g
Formaldehyde solution (37 wt.%)	2 ml
Ethyl 4-hydroxybenzoate (99+%)	3 g
Sodium chloride (NaCl, 99+%)	0 – 5 g



Figure 2.3 Manufacturing of gelatine based phantom material.

2.2.2 Measurement of electrical conductivity of the unique gelatin phantom sample

The van der Pauw method (vdP) is used in this study to obtain the electrical conductivity of gelatin phantom samples. Van der Pauw technique is based on measuring the voltage and current ratio [59]. In 1958, van der Pauw proposed a four-electrode structure when measuring the resistivity and Hall effect of solid-state materials with a uniform thickness and arbitrary shape [49] (see a cubic material in Figure 2.4).

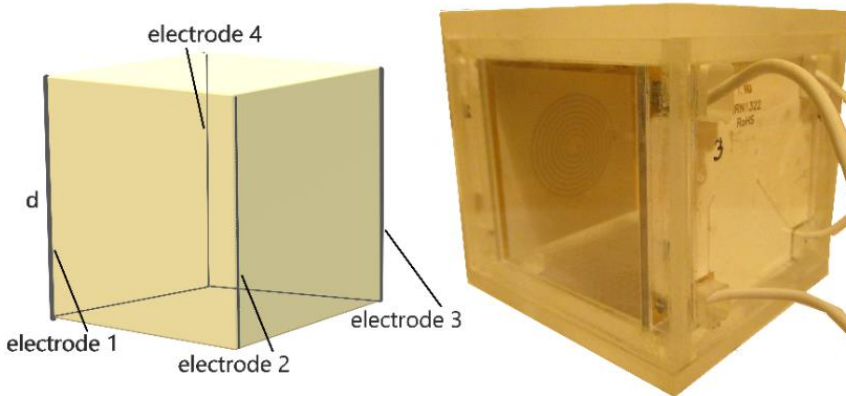


Figure 2.4 Illustrative drawing (left) and photo (right) of phantom cube with electrodes for vdP measurements.

Based on van der Pauw's theory, a system was developed for the measurement of electrical conductivity of gelatin phantom samples. The phantom mixture was placed into Plexiglas enclosure with two double-sided printed circuit boards (PCB) inside for VdP measurements. To simplify the model when calculating electrical conductivity of sample, dimensions of inner cube were specified 50mm x 50mm x 50mm. Designed PCB had two long electrodes for van der Pauw (vdP) method measurements and a planar coil for eddy-current measurements in addition (see Section 2.3.1). Long electrodes and planar coil on the inside were connected to the pads on the outer side of PCB where wire-leads were soldered. Enclosure was designed in AutoCad and CNC-milled from 10 mm Plexiglas.

The basic principle of van der Pauw's measurements on phantom cube is as follows: the phantom forms a cube of height d (Figure 2.4). Four thin electrodes are located at the corners of the cube, parallel to its axis. Neighboring electrodes 1 and 4 carry the electric current $i_{1,4}$ to the phantom sample, and at the same time the potential difference $V_{2,3}$ between the two remaining electrodes 2 and 3 is measured. The position of the current and voltage electrodes is then changed, so that current $i_{2,3}$ goes through electrode 2, and extracts through 3, and the potential difference $V_{1,4}$ between electrodes 1 and 4 is measured. From measured data it is possible to get resistances $R_{12,34}$ and $R_{23,14}$ respectively:

$$R_{12,34} = \frac{V_{34}}{i_{12}} \quad (25)$$

$$R_{23,14} = \frac{V_{14}}{i_{23}} \quad (26)$$

Based on vdP theory, the resistivity of sample could be found:

$$\exp\left(-\pi \frac{R_{12,34}d}{\rho}\right) + \exp\left(-\pi \frac{R_{23,14}d}{\rho}\right) = 1 \quad (27)$$

where d is the thickness of the sample and ρ is the resistivity of the material. The conductivity σ could be then calculated according to:

$$\sigma = \frac{1}{\rho} \quad (28)$$

To make the van der Pauw method compatible, some special requirements were followed in design of phantom shaping Plexiglas enclosure and conductivity measurement PCBs:

1. Direct contact: four thin electrode stripes on two specially designed PCB's on either side have direct contact exactly to corners of the gelatine phantom cube (Fig. 2.4). When viewed top down as 2D, the point-like electrodes are exactly in the corner of the sample [50].
2. Thin electrode strips used.
3. Uniform thickness of the sample [59].
4. The contacts are located across the edges and the resistance of the electrodes is sufficiently low compared to the sample resistance, like in this study, so according to [60] vdP method is reliable.
5. Homogeneity of sample ensured [49].

2.2.3 Calibration of the gelatine phantom material

Several different gelatine mixture compositions were used during calibrating phantoms in accordance to dielectric properties of body tissues calculated using the parametric model and the parameter values presented by C. Gabriel [61]. Different values of

material conductivity were achieved by adjusting different amounts of sodium chloride (as shown in Table 2.2).

It is important that long electrodes are placed exactly on the corners of the test object, otherwise it causes inaccuracies in the results [62]. The phantom sample's symmetry and its square shape could reduce measurement fault. The side length of the cube of the sample L was 50 mm and the diameter of electrodes s was 2 mm in the study. According to [30] [62] the measuring error due to the size of the contacts is under 10% since $s/L < 0.1$ [50]. For current and voltage measurements, electrodes were connected to the Wayne Kerr 6500B precision impedance analyser. The frequency range was set to 100 Hz to 100 MHz and conductivity calculations were made within a single frequency of 10 kHz. Since the electrical properties of phantom materials are temperature depending, the temperature of laboratory and phantom sample were maintained at constant temperature (23°C – 25°C) [50].

2.2.4 Results

Based on outcomes of the research [50], it was shown that the tissue mimicking phantom samples could be developed using a gelatine base with additives. By changing the amount of sodium chloride in the gelatine mixture, the conductivity of the phantom material could be adjusted. Through such phantom material calibrating, it is possible to produce reliable and stable over time samples to conduct research for development of bioimpedance applications. Also, measurements show that conductivity of the phantom is in proportion to the amount of sodium chloride in the phantom composition [50].

Table 2.2 shows measurement and calculation results at a frequency of 10kHz when different amount of NaCl was added to the gelatine samples. A good comparison of typical tissue conductivities at different frequencies is shown in Table 2.3.

Table 2.2 Electrical conductivities of phantom material, different amount of NaCl [50].

Sodium chloride (NaCl) amount, g	Electrical conductivity σ [$S \cdot m^{-1}$]
0 (0 wt/vol%)	0.08
0.5 (0.08 wt/vol%)	0.19
2.5 (0.4 wt/vol%)	0.75
5 (0.8 wt/vol%)	1.49

Table 2.3 Electrical conductivities of different tissues at frequency 10 kHz [61].

Tissue	Electrical conductivity σ [$S \cdot m^{-1}$]
Cancellous bone	0.08
Heart	0.15
Blood vessel	0.31
Muscle	0.34
Tendon	0.39
Blood	0.70
Body fluid	1.50

2.3 Validation of Simulations by Eddy Current Methods with Real Measurements on Phantom Materials

In biomedical applications, it is necessary to determine eddy current distribution in biological tissues. In this study simulations of eddy current measurements were validated with comparison to real measurements on produced phantom materials. Accurate modelling and simulation are valuable tool for research and development of novel biomedical applications and methods. COMSOL Multiphysics® FEM simulations of electric impedance of a planar coil on the phantom model were employed and compared to the results of eddy current real phantom measurements. The eddy current distribution was investigated in biological tissue phantom materials with valid electrical properties for biomedical engineering applications. The impedance of planar coil placed on the phantom material, were measured experimentally, and the simulation results were compared and discussed in order to evaluate FEM simulation accuracy of the eddy current measurement in biomedical applications [63].

2.3.1 Eddy current impedance measurements

To measure impedance of the phantom sample with eddy current sensors, planar coils placed on PCB were designed (Figure 2.5) and produced in a PCB factory. The main points taken into the consideration when designing coils were following:

1. Simplicity and availability of production
2. Small dimensions to fit the phantom enclosure

To measure impedance of the gelatine sample, PCBs were placed into the Plexiglas enclosure in a way that coils would be located on two opposite sides of the phantom and would have direct contact with it. The principle of the eddy current sensor is introduced in Section 1.2.

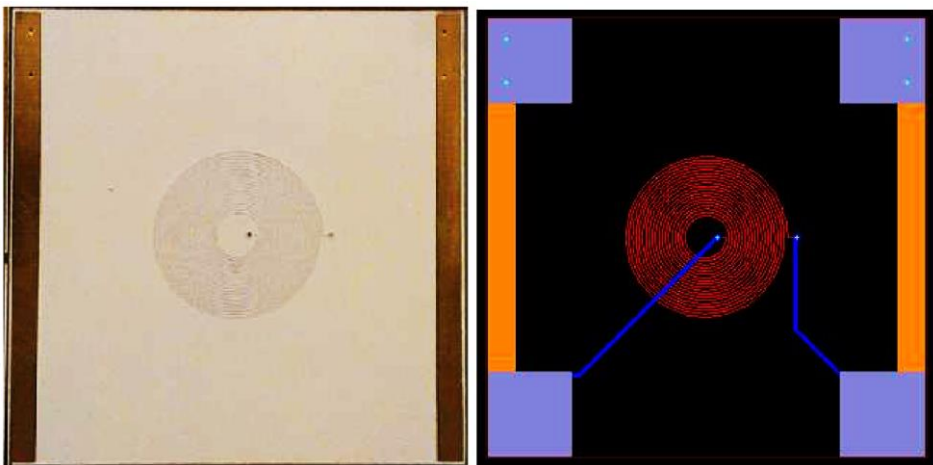


Figure 2.5 PCB with planar coil for eddy current measurements, and a long strip electrode for vdP measurement [63].

According to the Lenz law, an alternating current produces a primary alternating magnetic field. This field passes through phantom sample and eddy currents are induced,

and a secondary alternating magnetic field is produced. The primary field is created directly by the excitation coil and a voltage in the detection coil is induced. The impedance of probe coil was measured with the Wayne Kerr 6500 impedance analyzer at the frequency range 100Hz – 120MHz for two phantom materials with different frequency-dependent electrical conductivity (calculated by vdP method):

1. Material A (electrical conductivity $\sigma = 0.81 \text{ (S} \cdot \text{m}^{-1}\text{)}$ at the frequency of 10kHz);
2. Material B (electrical conductivity $\sigma = 0.16 \text{ (S} \cdot \text{m}^{-1}\text{)}$ at the frequency of 10kHz).

2.3.2 Modelling and simulation of eddy current impedance measurement

Simplified 2D axisymmetric model was created in COMSOL Multiphysics® 4.4 software using the AC/DC Module for simulating electric, magnetic, and electromagnetic fields. The AC/DC Module includes stationary and dynamic electric and magnetic fields. The AC/DC Module formulates and solves Maxwell’s equations together with material properties and boundary conditions. The equations were solved using the FEM with numerically stable edge element discretization [64].

A multi-turn coil was designed and solved as RLC coil group in AC/DC Module. The model was created in 2D view and axial symmetry (Figure 2.6). The dimensions of the model correspond to the dimensions of the experimental model and it consists of five main parts: (1) gelatine phantom, (2) multi-turn coil, (3) FR4 board, (4) layer of solder mask, and (5) air domain (Figure 2.7).

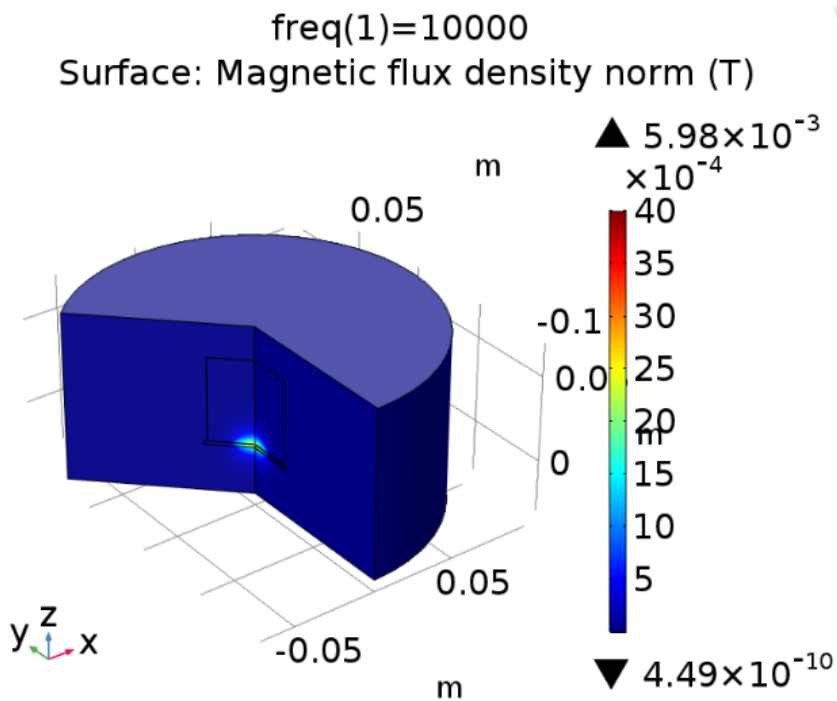


Figure 2.6 The 3D view of magnetic flux density distribution of eddy current measurement on phantom material.

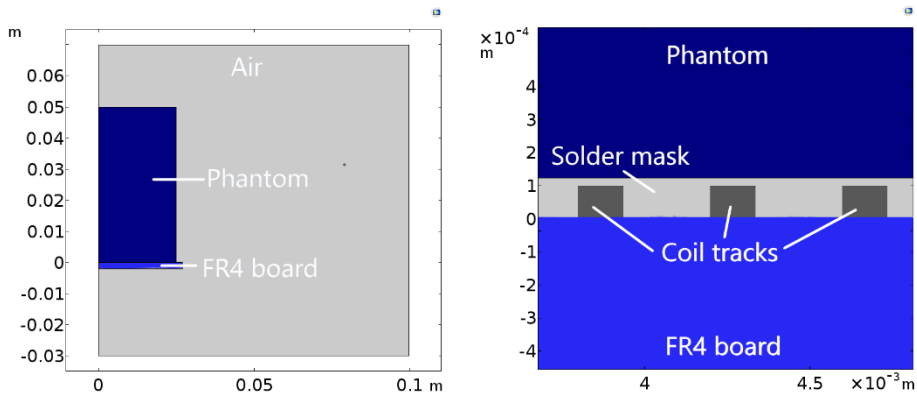


Figure 2.7 The 2D view of mode (left) with zoom extended (right).

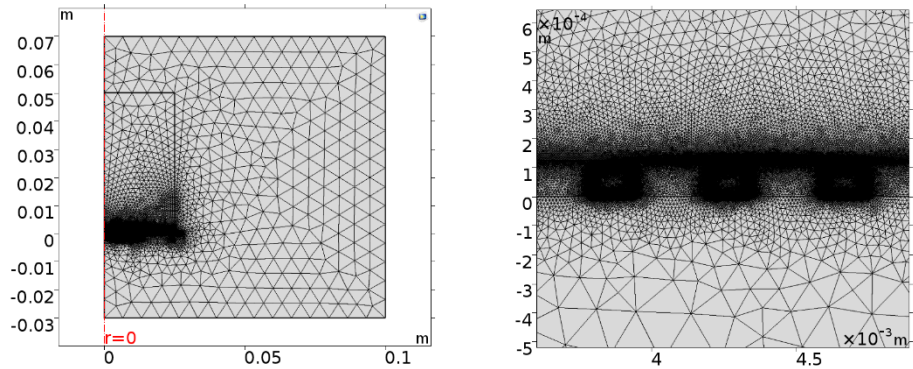


Figure 2.8 Mesh of the model (left) with zoom extended (right).

Materials and constitutive relations were defined in terms of permittivity, permeability and conductivity. Electrical conductivity of the gelatine phantom samples was defined as a frequency dependent interpolation function, based on experimental results of VdP method measurements [63]. The mesh of the model was created using automatic mesh algorithm with three different mesh sizes. Mesh consisted of 326584 elements (Figure 2.8). Model was solved for the frequency range from 10Hz to 120MHz for two different phantom materials: (1) – material A, and (2) – material B.

It should be mentioned that microscope measuring of produced coils (Figure 2.9) showed that real dimensions of coils were different from dimensions requested and forwarded to the PCB house (summarized in Table 2.4). It was also specified that the coil track consists of two different copper layers: (1) a plated copper layer, (2) and a pure copper layer. Plating is used to form vias to make interconnections in PCB and also plating is applied to the surface of the PCB to increase the copper thickness [65]. The difference in plated copper and pure copper layers need to be considered when modelling and simulating as plated copper is much more resistive than pure copper [65]. However, COMSOL Multiphysics® AC/DC module do not support creating of multi-layered RLC coil group. For that reason, the simulations were performed for single-layer coils. This probably could cause deviations in the simulation and the real measurement results presented in the next section.

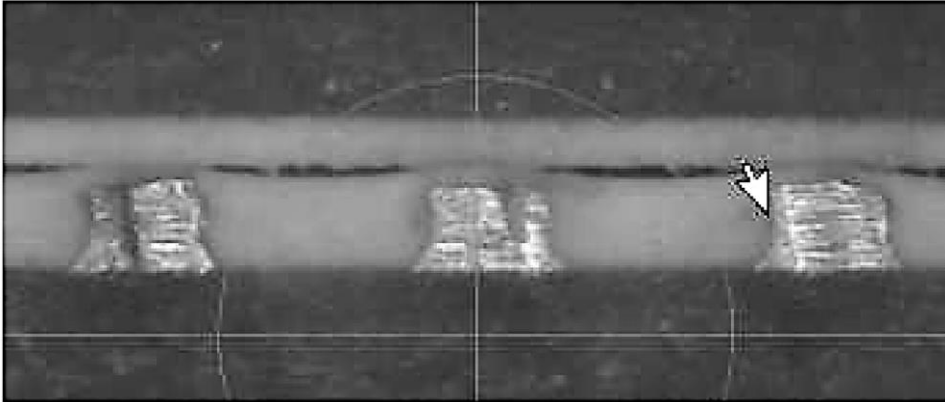


Figure 2.9 Photo of PCB cut-through under measurement microscope [63].

Table 2.4 Comparison of designed and actual coil dimensions.

Parameter	Required dimensions, mm	Actual average dimensions, mm
Thickness of copper layer	0.035	0.099
Coil track width	0.2	0.135
Spacing between coil tracks	0.2	0.264
Coil inner diameter	20.2	19.75
Coil diameter	4.6	5.07

2.3.3 Simulation results

Simulations of eddy current measurements were validated with comparison to actual measurements of phantom materials. Figure 2.10 and Figure 2.11 show the comparison of measured and simulated phase angle and impedance of materials A and B at frequency range from 100 Hz to 120 MHz. The results indicated that experimentally measured impedance and the simulation values are significantly higher at frequencies above 12 MHz. In addition, the resonance appeared on different frequencies. From the results, it is assumed that the FEM simulation method is reliable until 12 MHz frequencies. Further research in this area is needed, however, the reasons of the resulting distortion are suggested as follow:

1. Simplification of the simulation model
2. Actual coil track consists of two layers with different electrical conductivity, but only single layer coil was modelled due to limitations in simulation setup.
3. Limited measuring ability of the used tool on higher frequencies could cause inaccuracies in measurement results of the phantom material's electrical conductivity [63]. This could consecutively affect the simulation input and its outcome.

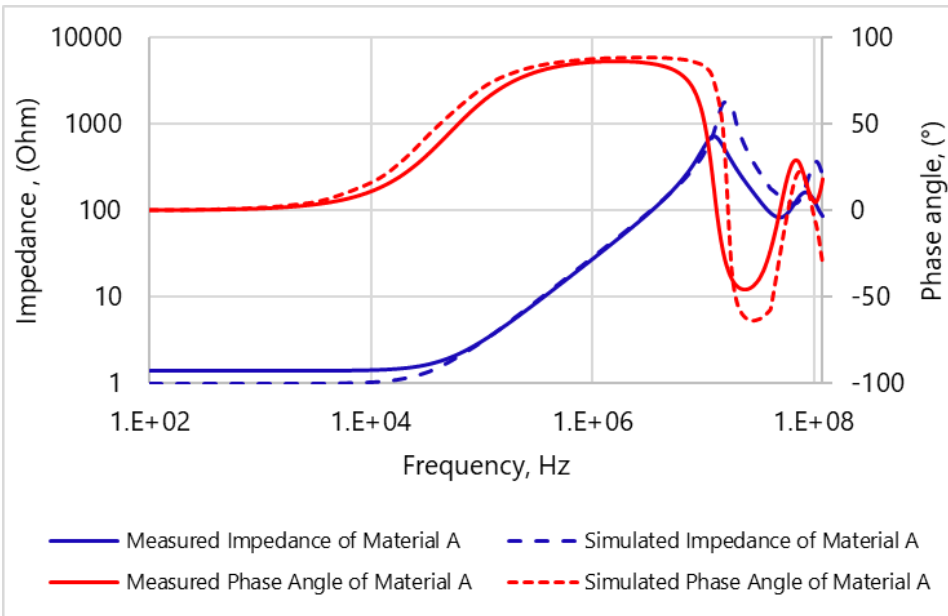


Figure 2.10 Comparison of simulation and measurement results for material A [63].

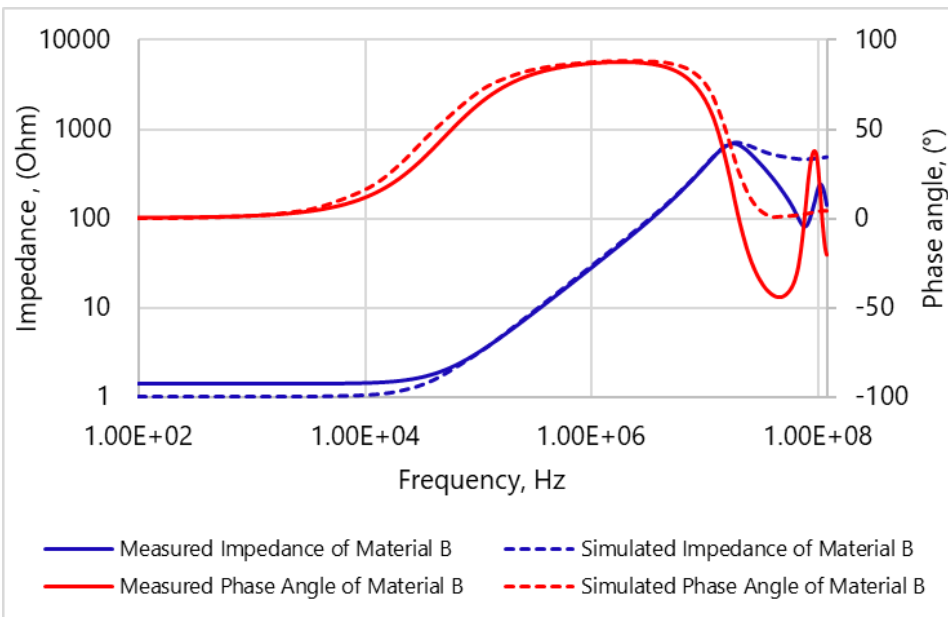


Figure 2.11 Comparison of simulation and measurement results for material B [63].

2.4 Chapter Summary

In this chapter the considerations for developing gelatine-based materials for a human forearm phantom are presented for bioimpedance analysis. It has been stated in literature that dielectric properties of biological tissues are complex and heterogeneous and the electrical response of tissues varies significantly for each individual tissue and its physiological state. Tissue properties mimicking phantoms are useful for research and since these are reproducible and stable with controlled properties, and could reduce animal and human experiments [58]. Sodium chloride (NaCl, 99+%) was utilized to achieve different electrical conductivities, typical to human body tissues. The results confirm that a tissue mimicking phantom samples could be produced using a gelatin base with additives and it is possible to construct materials that mimics specific tissue electrical properties for the purpose of biomedical engineering studies.

Also, the results of COMSOL Multiphysics® simulation of phantom material by eddy current measurements are presented in the chapter. Simulations of eddy current measurements are validated with comparison to actual measurements of phantom materials in order to evaluate FEM simulation accuracy of the eddy current measurement for biomedical applications. Accurate computer simulation with valid results is a valuable research tool in biomedical engineering. The results indicated, that experimentally measured impedance and the simulation values are comparative, and the phase angle differences are negligible in the frequency range below 12 MHz. The reasons of the non-compliance of results above the frequency of 12 MHz are suggested.

3 Electrode Placement Strategies for the Measurement of Radial Artery Bioimpedance

In this chapter the simulation and experimentation towards the selection of electrode configurations and placements for monitoring cardiac activity of human on radial artery is presented. As a continuous cardiac output is a significant matter that must be considered in monitoring the functioning of cardiovascular system, a non-invasive sensing system based on measuring electrical bioimpedance (EBI) variations of radial artery is proposed to evaluate the physical condition of patient [66]. To optimize the EBI signal acquisition, different electrode configuration and placement strategies are compared with the main focus to find the most suitable ones.

COMSOL Multiphysics® AC/DC module is used in this study to map the sensitivity field (S) distribution for different combinations of current carrying and voltage pick-up electrodes placed close to the radial artery on the forearm model. Regions of positive/(negative) sensitivity are defined where the measured impedance increases/(decreases) with an increase in the actual impedance of the sample [67]. The corresponding experimental EBI measurements on human wrist were utilized. Experimental results were compared to outcomes of simulation.

The simulation of sensitivity distribution and experimental measurements on radial artery are performed for circular (perpendicular to the forearm) and distal (along the forearm) electrode placements. Also, the modified electrode placement strategies, guided by the idea of focused impedance method (FIM), are investigated. In addition, a novel version of FIM is proposed: a five-electrode FIM strategy [66].

This chapter is based on the author's II and III publications. The chapter is organized as follows. The motivation and the principle of pulse wave monitoring on radial artery by measuring the EBI with resistive coupling is introduced in Section 3.1. Also, sensitivity distribution of EBI measurements is explained in the section. Details of different electrode placement and configuration strategies investigated in the study are presented in Section 3.2. Section 3.3 describes the model and simulation setup, also the technique for calculating sensitivity is presented. Methods and instrumentation used for experimental measurements of EBI with the goal of confirming placement strategies are presented in Section 3.4. Simulation and experimental results are demonstrated and discussed in Section 3.5. Section 3.6 concludes the chapter.

3.1 Introduction

The purpose and principles of simulation and experimentation towards the selection of electrode configurations and placements for monitoring blood pulsation in human radial artery is presented in this section.

3.1.1 Bioimpedance-based sensing of blood pulse wave in radial artery

One of the possible techniques to derive a blood pressure-related waveform from the radial artery is bioimpedance measurement. The wearable monitor for central aortic blood pressure curve by using electrical bioimpedance sensing is presented in [4]. The EBI measurement principle (Figure 3.1) is that a small current I is applied to the interested site through electrodes, and a voltage difference V is measured from other electrodes.

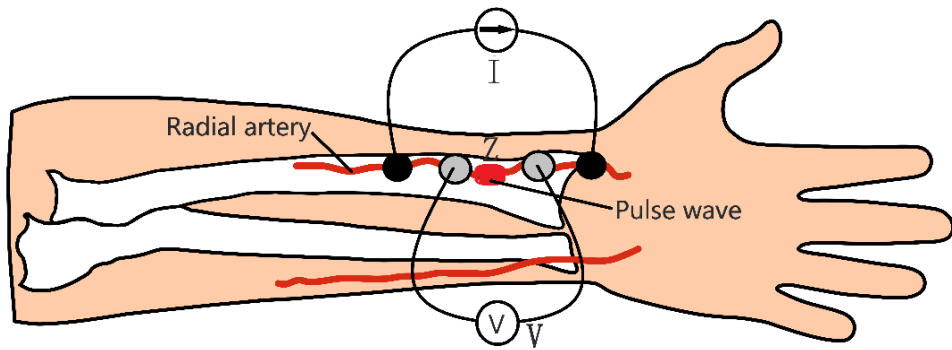


Figure 3.1 Illustration of a four-electrode bioimpedance measuring system for monitoring the pulse wave in radial artery.

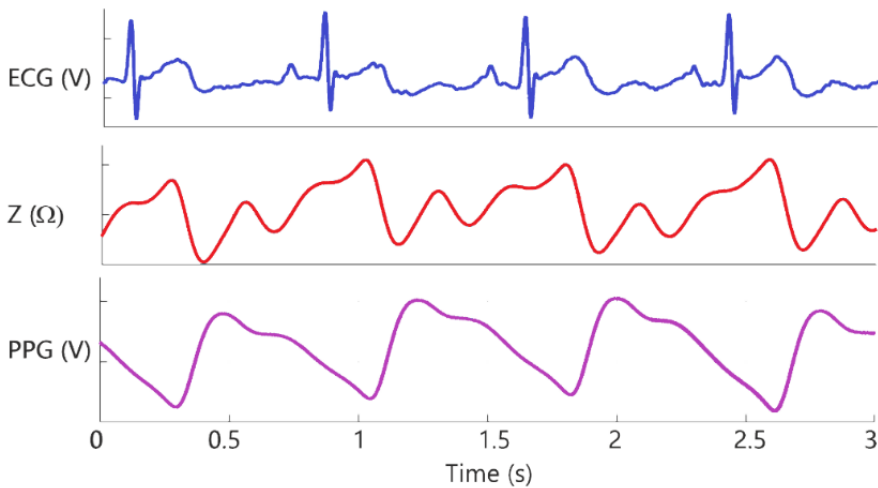


Figure 3.2 Illustration of pulse wave by the measured impedance $Z(\Omega)$ together with the reference photoplethysmography (PPG) and ECG signal modified from [44].

Bioimpedance is calculated from the applied current I and measured voltage V , which gives the change of the impedance during cardiac cycle. The volume of the blood changes within each heartbeat. This reflects in the impedance curve which corresponds to a blood pressure waveform. In the sense of EBI measurements, this means the detection of time varying change of impedance $\Delta Z(t)$, caused by changing amount of blood in artery. The impedance of the wrist (Z) can be described as a sum of invariable impedance of the local volume of wrist (Z_0) and impedance change caused by pulse wave ($\Delta Z(t)$).

$$Z = Z_0 + \Delta Z(t) \quad (29)$$

Due to conductive properties of blood, the impedance Z decreases with a pulse wave arriving and increases with dissolving of the pulse wave, so at the moment of the maximum volume of blood is present, the measured Z is the lowest one (Figure 3.2) [68]. As a result of such variations in the value of impedance, the pulse wave can be detected.

3.1.2 Sensitivity distribution

Sensitivity distribution of an EBI measurement gives a notion between the measured impedance Z induced by a given conductivity distribution in the 3D space of a tissue. It represents how effectively each region is contributing to the measured impedance signal [69]. The transfer impedance Z of an object can be approximated as a ratio between the measured voltage E by the pick-up (PU) electrodes and the injected current I by the current-carrying electrodes (CC) [67].

$$Z = \frac{E}{I} \quad (30)$$

The resistivity (ρ) of the object is defined as a ratio between the voltage (E) and current density (J):

$$\rho = \frac{E}{J} \quad (31)$$

As biological tissue is inhomogeneous, the total measured impedance Z could be expressed as a sum of all local resistivity ρ values of all small sub-volumes of the tissue and can be indicated by following equation:

$$Z = \iiint \rho \frac{J_{CC} \cdot J_{PU}}{I_{CC} \cdot I_{PU}} dv \quad (32)$$

where Z is impedance, ρ is the resistivity of the volume, J_{CC} is the current density under CC electrodes, and J_{PU} is the current density under PU electrodes [67]. The sensitivity S [m^{-4}] of EBI measurement is a scalar value representing the CC electrode current density lines J_{CC} projection on the PU electrode current density lines J_{PU} [67]:

$$S = \frac{J_{CC} \cdot J_{PU}}{I_{CC} \cdot I_{PU}} \quad (33)$$

Sensitivity S maintains positive value, if measured Z increases and negative value, if measured Z decreases.

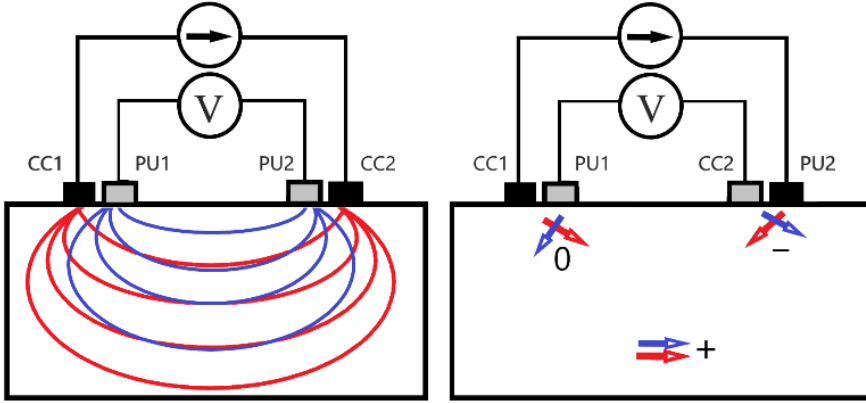


Figure 3.3 The sensitivity formation of a four-electrode impedance measurement in homogeneous volume. CC1 and CC2 form a current carrying electrode pair (red lines). PU1 and PU2 form a voltage pick-up electrode pair (blue lines) [66].

Figure 3.3 explains the sensitivity formation of the four-electrode impedance measurement in homogeneous volume. Sensitivity formation depends on the direction of current density vectors of the CC and PU electrode pairs:

- Sensitivity S will be positive, if vectors are in the same direction.
- Sensitivity S will be negative, if current density vectors are in the opposite direction.
- Sensitivity S will be maximum, if current density vectors are superimposed.
- Sensitivity S will be zero, if current density vectors are in perpendicular directions [67].

It should be noted that the sensitivity S does not directly describe bioimpedance measurement in our physical set-up, but it shows how much weight the local impedance is getting.

To find the local contribution to the measured transfer impedance Z , the volume impedance density (VID) should be examined [24]:

$$VID = \rho \cdot S \quad (34)$$

$$VID = \rho \cdot \frac{J_{CC} \cdot J_{PU}}{I_{CC} \cdot I_{PU}} \quad (35)$$

3.1.3 Study and motivation

The common approach for non-invasive CAP estimation is the applanation tonometry, but several limitations occur: (1), the readings could be operator dependent due to manual positioning of the tonometer over the artery, (2) difficulty to obtain high-quality pulse in subjects with lower blood pressure or with obesity, (3) calibration with brachial cuff technique is required, and (4) the blood vessel is flattened against the bone, so the blood flow is disturbed [46]. In this study, another, promising technique based on

bioimpedance measurement to derive a blood pressure-related waveform from the radial artery is presented. Wrist was chosen due to accessibility of radial artery and convenient positioning of wearable device. Important is to emphasize that this method does not require applying of any pressure to the artery. Only reliable electrical contact is needed. The main attention turns on this, how the high-quality contacts can be achieved with the help of electrodes.

The main purpose of the study is established by need of proposing the most suitable electrode placement and configuration for monitoring pulse wave in radial artery with the goal of non-invasive estimating of the CAP of blood by measuring the EBI of wrist. In order to gain the purpose of the research, several experimental measurements and sensitivity distribution simulations were performed by using variety of electrode placements and configurations. Standard ECG electrodes were used as sensors, resistively coupled to skin surface for the lowest skin-electrode contact impedance. In addition, FEM simulations of EBI measurement of radial artery were carried out using COMSOL Multiphysics® (version 5.3a) to map the sensitivity field S distribution for several arrangements of current carrying and voltage pick-up electrodes placed close to the radial artery on the forearm model. Regions of positive and negative sensitivities were mapped. However, sensitivity S does not reflect quantitatively what is experimentally measured, but it indicates the impact of the local impedance in a specific 3D sub-volume on the total measured impedance [67]. Simulations were performed with a goal to focus regions of maximum positive sensitivity on radial artery. The experimental measurement and the results of respective simulation were compared and discussed.

3.2 Electrode Configuration and Placement Strategies

Wrist can be considered to be of finite volume of layers of different conductivities that are located at certain fractions of total volume [70]. The unique person difference of physique reveals as differences in the volumes of body tissues and compartments. When focusing on the non-invasive EBI measurements of radial artery, the presence of tissue layers of different conductivities is expected to play important role. The acquisition of EBI measurement signal depends on several indicators: electrode number, geometry, orientation, spacing and configuration between electrode couples. Several electrode configuration strategies have been published and investigated, mostly for applications in electrical impedance tomography (EIT). In this study FEM simulation of sensitivity distribution and experimental EBI measurements on human forearm were utilized for several in-line four-electrode electrode configurations, several rectangular four-electrode configurations and focused (FIM) electrode configurations.

In the recent years, the approach of measuring the EBI of radial artery for determining cardiac activity in the form of pulse wave is gaining popularity. There are different electrode placement and configurations presented in literature. The circular electrode placement around the wrist represents a popular approach in experimental measurements [71] and also commercial devices (Fitness Tracker UP3™ by [72]). The Fitness Tracker UP3™ detects pulse rate by measuring the EBI with electrodes placed inline placed circularly around the wrist. The distal placement of electrodes is presented by [73], [74] and [75]. More sophisticated electrode placement strategies like FIM with variety of number of electrodes [76] has not been implemented to measure the pulse wave in radial artery. Nevertheless, utilization of FIM may propose competitive outcome – suggested by FEM simulation models [77].

3.2.1 In-line four-electrode impedance sensing on radial artery: distal and circular electrode placements

To determine the highest sensitivity of four-electrode measurement on radial artery, the spatial sensitivity distribution was researched for several in-line distal and circular placements [37]. Simulation of sensitivity distribution on human forearm model was utilized for distal and circular electrode placement shown in Figure 3.4.

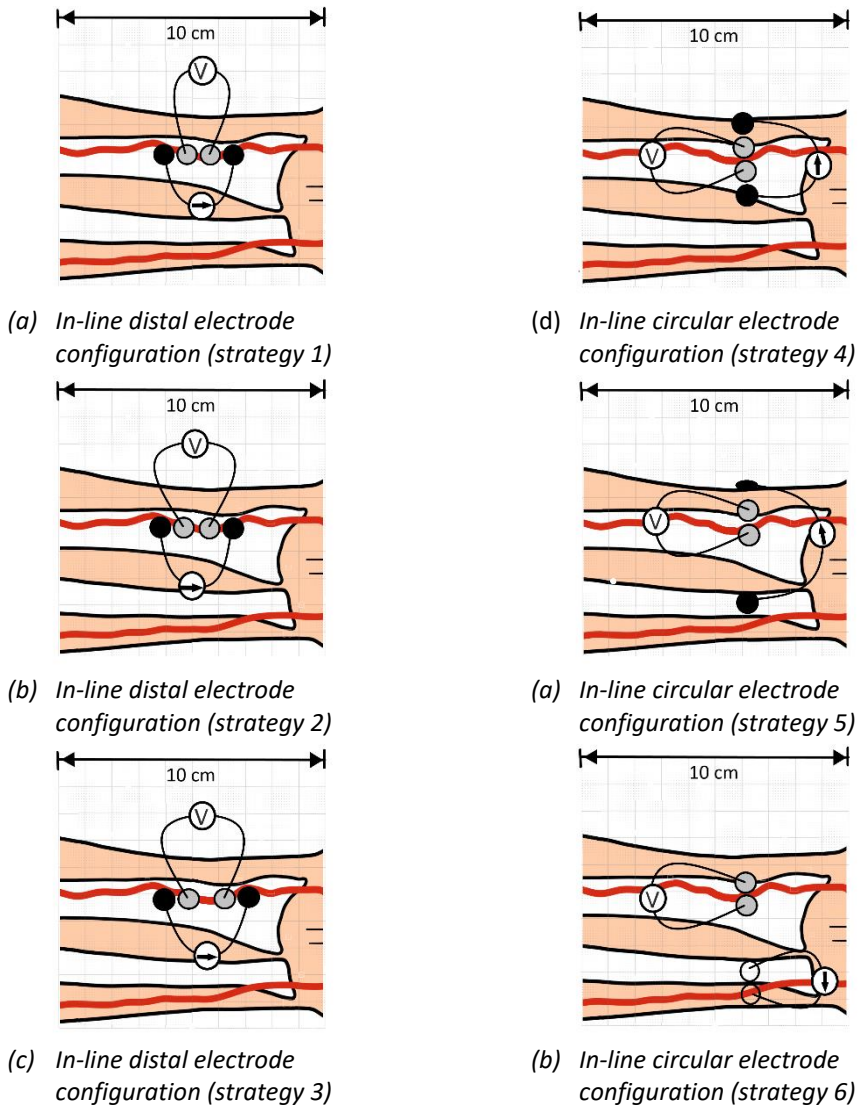


Figure 3.4 In-line electrode configuration strategies for EBI measurements on radial artery.

The four-electrode impedance measurement method, also referred as tetrapolar or Kelvin method, has been used to measure resistivity of material since the 1870's. A pair of electrodes is used to inject current into the object and another pair of electrodes is utilized to measure the resulting voltage drop. Four-electrode method is widely used in

different clinical procedures [6], [17]. The advantage of four-electrode setup if compare to two-electrode configuration is that only the transfer impedance of the tissue between the potential reading electrodes is determined since almost no current flows to the measuring instrument and the voltage drop in the measuring electrodes is negligible [78].

3.2.2 Impedance sensing on radial artery: various four-electrode placements and FIM electrode placements

In addition to classical in-line four-electrode distal and circular electrode placements several rectangular four-electrode configurations and FIM electrode configurations were investigated [66] (shown in Figure 3.6).

FIM, introduced by Rabbani [76], is a method for quantifying the electrical resistance in tissues of the human body with improved focused localization compared to classical methods. The FIM is based on placing of two classical four-electrode systems perpendicular to each other over a common zone at the centre and combining the results [76]. By adding the two measured impedance values, it is possible to obtain increased sensitivity over the central zone [76] (see Figure 3.5). It should be noted, that guided by the idea of focused impedance method (FIM) its novel version is proposed in the study: a five-electrode FIM strategy [66].

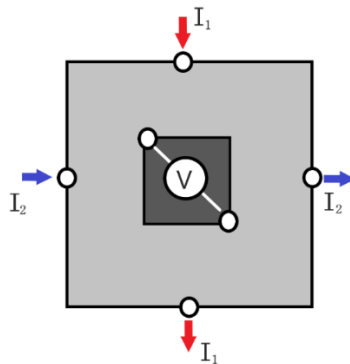
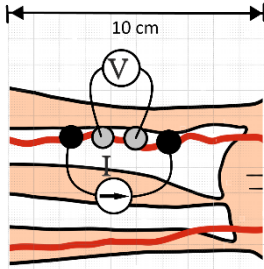


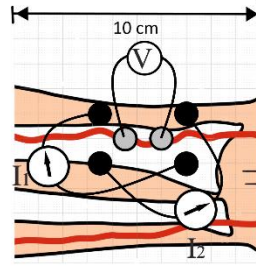
Figure 3.5 Basic concept of six-electrode FIM.

Simulation of sensitivity distribution and experimental EBI measurements on human forearm were executed with the following electrode configurations (shown in Figure 3.6) as follows:

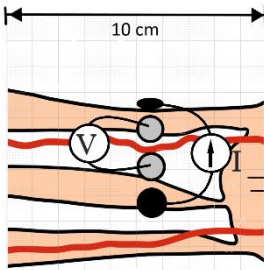
1. In-line four-electrode configuration with distal placement along radial artery.
2. In-line four-electrode configuration with circular placement around forearm.
3. Rectangular four-electrode configuration with the exciting pair on one side and the measuring pair on another side of radial artery.
4. Rectangular four-electrode configuration with the location of one exciting and one measuring electrode on either side of the radial artery.
5. Six electrode FIM with measuring electrodes placed along the radial artery.
6. Five electrode FIM (option A) with two exciting electrodes combined into one and measuring electrodes set between the excitation electrodes.
7. Five electrode FIM (option B) with two exciting electrodes combined into one and measuring electrodes set between the excitation electrodes.
8. Five electrode FIM (option C) with two exciting electrodes combined into one and measuring electrodes set between the excitation electrodes.



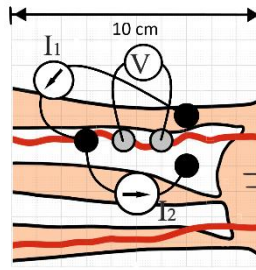
(a) *In-line distal electrode configuration (strategy 1)*



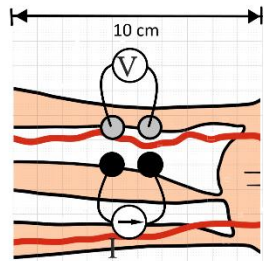
(e) *Six-electrode focused configuration (strategy 5)*



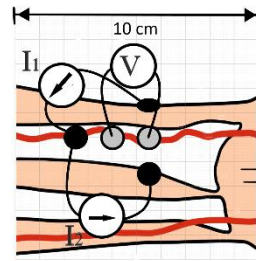
(b) *In-line circular electrode configuration (strategy 2)*



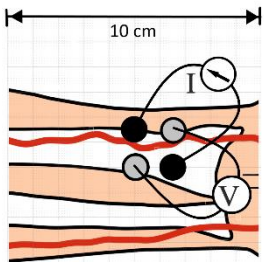
(f) *Five-electrode focused configuration (strategy 6)*



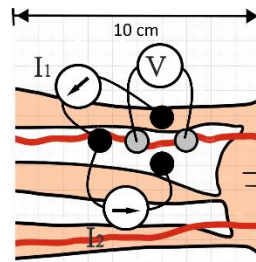
(c) *Rectangular four-electrode configuration (strategy 3)*



(g) *Five-electrode focused configuration (strategy 7)*



(d) *Rectangular four-electrode configuration (strategy 4)*



(h) *Five-electrode focused configuration (strategy 8)*

Figure 3.6 Electrode configuration strategies for EBI measurements on radial artery [66].

3.3 Simulation of Sensitivity Distribution for Radial Artery EBI Measurements

Finite element (FE) simulations of EBI measurement on radial artery were carried out using COMSOL Multiphysics® (version 5.3a) to map the sensitivity field (S) distribution for different combinations of current carrying and voltage pick-up electrodes placed close to the radial artery on the forearm model.

3.3.1 Building a geometry

The object of the study is a human forearm, which consists of matter of different conductivities: skin, fat, muscle, tendons, nerves, blood etc. (Figure 3.7). The forearm of the upper extremity runs from the elbow to the wrist. The forearm is formed by the radius and the ulna bones and have twenty muscles. The vascular supply is from the branches of ulnar and radial arteries, which backflow is ensured by veins: basilic, cephalic and median veins.

A simplified 3-D model of human left forearm fragment with length of 10 cm was developed. The geometry of the model was created by using Autodesk AutoCAD 2018 software. The dimensions of the structures were determined according to data and DICOM images available on an interactive anatomical atlas of the upper limb [79]. This atlas-based application is based on an axial magnetic resonance of entire upper limb of healthy human. The magnetic resonance imaging (MRI) dataset may be seen as a series of pictures of slices of the forearm, so these 2D pictures were combined and formed into 3D picture. The data was segmented into the most important tissue types: skin, fat, muscle, blood, bone, bone marrow and tendons. Obviously, there are more tissue types present, but a simplified model was created to conform capabilities of software.

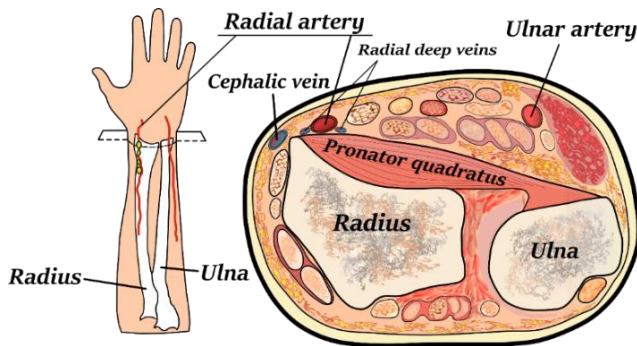


Figure 3.7 Human forearm and the cross section of the wrist on the right [46].

The geometry created in Autodesk was then implemented in COMSOL Multiphysics® (version 5.3a). Some smoothing and repair steps were applied after geometry import to improve the quality of the mesh and to reduce the size of the resulting mesh. A 3-D views of the model is shown in Figure 3.8.

Measuring electrodes were placed onto the radial artery close to scaphoid bone of the COMSOL model in accordance with placement strategy (Figure 3.4 and Figure 3.6). The dimensions and electrical conductivity of the electrodes were set in accordance to disposable wet adhesive AgCl electrodes widely used in clinical practice. Modelled electrodes are round shaped with radius of 3 mm and have a direct skin contact without conductive gel.

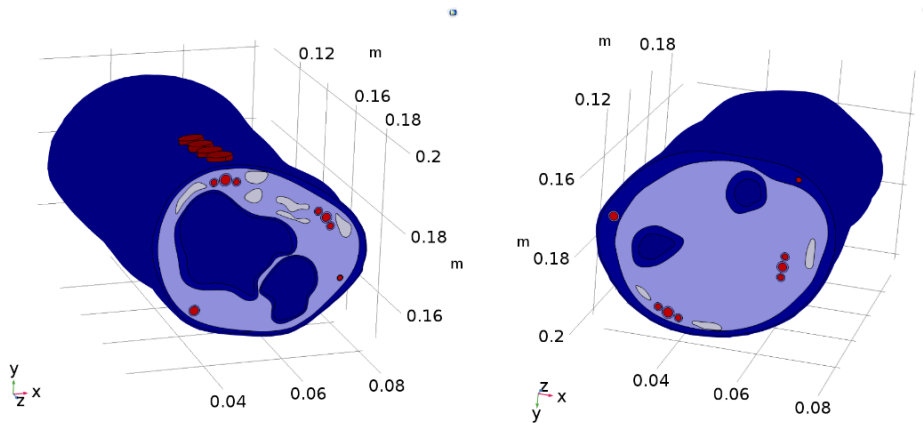


Figure 3.8 COMSOL Multiphysics® 3-D model of a fragment of human forearm.

However, as Ag/AgCl electrodes have a conductive gel placed between skin and electrode for optimal response, a comparative simulation with conductive gel layer added between the electrode-skin contact interfaces was performed to confirm the validity of simulations with respect to support the experimental results. The conductive layer had thickness 1 mm and electrical properties of the gel were set according to [80]. As expected, the study showed that there is an equal effect of gel layer presence on all the simulations, so conclusions remain unchanged [66].

3.3.2 Defining the material properties

Corresponding material properties were added to the model and assigned to all domains (shown in the Table 3.1).

Table 3.1 Material properties assigned to the model domains [51], * [80].

Material / Tissue	Electrical conductivity σ [$S \cdot m^{-1}$] at 10kHz
Air	0
Electrodes*	$5.99 \cdot 10^7$
Skin	$2.04 \cdot 10^{-4}$
Fat	$2.38 \cdot 10^{-2}$
Muscle	0.34
Cortical bone	$2.04 \cdot 10^{-2}$
Marrow bone	$2.73 \cdot 10^{-3}$
Tendon	0.39
Blood	0.70
Vessel	0.31

3.3.3 Adding a physics and defining physics boundary conditions

Defining the physics is an important step of simulation. It includes choosing the appropriate physics for the model, adding physical conditions and assigning the physics to geometric entities [81]. The simulation process was carried out by utilizing Electric Currents physics found under the AC/DC branch of COMSOL Multiphysics® menu. This interface is used to compute electric field, current, and potential distributions in conducting media by solving Maxwell's equations subject to certain boundary conditions [47]. Equations representing physical condition constrains within COMSOL Multiphysics® Electric Current physics are:

$$\nabla \cdot J = Q_{j,v} \quad (36)$$

$$J = \sigma E + j\omega D + J_e \quad (37)$$

$$E = -\nabla V \quad (38)$$

where E is electric field intensity [V/m], D is electric displacement or electric flux density [C/m^2], J is current density [A/m^2], σ is the electrical conductivity [S/m], J_e is an externally generated current density [A/m^2], ω is angular frequency [rad/s], Q is resistive loss and is V electrical potential [V] [47].

The EBI measurements could be simulated by adding stimuli to electrodes. Two Electric Currents physics interfaces were added: (1) ec to define stimuli in the current carrying electrodes (CC), and (2) $ec2$ to define the reciprocal current stimuli in the pick-up electrodes (PU). Ground and Terminal nodes were added to the model. The Ground node implemented zero potential as the boundary condition $V = 0$. The Terminal node provides a boundary condition for connection to a specified voltage $V_0 = 1V$.

3.3.4 Creating the mesh

Building the mesh is a significant step in the modelling. The mesh used for a model geometry plays an important role in how the model is solved and affects the computation process, including time to take a model to solve, the amount of memory required to compute a problem, and the accuracy of the solution [81].

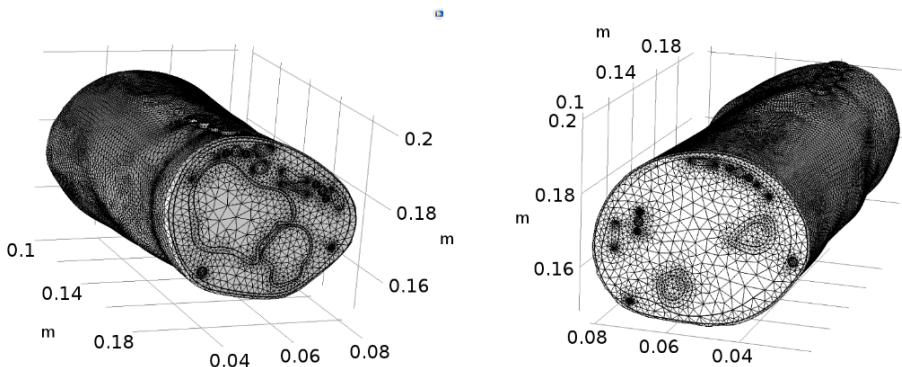


Figure 3.9 Two views of mesh of the simplified human forearm model.

The model was partitioned into mesh elements by using the Finite Element Method (FEM) where physical state variables (scalars) are calculated for the intersection points in the mesh and vectors along the lines between the mesh points (Figure 3.9).

The mesh strongly affects modelling requirements. Identifying the most appropriate mesh for particular model helps to reduce memory requirements by controlling the number, type, and quality of elements, thereby creating an efficient and accurate simulation [82]. Tetrahedral mesh element was chosen in this study and the mesh was built through a user-controlled mesh sequence. In order to reduce mesh elements, the mesh was customized to be more detailed at individual faces and domains of the electrodes and blood vessels and coarser throughout the rest of the geometry. The mesh consisted of about one million elements with an average element quality about 0.672. It should be noted, that there are some small deviations in these values in case of different electrode placements.

3.3.5 Simulation study steps and solving the model.

As a choice of solver is optimized for the typical case for each physics and study in COMSOL Multiphysics®, the suggested solver and configurations were used. The Frequency Domain study and study steps were set to compute the model at frequency 10 kHz for both Electric Currents (*ec* and *ec2*) physics.

3.3.6 Post-processing the results

There are a number of parameters that can be visualized in the results in COMSOL Multiphysics®. Some relevant parameters will be described in this section.

As the sensitivity S of an impedance measurement is represented by the current carrying (CC) current density lines J_{CC} projection on the pick-up (PU) current density lines J_{PU} (see Section 3.2.1), these current density lines were investigated.

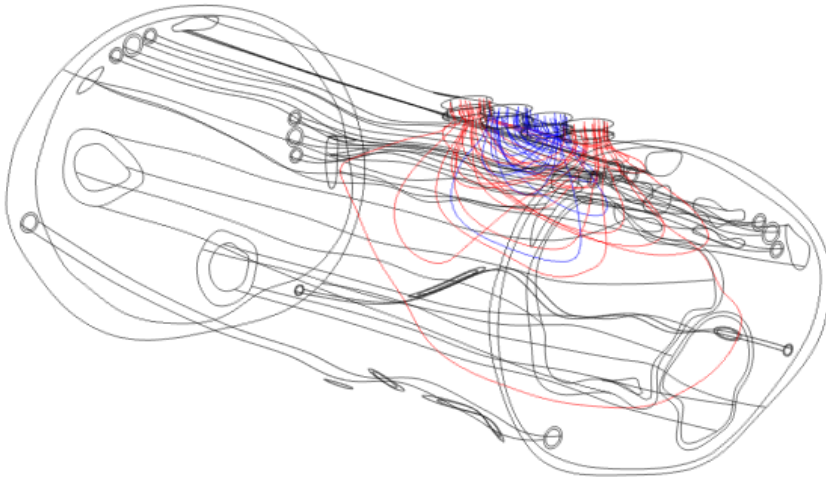


Figure 3.10 Current density lines in case of in-line distal four-electrode placement.

Figure 3.10 shows an examples of current density lines for distal electrode placement strategy. CC and PU current density lines are shown in the same plot, but with different colours.

As described in Section 3.2.1, the sensitivity S [m^{-4}] of EBI measurement is represented as follow:

$$S = \frac{J_{CC} \cdot J_{PU}}{I_{CC} \cdot I_{PU}} \quad (39)$$

Or as an expression in COMSOL Multiphysics®:

$$(ec.Jx*ec2.Jx+ec.Jy*ec2.Jy+ec.Jz*ec2.Jz)/((1[A])^2)$$

Since sensitivity S is a scalar value, the slice plots were used to visualize it (shown in Figure 3.11). The sensitivity S of EBI measurement was calculated and the corresponding sensitivity maps were obtained for the different electrode configuration strategies described in Section 3.2. The results of simulation are detailed in Section 3.5.

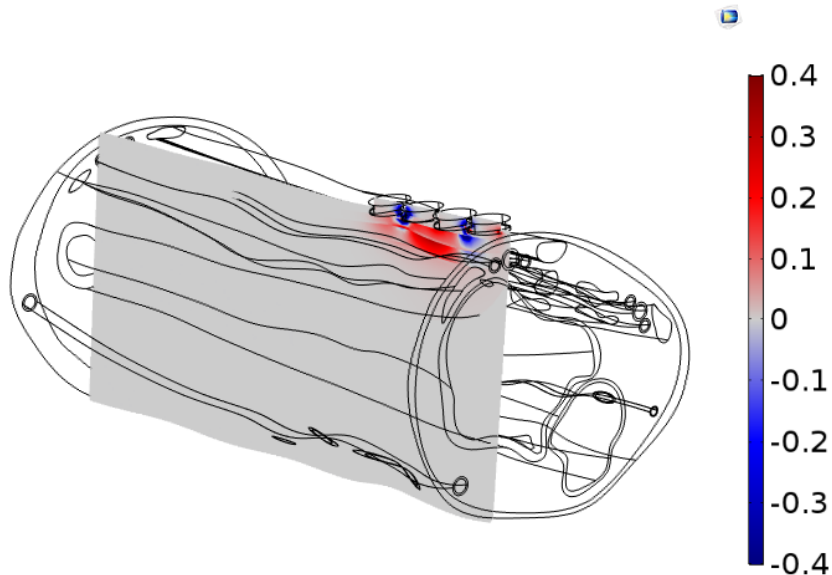


Figure 3.11 Example of obtained sensitivity map, S [m^{-4}].

3.4 Measurement

Methods and instrumentation used for measurement of EBI with the goal to make experiments for chosen electrode placement strategies are presented in this section.

3.4.1 Instrumentation

An adapted USB digital data acquisition (DAQ) module U2531A of Keysight Technologies (Santa Rosa, CA, USA) was used to perform the EBI measurements. The measurement setup together with the user interface is thoroughly described in [66] and [83]. The schematic visualization of measurement setup and the electrodes is presented in Figure 3.12.

Standard solid gel Ag/AgCl ECG monitoring electrodes (type T709 of Comepa Industries) were used in the experiments. The dimensions of the electrodes were modified by cutting their width approximately to 10 mm with the aim of placing the electrodes on top of the location of radial artery more densely [66].

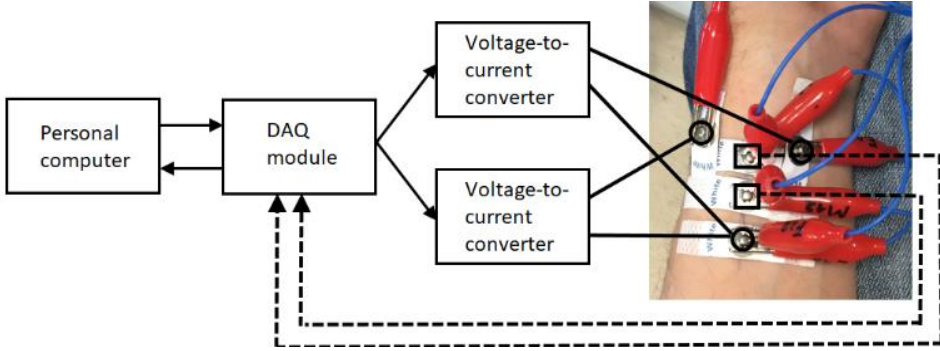


Figure 3.12 Visual representation of measurement setup for determination of $\Delta Z(t)$ caused by pulsating volume of blood in radial artery [66].

3.4.2 Measurement Method and Setup

The excitation signal at a frequency of 10 kHz and amplitude of 1 V was applied. As in the cases of focused impedance method (FIM), wherein two excitation channels are required, the excitation signals of equal parameters were used. The measurement experiments were performed on left forearm of a single volunteer (healthy adult male, age 35, height 183 cm and weight 71 kg), sitting comfortably on a chair with the arm lying on the armrest. The measurement procedure included two activities to follow: (1) sit quietly for 20 seconds, and (2) rhythmically clenching the first for 20 seconds. The goal of the study was to define the best access to the pulsating blood in radial artery by comparing different electrode placement strategies. The following two parameters were estimated:

- The amount of change in measured $Z(t)$, caused by the pulsating volume of blood: marked as $\Delta Z(t)_{pulse}$.
- The amount of change in measured $Z(t)$, caused by the movements of the hand: marked as $\Delta Z(t)_{move}$.

$\Delta Z(t)_{pulse}$ and $\Delta Z(t)_{move}$ were determined by calculating the difference between the minimum and maximum points of the measured signal of EBI during pulse and move respectively (Figure 3.13). It should be noted, that pulse was not visually identifiable in the gained signal of $Z(t)$ while the movements of hand were implemented [66].

As the non-invasive connection of electrode to skin surface is highly dependent on several factors such as placement of electrodes, external pressure, skin condition, etc. the ratio (marked as $R_{\Delta Z(t)}$, %) between $\Delta Z(t)$ and $Z(t)_{max}$ was also calculated in comparability reasons for each case according to:

$$R_{\Delta Z(t)} = \frac{\Delta Z(t) \cdot 100}{Z(t)_{max}} \quad (40)$$

and represented by $R_{\Delta Z(t)_{pulse}}$ and $R_{\Delta Z(t)_{move}}$ respectively in the following discussion.

Eight different electrode placement strategies on top of the location of radial artery in forearm were experimented as listed in Section 3.5.2 (strategies 1-8). The results of measurement are detailed in Section 3.5.3.

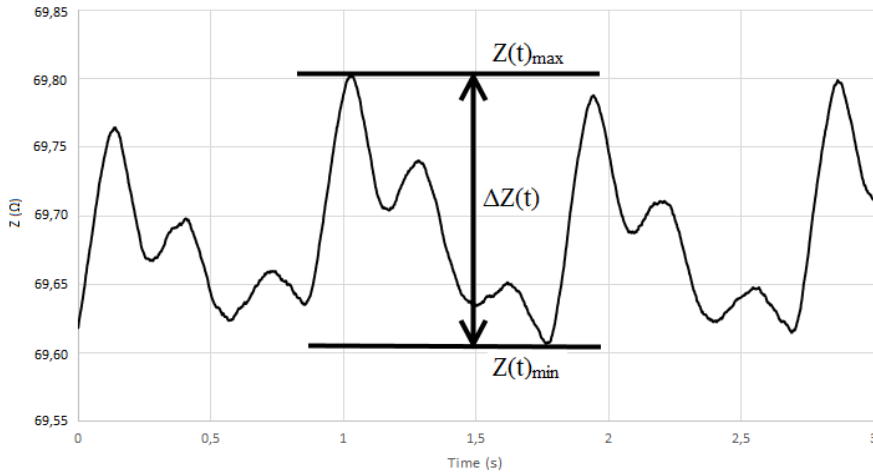


Figure 3.13 The determination of $\Delta Z(t)$ in the $Z(t)$ waveform, corresponding to a blood pulse [66].

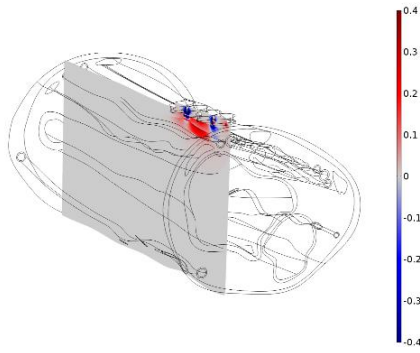
3.5 Results

This section is based on results of two studies presented in [37] and [66]. To understand the sensitivity distribution in measured region, essential is to link with experimental results with different electrode configurations. The results of simulation and practical experimentation are presented in this section.

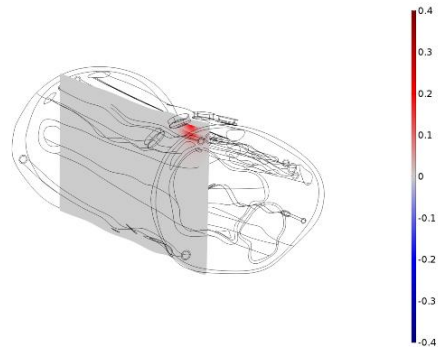
3.5.1 Simulation results: in-line distal and circular four-electrode placements

Sensitivity maps were obtained for different electrode configuration strategies as listed in Section 3.2.1 (Figure 3.4). Scaling of the colour map was kept the same within each simulation. Positive values of sensitivity are indicated with red colour and negative values with blue colour.

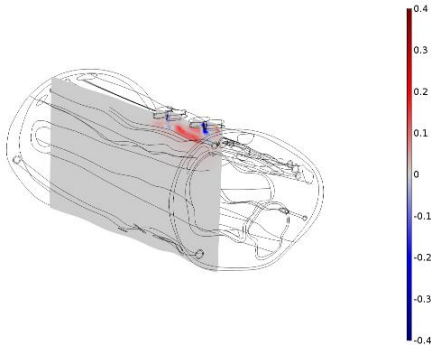
- A. The disadvantage of the classical in-line four-electrode impedance measurement strategy is in emerging opposite (negative) sensitivity in the regions between the respective current and potential electrodes [84]. The measurement is the most accurate when it has dominating, either positive or negative sensitivity, on the region of radial artery. If radial artery is placed in the regions with both (positive and negative) sensitivities, the measured transfer impedance will decrease due to opposite sensitivity impact [66]. The results of the study showed that the positive sensitivity is concentrated in regions close to the surface of forearm. However, a considerable region of negative sensitivity lay often near the electrodes placed on the surface, and for several measurements, could have an opposite contribution to the measured value. Such the results showed all strategies with distal electrode placement (strategies 1–3, Figure 3.14a – Figure 3.14c).
- B. On the other hand, strategies with circular electrode placement (strategies 4–6) showed no presence of negative sensitivity region on the radial artery and probably have no opposite contribution to the measured signal (Figure 3.14d – Figure 3.14f). But, the positive sensitivity maximum value showed to be significantly smaller for strategies with circular placement, than compared to distal placement.



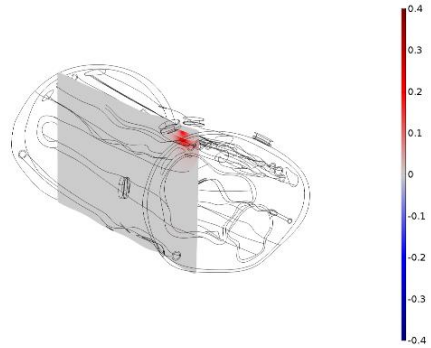
(a) *Distal electrode configuration (strategy 1)*



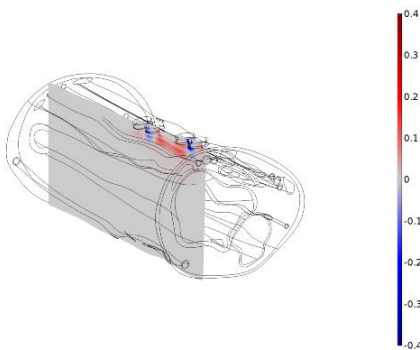
(d) *Circular electrode configuration (strategy 4)*



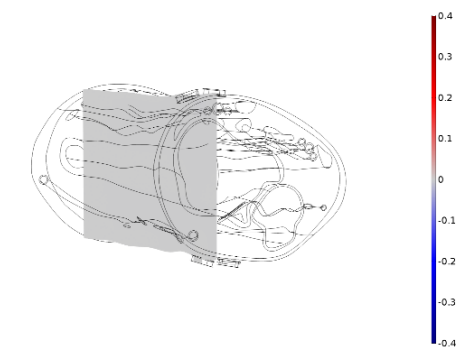
(b) *Distal electrode configuration (strategy 2)*



(e) *Circular electrode configuration (strategy 5)*



(c) *Distal electrode configuration (strategy 3)*



(f) *Circular electrode configuration (strategy 6)*

Figure 3.14 Sensitivity $S [m^{-4}]$ map obtained for in-line electrode placement strategies.

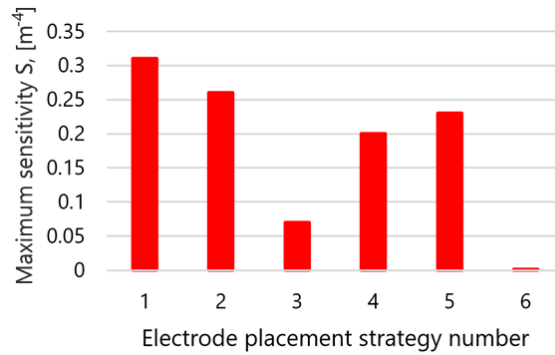


Figure 3.15 Maximum sensitivities of measurement in radial artery area.

It is important to consider the sensitivity value when an approximate location of expected impedance change is known – the change in measured EBI signal is the largest with the highest sensitivity [69]. Maximum sensitivities of the measured area of radial artery were calculated for each electrode configuration. The results are given in Figure 3.15.

3.5.2 Simulation results: various four-electrode placements and FIM electrode placements

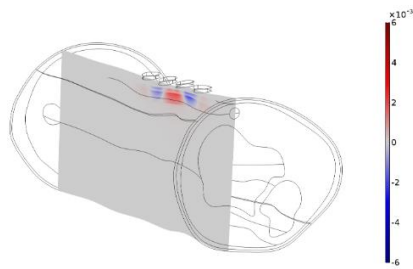
Another study focused on investigation of sensitivity distribution of EBI measurement for different electrode configurations was performed [66] and the results are presented in this section. Sensitivity colour maps were obtained for eight different electrode configuration strategies as listed in Section 3.2.2 and are shown on Figure 3.16a – Figure 3.16h. As in previous study, scaling of the colour map is kept the same within each simulation: positive values are indicated with red colour and negative values are indicated with blue colour.

Colour maps of distal (strategy 1) and circular 2 (strategy 2) electrode placements are shown in Figure 3.16a and Figure 3.16b respectively. As previously reported, the disadvantage of the in-line four-electrode impedance measurement strategy is an emerging negative sensitivity in the regions between the respective current and potential electrodes [84]. If radial artery is placed in these regions, the measured transfer impedance will decrease due to negative sensitivity impact [66].

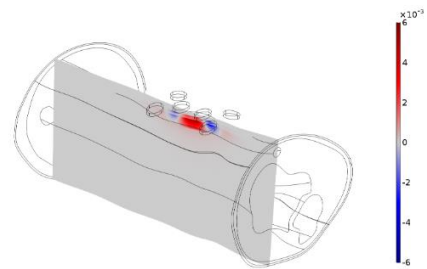
With the goal of investigating the effect of electrodes misplacement on the sensitivity distribution, two modified four-electrode placement strategies (3 and 4) were simulated and the result are shown in Figure 3.16c and Figure 3.16d.

In addition, four different electrode strategies based on focused (FIM) approach by using five (Figure 3.16f – Figure 3.16h) and six (Figure 3.16e) electrodes were simulated. FIM is well known approach which is proposed to reduce the opposite sensitivity impact in the neighbouring zones [76]. The advantage of the method is based on its ability to localize a small region in a volume conductor. The transfer impedances in the two orthogonal directions are merged, so the small negative sensitivity on one side is cancelled by a small positive sensitivity [69]. Furthermore, the negative sensitivity becomes insignificant with depth because of growing predominance of positive focused sensitivity [69].

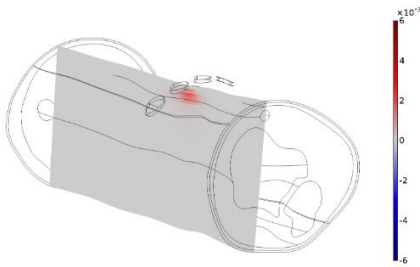
As it is important to consider the sensitivity value difference between the absolute values of maximum negative and maximum positive sensitivities in the region of radial artery, it is calculated and presented in Figure 3.17.



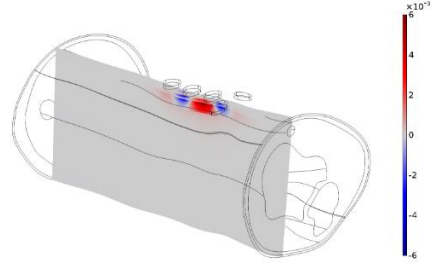
(a) *In-line distal electrode configuration (strategy 1)*



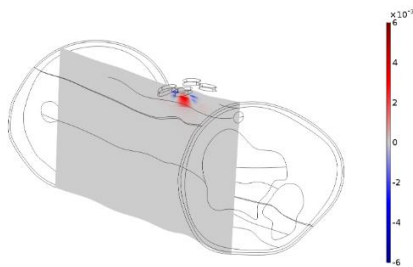
(e) *Six-electrode focused configuration (strategy 5)*



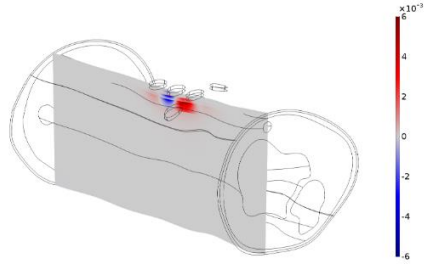
(b) *In-line circular electrode configuration (strategy 2)*



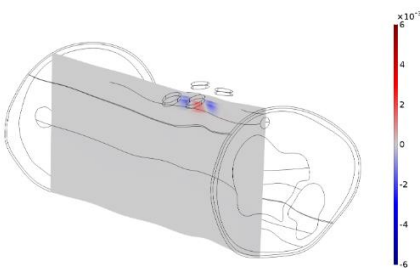
(f) *Five-electrode focused configuration (strategy 6)*



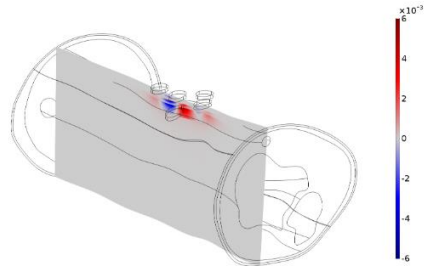
(c) *Rectangular four-electrode configuration (strategy 3)*



(g) *Five-electrode focused configuration (strategy 7)*



(d) *Rectangular four- electrode configuration (strategy 4)*



(h) *Five-electrode focused configuration (strategy 8)*

Figure 3.16 Sensitivity $S [m^{-4}]$ maps obtained for several electrode configuration strategies.

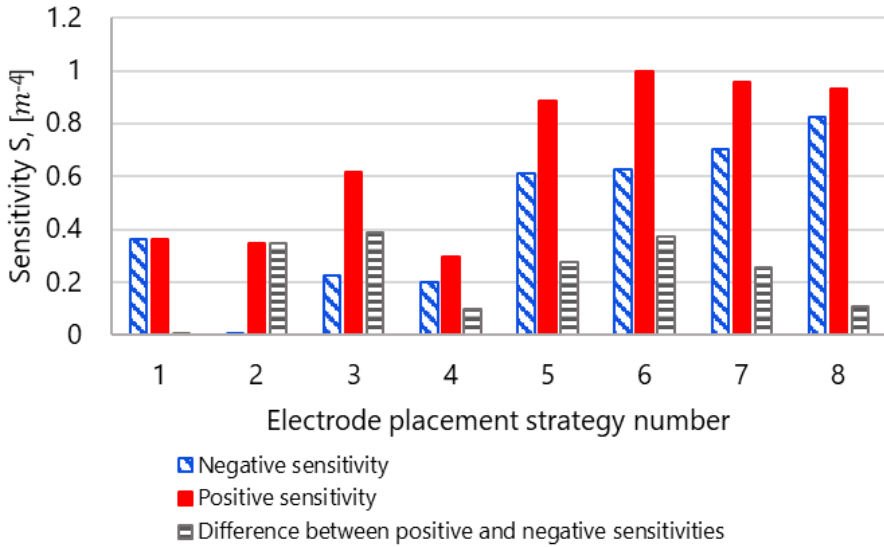


Figure 3.17 Ratio of maximum negative and maximum positive sensitivities (absolute values) and the difference between these values along the radial artery for electrode configuration strategies described in Section 3.2.2 [66].

3.5.3 Experimental results: various four-electrode and focused (FIM) electrode placements

Comparable experimental research directed on investigation EBI measurement for different electrode configurations (strategies presented in Section 3.2.2) was performed [66] and the results are presented in this section.

Single measurement of $Z(t)$ of the forearm was performed for each electrode placement to obtain data for comparison with other electrode placement strategies and the results of simulation. Figure 3.18 demonstrates the results represented by the calculated $R_{\Delta Z(t)pulse}$ and $R_{\Delta Z(t)move}$ shown in percentages (see Section 3.4.2). The presentation of the results by using the calculated $R_{\Delta Z(t)pulse}$ and $R_{\Delta Z(t)move}$ provides opportunity to compare the different electrode placement strategies on the same basis which can be considered as sensitivity of the placement to volume changes in underlying tissues [66]. Difference between various electrode placement strategies was clearly indicated in the sense of the amount of pulsating blood in radial artery and the concurrent movements. The measured impedance changes $Z(t)$, caused by the pulsating volume of blood ($\Delta Z(t)_{pulse}$) and the changes, caused by the movements of hand ($\Delta Z(t)_{move}$) shown in Ohms, are both visible in Figure 3.19.

When designing a wearable device, a major impact has the effect of concurrent resistive movements ($R_{\Delta Z(t)move}$). To evaluate the motion artefact of different strategies, a following equation (Eq. 41) could be used, see also Table 3.2:

$$R_{\Delta Z(t)portion} = \frac{\Delta Z(t)_{pulse} \cdot 100}{Z(t)_{move}} \quad (41)$$

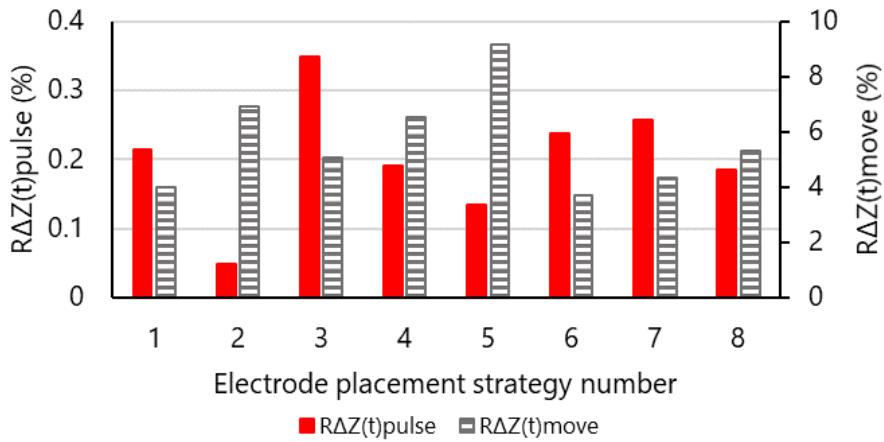


Figure 3.18 The comparison of the calculated $R\Delta Z(t)_{pulse}$ and $R\Delta Z(t)_{move}$ in the cases of the chosen electrode placement strategies [66].

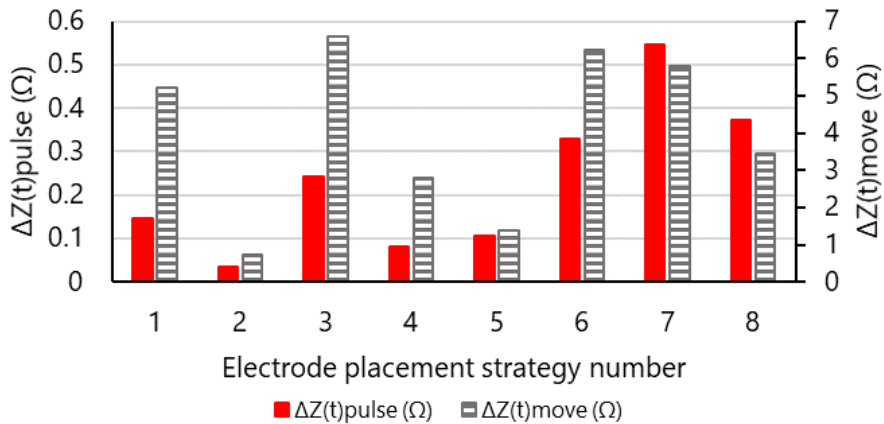


Figure 3.19 The comparison of the calculated $\Delta Z(t)_{pulse}$ and $\Delta Z(t)_{move}$ in the cases of the chosen electrode placement strategies [66].

Table 3.2 The percentages of measured $\Delta Z(t)_{pulse} / \Delta Z(t)_{move}$ [66].

Electrode placement strategy no. (see Section 3.2.2)	$R_{\Delta Z(t)_{portion}}, \%$
1	5.229
2	0.721
3	6.603
4	2.794
5	1.382
6	6.238
7	5.786
8	3.460

3.5.4 Comparative evaluation of the simulation and experimental results

The sensitivity distribution in forearm volume is predicted by the depth of modulation on the measured EBI signal, caused by continuous pulsation of blood in radial artery. The simulation results of the studies [37] and [66] demonstrated that most of the measurement sensitivity is concentrated in regions close to the surface of forearm model. The emergence of negative sensitivity on radial artery appears in all distal electrode placement strategies, but not in circular electrode placement strategies. At the same time, the positive sensitivity value shows to be lower in circular placement strategies compared to distal placement strategies. The change in measured signal is the largest with the highest sensitivity, so the distal electrode placement shows to be more suitable for the approach if compare to circular placement.

Also, the worst experimental result in the cases of $R_{\Delta Z(t)pulse}$ and $\Delta Z(t)pulse$ is clearly delivered by the circular electrode placement [66] – confirming the simulation results. Similar conclusion has been reported earlier in the literature [70], related to the suitability of the circular placement of electrodes. The experimental evaluation shows that the relatively small diameter of radial artery expects the usage of small electrodes to precisely set the sensitivity region to desired area. The accurate positioning of electrodes on radial artery have a great importance, as an unachievable measurement data is appearing in case of displacement [70].

Surprisingly, the best result in the case of experimentally gained $R_{\Delta Z(t)pulse}$ is achieved by using the approach of electrode placement strategy 3 introduced in Section 3.2.2 [66], (see Figure 3.20). The experimental results are also confirmed by simulation – this electrode placement strategy shows to have the highest sensitivity among the four-electrode strategies. However, similar electrode placements have been presented earlier in literature with satisfactory results [73].

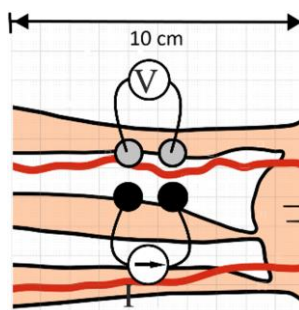


Figure 3.20 Rectangular four-electrode configuration (strategy 3).

The simulation results of FIM electrode placement strategies also show the presence of negative sensitivity impact. However, the negative sensitivity becomes less significant as the positive sensitivity tends to be higher. Simulation results confirm claimed FIM electrode placement strategies focusing ability in front of four-electrode approaches. Moreover, the proposed novel five-electrode FIM options provide comparably good and evidently better result as six-electrode FIM [66]. However, the measuring electrodes must remain disclosed by the area, induced by the exciting electrode pairs, so the difference between the positive and negative sensitivities becomes the highest.

When designing a wearable device, a major impact has the effect of concurrent movements ($R_{\Delta Z(t)move}$). From this point of view, the best result showed to be gained by using five-electrode FIM placement strategy 6 introduced in Section 3.2.2. The expectation

that the measuring electrodes must rest between a triangle of excitation electrodes in case of five-electrode FIM, is confirmed by deteriorating result of calculated $R_{\Delta Z(t)pulse}$ for the strategy 8 if compared to the strategies 6 and 7 (Section 3.2.2).

According to the results (demonstrated in Table 3.2) the top three of the most suitable electrode placement options for a smart wearable device could be proposed: the four-electrode placement strategy 3 and the five-electrode FIM strategies 6 and 7 (Section 3.2.2).

3.6 Chapter Summary

In this chapter a non-invasive technique based on bioimpedance measurement to estimate CAP of blood from the radial artery was presented. With the main purpose established by the need of proposing the most suitable electrode placement and configuration for a monitoring pulse wave in radial artery, several experimental measurements and sensitivity distribution simulations were performed using variety of electrode placements and configurations. Standard ECG electrodes were used as sensors during experimental measurements. FEM simulations of EBI measurements of radial artery were carried out using COMSOL Multiphysics® (version 5.3a).

The sensitivity S distribution for several combinations of current carrying and voltage pick-up electrodes placed close to the radial artery on the forearm model were mapped and compared to experimental measurement outcomes. The outcomes of simulation and experimentation confirmed that the amount of change in the measured EBI signal, caused by the pulsating blood in arteries, is strongly affected by the chosen electrode placement strategy. The results of measurements were generally in line with the outcome of simulation. Some deviations can be explained by the idealization and the static essence of the computer simulation model when compared to real living and highly dynamic biological object.

The proposed novel five-electrode FIM placement strategy shows to be a top two position in the point of view of motion artifact resistance. According to the study results, the best determined electrode placement strategy was proposed: a simple rectangular placement of four-electrode configuration EBI measuring setup, where the location of radial artery remains between the exciting and measuring pair (see Figure 3.20).

4 Eddy Current Sensing of Radial Artery Bioimpedance

The principle of the eddy current approach is based on the interaction between magnetic field source and the test material. Since the 1950s the role of eddy current testing has developed increasingly and have many applications. Biological tissues have a complex impedance, which changes with respect to frequency. This is caused by dispersion mechanisms which regulates the electromagnetic field interactions with the tissue. Measuring the bio-impedance spectra of a biological sample can potentially give an insight into the sample's properties [85]. This has apparent applications in the food-based, pharmaceutical and also medical industrial domains [85]. However, measuring the bio-impedance spectra with eddy current method presents several challenges. The low conductivity of the materials requires a highly sensitive measurement instrumentation.

In this chapter, a review of the eddy current method as it is used for EBI measurements for cardiac activity of human is presented. The measurement approach sensitivity is investigated by using magnetic flux and current density FEM simulations and practical experiments. Several induction coil sensors are described and are compared with the goal to evaluate the most suitable ones for EBI based monitoring of cardiac activity.

This chapter is based on the author's publications IV and V. The chapter is organized as follows. The Section 4.1 gives us an introduction to EBI measurement approach with inductive coupling. Simulation study of radial artery bioimpedance sensing with different coil types is presented in the Section 4.2. The Section 4.3 focuses on simulations of radial artery EBI sensing with toroidal core coil with concentrated to radial artery winding position. A feasibility study of utilization of air gapped toroidal magnetic cores for monitoring changing volume of pulsating blood in radial artery is introduced in the Section 4.4. The Section 4.5 summarizes the Chapter.

4.1 Introduction

The introduction and purpose of simulation and experimentation towards the selection of inductive sensor for monitoring blood pulsation in human radial artery is presented in this section.

4.1.1 Inductive sensors

EBI of the biological tissue can be measured not only by resistive coupling where electrodes are placed on the body (Chapter 3), but also by using inductive coupling, which is a known method for detecting material imperfections and the proximity of objects such as non-destructive testing (NDT) and flow of conductive matter in tube [86]. Electromagnetic blood flow meters rely on the conductive properties of blood: blood is considered as a conductor which is excited externally by using alternating electromagnetic field while the responsive voltage is measured with electrodes in direct contact [86]. Inductive coils can be used to determine pulse wave by inducing eddy currents in artery and detecting the emerging secondary alternating electromagnetic field [87]. Understanding the principles of the eddy current application helps to construct suitable inductive sensors.

There are many types of coil for eddy current sensing. Two main designs of coils sensor are air coil and core coil. The ferromagnetic materials can be used for shielding the field in the other directions. Also, ferromagnetic material placed inside the coil provides a focusing effect to the applied field. Since, the ferrite enhances the magnetic field strength inside the coil it is widely used in order to increase the signal to noise ratio.

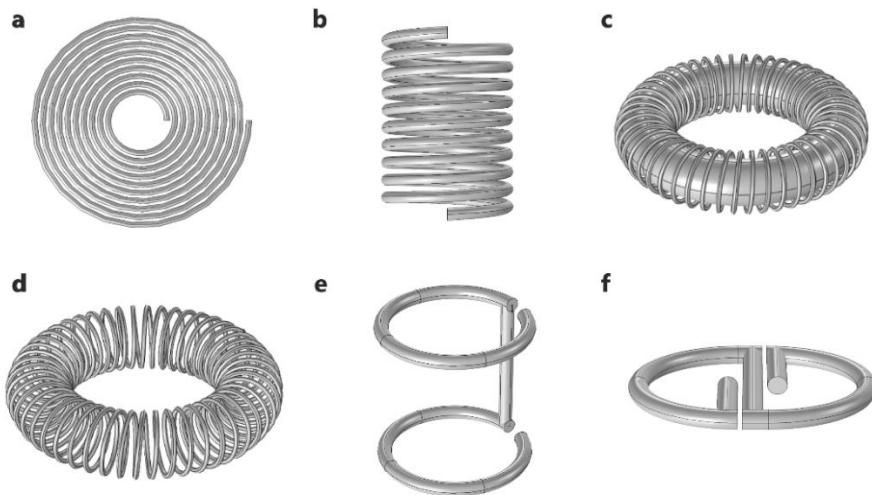


Figure 4.1 Planar circular coil (a), solenoid air coil (b), toroidal core coil (c), Rogowski coil (d), co-axial first-order gradiometer (e) and planar first-order gradiometer (f).

In addition, the shape and sizing of the coil is important. The extent of the magnetic field is decided by coil physical dimensions. The shape of the coil determines the shape of the generated magnetic field and therefore the change in inductance in the presence of a target object.

The following are common types of coils (Figure 4.1):

- *Planar coils* (with different shapes such as circular, square, hexagonal, rectangular etc.)
- *Solenoid coils* (air solenoid coils, core solenoid cores, irregular solenoid coils)
- *Toroidal core coils*
- *Rogowski coil*
- *Gradiometer coils* (with vertical, horizontal, asymmetrical arrangement etc.)

Similarly, as the prediction of current distribution in an object in the case of resistive coupling, the studies of sensitivity distribution for different positioning of inductive coil(s) for monitoring cardiac [88] and respiratory activity [89] have been presented. The simulation of sensitivity distribution caused by different coils can give a concern about the best configurations and coil types for the EBI approach for cardiac activity monitoring. The inductive coupling EBI measurement FEM simulations and experimentations have been performed on different parts of body like wrist [90], heart [91] and thorax [89].

4.1.2 Study and motivation

The idea presented in the thesis is that the inductive sensor integrated into wearable device is placed onto the radial artery on the wrist of human. The magnetic field is directed towards the surface under the probe. The coil that is carrying the external current also is sensor of changes taken place in impedance (absolute probe). However, another coil for sensing could be used.

The main purpose of this study is established by need of finding and proposing the most suitable inductive sensor for monitoring pulse wave in radial artery with the goal of non-invasive estimating of the aortic pressure (CAP) of blood by measuring the EBI of wrist. The approach for non-invasive CAP of blood by measuring EBI with resistive coupling (presented in previous Chapter) faces substantial problems caused by its direct contact: motion artefacts and comfort reduction due to need of direct electrical contact with skin in sense of wearable device. To pass through these obstacles, the non-contact sensing methods are of interest by using inductive coupling. For that reason, a technique based on bioimpedance measurement with inductive coupling to derive a blood pressure-related waveform from the radial artery is presented. In order to gain the purpose of the research, several experimental measurements and eddy current simulations were performed by using variety of coils and their configurations. FEM simulations of EBI measurement of radial artery were carried out by using COMSOL Multiphysics® (version 5.3a) to map the magnetic flux and current density distribution for coils placed close to the radial artery on the forearm 3D model. The experimental measurement and the results of respective simulation were compared and discussed.

4.2 Simulation Study of Radial Artery Bioimpedance Sensing with Different Coil Types

In this section, a simulation study for comparison of several coil sensors is presented. Planar, solenoid and toroidal core coils are placed on the simplified forearm 3D model to map the magnetic flux and current density distribution.

4.2.1 Simplified forearm model description

A simple 3D model was created in COMSOL Multiphysics® (version 5.3a) to simulate current and magnetic flux densities for eddy current measurement of forearm EBI. More realistic forearm model was used in Chapter 3 for EBI measurement with resistive coupling. Since this more realistic model mesh requires more computation resources and time for solving Magnetic Field physics, it was decided to use simplified model to address feasibility study and the realistic forearm 3D model as the subject of next works.

The geometry of this model includes: (1) muscle tissue domain, which has shape cylinder, (2) skin layer covers the muscle, (3) cylinder shaped bone domain, (4) cylinder shaped blood vessel representing the radial artery, (5) air domain, and (6) a coil from selection described in the Section 4.2.2. The model geometry without coil is shown in Fig.4.2. Corresponding material properties were added to the model and assigned to all domains according to [51] and COMSOL Multiphysics® built-in material library. The relative permittivity of magnetic material of core and shielding was set to 20 since this is a commercially available material.

The simulation process was carried out by utilizing Magnetic Field physics found under the AC/DC branch to compute the magnetic field and induced current distributions around the coil. The physics interface solves Maxwell's equations, which are formulated

using the magnetic vector potential and the scalar electric potential as the dependent variables for coils. The magnetic flux density B , magnetic field H and magnetic vector potential are related through the magnetic permeability μ as follow:

$$B = \nabla \times A \quad (42)$$

$$B = \mu H \quad (43)$$

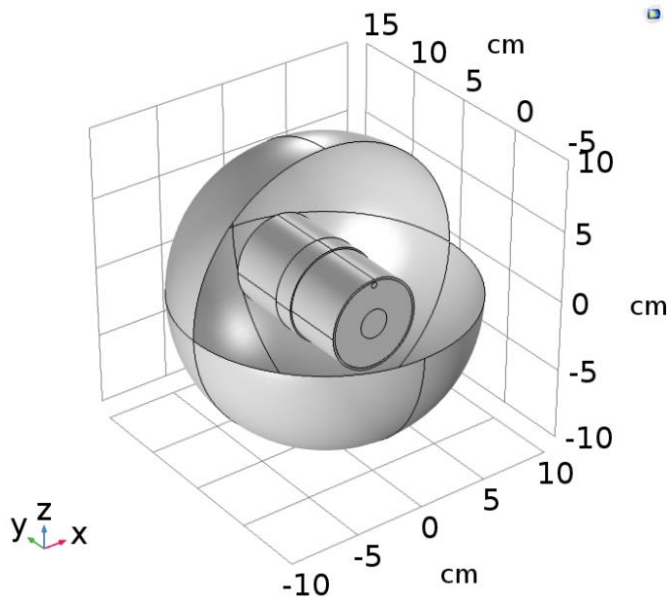


Figure 4.2 Simplified model of forearm.

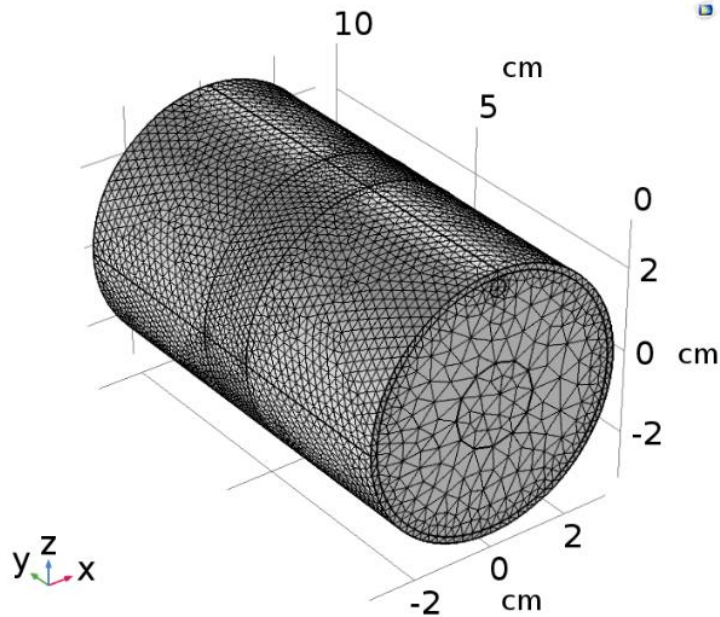


Figure 4.3 A Mesh of the forearm model.

The main node is Ampère's Law, which adds the equation for the magnetic vector potential and defines the constitutive relations and its associated properties [47]. In order to simulate physics, mathematical equations were assigned for different parts of the model through defining physics boundary conditions. The homogenised multi-turn numerical coil was added to the model (with exception in cases of planar coils), where single conductor coil type was chosen. The coil current excitation was set to 1A.

Physics-controlled mesh with fine tetrahedral mesh element type was chosen in this study (Figure 4.3).

As a choice of solver is optimized for the typical case for physics and study in COMSOL Multiphysics®, the said suggested solver and configurations were used. The Frequency Domain study and study steps were set to compute the model at frequency 1 MHz.

4.2.2 Types of coils used in FEM simulation

Simulation of eddy current measurement on human forearm model was utilized for following coil type and configurations (shown in Figure 4.4 – Figure 4.9):

1. Planar coil without ferromagnetic shielding placed on top of radial artery;
2. Planar coil with ferromagnetic shielding placed on top of radial artery;
3. Solenoid coil with ferromagnetic core placed on top of radial artery;
4. Solenoid air coil placed as a wristband around the forearm;
5. Toroidal core coil with equally distributed placed as a wristband around the forearm;
6. Toroidal core coil with concentrated to radial artery winding position placed as a wristband around the forearm.

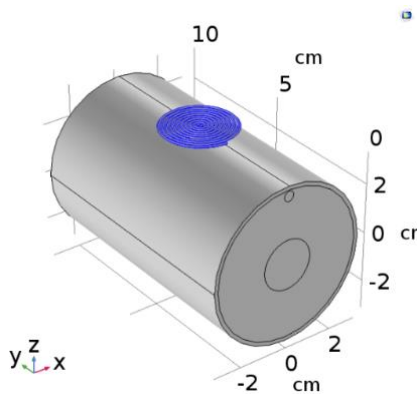


Figure 4.4 Planar coil on top of radial artery.

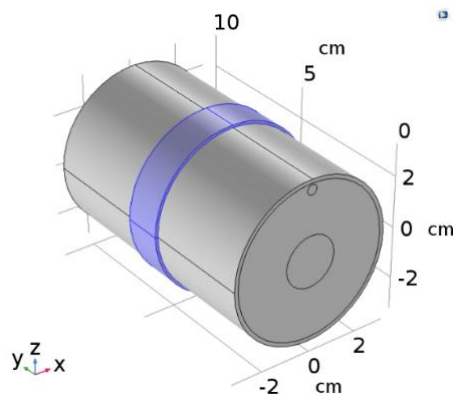


Figure 4.7 Solenoid coil with winding around the forearm.

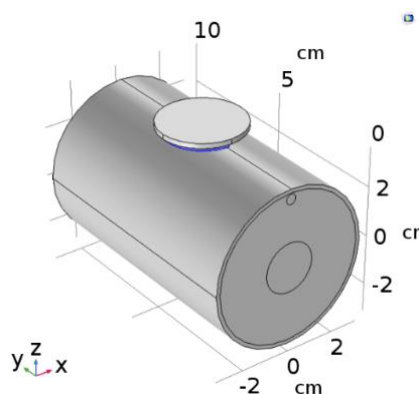


Figure 4.5 Planar coil with ferromagnetic shielding on top of radial artery by a magnetic shunt.

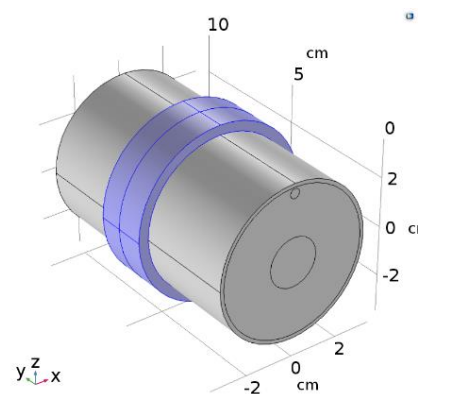


Figure 4.8 Toroidal core coil with equally distributed windings.

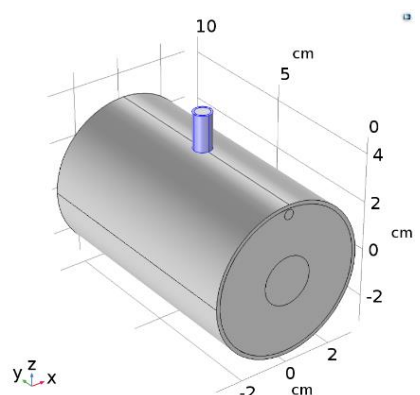


Figure 4.6 Core solenoid coil on top of radial artery.

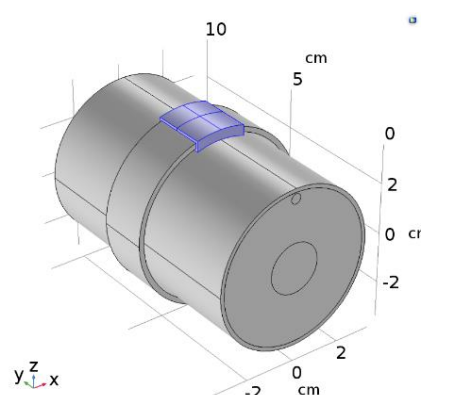


Figure 4.9 Toroidal core coil with windings concentrated to radial artery.

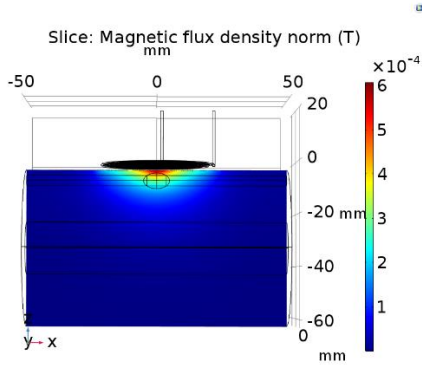
The dimensions and specifications of the coils were considered with the aim to fit wearable device. The details of utilized coil configuration are summarized in Table 4.1.

Table 4.1 Details of coils used in FEM simulation of eddy current sensing.

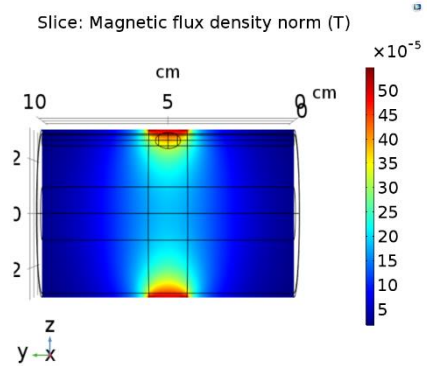
Description	Specifications	Magnetic core or shielding	Placement
Planar coil	Diameter: D=44mm Number of turns: 10 Coil inductance: 1.8 μ H Copper wire: d=1 mm	No	On top of radial artery
Planar coil with shielding	Diameter: D=44mm Number of turns: 10 Coil inductance: 1.8 μ H Copper wire: d=1 mm	Shielding on top of the coil	On top of radial artery
Solenoid core coil	Diameter: D=7.4mm Number of turns: 10 Coil inductance: 1.26 μ H Copper wire: d=0.8mm	Core	On top of radial artery
Solenoid coil	Diameter: D=64 mm Number of turns: 10 Coil inductance: 9.01 μ H Copper wire: d=0.8mm	No	Around the forearm
Toroidal core coil with equally distributed winding	Diameter of core: D=69 mm Number of turns: 10 Coil inductance: 48.7 μ H Copper wire: d=0.8mm	Core	Around the forearm
Toroidal core coil with concentrated winding position	Diameter of core: D=69mm Number of turns: 10 Coil inductance: 2.61 μ H Copper wire: d=0.8mm	Core	Around the forearm with windings concentrated to radial artery

4.2.3 FEM simulation results

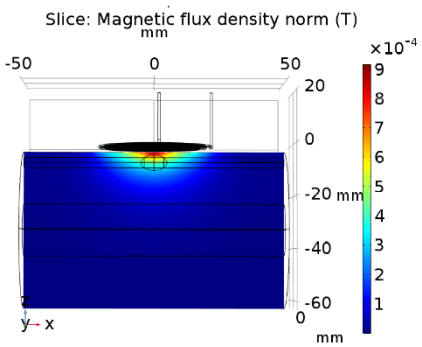
Figure 4.10a – Figure 4.10f show the magnetic flux density plot on a plane placed along the radial artery. The current density plots of a plane placed along the radial artery are presented in Figure 4.11a – Figure 4.11f. When implementing an eddy current method, material changes can be detected by monitoring the alternating current in the excitation coil (in case of single coil arrangement) or in sensing coil (when using a separate coil for sensing) to monitor the induced electromagnetic field. The variations in material properties will alter the strength and distribution of an induced eddy current flow, which, in turn, will result changes in the inducing coil or sensing coil currents. These changes can be expressed as a change in the coil's electrical impedance. So, the changes in material properties could be associated with specific changes in the impedance of either the excitation or sensor coils. The variations in current flow, both phase and amplitude, can be detected, amplified, displayed, and analysed as eddy current test results.



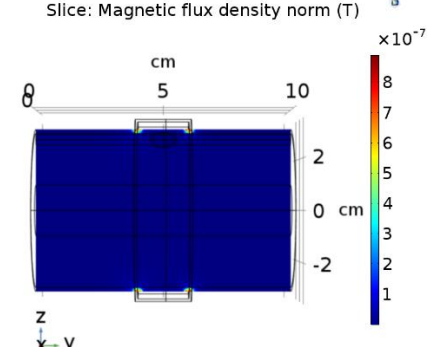
(a) Planar coil



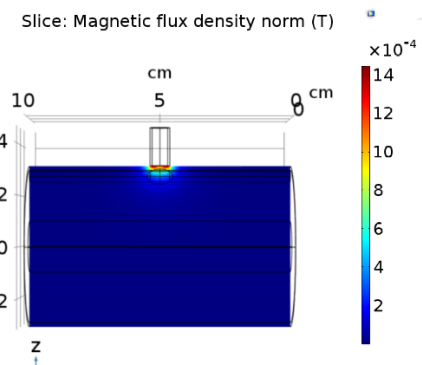
(d) Solenoid coil with a winding around the forearm.



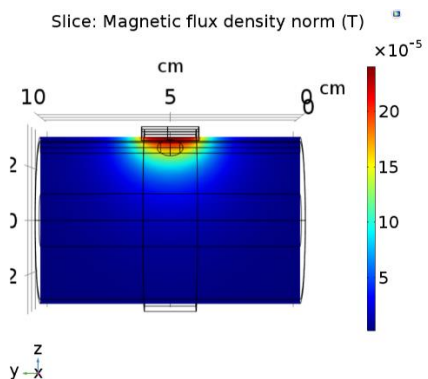
(b) Planar coil with ferromagnetic shielding



(e) Toroidal core coil with equally distributed windings

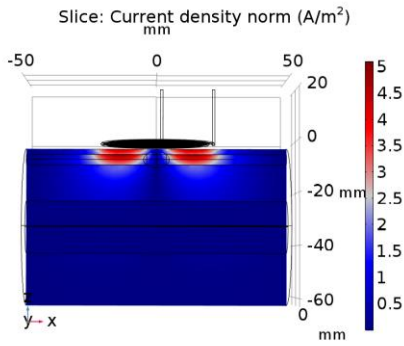


(c) Core solenoid coil placed on top of radial artery

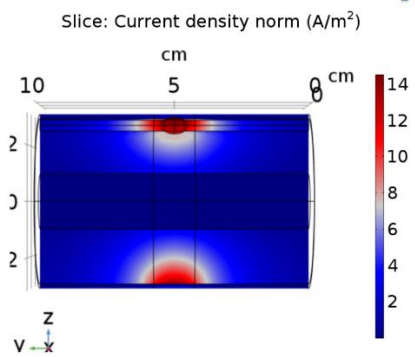


(f) Toroidal core coil with concentrated winding position

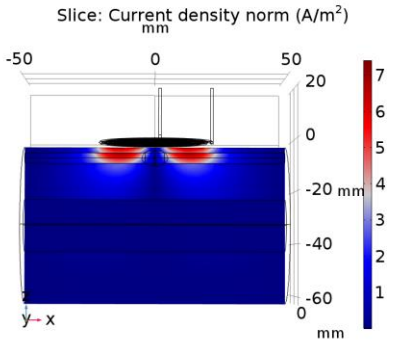
Figure 4.10 Magnetic flux density in case of different coils.



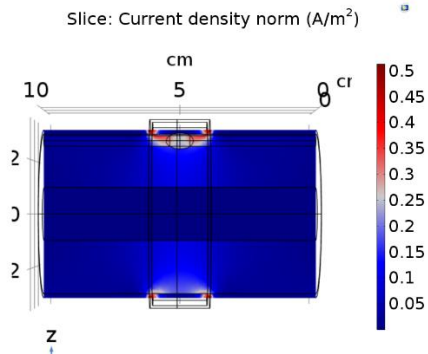
(a) Planar coil



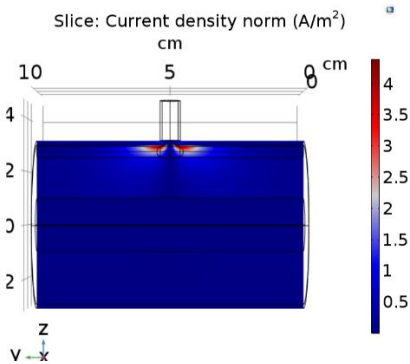
(d) Solenoid coil with a winding around the forearm



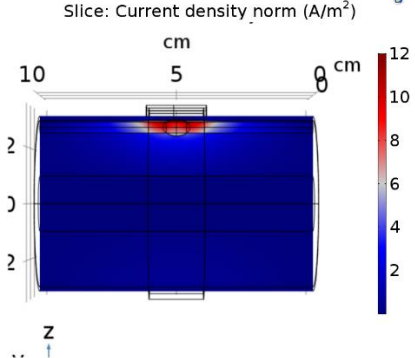
(b) Planar coil with ferromagnetic shielding



(e) Toroidal core coil with equally distributed windings



(c) Core solenoid coil placed on top of radial artery



(f) Toroidal core coil with equally distributed windings

Figure 4.11 Current density in case of different coils.

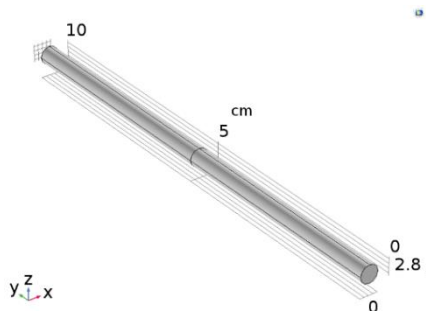


Figure 4.12 Radial artery as a simple cylinder representing no blood volume increasing due to pulse.

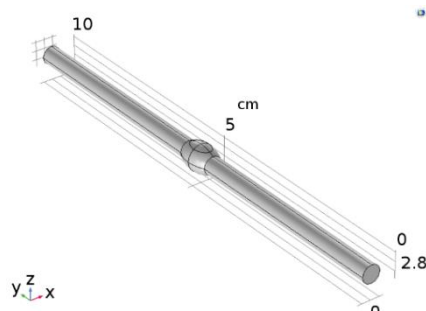


Figure 4.13 Radial artery with a dilation in the middle representing blood volume increasing due to pulse.

The simulations of eddy current sensing were performed for two cases: (1) radial artery is a simple cylinder representing no presence of blood volume increasing due to pulse (Figure 4.12), and (2) radial artery has a dilation in the middle representing blood volume increasing due to pulse (Figure 4.13).

Guided by the idea of [92] the impedance of the coil Z can be expressed as the sum of the coil impedance in case of no pulse Z_{np} (base impedance) and the impedance change due to the presence of the pulse Z_p :

$$Z = Z_{np} + \Delta Z_p \quad (44)$$

Table 4.2 shows complex values of impedances as a result of simulations in case of: (1) no pulse (Z_{np}) and (2) pulse (Z_p). When a complex value of impedance is used, the resistance is represented by the real part and then the reactance of the inductor is treated as imaginary number. It is proposed, that the coil type with largest impedance change due to pulse is the most sensitive for particular eddy current sensing application. The change in percentage of coil impedance real component ΔReZ due to the pulse is calculated and presented in the Table 4.2.

Table 4.2 Coil impedance simulation results for different coil types.

Coil type	Z_{np} , Ohm	Z_p , Ohm	ΔReZ , %
Planar coil	0.135094+10.640i	0.135068+10.639i	0.0151
Planar coil with ferromagnetic shielding	0.220019+15.426i	0.220052+15.427i	0.0161
Core solenoid coil on top of radial artery.	0.0073351+7.9530i	0.0073352+7.9530i	0.0014
Solenoid coil with winding around the forearm.	0.076458+56.594i	0.076467+56.594i	0.0118
Toroidal core coil	0.015888+3.0580i	0.015888+3.0580i	0
Toroidal core coil with concentrated to radial artery winding position	0.016307+16.374i	0.016310+16.374i	0.0184

As seen, the toroidal core coil with concentrated to radial artery winding position has the largest change of coil-impedance real component ReZ . According to these results, this coil is proposed to be the most suitable for the EBI measurement of radial artery with inductive coupling among other simulated coils. Additional simulation (see Chapter 4.3) and experimental) studies (see Appendix 6) were performed to evolve the approach.

4.3 Simulation Study of Radial Artery Bioimpedance Sensing by Using Toroidal Core Coil with Concentrated to Radial Artery Winding Position

Previous simulation (see Section 4.2) showed that the toroidal core coil with concentrated to radial artery winding position provides the best results of bioimpedance eddy current sensing on radial artery. For that reason, it was decided to investigate this setup extensively. Additional simulations were carried out with the aim to investigate if it is possible to further improve the results through coil parameters and setup changing. The geometry of the model and material properties remained the same as in previous section. Coil current excitation was set to 10mA and simulations were carried out at frequency 10MHz. Electric Circuit physics was used to add components for resonance LC circuit. The simulations were performed by changing several settings to find out their effect on the result:

1. Two capacitive electrodes were added to the model to direct current density lines.
2. Several values of relative permeability of coil core material were set and compared.
3. Simulations at several frequencies were evaluated and compared. Also, the circuit was set to the resonance trough addition of a parallel capacitor with fixed capacitance.

4.3.1 Determination of the effect of capacitive electrodes adding on the simulation results

Figure 4.14 demonstrates evaluation of functioning of human cardiopulmonary activity through simultaneous measurement of impedance variation of lungs, heart and vascular system of hand. The current i_i induced in the wrist by a generator G flows through the hand and conductive belt and closes through both heart and lungs. To measure the blood pulsation in the wrist (taking not into account other parts of the body), the model was supplemented with two capacitive electrodes connected through a wire (Figure 4.15). The simulation results are shown in Figure 4.16 – Figure 4.18. It should be noted, that the colour map scale is kept the same within all the corresponding figures. Figure 4.16 demonstrates the effect of adding capacitive electrodes to the model: the current density lines induced by coil seek to close through the electrodes. Also, the current density value is higher in case with added capacitive electrodes (Figure 4.17) and concentrates in the area of radial artery.

In addition, the effect of capacitive electrode placement was determined. Simulations were held for three different position of the electrodes (results are presented in Figure 4.18 and Table 4.3):

1. Distance between core and capacitive electrodes is 2mm (Figure 4.18b);
2. Distance between core and capacitive electrodes is 10mm (Figure 4.18c);
3. Distance between core and capacitive electrodes is 20mm (Figure 4.18d).

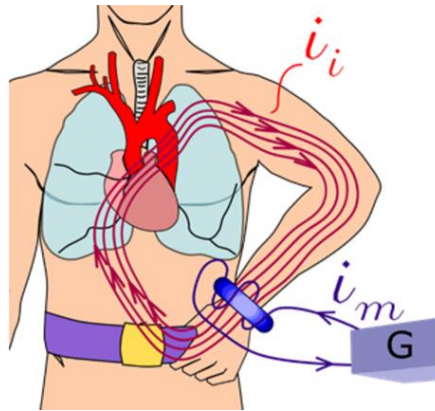


Figure 4.14 Schematic diagram of magnetic impedance measurement for cardiopulmonary monitoring.

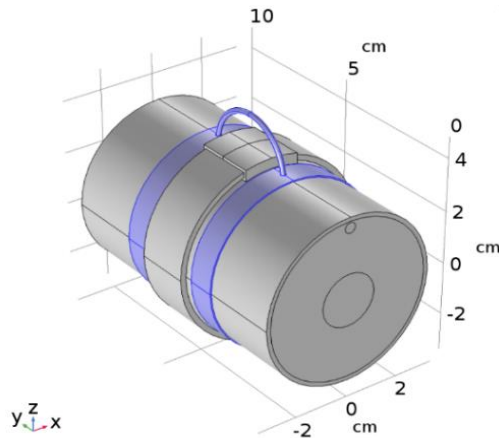


Figure 4.15 Illustration of the model with two capacitive electrodes added.

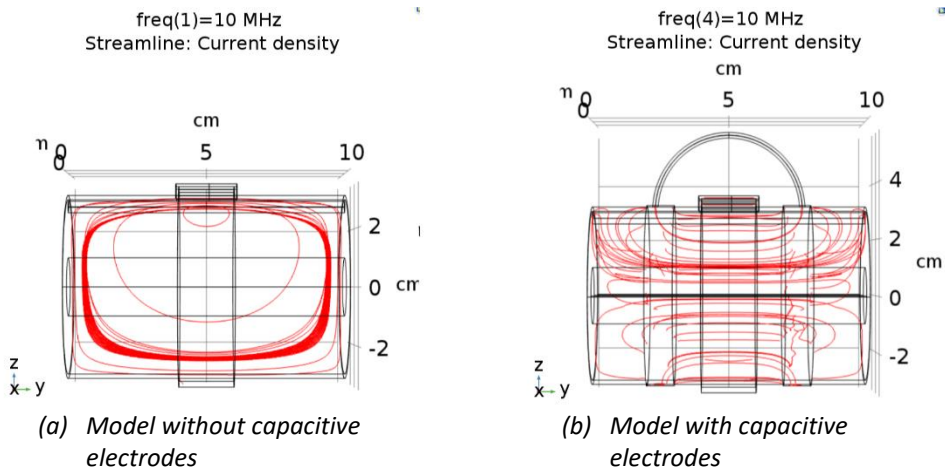


Figure 4.16 Effect of capacitive electrodes on the current density lines.

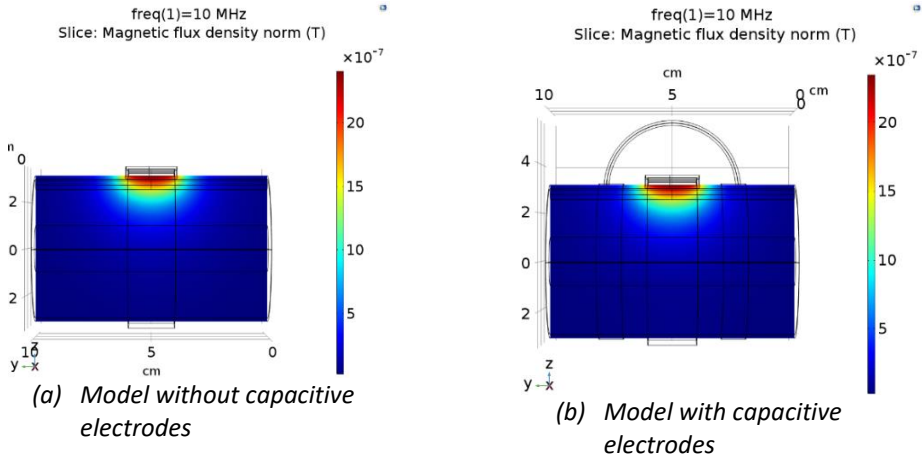


Figure 4.17 Effect of capacitive electrodes on the magnetic flux.

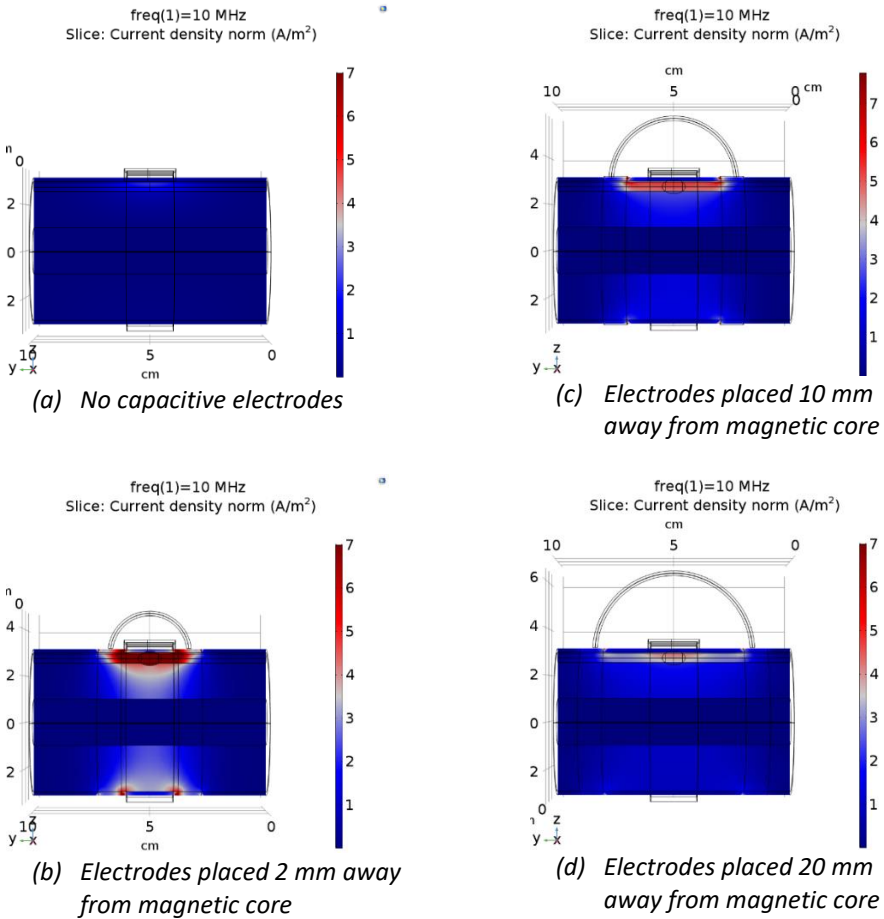


Figure 4.18 Current density depending on electrodes distance from magnetic core.

Table 4.3 Change of coil impedance real component ReZ due to pulse for different placement of capacitive electrodes.

Distance between magnetic core and capacitive electrodes, mm	$\Delta ReZ, \%$
2	0.049
10	0.184
20	0.089

The simulation outcome presented in the section demonstrates that it is possible to close the induced current lines through the capacitive electrodes. Furthermore, a significant increasing of current density in the radial artery region was detected when these electrodes added. The change of real component ReZ of coil impedance due to the pulse was calculated for three different distances between coil core and capacitive electrodes. The biggest change of coil impedance real component ReZ due to the pulse was detected in case of 1 cm distance between coil core and capacitive electrode.

4.3.2 Determination of the magnetic core permeability effect on the simulation results of induced current sensing on radial artery

Since magnetic core has high permeability and the initial coil impedance is higher than the permeability of air-core coils, the permeability effect on the induced current sensing on radial artery was investigated. The high permeability, relative to the surrounding air, causes the magnetic field lines to be concentrated in the core material. Larger relative permeability μ_r of the coil core can result in a significant increase of the sensor sensitivity. The transfer function of coil sensor $V = f(B)$ with magnetic core results from the fundamental Faraday's law of induction:

$$V = -\mu_0 \cdot \mu_r \cdot n \cdot A \cdot \frac{dH}{dt} \quad (45)$$

where A is an area and n is a number of turns of the coil. Simulations were performed for several values of magnetic core relative permeability μ_r : 5, 20, 50, 100 200 800. Magnetic flux densities are shown in Figure 4.19. Simulation outcomes showed, that the largest change of coil impedance real component due to the pulse was detected in case of relative permeability 20 (Table 4.4).

Table 4.4 Change of real component ReZ of coil impedance due to pulse for different values of relative permeability of coil core.

Relative permeability μ_r	$\Delta ReZ, \%$
5	0.199
20	0.454
50	0.416
100	0.323
200	0.210
800	0.041

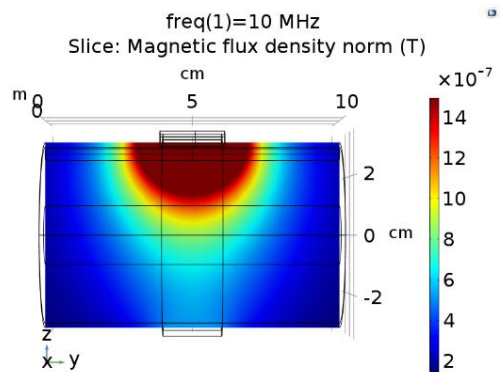
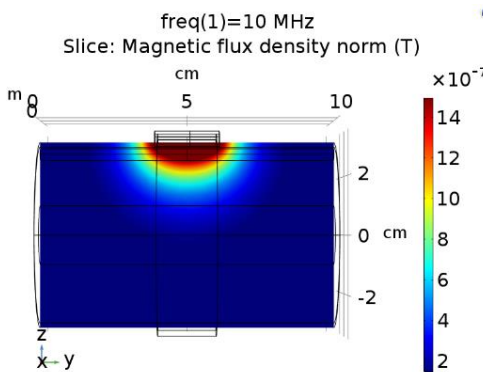
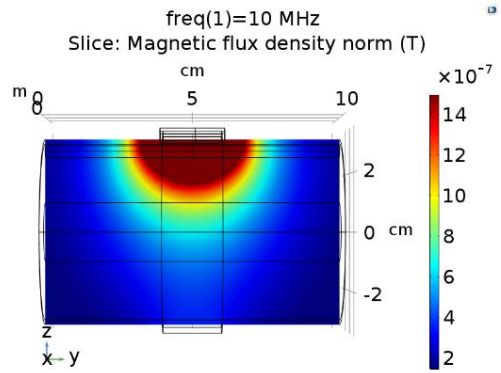
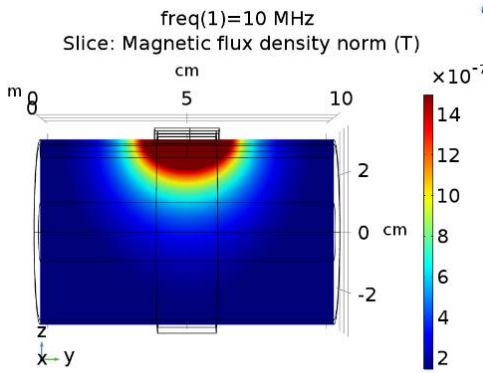
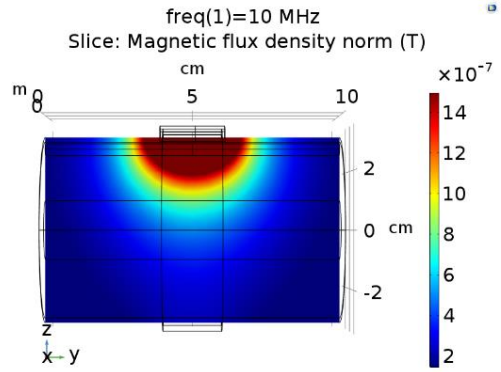
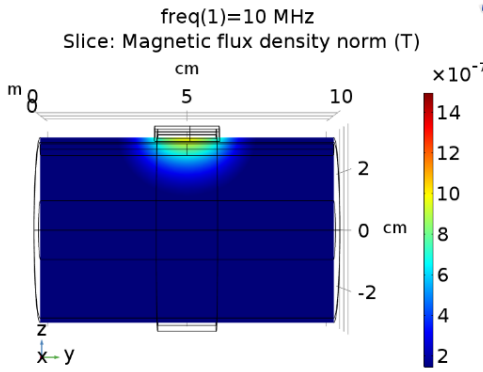


Figure 4.19 Magnetic flux density in case of different μ_r values of magnetic core.

4.3.3 Determination of the frequency effect on the simulation results of induced current sensing on radial artery

In addition, the EBI measurement frequency effect on the induced current sensing on radial artery was investigated. It is obvious that in order to obtain the output voltage signal of the sensor, the flux density must be varying in time [93]. The coil sensors are capable of measuring only the changing magnetic field. The output signal depends linearly on frequency, but due to the internal resistance R , inductance B and self-capacitance C of the sensor the dependency $V = f(f)$ is more complex [93] as follows:

$$V = 0.5 \cdot \pi^2 \cdot f \cdot n \cdot D^2 \cdot B \quad (46)$$

where f is a frequency of the induced field, n is a number of turns of the coil, D is diameter of the coil, B is the measured flux density.

Simulations were performed for several values of frequencies f : 1, 2, 5, 10 MHz. The current density plots of a plane placed along the radial artery are presented in Figure 4.20. Table 4.5 shows calculated change of coil impedance real component ReZ due to the pulse for these frequency values. Calculations showed, that the biggest change of real component of coil impedance due to the pulse was detected in case of frequency 10MHz.

Table 4.5 Change of real part ReZ of coil impedance due to pulse for different frequencies.

Frequency f , MHz	ΔReZ , %
1	0.012
2	0.171
5	0.231
10	0.454

When designing an inductive-sensing system, a capacitor C could be placed in parallel or series with the coil to create a resonant circuit. Resonance frequency f_0 is provided by the following equation:

$$f_0 = \frac{1}{2\pi\sqrt{LC}} \quad (47)$$

To measure the loss resistance directly (real part of the complex impedance value), an additional capacitor is implemented into the circuit with the goal to have a resonance. When the frequency is set to the resonant frequency, the imaginary parts of impedance of capacitor and inductance are equal, and the impedance of the LC circuit reaches the lowest value equal to real part of complex impedance.

At the frequency $f = 10MHz$ and coil inductance $L = 2.61mH$, a capacitor value was calculated ($C = 97,20pF$) for serial resonance according to:

$$C = \frac{1}{4\pi^2 f^2 L} \quad (48)$$

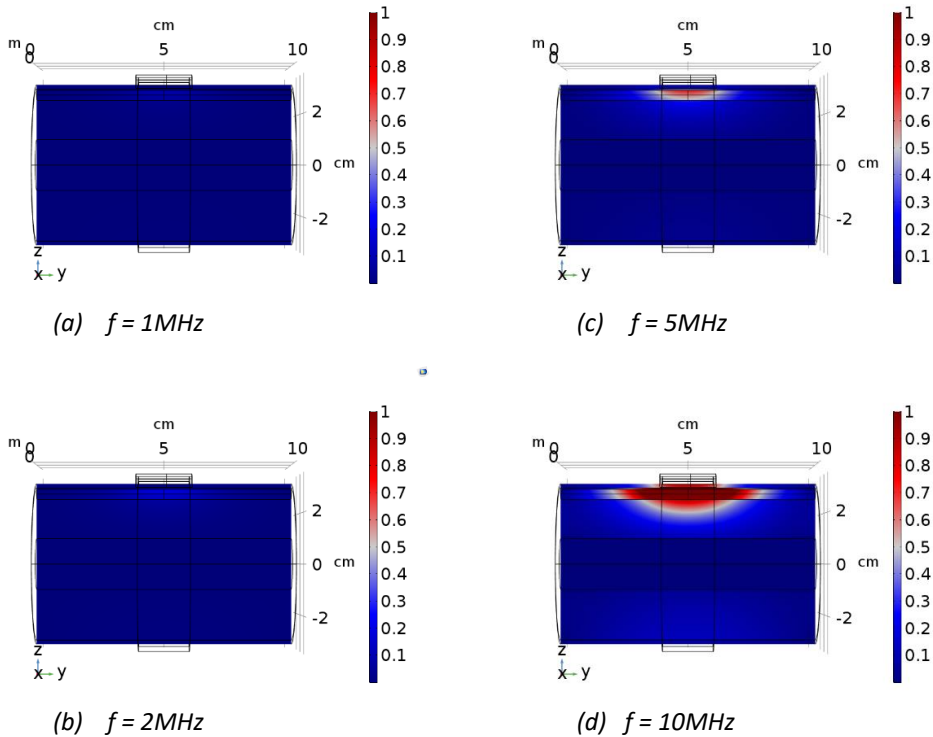


Figure 4.20 Current density J [A/m^2] distribution at different frequencies.

4.4 Experimentation and Simulation Study for Detecting Pulse Wave in Radial Artery by Using Air Gapped Toroidal Magnetic Cores

Another feasibility study of utilization of air gapped toroidal magnetic cores for monitoring changing volume of pulsating blood in artery was published by author [94]. The possibility of monitoring pulse wave by positioning the air gap of toroidal core noninvasively on top of the radial artery in forearm was investigated. Details and results of the study are presented in this Section. A single solid core copper wire connected to the close circuit with potentiometer was implemented to represent the changing impedance of conductive path of blood. Toroidal magnetic cores with two different shapes of air gaps and same windings were utilized to induce current in the copper wire. With theoretical expectation of focusing most of the reluctance of emerging magnetic field into the air gap, practical experimentation and simulations were performed. By placing the pulsating volume of blood in largest contribution of reluctance, its effect on magnetic field can be expected to be the largest [94].

4.4.1 Experimental measurement setup

Two configurations of toroidal cores were utilized during the experimentation (shown in Figure 4.21):

1. Toroid core with 180° cut air gap (width of 1.2 mm).
2. Toroid core with 0° cut air gap (width of 4 mm).

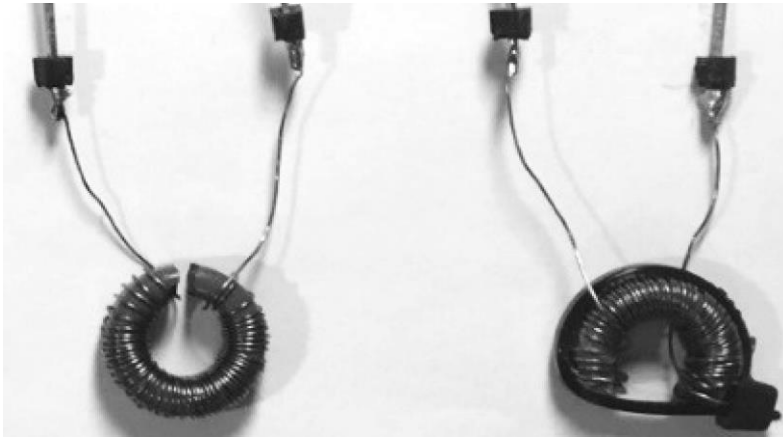


Figure 4.21 Configurations of toroidal cores with horizontally (angle of 0°) cut air gap (left) and with straight (angle of 180°) cut air gap (right).

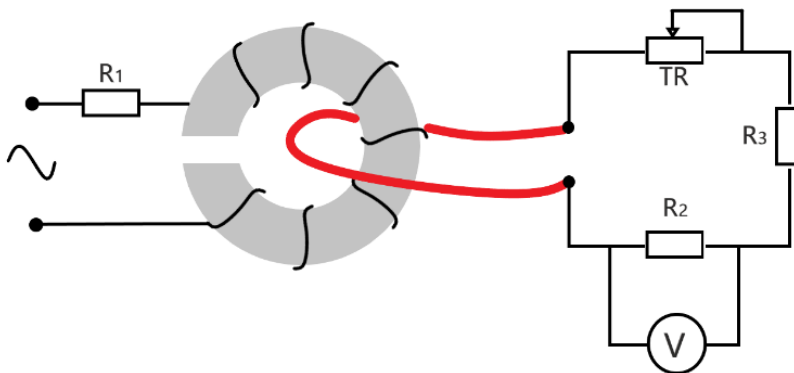


Figure 4.22 Illustration of measurement set up in the experiments where the imitation of conductive path of blood is represented by a single insulated copper wire.

Copper wire with diameter of 0.4 mm was wound on each toroidal core with the number of 50 turns. To represent conductive part of blood in radial artery a single insulated solid core copper wire with diameter of 0.5 mm was utilized. The copper wire was placed in three positions relative to toroidal core and air gap:

1. Copper wire placed in the center of the core,
2. Copper wire placed in the center of the air gap
3. Copper wire placed outside of the toroidal core about 1 mm above the gap.

The illustration of experimental measurement set up is shown in Figure 4.22. Measurements were performed with the goal of determining the effect of varying resistance of potentiometer onto the amplitude of detected sine wave. The measured electrical parameters of the wound coils at excitation signals and measurement setup are detailed in [94].

4.4.2 Simulations of magnetic flux density distribution

FEM simulations of magnetic flux density distribution were performed with the goal to validate the results of measurements. The geometries and material properties of toroid cores and copper wire were implemented according to experimentations (Figure 4.23).

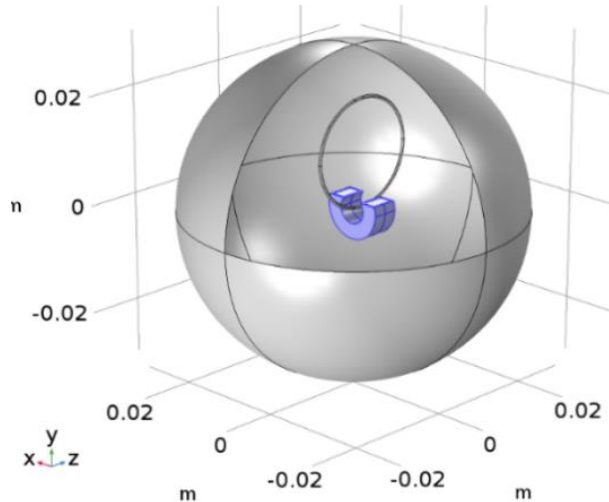


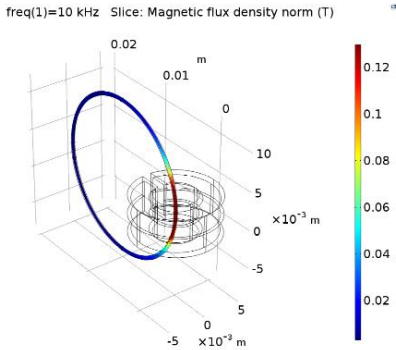
Figure 4.23 Model for simulation study for detecting pulse wave in radial artery by using air gapped toroidal magnetic cores.

The simulations were carried out by utilizing Magnetic Field physics. Electrical circuit physics was also used to add needed electrical circuit components and measure voltage in a wire. The homogenised multi-turn coil was added having of wire 50 turns and 1A excitation current. Physics-controlled mesh with fine tetrahedral mesh elements was used. The locations of wire that represent the conductive path of blood relative to toroidal core were identical to experimental measurement setup.

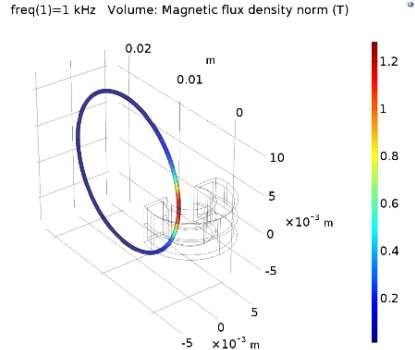
4.4.3 Results and discussion

The results are detailed in [94]. The voltage, induced by the emerging flux of magnetic field, applying onto the wire, was calculated and compared. The visual representation of emergence of magnetic flux density distribution in FEM model (Figure 4.24) is shown for all the setups with the implemented air gap. Table 4.6 shows the results of experimental measurement and simulations for different toroidal core configurations. The results of simulation of the same setup confirm the outcome of on-desk measurements. It should be noted, that the results of simulation lower than in the case of on-desk measurements. These differences come from the implementation of toroidal core and its application in COMSOL Multiphysics® simulations. However, the results in both cases are comparable in magnitude, being a direct reflection of the density of induced magnetic flux [94].

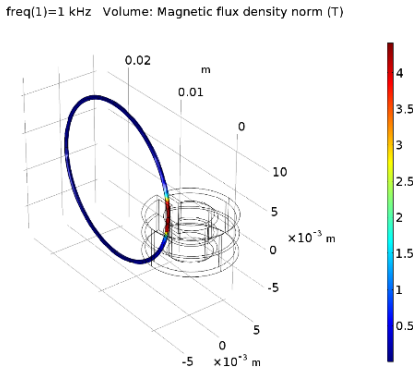
The outcome shows that the expectation of focusing the reluctance of magnetic field into the air gap of toroidal core does not result as highest value of induced current in copper wire. The best result was achieved, when placing the copper wire through the center of the core. The location of wire outside of the air gap showed the lowest result of the measured signal amplitude. The setups of toroidal cores with 0° cut air gap demonstrates even worse results.



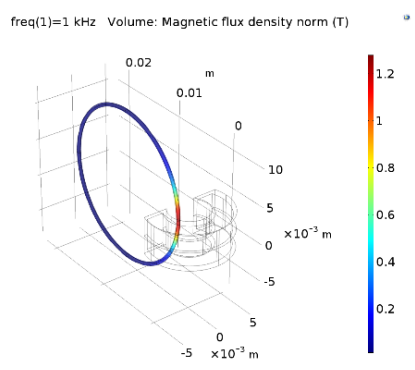
(a) Wire in a center of core with 0° cut air gap



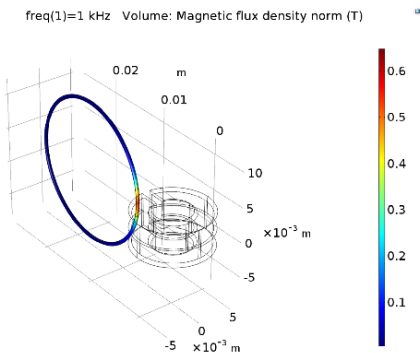
(d) Wire in a center of core with 180° cut air gap



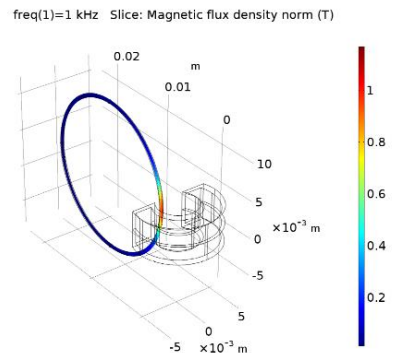
(b) Wire in a center of 0° cut air gap



(e) Wire in a center of 180° cut air gap



(c) Wire outside core with 0° cut air gap



(f) Wire outside core with 180° cut air gap

Figure 4.24 Magnetic flux density in copper wire in case of different wire placements and core cuts.

Table 4.6 EBI measurement and simulation results, modified from [94].

Air gap	Placement of copper wire	Experimental: ΔV_{ppV1} (OR \rightarrow 100R) (mV)	Simulation: Vsim (V)
Cut 180°	Center of toroidal core	2.40	2.03
Cut 180°	Center of air gap	1.73	0.93
Cut 180°	Outside of toroidal core	0.68	0.19
Cut 0°	Center of toroidal core	0.58	0.73
Cut 0°	Center of air gap	0.04	0.70
Cut 0°	Outside of toroidal core	0.01	0.54

The experimental result shows, that the original idea of placing the cut side of the toroidal magnetic core set on top of the location of radial artery on the surface of skin with the goal of inducing current in relatively good conductive blood, will not result as enough magnitude of emerging voltage.

4.5 Chapter Summary

In this section a possible usage of magnetic induction EBI sensing method for monitoring the pulse wave in radial artery was reaserched. The simulations in COMSOL Multiphysics® were implemented by using the finite element method (FEM) on the models of several coil types with different shapes and properties.

The current density and magnetic flux density distribution for coils placed close to the radial artery on the forearm model were mapped and compared. The outcomes of simulation confirmed that the amount of change in the measured EBI signal, caused by the blood pressure pulse in artery, depends strongly on the type and properties of the inductive coil sensor. The best coil set-up was found as follows: a toroidal coil with concentrated to radial artery winding position and capacitive electrodes added to close the induced current flow. The simulation outcome demonstrates clearly the effectiveness to close the current lines through the capacitive electrodes placed to the forearm. Furthermore, a significant increasing of current density in the radial artery region was detected when these electrodes were added. The largest change in the real part of impedance of toroidal core coil was achieved in case of: (1) core relative permeability value was 20, (2) the frequency was set to 10MHz and (3) the distance between capacitive electrodes and coil core was 10 mm. In addition, a capacitor was placed in series with the coil to create a resonant circuit having resonance at 10MHz. This case is certainly of practical value (see Appendix 6).

Also, the feasibility study of utilization of air gapped toroidal magnetic cores for monitoring changing volume of pulsating blood in artery was presented. The results of corresponding experimental measurements were validated with FEM simulations.

Conclusions

This thesis concerned the development of a non-invasive method for continuous monitoring of central aortic blood (CAP) pressure curve by using of electrical bioimpedance (EBI) sensing on the human forearm. Measured EBI variations ($\Delta Z(t)$) correspond to variations of blood volume due to the heart's activity in each cardiac cycle. The aim was to have a sensor at small size to fit wearable device, capable of movement artefacts proof operations at low consumption electrical power.

First, a tissue-mimicking phantom material was developed to use for evaluating EBI measurement systems before applying them on the real object. The electric conductivity of the gelatin-based phantom materials was adjusted by changing its composition and using the van der Pauw method for conductivity validation.

Second, the non-invasive method based on central aortic pressure evaluating by measuring the EBI of radial artery with resistive coupling was investigated.

To optimize the EBI signal acquisition, different electrode placement and configuration strategies were compared with the goal of finding the most suitable ones. A novel version of focused impedance method (FIM) was proposed: a five-electrode FIM strategy. The finite element method (FEM) simulation of sensitivity distribution and experimental measurements on radial artery were performed.

Third, investigations of several coil types were performed with the goal of determining the most suitable coil for noninvasive acquisition of the aortic blood pressure waveform by using inductive coupling. Chapter 4 attempted to obtain a better understanding of different coil characteristics. Six different types of coils were investigated, two of which were planar, two were solenoids and the other two were toroidal core coils. These coils were characterised as models and the FEM simulation of EBI measurements was performed. It was determined that the toroidal core coil with concentrated to radial artery winding position had the largest impedance change due the presence of pulse.

COMSOL Multiphysics® 3D modelling was used in this work as a main tool to employ FEM simulations to support the design process of EBI sensors for continuous monitoring of central aortic blood (CAP) pressure curve on human forearm. The results show the firm agreement between FEM simulations and experiments. This indicates that 3D FEM could be used for future development of EBI sensors.

Study results in the form of Q and A:

1. *Is the gelatin-based tissue mimicking phantom material manipulated with NaCl reliable for bioimpedance measurement?*

Answer: Results of developing a tissue-mimicking phantom material testing for the EBI sensing demonstrated a good prospect on used materials and methods. Low-cost and easily obtainable gelatine samples with electrical properties similar to biological tissues were produced. By changing the amount of sodium chloride in the mix, the conductivity of the phantom material was adjusted and verified with van der Pauw method. After calibrating a reliable and stable over time samples to conduct research for development of bioimpedance applications were achieved. Phantom materials were validated by simulations and measurements. FEM simulation accuracy of the eddy current measurement was verified as sufficient in the present approach.

2. *Which resistive coupling electrode configuration and placement strategy has the highest EBI measurement sensitivity in the region of the radial artery?*

Answer: The sensitivity distribution from FEM simulation results showed the presence of negative sensitivity impact in all investigated electrode placement strategies, but not in circular electrode placement strategies, only. At the same time, the positive sensitivity value showed to be lower in circular placement strategies. The change in measured signal is the largest due to the highest sensitivity, and the negative sensitivity becomes less significant, as the positive sensitivity tends to be higher. According to outcomes of FEM simulations, rectangular four-electrode configuration with the exciting pair on one side and the measuring pair on another side of radial artery, and five electrode FIM with measuring electrodes set between the excitation electrodes, are found to have the highest EBI measurement sensitivity in the region of radial artery.

3. *What kind of resistive coupling electrode placements and configurations on the forearm provide the highest extent of changes in measured impedance $Z(t)$, caused by the pulsating volume of blood in the radial artery?*

Answer: According to experimental measurement results the biggest amount of change in measured $Z(t)$, caused by the pulsating volume of blood in radial artery is provided by: rectangular four-electrode configuration with the exciting pair on one side and the measuring pair on another side of radial artery and a five-electrode FIM with measuring electrodes set between the excitation electrodes.

4. *Which coils provide the highest response in measured impedance caused by the pulse in radial artery?*

Answer: Based on the FEM simulation outcomes the biggest amount of change in measured $Z(t)$, caused by the pulse in radial artery gives the toroidal magnetic core coil with concentrated to radial artery winding position.

5. *Is it possible to increase the extent of changes in measured impedance, caused by the pulse in radial artery in case of the toroidal magnetic coil with a winding concentrated to radial artery position? We applied: (1) – changing relative permeability of the core material, (2) – changing of measurement frequency, and (3) – adding capacitive electrodes for the directing of current density lines.*

Answer: Yes, the effect of relative permeability of core material on the result was determined. Simulation outcomes showed, that the biggest change of real part of coil's impedance due to the pulse was detected in case of core with relative permeability equal to 20. (2) Yes, the effect of measurement frequency on the result was determined. Simulation outcomes showed, that the biggest change of coil impedance real component due to the pulse was detected in case of 10 MHz in our case. In general, higher frequency gives also higher response. (3) Yes, the simulation outcome demonstrates, that it is possible to close the current lines through the capacitive electrodes to increase current density in the radial artery region. The biggest change of real part of coil's impedance due to the blood pulse was detected in case of 1 cm distance between coil core and capacitive electrode.

6. *Is it possible to utilize air-gapped toroidal magnetic cores for monitoring volume changes of pulsating blood in radial artery?*

Answer: The experimental and simulation result showed that utilized configuration and circumstances the original idea of placing the cut side of the toroidal magnetic core set on top of the location of radial artery on the surface will not result enough in the magnitude of emerging voltage. On the basis of the obtained research results it is not effective to use air gapped toroidal magnetic core.

Future work:

The modelling methods based on Maxwell's equations were developed for the electrical bioimpedance (EBI) based investigation of arterial blood flow and pulsation processes by the aid of COMSOL Multiphysics® software, are intended to support the design of wearable sensors of blood pressure curves in peripheral arteries. The expectation is that using of the developed modelling and simulation methods will help us to understand the blood pulsation and pressure processes in peripheral vessels. Getting a better understanding, we will aim to find the appropriate electrodes to measure the flow and pulsation processes physically and to optimize the configuration and parameters of electrodes found as the best in every special measurement case.

Intensive research and development work, including prototyping and primary product development of wearable devices for cardiovascular and cardiopulmonary monitoring is going on in Thomas Johann Seebeck Department of Electronics at Tallinn University of Technology (TalTech). The future task is to adapt the developed modelling and simulation methods with the design of specific practical solutions of electrode and sensor systems. The research work will continue in this direction. For example, the first prototype and experimental results with the EBI measurement of radial artery by the aid of electromagnetic induction are introduced in Appendix 6. The modelling and simulation of this specific system is going on to support the development of original patent pending medical device.

Next possible direction of future research could be adding of dynamics (blood flow dynamics, mechanical movements of electrodes, deformation of blood vessels in time, etc.) to the developed model applied to simulation of the designed electrode and sensor systems. Such analyses will help identify critical points in the systems, thus enables to perform more detailed component-level structural analyses. It also gives the freedom to analyze forces experienced by segments of the structure, and stresses generated in flexible parts.

List of Figures

Figure 0.1 Flow diagrams showing the sequence of activities within the research made.	17
Figure 1.1 Impedance vector Z with real (ReZ) and imaginary (ImZ) parts. Remark: imaginary axis represents negative values here.	23
Figure 1.2 Single cell with equivalent circuit (a), its simplified mode (b) and Fricke-Morse model (c).	24
Figure 1.3 Graphical representation of current flow through a tissue at low frequency (a) and high frequency (b).	24
Figure 1.4 Idealized graph of magnitude of the tissue's impedance.	25
Figure 1.5 Dispersion regions for a tissue, idealized. Modified from Schwan (1988) [32].	26
Figure 1.6 Basic model of eddy current measurement.	28
Figure 1.7 Illustration of the electromagnetic field penetration inside a material at low frequency (a) and high frequency (b).	29
Figure 1.8 Central aortic pressure waveform as a sum of forward and reflected waves.	30
Figure 1.9 Amplification of blood pressure (BP) curve from aorta to peripheral arteries.	30
Figure 1.10 CAP waveform reconstruction from measured cycle of EBI waveform by the aid of transfer function TF.	31
Figure 2.1 Bode plot (a) and Nyquist (Cole) plot (b) for representing the impedance of parallel RC circuit.	36
Figure 2.2 Forearm phantom prepared for EBI measurement [4].	37
Figure 2.3 Manufacturing of gelatine based phantom material.	39
Figure 2.4 Illustrative drawing (left) and photo (right) of phantom cube with electrodes for vdP measurements.	39
Figure 2.5 PCB with planar coil for eddy current measurements, and a long strip electrode for vdP measurement [63].	42
Figure 2.6 The 3D view of magnetic flux density distribution of eddy current measurement on phantom material.	43
Figure 2.7 The 2D view of mode (left) with zoom extended (right).	44
Figure 2.8 Mesh of the model (left) with zoom extended (right).	44
Figure 2.9 Photo of PCB cut-through under measurement microscope [63].	45
Figure 2.10 Comparison of simulation and measurement results for material A [63].	46
Figure 2.11 Comparison of simulation and measurement results for material B [63].	46
Figure 3.1 Illustration of a four-electrode bioimpedance measuring system for monitoring the pulse wave in radial artery.	49
Figure 3.2 Illustration of pulse wave by the measured impedance $Z(\Omega)$ together with the reference photoplethysmography (PPG) and ECG signal modified from [44].	49
Figure 3.3 The sensitivity formation of a four-electrode impedance measurement in homogeneous volume. CC1 and CC2 form a current carrying electrode pair (red lines). PU1 and PU2 form a voltage pick-up electrode pair (blue lines) [66].	51
Figure 3.4 In-line electrode configuration strategies for EBI measurements on radial artery.	53
Figure 3.5 Basic concept of six-electrode FIM.	54

Figure 3.6 Electrode configuration strategies for EBI measurements on radial artery [66].	55
Figure 3.7 Human forearm and the cross section of the wrist on the right [46].	56
Figure 3.8 COMSOL Multiphysics® 3-D model of a fragment of human forearm.	57
Figure 3.9 Two views of mesh of the simplified human forearm model.	58
Figure 3.10 Current density lines in case of in-line distal four-electrode placement.	59
Figure 3.11 Example of obtained sensitivity map, $S [m - 4]$.	60
Figure 3.12 Visual representation of measurement setup for determination of $\Delta Z(t)$ caused by pulsating volume of blood in radial artery [66].	61
Figure 3.13 The determination of $\Delta Z(t)$ in the $Z(t)$ waveform, corresponding to a blood pulse [66].	62
Figure 3.14 Sensitivity $S [m - 4]$ map obtained for in-line electrode placement strategies.	63
Figure 3.15 Maximum sensitivities of measurement in radial artery area.	64
Figure 3.16 Sensitivity $S [m - 4]$ maps obtained for several electrode configuration strategies.	65
Figure 3.17 Ratio of maximum negative and maximum positive sensitivities (absolute values) and the difference between these values along the radial artery for electrode configuration strategies described in Section 3.2.2 [66].	66
Figure 3.18 The comparison of the calculated $R\Delta Z(t)$ pulse and $R\Delta Z(t)$ move in the cases of the chosen electrode placement strategies [66].	67
Figure 3.19 The comparison of the calculated $\Delta Z(t)_{\text{pulse}}$ and $\Delta Z(t)_{\text{move}}$ in the cases of the chosen electrode placement strategies [66].	67
Figure 3.20 Rectangular four-electrode configuration (strategy 3).	68
Figure 4.1 Planar circular coil (a), solenoid air coil (b), toroidal core coil (c), Rogowski coil (d), co-axial first-order gradiometer (e) and planar first-order gradiometer (f).	71
Figure 4.2 Simplified model of forearm.	73
Figure 4.3 A Mesh of the forearm model.	74
Figure 4.4 Planar coil on top of radial artery.	75
Figure 4.5 Planar coil with ferromagnetic shielding on top of radial artery by a magnetic shunt.	75
Figure 4.6 Core solenoid coil on top of radial artery.	75
Figure 4.7 Solenoid coil with winding around the forearm.	75
Figure 4.8 Toroidal core coil with equally distributed windings.	75
Figure 4.9 Toroidal core coil with windings concentrated to radial artery.	75
Figure 4.10 Magnetic flux density in case of different coils.	77
Figure 4.11 Current density in case of different coils.	78
Figure 4.12 Radial artery as a simple cylinder representing no blood volume increasing due to pulse.	79
Figure 4.13 Radial artery with a dilation in the middle representing blood volume increasing due to pulse.	79
Figure 4.14 Schematic diagram of magnetic impedance measurement for cardiopulmonary monitoring.	81
Figure 4.15 Illustration of the model with two capacitive electrodes added.	81
Figure 4.16 Effect of capacitive electrodes on the current density lines.	81
Figure 4.17 Effect of capacitive electrodes on the magnetic flux.	82
Figure 4.18 Current density depending on electrodes distance from magnetic core.	82
Figure 4.19 Magnetic flux density in case of different μr values of magnetic core.	84

Figure 4.20 Current density J [A/m^2] distribution at different frequencies.	86
Figure 4.21 Configurations of toroidal cores with horizontally (angle of 0°) cut air gap (left) and with straight (angle of 180°) cut air gap (right).	87
Figure 4.22 Illustration of measurement set up in the experiments where the imitation of conductive path of blood is represented by a single insulated copper wire.	87
Figure 4.23 Model for simulation study for detecting pulse wave in radial artery by using air gapped toroidal magnetic cores.	88
Figure 4.24 Magnetic flux density in copper wire in case of different wire placements and core cuts.	89

List of Tables

Table 1.1 Dielectric dispersion regions [32].	27
Table 1.2 Comparison of different devices using tonometry method to measure CAP, modified from [4].	32
Table 2.1 Gelatin tissue mimicking phantom mixture ingredients [50].	38
Table 2.2 Electrical conductivities of phantom material, different amount of NaCl [50].	41
Table 2.3 Electrical conductivities of different tissues at frequency 10 kHz [61].	41
Table 2.4 Comparison of designed and actual coil dimensions.	45
Table 3.1 Material properties assigned to the model domains [51], * [80].	57
Table 3.2 The percentages of measured $\Delta Z(t)_{\text{pulse}} / \Delta Z(t)_{\text{move}}$ [66].	67
Table 4.1 Details of coils used in FEM simulation of eddy current sensing.	76
Table 4.2 Coil impedance simulation results for different coil types.	79
Table 4.3 Change of coil impedance real component ReZ due to pulse for different placement of capacitive electrodes.	83
Table 4.4 Change of real component ReZ of coil impedance due to pulse for different values of relative permeability of coil core.	83
Table 4.5 Change of real part ReZ of coil impedance due to pulse for different frequencies.	85
Table 4.6 EBI measurement and simulation results, modified from [94].	90

References

- [1] "European cardiovascular disease statistics," ESC, 2017.
- [2] C. T. Phua, Novel method of blood pulse and flow measurement using the disturbance created by blood flowing through a localized magnetic field, 2013.
- [3] N. Ghasemzadeh and A. M. Zafari, "A Brief Journey into the History of the Arterial Pulse," *Cardiology Research and Practice*, 2011.
- [4] H. Kõiv, M. Rist and M. Min, "Development of bioimpedance sensing device for wearable monitoring of the aortic blood pressure curve," *Technisches Messen*, vol. 85, no. 5, p. 366–377, 2018.
- [5] H. Saner, S. E. J. Knobel, N. Schuetz and T. Nef, "Contact-free sensor signals as a new digital biomarker for cardiovascular disease: chances and challenges," *European Heart Journal - Digital Health*, vol. 1, pp. 30-39, 2020.
- [6] T. K. Bera, "Bioelectrical Impedance Methods for Noninvasive Health Monitoring: A Review," *Journal of Medical Engineering*, 2014.
- [7] E. C. Hoffer, C. K. Meador and D. C. Simpson, "Correlation of whole-body impedance with total body water volume," *Journal of Applied Physiology*, vol. 27, no. 4, p. 531–534, 1969.
- [8] U. G. Kyle, I. Bosaeus and A. D. De Lorenzo, "Bioelectrical impedance analysis-part I: review of principles and methods," *Clinical Nutrition*, vol. 23, no. 5, p. 1430–1443, 2004.
- [9] D. A. Schoeller, "Bioelectrical impedance analysis. What does it measure?," *Annals of the New York Academy of Sciences*, vol. 904, p. 159–162, 2000.
- [10] G. Anand, A. Lowe and A. Al-Jumaily, "Tissue phantoms to mimic the dielectric properties of human forearm section for multi-frequency bioimpedance analysis at low frequencies," *Materials Science and Engineering*, vol. 96, pp. 496–508, 2019.
- [11] J. R. Macdonald, "Impedance spectroscopy," *Annals of Biomedical Engineering*, vol. 20, no. 3, p. 289–305, 1992.
- [12] T. K. Bera, J. Nagaraju and G. Lubineau, "Electrical impedance spectroscopy (EIS)-based evaluation of biological tissue phantoms to study multifrequency electrical impedance tomography (Mf-EIT) systems," *Journal of Visualization*, 2016.
- [13] J. R. Mager, S. D. Sibley, T. R. Beckman, T. A. Kellogg and C. P. Earthman, "Multifrequency bioelectrical impedance analysis and bioimpedance spectroscopy for monitoring fluid and body cell mass changes after gastric bypass surgery," *Clinical Nutrition*, vol. 27, no. 6, pp. 832–841, 2008.
- [14] E. Atzler E and G. Lehmann, "Über ein Neues Verfahren zur Darstellung der Herztätigkeit (Dielektrographie)," *Arbeitsphysiol*, vol. 6, pp. 636–680, 1932.
- [15] J. Nyboer, "Electrical impedance plethysmography; a physical and physiologic approach to peripheral vascular study," *Circulation*, vol. 2, no. 6, p. 811–821, 1950.
- [16] R. V. Hill, J. C. Jansen and J. L. Fling, "Electrical impedance plethysmography: a critical analysis," *Journal of Applied Physiology*, vol. 22, no. 1, p. 161–168, 1967.
- [17] J. C. Denniston, J. T. Maher and J. C. Reeves, "Measurement of cardiac output by electrical impedance at rest and during exercise," *Journal of Applied Physiology*, vol. 40, no. 1, pp. 91–95, 1976.

- [18] J. C. Miller and S. M. Horvath, "Impedance cardiography," *Psychophysiology*, vol. 15, no. 1, pp. 80–91, 1978.
- [19] R. P. Patterson, "Fundamentals of impedance cardiography," *IEEE Engineering in Medicine and Biology Magazine*, vol. 8, pp. 35–38, 1989.
- [20] R. P. Henderson and J. G. Webster, "An Impedance Camera for Spatially Specific Measurements of the Thorax," *EEE Trans. Biomed. Eng.*, vol. 25, no. 3, p. 250–254, 1978.
- [21] D. S. Holder, *Electrical impedance tomography: methods, history and applications*, 2005.
- [22] M. Cheney, D. Isaacson and J. C. Newell, "Electrical Impedance Tomography," *Society for Industrial and Applied Mathematics*, vol. 41, no. 1, pp. 85–101, 1999.
- [23] S. Grimnes and O. G. Martinsen, "Bioimpedance," in *Wiley Encyclopedia of Biomedical Engineering*, 2006, pp. 438–446.
- [24] C. Tronstad, G. E. Gjein, S. Grimnes, O. G. Martinsen, A. L. Krogstad and E. Fosse, "Electrical measurement of sweat activity," *Physiological Measurement*, vol. 29, no. 6, p. S407–S415, 2008.
- [25] F.-J. Pettersen and J. O. Høgetveit, "From 3D tissue data to impedance using Simpleware ScanFE+IP and COMSOL," *Journal of Electrical Bioimpedance*, vol. 2, pp. 13–32, 2011.
- [26] L. A. Geddes and L. E. Baker, *Principles of Applied Biomedical Instrumentation*, New York: John Wiley, 1989.
- [27] M. Akay, *Wiley Encyclopedia of Biomedical Engineering*, 6 Volume Set, 2006.
- [28] H. Fricke, "A mathematical treatment of the electric conductivity and capacity of disperse systems. II. The capacity of a suspension of conducting spheroids surrounded by a non-conducting membrane for a current of low frequency," *Physical Review* 26, 1925.
- [29] A. Ivorra, "Tissue Electroporation as a Bioelectric Phenomenon: Basic Concepts," in *Irreversible Electroporation*, 2009, pp. 23–61.
- [30] K. S. Cole and R. H. Cole, "Dispersion and Absorption in Dielectrics I. Alternating Current Characteristics," *The Journal of Chemical Physics*, vol. 9, no. 4, pp. 341–351, 1941.
- [31] C. Polk and E. Postow, *Handbook of biological effects of electromagnetic*, 2nd ed., CRC Press, 1996.
- [32] G. J. Tortora, *Principles of Anatomy and Physiology* 7th edition, 1993.
- [33] S. Grimnes and O. Martinsen, *Bioimpedance and Bioelectricity Basics*, 2nd ed., 2008.
- [34] S. Grimnes and Ø. Martinsen, "Alpha-dispersion in human tissue," *Journal of Physics: Conference Series*, vol. 224, 2010.
- [35] E. Priidel, M. Min, K. Pesti, J. Ojarand and O. Martens, "FPGA-based 16-bit 20MHz device for the inductive measurement of electrical bio-impedance," 2021.
- [36] M. Cecconi, D. De Backer, M. Antonelli, R. Beale, J. Bakker and C. Hofer, "Consensus on circulatory shock and hemodynamic monitoring. Task force of the European Society of Intensive Care Medicine.," *Intensive Care Med.*, vol. 40, no. 12, p. 1795–1815, 2014.

- [37] . V. Salmasi, K. Maheshwari, D. Yang, E. J. Mascha, A. Singh and D. I. Sessler, "Relationship between intraoperative hypotension, defined by either reduction from baseline or absolute thresholds, and acute kidney and myocardial injury after noncardiac surgery: a retrospective cohort analysis," *Anesthesiology*, vol. 126, no. 1, p. 47–65, 2017.
- [38] K. Pesti, H. Kõiv and M. Min, "Simulation of the Sensitivity Distribution of Four-Electrode Impedance Sensing on Radial Artery," in *SAS Proceedings*, 2018.
- [39] B. Freeman and J. Berger, "Invasive Arterial Blood Pressure Monitoring," in *Anesthesiology Core Review*, 2016.
- [40] M. L. Muiesan, M. Salvetti, F. Bertacchini, C. Agabiti-Rosei, G. Maruelli, E. Colonetti and A. Paini, "Central blood pressure assessment using 24-hour brachial pulse wave analysis," *Journal of Vascular Diagnostics and Interventions*, vol. 2, 2014.
- [41] "Arterial Catheterization," The American Thoracic Society, [Online]. Available: <https://www.thoracic.org/patients/patient-resources/resources/arterial-catheterization.pdf>.
- [42] A. Avolio, M. Butlin and A. Walsh, "Arterial blood pressure measurement and pulse wave analysis – their role in enhancing cardiovascular assessment," *Physiological Measurement*, vol. 31, no. 1, p. R1–R47, 2009.
- [43] C. F. Babbs, "Oscillometric measurement of systolic and diastolic blood pressures validated in a physiologic mathematical model," *Biomed Eng Online*, vol. 11, no. 56, 2012.
- [44] P. S. Lewis, "Oscillometric measurement of blood pressure: a simplified explanation. A technical note on behalf of the British and Irish Hypertension Society," *Journal of Human Hypertension*, vol. 33, p. 349–351, 2019.
- [45] I. Bassem, N. Viswam and J. Roozbeh, "Exploration and Validation of Alternate Sensing Methods for Wearable Continuous Pulse Transit Time Measurement Using Optical and Bioimpedance Modalities," in *39th Annual International Conference of the IEEE Engineering in Medicine and Biology Society (EMBC)*, 2017.
- [46] K. Sel, D. Kireev, A. Brown, B. Ibrahim, D. Akinwande and R. Jafari, "Electrical Characterization of Graphene-based e-Tattoos for Bio-Impedance-based Physiological Sensing," in *EEE Biomedical Circuits and Systems Conference*, Nara, 2019.
- [47] M. Min, K. Hip, E. Priidel, K. Pesti and P. Annus, "Noninvasive Acquisition of the Aortic Blood Pressure Waveform," in *Wearable Devices - the Big Wave of Innovation*, IntechOpen, 2019.
- [48] "AC/DC Module User's Guide," 2018.
- [49] L. J. Van der Pauw, "A Method of Measuring the Resistivity and Hall Coefficient on Lamellae of Arbitrary Shape," *Philips Technical Review*, pp. 220-224, 1958.
- [50] H. Kõiv, R. Gordon and K. Pesti, "Electric impedance measurement of tissue phantom materials for development of medical diagnostic systems," in *International Workshop of Impedance Spectroscopy IWIS 2013*, Chemnit, 2014.
- [51] S. Gabriel, R. W. Lau and C. Gabriel, "The dielectric properties of biological tissues: II. Measurements in the frequency range 10 Hz to 20 GHz," *Physics in Medicine & Biology*, vol. 41, 1996.

- [52] J. R. Cook, R. R. Bouchard and S. Y. Emelianov, "Tissue-mimicking phantoms for photoacoustic and ultrasonic imaging," *BIOMEDICAL OPTICS EXPRESS*, vol. 2, pp. 3193–3206, 2011.
- [53] A. W. Guy, "Analyses of Electromagnetic Fields Induced in Biological Tissues by Thermographic Studies on Equivalent Phantom Models," *IEEE Transactions on Microwave Theory and Techniques*, vol. 19, no. 2, pp. 205–214, 1971.
- [54] M. Lazebnik, E. L. Madsen, G. R. Frank and S. C. Hagness, "Tissue-mimicking phantom materials for narrowband and ultrawideband microwave applications," *Physics in Medicine & Biology*, vol. 50, no. 18, p. 4245, 2005.
- [55] T. Dec, C. Snooks, S. Nelson, J. Schoneman and A. Connelly, "Human Dielectric Equivalent Phantom," 2015.
- [56] A. Hunt, A. Ristolainen, P. Ross, R. Öpik, A. Krumme and M. Kruusmaa, "Low cost anatomically realistic renal biopsy phantoms for interventional radiology trainees," *European Journal of Radiology*, vol. 82, pp. 594–600, 2013.
- [57] M. J. Burns, "Quick & dirty review of resistivity measurement techniques," 2000.
- [58] A. T. Mobashsher and A. M. Abbosh, "Artificial Human Phantoms: Human Proxy in Testing Microwave Apparatuses That Have Electromagnetic Interaction with the Human Body," *IEEE Microwave Magazine*, vol. 16, no. 6, 2015.
- [59] T. Matsumura and Y. Sato, "A Theoretical Study on Van Der Pauw Measurement Values of Inhomogeneous Compound Semiconductor Thin Films," *Journal of Modern Physics*, vol. 1, pp. 340–347, 2010.
- [60] C. Kasl and M. J. R. Hoch, "Effects of sample thickness on the van der Pauw technique for resistivity measurements," *Review of Scientific Instruments*, vol. 76, no. 3, 2005.
- [61] C. Gabriel, "An Internet resource for the calculation of the Dielectric Properties of Body Tissues in the frequency range 10 Hz - 100 GHz," 2018. [Online]. Available: <http://niremf.ifac.cnr.it/tissprop/>.
- [62] D. K. Schroder, *Semiconductor Material and Device Characterization*, Third Edition, John Wiley & Sons, Inc., 2006.
- [63] K. Pesti, H. Kõiv and R. Gordon, "Validation of simulations of eddy current methods with measurements on phantom Materials for biomedical engineering R&D," *International Journal of Bioelectromagnetism*, vol. 17, no. 2, p. 57–63, 2015.
- [64] Comsol, "Simulate Static and Low-Frequency Electromagnetics with the AC/DC Module," 2018. [Online]. Available: <https://www.comsol.com/acdc-module>.
- [65] R. Kollman, "Constructing your power supply – layout considerations," Texas Instruments Incorporated, 2005.
- [66] K. Pesti, M. Metshein, P. Annus, H. Kõiv and M. Min, "Electrode Placement Strategies for the Measurement of Radial Artery Bioimpedance: Simulations and Experiments," *IEEE Transactions on Instrumentation and Measurement*, 2021.
- [67] C. Canali, C. Mazzoni, L. B. Larsen, A. Heiskan, M. Dufva and J. Emnéus, "An impedance method for spatial sensing of 3D cell constructs – towards applications in tissue engineering," *Analyst*, vol. 140, pp. 6079–6088, 2015.

- [68] M. Metshein, P. Annus, R. Land, M. Min and A. Aabloo, "Availability and variations of cardiac activity in the case of measuring the bioimpedance of wrist," in *IEEE International Instrumentation & Measurement Technology Conference*, 2018.
- [69] P. Kauppinen, J. Hyttinen and J. Malmivuo, "Sensitivity distribution visualizations of impedance tomography measurement strategies," *International Journal of Bioelectromagnetism*, vol. 8, pp. 64–71, 2006.
- [70] M. Metshein, Doctoral Thesis: Wearable Solutions for Monitoring, Talinn: TTÜ Press, 2018.
- [71] S.-H. Liu, D. C. Cheng and C. -H. Su, "A Cuffless Blood Pressure Measurement Based on the Impedance Plethysmography Technique," *Sensors*, vol. 17, no. 5, 2017.
- [72] Jawbone, "A smarter activity tracker for fitter you.," 2018. [Online].
- [73] M. Moderhak, M. Madej, J. Wtorek and B. Truyen, "Pulse pressure velocity measurement – a wearable sensor," in *Federated Conf. On Comp. Sci. And Inform. Sys. (FedCSIS)*, 2011.
- [74] J. He, M. Wang, X. Li, L. Gang and L. Ling, "Pulse wave detection method based on the bio-impedance of the wrist," *Review of Scientific Instruments*, vol. 87, 2016.
- [75] M. Cho, J. Y. Kim and S. H. Cho, "A bio-impedance measurement system for portable monitoring of heart rate and pulse wave velocity using small body area," in *IEEE International Symposium on Circuits and Systems*, 2009.
- [76] K. S. Rabbani, M. Sarker, M. H. R. Akond and T. Akter, "Focused impedance measurement (FIM): a new technique with improved zone localization," *Ann. NY Acad. Sci.*, vol. 873, pp. 208–220, 1999.
- [77] F. J. Pettersen, H. Ferdous, H. Kalvøy and Ø. G. Martinsen, "Comparison of four different FIM configurations--a simulation study," *Physiol Meas*, vol. 35, no. 6, pp. 1067–1082, 2014.
- [78] S. Guttke, M. Laukner and P. Weber, "Cross sensitivity of different electrode types for impedance plethysmography under motion conditions," *Journal of Physics: Conference Series*, vol. 434, 2013.
- [79] IMAIOS, "Anatomy," 2018. [Online]. Available: <https://www.imaios.com/en>.
- [80] A. R. Ward , "Electrode Coupling Media for Transcutaneous Electrical Nerve Stimulation," *Australian Journal of Physiotherapy*, vol. 30, 1984.
- [81] 2020. [Online]. Available: <https://www.comsol.com/learning-center>.
- [82] C. Fairclough, "Efficiently Mesh Your Model Geometry with Meshing Sequences," 2016. [Online]. Available: <https://www.comsol.com/blogs/efficiently-mesh-your-model-geometry-with-meshing-sequences/>.
- [83] T. Palo, "B.Sc. thesis Synchronous two-channel electric bioimpedance measurement system for detecting pulse wave from radial artery," Tallinn Univ. of Technology, 2019.
- [84] A. R. Abir and K. S. Rabbani, "Sensitivity study for a 4-electrode focused impedance method (FIM) using finite element method analysis," *Bangladesh Journal of Medical Physics*, vol. 17, 2014.

- [85] M. D. O’Toole, L. A. Marsh, J. L. Davidson, Y. M. Tan, D. W. Armitage and A. J. Peyton, “Non-contact multi-frequency magnetic induction spectroscopy system for industrial-scale bio-impedance measurement,” *Measurement Science and Technology*, vol. 26, 2014.
- [86] J. D. Folts, “The electromagnetic flowmeter and its use in the operating room,” *Journal of ExtraCorporeal Technology*, vol. 6, pp. 127-136, 1974.
- [87] D. Teichmann, “MonitoRing – Magnetic induction measurement at your fingertip,” *Journal of Physics: Conference Series*, 2013.
- [88] A. Cordes, K. Heimann and S. Leonhardt, “Magnetic induction measurements with a six channel coil array for vital parameter monitoring,” in *Annu Int Conf IEEE Eng Med Biol Soc*, 2012.
- [89] D. Teichmann, J. Foussier, J. Jia, S. Leonhardt and M. Walter, “Noncontact monitoring of cardiorespiratory activity by electromagnetic coupling,” *IEEE Trans Biomed Eng*, vol. 60, no. 8, pp. 2142–2152, 2013.
- [90] C. Isop, “Pöörisvoolu mähisega vere pulsatsioonni mõõtmise simulatsioon inimese pindmistes kudedes,” Tallinn University of Technology, 2017.
- [91] S. O. Gi, Y. J. Lee, H. R. Koo and etc., “Application of a Textile-based Inductive Sensor for the Vital Sign Monitoring,” *Journal of Electrical Engineering and Technology*, vol. 10, no. 1, pp. 364–371, 2015.
- [92] Y. Yu and D. Pingan, “Two approaches to coil impedance calculation of eddy current sensor,” *Journal of Mechanical Engineering Science*, pp. 507–515, 2007.
- [93] S. Tumanski, “Induction Coil Sensors - a review,” *Measurement Science and Technology*, vol. 18, no. 3, 2007.
- [94] M. Metshein, K. Pesti, M. Min, P. Annus and O. Märtnens, “Feasibility of Utilizing Air Gapped Toroidal Magnetic Cores for Detecting Pulse Wave in Radial Artery,” in *2020 17th Biennial Baltic Electronics Conference Proceedings*, 2020.
- [95] H. P. Schwan, “Electrical Properties of Tissue and Cell Suspensions,” *Advances in Biological and Medical Physics*, vol. 5, pp. 147–209, 1957.
- [96] J. Garrett and E. Fear, “Stable and Flexible Materials to Mimic the Dielectric Properties of Human Soft Tissues,” *IEEE Antennas and Wireless Propagation Letters*, vol. 13, pp. 599–602, 2014.
- [97] C. Marchal, M. Nadi, A. J. Tossier, C. Roussey and M. L. Gaulard, “Dielectric properties of gelatine phantoms used for simulations of biological tissues between 10 and 50 MHz,” *International Journal of Hyperthermia*, vol. 5, pp. 725–732, 1989.
- [98] “ENVIRONMENTAL HEALTH CRITERIA 137,” 1993.
- [99] “Eddy Current Testing,” [Online]. Available: https://www.nde-ed.org/EducationResources/CommunityCollege/EddyCurrents/cc_ec_index.htm.

Acknowledgements

I would like to acknowledge the Thomas Johann Seebeck Department of Electronics at Tallinn University of Technology for offering me the opportunity to pursue a PhD degree. I would like to express my gratitude to my supervisor Professor Mart Min for his enthusiastic support, time and keeping my research focused. I would also convey my thanks to my co supervisor Dr. Margus Metshein for the assistance and great support he provided me. I appreciate Rauno Gordon, who was my supervisor for the first years of the study. I also thank colleagues at Tallinn University of Technology and in particular Hip Kõiv, Paul Annus, Raul Land, Jaan Ojarand and Olev Märtens.

To my family and friends whose consistent support gave me the perseverance in my pursuit of a PhD.

This work has been supported financially the following entities:

- Estonian Research Council, grant EAG34
- European Social Fund through ICT Doctoral School at Tallinn University of Technology
- European Union European Regional Development Fund through Estonian Estonian Centre of Excellence in ICT Research
- OÜ ELIKO Technology development center; AS Ida-Tallinna Keskhaigla (East-Tallinn Central Hospital)

Abstract

Modelling and Simulation of Arterial Blood Pulsation via Bioimpedance

Continuous cardiac output is a significant matter that must be considered in monitoring the functioning of the cardiovascular system of humans. Among the existing techniques of continuous hemodynamics monitoring, the most common in clinical application is intra-arterial catheters. However, the procedure is invasive and could lead to several complications. A non-invasive sensing system that is based on measuring electrical bioimpedance variations of radial artery is presented in this thesis. The thesis introduces simulations, experiments and results in developing the wearable monitor for central aortic blood pressure curve by using electrical bioimpedance measurement.

First, a tissue-mimicking phantom material was developed for the EBI based sensing to monitor the central aortic pressure (CAP) of blood. Many bioelectrical non-invasive impedance-based methods such as bioelectrical impedance analysis (BIA), impedance cardiography (ICG), electrical impedance spectroscopy (EIS) and electrical impedance tomography (EIT) have been proposed and applied for biomedical applications. The phantoms can be used to calibrate, compare and evaluate these systems before applying them on the real object. In the thesis, a gelatin-based phantom material that allows in-lab investigation of the bioimpedance measurement is presented. The electric conductivity of the phantom materials was adjusted by changing their composition and by using the van der Pauw method for conductivity validation. The results obtained from experiments showed that conductivity of the material increased linearly with NaCl concentration and reliable forearm tissues mimicking samples were produced. The finite element method (FEM) simulation of electric impedance of a planar coil on the tissue model was compared to impedance measurements of the planar coil on real phantom material with the same properties.

Second, the non-invasive method of central aortic pressure evaluating by measuring the electrical bioimpedance (EBI) of the radial artery with resistive coupling is introduced. The method provides low complexity in electronic design, and since the EBI is measured non-invasively near the location of radial artery, the device could be integrated into wristband of another wearable device. However, the EBI measurement instrumentation is sensitive to noise and, therefore, even small errors in the measured data can be translated into large uncertainties in the results. To optimize the signal acquisition, different electrode placement and configuration strategies were compared with the goal of finding the most suitable ones. The finite element method (FEM) simulation of sensitivity distribution and experimental measurements on radial artery were performed for experimenting circular and distal electrode placements. Also, the modified electrode placement strategies, guided by the idea of focused impedance method (FIM), were investigated. A novel version of FIM was proposed: a five-electrode FIM strategy. The simulation results were compared to experimental outcomes. The research results show the significance of the exact positioning and the need for a conscious choice of configurations and placements of EBI sensors. The most suitable positions and configurations of resistive coupling electrodes have been determined and proposed by experimentation and simulation.

Third, the research on possible usage of magnetic induction sensing method for monitoring the pulse wave in the radial artery was presented. The potentiality of monitoring pulse wave by positioning different induction sensors noninvasively onto the

location of the radial artery in the forearm was investigated. The simulations in Comsol Multiphysics were implemented by using the FEM on the models of several coil types with different dimensions and properties. In addition, the feasibility study of utilization of air gapped toroidal magnetic cores for monitoring changing volume of pulsating blood in artery is presented. Toroidal magnetic cores with two different shapes of custom implemented air gaps and desired number of windings were used to induce current in copper wire. The theoretical expectation of the possibility to focus most of the reluctance of emerging magnetic field into the air gap was investigated. The results of experimental measurements were validated with simulation of magnetic flux density distribution. As a result, a coil which provides the biggest rate of change in measured EBI caused by the pulse in radial artery was proposed.

Lühikokkuvõte

Arteriaalse verepulsatsiooni modelleerimine ja simuleerimine bioimpedantsi kaudu

Südame aktiivsuse pidevjalgimine erinevate kardiovaskulaarsete patoloogiate leidmise ja varase avastamise seisukohalt on ülimalt oluline, kuid samas keeruline protsess. Tehnikate seas, mida tänasel päeval kasutatakse hemodünaamiliste parameetrite pidevjalgimiseks, on kliinilises kasutuses kõige levinumad arterisisesed kateetrid. Nimetatud protseduur on aga invasiivne ja võib põhjustada mitmeid tüsistusi. Käesolevas töös on esitatud mitteinvasiivne mõõtmise süsteem, mis põhineb radiaalarteri elektrilise bioimpedantsi variatsioonide mõõtmisel. Töös tutvustatakse kehal kantava aordi tsentraalse vererõhu kõvera jälgimise seadme väljatöötamise eesmärgil läbiviidud eksperimentaalseid mõõtmisi ja simulatsioone, mis põhinevad elektrilist bioimpedantsi mõõtmise meetodil.

Esmalt töötati välja kude jäljendav fantoommaterjal arteriaalse vererõhu jälgimiseks mõeldud bioimpedantsi mõõtmise meetodi arendamiseks. Bioimpedantsi mõõtmisel põhinevat meetodit kasutatakse paljudes biomeditsiinilistes rakendustes, nagu näiteks bioelektrilise impedantsi analüüs (BIA), impedants-kardiograafia (ICG), elektrilise impedantsi spektroskoopia (EIS) ja elektrilise impedantsi tomograafia (EIT). Fantoom saab kasutada nimetatud mõõtemetodite kalibreerimiseks, võrdlemiseks ja hindamiseks veel enne nende rakendamist katsealusel või patsiendil. Käesolevas töös kirjeldatud fantoommaterjal põhineb želatiinil ja on läbinud elektrilise bioimpedantsi mõõtmise katsed laboritingimustel. Fantoommaterjalide elektrijuhtivust kalibreeriti muutes selle koostist ja kasutades juhtivuse valideerimiseks van der Pauw' meetodit. Läbiviidud mõõtmiste tulemused näitasid, et materjali juhtivus suurenes koos NaCl kontsentratsiooni kasvuga lineaarselt. Kalibreerides fantoommaterjali omadusi vastavalt kirjandusest leitavate reaalsete impedantsi mõõtetulemustega, loodi küünarvarre kudesid jäljendavaid materjale. Materjalide karakteriseerimine viidi läbi nii simulatsiooni keskkonnas kui reaalsel loodud katsetükkidel, kasutades selleks elektrilise impedantsi mõõtmise planaarmähiseid.

Seejärel tutvustati arteriaalse vererõhu mitteinvasiivset mõõtmismeetodit, mis põhineb elektrilise bioimpedantsi mõõtmisel, kasutades selleks galvaanilist sidestust. Meetod tagab elektroonilise disaini lihtsuse ja kuna elektrilist bioimpedantsi mõõdetakse radiaalarteri asukoha lähedal, on seadet võimalik integreerida kantava seadme randmepaela sisse. Kuna bioimpedantsi mõõteseadmed on üsna müratundlikud, siis isegi väikesed vead mõõdetud signaalis võivad tekitada suuri ebakõlasid lõpptulemuses. Signaali täpsuse optimeerimiseks võrreldi erinevaid elektroodide paigutuse ja konfiguratsiooni strateegiaid eesmärgiga leida loodud rakenduse jaoks kõige sobivamad. Tundlikkuse jaotuse simulatsioon ja eksperimentaalmõõtmised olid läbi viidud elektroodide risti ja piki paigutustel radiaalarteri suhtes. Lisaks uuriti modifitseeritud elektroodide paigutuse strateegiaid juhindudes fokuseeritud impedantsi meetodist. Märkimist väärib see, et pakuti välja ka uudne versioon fokuseeritud impedantsi meetodist: viie elektroodiga fokuseerimise meetod. Simuleerimistulemusi võrreldi eksperimentaalsete mõõtetulemustega, tuues esile täpse ja teadliku elektroodide paigutuse strateegiate olulisuse.

Kolmandaks, esitleti elektrimagneetilise induktsiooni meetodi kasutamise võimalusi puudutatavat uurimust, mille eesmärk oli jätkuvalt pulsiline jälgimine radiaalarteris.

Selleks olid läbi viidud erinevate kujude ja omadustega mähiste bioimpedantsi mõõtmise simulatsioonid.

Lisaks uuriti ka pulseeriva vere mahu muutuse jälgimise võimalust radiaalarteris, kasutades selleks õhupiluga toroidsüdamikke. Arteris, mida imiteeris lihtne vasktraat, indutseeriti vool, kasutades selleks erineva kujuga õhupiludega rõngaspoole - toetudes teoreetilisele eeldusele et suurem osa tekkivast magnetväljast kontsentreerub õhupilusse. Eksperimentaalsete mõõtmiste tulemused erineva kujuga õhupiludega rõngaspoolidega läbiviidud katsetes dubleeriti arvutimudelina ning tulemused said kinnituse simuleerides magnetvoo ja voolutiheduste jaotusi.

Appendix 1

Publication I

Pesti, Ksenija; Kõiv, Hip; Gordon, Rauno (2015). Validation of simulations of eddy current methods with measurements on phantom materials for biomedical engineering R&D. *International Journal of Bioelectromagnetism*, 17 (2), 57–63.

Validation of Simulations of Eddy Current Methods with Measurements on Phantom Materials for Biomedical Engineering R&D

Ksenija Pesti^a, Hip Kõiv^a, Rauno Gordon^a

^aThomas Johann Seebeck Department of Electronics, Tallinn University of Technology
Tallinn, Estonia

Correspondence: K Pesti, Thomas Johann Seebeck Department of Electronics, Tallinn University of Technology, Ehitajate tee 5, EE- 19086 Tallinn, Estonia. E-mail: ksenija.pesti@gmail.com

Abstract. In this paper simulations of eddy current measurements are validated with comparison to real measurements on phantom materials. Accurate computer simulation with valid results is a valuable research tool for development of novel medical diagnostic methods. Eddy current methods can potentially provide affordable noninvasive diagnostics and treatment. Using gelatin-based materials with calibrated electrical conductivity allowed making tissue phantoms with realistic electrical properties. The electric conductivity of the phantom materials was adjusted by changing its composition and using van der Pauw method for conductivity validation. Then Comsol Multiphysics simulations (using finite element method) of electric impedance of a planar coil on the tissue model are compared to impedance measurements of the planar coil on real phantom material with the same properties. From the results, it was evident that the finite element method can be used for eddy currents in biomedical engineering R&D up to 12 MHz frequency.

Keywords: Bioimpedance; Eddy Current; Finite Element Method; Gelatin-Based Phantom; van der Pauw method

1. Introduction

In several biomedical applications, it is necessary to determine eddy current distribution in biological tissues. A variety of methods can be used to model the eddy current distribution in conducting materials. In this paper, we employ FEM (the finite element method) simulation and compare it to eddy current real phantom measurements to investigate the eddy current distribution in biological tissue phantom materials with valid electrical properties for biomedical engineering applications.

Gelatin-based tissue phantom materials with defined electric conductivity were produced. Those phantoms would be used in development of medical diagnostic systems that use bioimpedance measurement with eddy currents to estimate the health state or pathologic condition in the patient [6]. Electrical conductivity of the material was measured and calculated by van der Pauw method at frequency range 100 Hz to 1 MHz. The result was used as material parameters for FEM simulation in COMSOL Multiphysics.

The impedance of the material, measured with eddy current sensors, and simulation results were compared and discussed in order to evaluate FEM simulation accuracy of the eddy current measurement in biomedical applications.

2. Methods of measurements

To compare impedance of phantom measured by eddy current and simulation results, a special measurement method was worked out. This method included: (1) preparing the tissue mimicking phantoms, (2) designing of PCB-s with planar coils for eddy current measurements and long electrodes for van der Pauw impedance measurements, (3) calculating conductivity of the material with van der Pauw method, and (4) impedance measurements with planar coil sensors.

2.1. Gelatin Phantom Preparation

Two different gelatin-based tissue phantoms with conductivities similar to blood and brain grey matter were developed. To produce biological tissue mimicking phantoms with realistic tissue properties, the respective electric conductivities were obtained from the internet database and used as guidelines in phantom development (see Table 1) [7].

Gelatin-based material was used as the tissue-mimicking material as it is self-supportive with a relatively simple manufacturing process. The composition and production process has been well reported in several previous researches [5, 6]. The mixture generally consist of distilled water, sodium chloride (NaCl), ethyl 4-hydroxybenzoate, formaldehyde solution and gelatin powder. Different electrical conductivities of phantoms were achieved by adjusting different amounts of sodium chloride. The phantom mixture was placed into Plexiglas enclosure with two double-sided printed circuit boards (PCB) for measurements and calibration of phantom.

Table 1. *Electrical conductivity of tissues [7].*

<i>Tissue</i>	<i>Electrical conductivity at 10 kHz, [S/m]</i>	<i>Electrical conductivity at 1 MHz, [S/m]</i>	<i>Electrical conductivity at 10 MHz, [S/m]</i>
Blood	0.70290	0.82211	1.09670
Brain grey matter	0.11487	0.16329	0.29172

2.2. Calibration of the Gelatin Phantom

Van der Pauw method was used to calibrate the conductivity of the produced phantom material. The required tissue phantom conductivity was achieved by several and continues adjusting of material mixture recipe in respect to van der Pauw conductivity measuring results.

To make the van der Pauw method compatible, some special requirements were followed in design of phantom shaping Plexiglas enclosure and conductivity measurement PCBs:

- Four thin electrode stripes, on two PCBs on either side, had direct contact to the gelatin sample cube. When viewed top down as 2D, the point-like electrodes are exactly in the corner of the sample.
- The thickness of the sample must be constant and homogeneous [3].

Research made by Kasl and Hoch [10] shows that when the contacts are located across the edges and the resistance of the electrodes are sufficiently low compared to the sample resistance, like in this research, van der Pauw method is reliable [10].

Van der Pauw technique is based on measuring the voltage and current ratio. The measurement and calculation methods have been well reported in previous research [6]. Measuring was carried out with Wayne Kerr 6500 impedance analyzer at frequency range from 100 Hz to 120 MHz, however the measurement result accuracy was limited on a frequencies higher than 1 MHz due to measuring ability of the used tool and methods. For this reason, the values of electrical conductivity only at frequency range from 100 Hz to 1 MHz were used in following simulation. After measuring the resistivity and conductivity of the sample can be calculated.

2.3. Planar Coil Sensor Design

To measure impedance of the sample with eddy currents, planar coils were designed on the same PCB-s (Fig.1). The PCBs were ordered from the factory and the diameter of planar coil had to be 20.2 mm and trace width had to be 0.2 mm according to the design. The microscope measuring showed that the real dimensions of coils were different from designed ones (summarized in Table 2).

Table 2. *Comparison of ordered and real coil dimensions*

<i>Dimensions of coil</i>	<i>Factory order</i>	<i>Average microscope measurement</i>
Thickness of copper layer, [mm]	0.099	0.035
Coil track width, [mm]	0.135	0.2
Spacing between coil tracks, [mm]	0.264	0.2
Coil inner diameter, [mm]	4.6	5.07
Coil outer diameter, [mm]	20.2	19.75

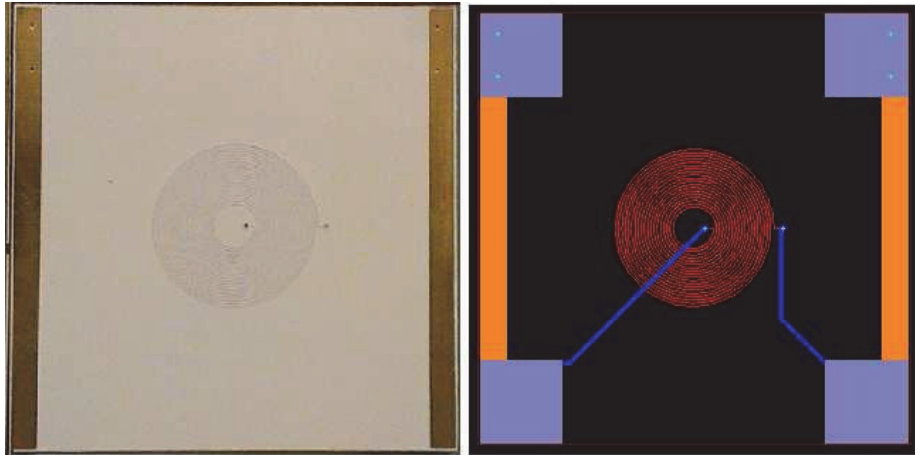


Figure 1. PCB with planar coil in the middle and long strip electrodes on sides

It was also specified that coil track consists of two different layers: (1) a pure copper layer, (2) and plated copper layer. The plated copper layer is much more resistive than pure copper [2].

2.4. Planar Coil Impedance Measurements

To measure impedance of the gelatin sample, PCBs were placed into the Plexiglas enclosure in a way that coils would be located on two opposite sides of the phantom and would have direct contact with it. Measurements were carried out with Wayne Kerr 6500 impedance analyzer at frequency range 100 Hz – 120 MHz. The induced voltage created by the eddy currents is proportional to the frequency and lags the primary excitation field by 90° [9].

3. Methods of Simulation

To simulate measurement results the model of gelatin phantom including planar coil sensor was designed using COMSOL Multiphysics 4.4 software. Material properties were specified and added to the necessary parts of the model geometry. Using the software, simulation was performed and results were visualized.

3.1. General Description of the Model

Simplified 2D axisymmetric model was created using the AC/DC Module for simulating electric, magnetic, and electromagnetic fields.

The AC/DC Module includes stationary and dynamic electric and magnetic fields. The AC/DC Module formulates and solves Maxwell's equations together with material properties and boundary conditions. The equations are solved using the FEM with numerically stable edge element discretization [1]. A multi-turn coil was designed and solved as RLC coil group in AC/DC Module.

3.2. Geometry of the Model

Model was created in 2D view and axial symmetry (shown on Fig. 2). The geometry dimensions are 100 mm x 100 mm and it consists of five main parts: (1) gelatin phantom, (2) air, (3) FR4 board, (4) layer of solder mask, and (5) multi-turn coil (summarized in Table 3, Fig.2).

As it was mentioned above, it was specified that coil track consists of plated copper layer and pure copper layer. Unfortunately, COMSOL was not able to solve the double-layered RLC coil group. For this reason, simplified single-layer coil track was designed. Coil tracks were coated by thin solder mask layer.

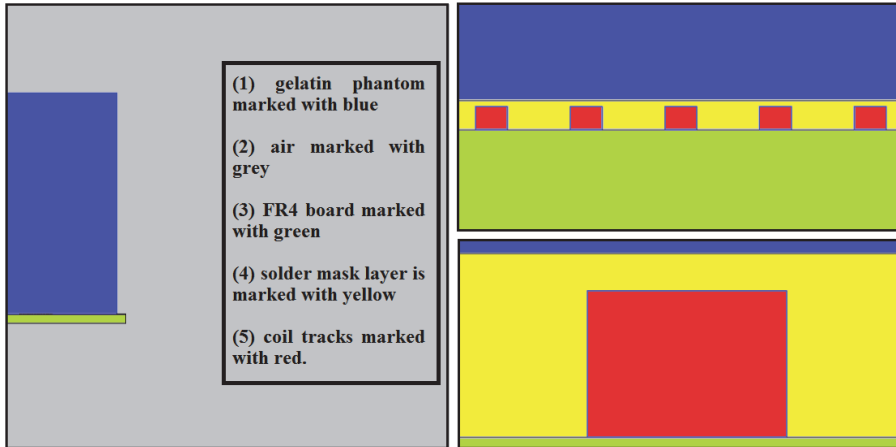


Figure 2. Geometry of phantom model, zoomed in on right side.

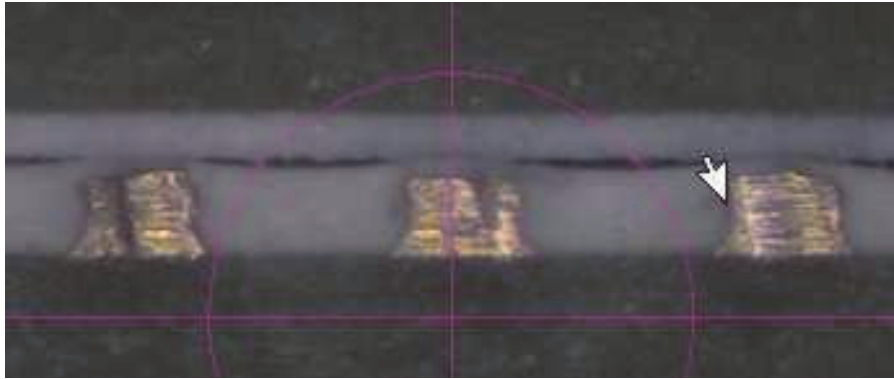


Figure 3. Photo of PCB cut-through under measurement microscope.

Table 3. Geometry Dimensions

Geometry part	Width, [mm]	Height, [mm]
Gelatin phantom	25	50
Air	100	100
FR4 board	27	2
Solder mask layer	27	0.025
Coil track	0.135	0.099

3.3. Material Properties of the Model

Materials and constitutive relations were defined in terms of permittivity, permeability and conductivity. Material properties were allowed to be spatially varying, time dependent, anisotropic, and have losses [1].

Electrical conductivity of the gelatin in the model was defined as results of van der Pauw method measurements and calculation for two different phantom materials: material A and material B.

Table 4. Electrical conductivity of materials in Comsol

Material	Electrical conductivity, [S/m]
Air [3]	1×10^{-6}
FR4 [3]	0.004
Solder mask [4]	1×10^{-5}
Pure copper [3]	5.88×10^7

3.3. Meshing and Solving the Model

Meshing of the geometry is dividing model into small elements. A free mesh consisting of triangular elements was created for the 2D geometry with COMSOL automatic mesh algorithm with three different mesh sizes. Mesh consisted of 326584 elements. Model was solved for the frequency range from 10 Hz to 120 MHz for two different materials.

4. Results

In this part, the results of simulation and planar coils measurements are presented. Fig. 4 shows the phase angle and impedance of material A at frequency range 100 Hz to 120 MHz. Later material B with different conductivity was simulated (Fig. 5). It was evident that measured impedance and the simulation values are good enough to facilitate simulation-research until 12 MHz. Phase angle differences are also manageable in the same frequency range.

It was also determined that planar coils are suitable for measuring homogeneous tissue mimicking materials in biomedical applications. Using planar coil on different phantom samples it is possible to see changes in impedance values depending on material conductivity (Fig. 6).

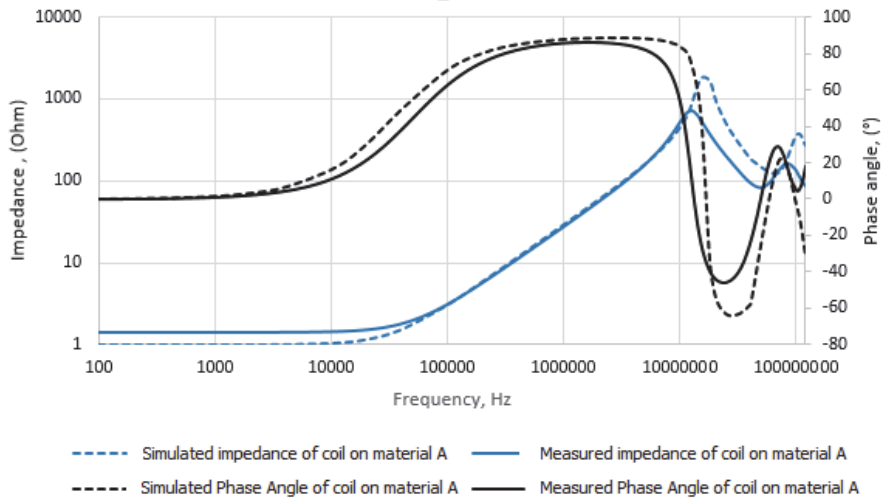


Figure 4. Comparison of simulation and measurement results on material A.

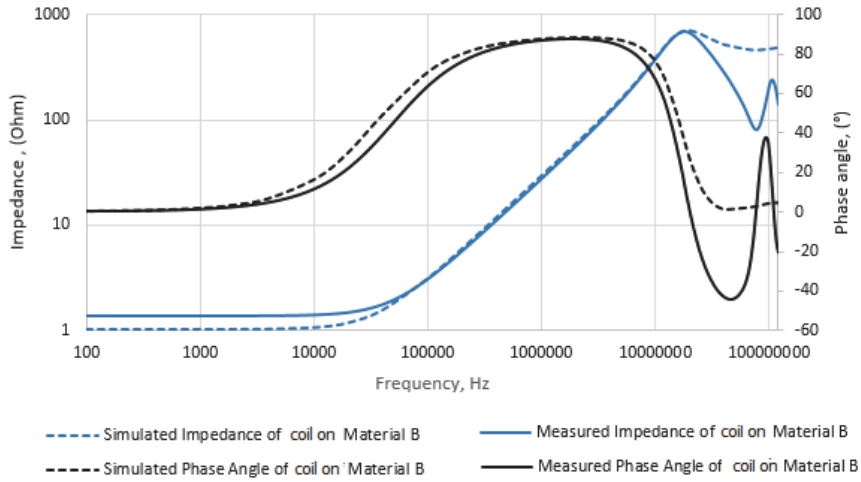


Figure 5. Comparison of simulation and measurement results on material B.

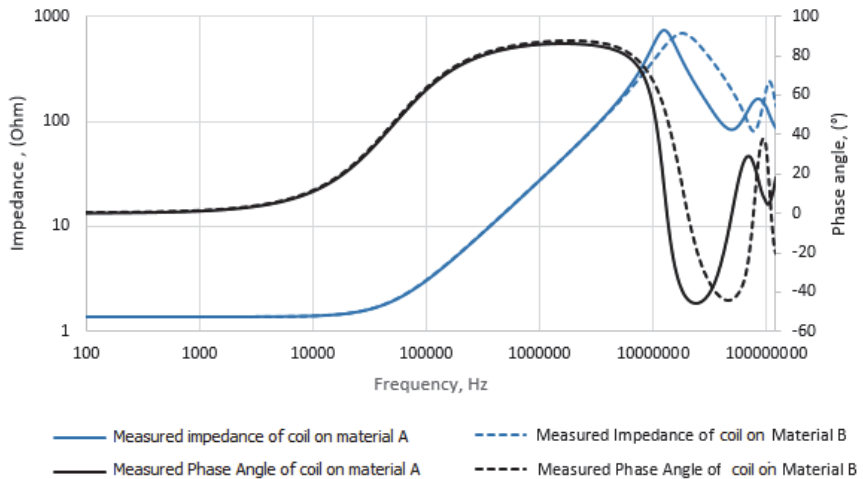


Figure 6. Comparison of measurements results on materials A and B.

5. Discussion

If as a result of the phantom material calibration experiments with van der Pauw method the composition of the material was mapped to the material properties. Electrical conductivity of investigated materials can be separately adjusted by changing of concentration of NaCl.

To evaluate the FEM simulation accuracy for developing of eddy current measurement method, a set of simulations was performed in COMSOL Multiphysics. From the results, it could be assumed that the FEM simulation method is reliable until 12 MHz frequencies. The difference in the simulated and measured signal was significantly higher at frequencies above 12 MHz. In addition, the resonance of signal appeared on different frequencies. Further research in this area is needed; however, the reasons of the resulting distortion could be suggested:

- Simplification of the COMSOL model geometry.
- Real material properties need to be investigated for every part of produced PCB.

- It was also specified that coil track consists of two layers with different electrical conductivity, but only one layer coil was modelled.

- Due to limited measuring ability of the used tool and methods, the electrical conductivity of phantom was measured and calculated only at limited frequency range (100 Hz to 1 MHz). However, the simulation was carried out also for higher frequencies.

In our future work we intend to focus on developing of eddy current sensors for biomedical engineering applications and to investigate more complex (inhomogeneous and multilayered) phantom samples with more realistic properties.

6. Conclusion

A planar coil with a diameter of 20 mm was positioned directly against the phantom material and was supplied with an AC current. Two different phantoms had conductivities similar to blood and brain gray matter, these were measured and calculated by van der Pauw method. COMSOL Multiphysics software was used to simulate the gelatin-based phantoms with calculated electrical conductivity. The results of simulation were compared to measurement with planar coil to evaluate FEM simulation accuracy for developing eddy current methods in biomedical applications.

Acknowledgements

This research was supported by the European Union through the European Regional Development Fund in the frames of the center of excellence in research CEBE, competence center ELIKO, of the Competence Centre program of Enterprise Estonia, National Development Plan for the Implementation of Structural Funds Measure 1.1 project 1.0101.01-0480 and also by Estonian Science Foundation Grant 9394.

References

- [1] <http://www.comsol.com/acdc-module>
- [2] R. Kollman. Constructing your power supply – layout considerations. Texas Instruments Incorporated, 2005.
- [3] COMSOL Multiphysics 4.4 Material library
- [4] R. Tarzwell, K. Bahl. High voltage printed circuit design & manufacturing notebook, 2004, 11
- [5] A. Hunt, A. Ristolainen, P. Ross, R. Öpik, A. Krumme, M. Kruusmaa. Low cost anatomically realistic renal biopsy hantoms for interventional radiology trainees. *European Journal of Radiology* 82, 2013.
- [6] H. Kõiv, R. Gordon, K. Pesti. Electric impedance measurement of tissue phantom materials for development of medical diagnostic systems. *Proceedings of International Workshop of Impedance Spectroscopy*, 2014.
- [7] D. Andreuccetti, R. Fossi and C. Petrucci. An internet resource for the calculation of the dielectric properties of body tissues in the frequency range 10 Hz - 100 GHz <http://niremf.ifac.cnr.it/tissprop/>. IFAC-CNR, Florence (Italy), 1997. Based on data published by C.Gabriel et al. in 1996.
- [8] T. Matsumura, Y. Sato. A theoretical study on Van der Pauw measurement values of inhomogeneous compound semiconductor thin films. *J.Mod. Phys., Japan*, 2010, 340-347.
- [9] C. H. Riedel, M. Golombek, O. Dössel. Simulation of non-contact measurement of the electrical impedance using an anatomical model, 2002.
- [10] C. Kasl, M. J. R. Hoch. Effects of sample thickness on the van der Pauw technique for resistivity measurements. *Review of scientific instruments* 76, 033907, South Africa, February, 2005.

Publication II

Pesti, Ksenija; Kõiv, Hip; Min, Mart (2019). Simulation of the Sensitivity Distribution of Four-Electrode Impedance Sensing on Radial Artery. IEEE Sensors Applications Symposium (SAS) Proceedings, Sophia Antipolis, France, 279–285.

Simulation of the Sensitivity Distribution of Four-Electrode Impedance Sensing on Radial Artery

Ksenija Pesti
Thomas Johann Seebeck Department of
Electronics
Tallinn University of Technology
Tallinn, Estonia
ksenija.pesti@taltech.ee

Hip Kõiv
Thomas Johann Seebeck Department of
Electronics
Tallinn University of Technology
Tallinn, Estonia
hip.koiv@taltech.ee

Mart Min
Thomas Johann Seebeck Department of
Electronics
Tallinn University of Technology
Tallinn, Estonia
mart.min@taltech.ee

Abstract—Recording of pulsatile blood pressure waveform plays important role in monitoring of functioning of cardiovascular system of patient in medical applications. This study presents simulation of non-invasive sensing to evaluate the physical condition of patient through measuring continuous cardiac output on radial artery of human. In order to optimize the signal acquisition, the measurement should possess highest sensitivity in the region. Finite modeling and simulation of the arterial network of human forearm is described in this work. The spatial sensitivity of four-electrode system for bioimpedance measurements is estimated for different electrode setups and the sensitivity field is described graphically based on FEM simulation.

Keywords—radial artery, blood flow, four-electrode impedance measurement, FEM simulation, sensitivity distribution

I. INTRODUCTION

Continuous cardiac output and hemodynamic monitoring play a pivotal role in diagnosing and establishing the right treatment of patient in the cardiac intensive care unit, also used to estimate the human state of health or fitness in sport. Measurement of arterial blood pressure is the mainstay for the assessment of tissue perfusion [1]. Cuff sphygmomanometers are often used for measuring of arterial blood pressure in medical sector. However, in case of critical illness it is not useful practically, because the measurement is episodic. Furthermore, placing of sphygmomanometers could be problematic on burned extremities. For this reason, using intra-arterial catheters is generally preferable in clinical application, but the disadvantage of this method is invasiveness of the procedure. The invasive procedures are complicated and can cause several complications to the patient [2, 3].

Alternative non-invasive approaches of long-term pulse and CAP monitoring are mechanical [4, 5, 6], optical [7, 8, 9] and electrical bioimpedance (EBI) sensing methods. The mechanical method (applanation tonometry) involves placing a tension sensor on skin surface over radial artery [10]. A disadvantage of this method is that the tonometry plunger system compresses the radial artery against the radius bone altering the shape and properties of pressure wave [11, 12]. This could be another source of error in measured signal.

An optical method is based on light transmission [7] or reflection [8]. This method is non-invasive and does not require artery deformation like in case of mechanical tonometry. The transmission-based method could be applied only on certain thin body areas because of penetration ability. The reflection based method is less limited [10]. Some limitations of optical approach are reported: low accuracy of diastolic blood pressure measurement, movement artifacts effects the result [13]. The main application of the optical approach is measuring heart rate.

A non-invasive EBI sensing method for measurements on pulsating radial artery for central aortic pressure (CAP) estimation is presented in this study. This method is also non-invasive method and does not require artery deformation. The approach provides low complexity in the electronics design [11]. In the previous research the main attention was paid on the synthesis of transfer functions connecting central aortic and radial artery blood pressure curves [14]. Results showed that the measured blood vessel volume changes with EBI can be later interpreted into the aortic blood pressure wave by using a transfer function [11]. It was concluded that presented bioimpedance sensing method could be a useful complementary part of tonometry or even replace it in the future developments [14]. Therefore, there is a need to investigate sensitivity distribution of electrodes, because measured EBI signal is tiny and the risk of artifacts is serious.

The approach of monitoring cardiac activity in the form of pulse wave by using EBI of radial artery have been gaining more importance with last decades. One advantage of measuring on radial artery is that the radial artery locates close to the skin, so the electrodes could be placed exactly on radial artery [15]. Also, the wrist is the place for wearing a wristwatch, so the EBI measurement device could be integrated into some wearable device [15].

As non-invasive sensing instruments for bioimpedance measurement on radial artery are sensitive to noise, small errors on the measured data could translate into large uncertainties in the results. In order to optimize the signal acquisition, measurement should possess the highest possible sensitivity of the region.

Different experimental EBI measuring EBI on radial artery are earlier researched and reported. The exposing of pulse wave in arteries in forearm using EBI measurement has been reported by variety of electrode placement. Two main electrode placement used to measure the EBI of radial artery are distal [16, 17] and circular [18] placement relative to wrist [15].

Many studies of sensitivity distribution in different simplified homogeneous virtual models have been presented [19, 20, 21]. However, only few reports [22, 23] are available about sensitivity distribution in order to compare different configurations of EBI electrodes placed on radial artery [15].

To determine the highest sensitivity of four-electrode measurement on radial artery, the spatial sensitivity distribution is researched in this work. Spatial sensitivity is a frequently discussed topic in the field of impedance measurements [24].

The sensitivity field S expresses by the following equation [25]:

$$S = J'_{rec} \cdot J'_{cc} \quad (1)$$

J'_{cc} and J'_{rec} are current density vectors, where J'_{cc} is current density and J'_{rec} reciprocal density.

To obtain the sensitivity field distribution, a four-electrode impedance measuring on human forearm was simulated using Comsol Multiphysics 3D finite element (FE) model of human forearm with four electrodes placed nearby radial artery was created from the magnetic resonance imaging data [26]. The simulation results show the best sensitivity areas for impedance measurement depending on electrode alignment and configuration on forearm.

II. MATERIALS AND METHODS

A. Pressure wave contour

Monitoring of the aortic waveform (Fig.1) provides clinically useful information.

Pressure waveform contributes insights into the diagnosis and management of many disease states like hypertension, coronary artery disease, obstructive sleep apnea, diabetes etc.

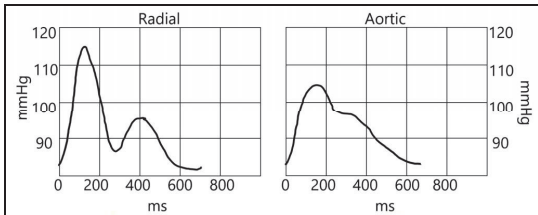


Fig. 1 Comparison of radial pressure waveform and the derived central pressure waveform. Left panel shows a magnified radial arterial waveform. The right panel shows a magnified derived central pressure waveform

The pressure wave contour in any artery is the result of the summation of the forward transmission of the cardiac pressure impulse and a backward reflection generated by the peripheral vascular system at the interface between large arteries, arteries and arterioles [27].

Pressure recorded anywhere in the arterial network depends on 3 factors: the amplitude and duration of ventricular ejection, the amplitude of the reflected wave, and the velocity of the reflected wave from the periphery [27]. These 3 key parameters are associated with state of health and fitness of the patient and other body specificity.

To determine the pulse rate, bioimpedance measurements could be used. The pulse wave changes the cross section of the arteries. The change can be measured as a change in the transfer impedance ΔZ [28].

B. Four electrode measuring

The study presents a non-invasive sensing method to evaluate the physical condition of patient through measuring continuous cardiac output on radial artery of human with four-electrode impedance measurement. Four-electrode impedance measurement method is widely used in different EBI applications. It includes two electrodes for voltage pick-up (PU) and two electrodes for current excitation (CC). The use of four-electrode configuration provides great advantage in comparison to the two-electrode configuration, since only the transfer of the tissue between the potential reading electrodes is determined [29].

The principle of four-electrode impedance measurement is illustrated in Fig. 2.

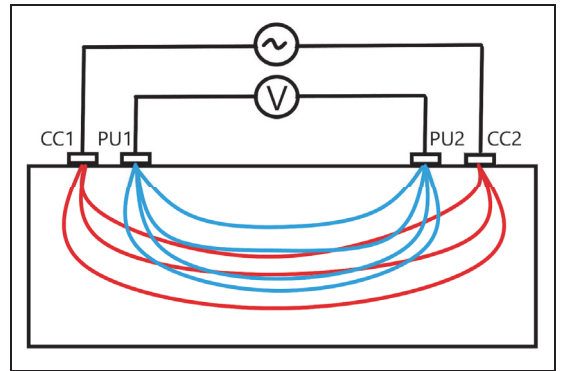


Fig. 2 Simplified sensitivity distribution of a four-electrode impedance measurement. CC1 and CC2 form the current-carrying couple; PU1 and PU2 form the voltage pick-up couple

One of the parameters to consider in EBI measurements is configuration between electrode couples. Several configuration strategies have been published and investigated, mostly for applications in electrical impedance tomography (EIT). Some of these are neighboring method, cross method, opposite method and adaptive method [30].

C. Sensitivity

The main objective of this work was to describe the spatial sensitivity field for four electrodes placed on radial artery. The sensitivity field in EBI measurements depends on several parameters: electrode number, geometry, orientation, spacing and configuration between electrode couples.

The transfer impedance (Z) can be approximated as the ration measured between the PU couple voltage (E) and the injected between the CC couple current (I).

$$Z = \frac{E}{I} \quad (2)$$

As a biological tissue is inhomogeneous, the total measured impedance (Z) is the sum of all local resistivity (ρ) values of all small sub-volumes in the sample and can be written as following [31]:

$$Z = \iiint \rho \cdot \frac{J_{CC} \cdot J_{PU}}{I_{CC} \cdot I_{PU}} dV \quad (3)$$

The sensitivity (S) of an impedance measurement is the scalar value representing the CC current density lines (J_{CC}) projection on the PU current density lines (J_{PU}) [31].

$$S = \frac{J_{CC} \cdot J_{PU}}{I_{CC} \cdot I_{PU}} \quad (4)$$

S is positive (or negative) value if measured impedance Z increases (or decreases) when the impedivity of that region increases [31].

The spatial sensitivity of four electrodes for bioimpedance measurements is described graphically based on FEM simulation in this work.

D. Forearm 3-D model

The objective of the study is a forearm of human. The forearm (antebrachium) consists of the radius and ulna, which are covered by muscle tissue. In addition, the forearm have skin tissue, fat tissue, nerves, tendons and blood vessels. The vascular supply to the forearm muscles is from branches of the ulnar and radial arteries. In the distal forearm, the radial artery lies lateral to the flexor carpi radialis tendon [32].

First, a 3-D model of human forearm slice with length of 10 cm was developed using AutoCAD 2018. Model includes different structures of human forearm: skin, fat, muscle, tendons, cortical bone, bone marrow, blood vessels and blood. The dimensions of the structures were determined from the cross sectional magnetic resonance imaging (MRI) of the upper extremity anatomy of human (Fig. 3) [26].

Latter, the model was implemented in COMSOL Multiphysics (version 5.3a) and the electrical properties of tissue were set according to Gabriel [33].

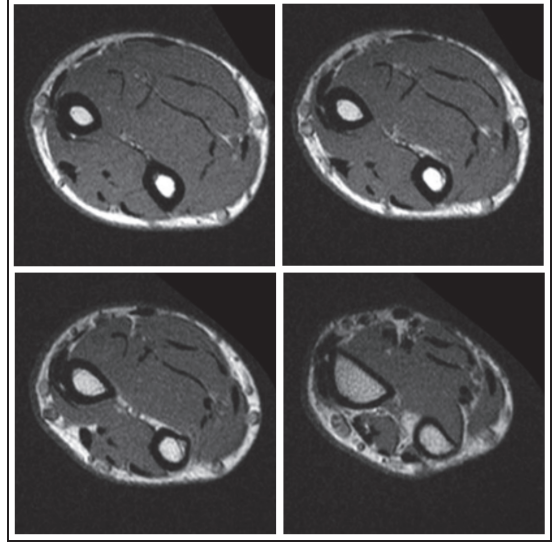


Fig. 3 Cross sectional magnetic resonance imaging (MRI) of the upper extremity anatomy of human [26]

The model includes four electrodes placed onto the radial artery close to scaphoid bone. The dimensions and electrical properties of electrodes are set in accordance to the disposable wet adhesive Ag/AgCl electrodes widely used in clinical practice, these have a round contact and are suitable for recording surface EMG, ECG, EOG, etc. Modeled electrodes have a shape of right circular cylinder with radius 3mm and height 1.5 mm. The influence of the electrode area has been taken in consideration. It was assumed that diameter of the electrode should be slightly bigger than diameter of the radial artery. The electrodes have a direct dry contact with the skin. It should be noted, that Ag/AgCl common hydrogel layer is not added between skin and electrode in the model, because the contact with skin is tight and has no gap between skin and electrode in the model. The model is shown in Fig. 4.



Fig. 4 Comsol Multiphysics 3-D model of human forearm

The model was partitioned into mesh elements using finite element method (FEM) (Fig. 5). Complete mesh consists of approximately 900000 elements and increasing the mesh density around the electrodes had a minimal effect on the results.

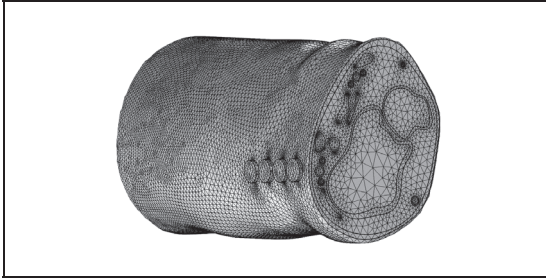


Fig. 5 Mesh of Comsol Multiphysics 3-D model

The voltage excitation was used in this research because of the technological simplicity. The electrical input was 1V for the simulation, and model was solved for the frequency 10 kHz. Measuring was simulated for different electrode setups and different configuration between electrode couples. Results were compared and the sensitivity distribution was calculated.

III. RESULTS

A. Sensitivity distribution evaluation

As the sensitivity (S) of an impedance measurement represents the CC current density lines (J_{cc}) projection on the PU current density lines (J_{pu}) these current density lines were investigated for each electrode setup. Examples of current density lines are presented in Fig. 6 and 7.

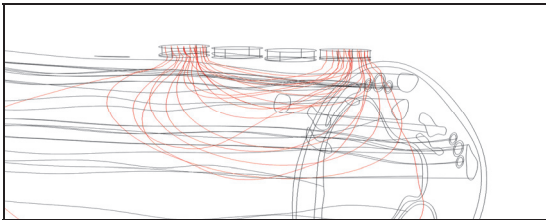


Fig. 6 Outer electrode pair current density lines

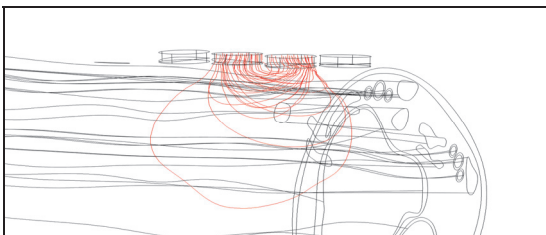


Fig. 7 Inner electrode pair current density lines

By using vectors of current density lines, the sensitivity of bioimpedance measurement was calculated for different electrode configurations. Fig. 8 represents examples of calculated sensitivity maps obtained for different electrode configurations. Scaling of the color map is kept the same within each simulation. The sensitivity is shown in the color map: positive values are indicated with red color and negative values are indicated with blue color.

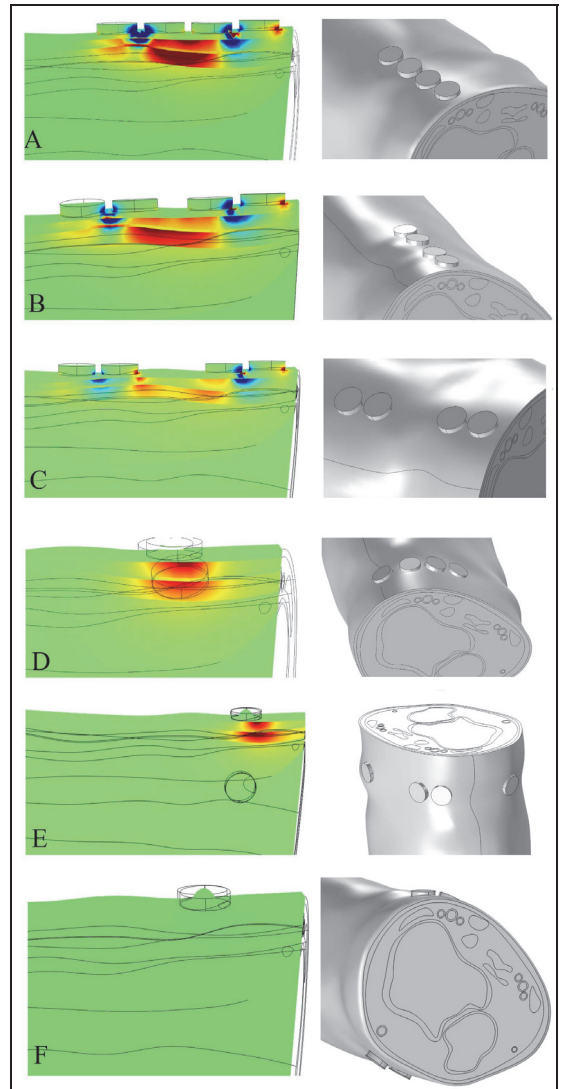


Fig. 8 Sensitivity maps obtained for different electrode configurations

B. Optimization of measurement sensitivity areas

Correct measurement results can be obtained only if the measuring area of radial artery has only one type of sensitivity range, either positive or negative [23]. To achieve more accurate results, the sensitivity distribution areas need to be optimized by changing the position of the electrodes.

Fig. 8 represents calculated sensitivity maps obtained for different electrode configurations. These examples of individual sensitivity distributions have regions of both positive and negative sensitivities. Sensitivity distributions being the most accurate to detect the radial artery have only positive (or negative) sensitivity on the radial artery and these are illustrated in Fig. 8A, 8B and 8C.

Maximum sensitivities in the center of measured area were calculated for the electrode configuration. The sensitivity is evaluated at a single point in the center of the measured area of radial artery. The results are given in Table 1. The values are presented in percentages as compared against other configuration. The maximum value for the parameter is 100%.

TABLE I. MAXIMUM SENSITIVITY VALUE ON RADIAL ARTERY

Electrode configuration (see Fig. 8)	Maximum sensitivity value, %
A	100
B	84
C	23
D	65
E	74
F	0

IV. DISCUSSION

The results of the study showed that most of the measurement sensitivity is concentrated in regions close to the surface of forearm. The radial artery is located near the surface in the positive sensitivity region. However, a considerable region of negative sensitivity lay often near the electrodes placed on the surface and for several measurements could have an opposite contribution to the measured value (Fig. 8A, 8B, 8C).

Sensitivity distributions being the most accurate to detect the radial artery have only positive (or negative) sensitivity on the radial artery and these are illustrated in Fig. 8D, 8E and 8F. Also, the maximum sensitivity value on radial artery was calculated. The sensitivity value might be important when the approximate location of expected impedance change is known [30]. Then the change in detected signal is the largest [30]. This study focuses on measurement of EBI on pulsating radial artery, so the location of expected impedance change is known and the sensitivity value is important to consider.

Based on the results, an indication of the preference of electrode configuration to use in EBI on radial artery is given. However, in reality, the forearm is more complex than this simplified model and differs for every individual person. Also,

noise level and the implementation of EBI instrumentation impact on the data acquisition method should be considered.

V. CONCLUSION

A four-electrode impedance measuring on human forearm simulation with different setups and configuration between electrode couples is described in this work. The purpose of the study was to describe the spatial sensitivity field for four electrodes placed on radial artery of human forearm in order to optimize the bioimpedance measurement acquisition of hemodynamics of human. The measurement should possess highest sensitivity in the region.

The novelty of this work is using FEM simulation in order to determine the most optimal configuration of electrodes placed on radial artery for EBI measurement. A 3-D model of human forearm was created in COMSOL Multiphysics and several measurements were simulated and visualized in respect to their measurement sensitivity distributions for different electrode setups. The maximum sensitivity value of measuring on radial artery was calculated.

The voltage excitation was used in this simulation. The same simulation will be repeated using current excitation in the future.

Based on the results, an indication of the electrode configuration preference to use in EBI on radial artery is given.

ACKNOWLEDGMENT

The research was supported by Estonian Research Council (grant IUT1911), EC project H2020 – Flag-ERA JTC 2016 CONVERGENCE, and Estonian ICT Center of Research Excellence EXCITE.

REFERENCES

- [1] K. K. Chung, and S. E. Wolf, "Total Burn Care (Fourth Edition). Chapter 33 - Critical care in the severely burned: Organ support and management of complications," 2012, pp. 377-395
- [2] B. Freeman, and J. Berger, "Anesthesiology Core Review: Part 2, Chapter 1: Invasive Arterial Blood Pressure Monitoring," Cengage® Publisher Services, 2016.
- [3] C. M. McEniery, J. R. Cockcroft, M. J. Roman, S.S. Franklin, and I. B. Wilkinson, "Central blood pressure: current evidence and clinical importance," *Eur. Heart J.*, vol 35, no 26, 2014.
- [4] G. L. Pressman, and P. M. Newgard, "A transducer for the continuous external measurement of arterial blood pressure", *IEEE Trans. Bio-Med. Electron*, 1963, pp 73-81.
- [5] B. Lee, J. Jeong, J. Kim, B. Kim, and K. Chun, "Cantilever arrayed blood pressure sensor for arterial applanation tonometry," *IET Nanobiotechnol*, 2014.
- [6] E. Kaniusas, H. Pflutzner, L. Mehnen, J. Kosel et. al, "Method for continuous non-disturbing monitoring of blood pressure by magnetoelastic skin curvature sensor and ECG", *IEEE Sens J.*, 2006, pp. 819-828.
- [7] H. Lin, W. Xu, N. Guan, D. Ji, Y. Wei, and W. Yi, "Noninvasive and continuous blood pressure monitoring using wearable body sensor network," *IEEE Intell. Syst.*, vol.30, 2014.
- [8] M.K. Chaithanya, K. V. K. Kishore, and A. Srinivasulu, "Continuous blood pressure measurement and data logging device with SMS alert," *Multimed. Ubiquitous Eng.*, 2019.

- [9] D. Borchevkin, A. Shestakov, V. Petrov, S. Botman et. al. "Method of photoplethysmography diagnostics of domesticated animals cardiovascular diseases," *Vet.Sci. Technol*, vol.7, 2016.
- [10] Y. J. Wang, C. H. Chen, C. Y. Sue, W. H. Lu, and Y. H. Chiuo, "Estimation of blood pressure in the radial artery using strain-based pulse wave and photoplethysmography sensor," *MDPI Micromachines*, 2018.
- [11] H. Kõiv, M. Rist, and M. Min, "Development of bioimpedance sensing device for wearable monitoring of the aortic blood pressure curve", *Technisches Messen*, vol. 85(5), 2018.
- [12] M. T. Gabeleira, "Optical measurement of the arterial pulse wave and determination of pulse wave velocity", MSc, 2010.
- [13] M. Raghunath, V. Kiran, and S. Aravapalli, "Design of an optical blood pressure sensor for noninvasive monitoring of blood pressure," *IJSEAT*, vol. 3 (12), 2015.
- [14] M. Min, P. Annus, H. Kõiv, A. Krivosei, T. Uuetoa, and J. Lamp, "Bioimpedance sensing – a viable alternative for tonometry in non-invasive assessment of central aortic pressure," *MeMeA*, 2017.
- [15] M. Metshein, "Wearable solutions for monitoring cardiorespiratory activity," Phd, Tallinn University of Technology, 2018
- [16] M. C. Cho, J. Y. Kim, and S. Cho, "A bio-impedance measurement system for portable monitoring of heart rate and pulse wave velocity using small body area," *IEEE International Symposium on Circuits and Systems*, 2009, pp. 3106-3109.
- [17] J. J. Huang, Y. M. Huang, and A. R. See, "Studying peripheral vascular pulse wave velocity using bio-impedance plethysmography and regression analysis," *ECTI-CIT*, vol.11 (1), 2017.
- [18] S. H. Liu, D. C. Cheng, and C. H. Su, "A cuffless blood pressure measurement based on the impedance plethysmography technique," *Sensors*, vol. 17 (5), 2017
- [19] S. P. Ahmed, M. A. Kadir, G. D. A. Quaderi, R. Rahman, and K. S. Rabbani, "Improved understanding of the sensitivity of linear tetrapolar impedance measurement (TPIM) and 8-electrode focused impedance method (FIM) in a volume conductor," *Bangladesh Journal of Medical Physics*, vol. 8 (1), 2017, pp. 22-31.
- [20] O. I. Shuvo, and M. N. Islam, "Sensitivity Analysis of tetrapolar electrical impedance measurement system using Comsol Multiphysics for non-uniform and inhomogeneous medium," *Dhaka University Journal of Science*, vol. 64 (1), 2016, pp. 7-13.
- [21] F. J. Pettersen, H. Ferdous, H. Kalvøy, G. Martinsen, and J. O. Hogetveit, "Comparison of four different FIM configurations – a simulation study," *Physiological Measurement*, vol. 35 (6), 2014.
- [22] I. Jivet, "Wrist pulse monitoring by electrical impedance using a 3D model of the arm," *ISETC*, 2014.
- [23] A. Krotov, "Simulation of electric impedance measurement on a 3D human arm model," BSc., Tallinn University of Technology, 2017.
- [24] P. Høyum, H. Kalvøy, G. Martinsen, and S. Grimnes, "A finite element model of needle electrode spatial sensitivity," *IOP Publishing, Physiological Measurement*, 2010.
- [25] D. B. Geselowitz, "An application of electrocardiographic lead theory to impedance plethysmography," *Biomedance Engineering*, vol. 18, 1971, pp. 38 – 41.
- [26] "Arm, forearm, and hand: MRI of anatomy", *IMAIOS*, 2018. [Online]. Available: <https://www.imaios.com/en/e-Anatomy/Limbs/Upper-extremity-MRI>. [Accessed: 10- Dec- 2018].
- [27] M. R. Nelson, J. Stepanek, M. Cevette, M. Covalciuc, R. T. Hurst, and A. J. Tajik, "Noninvasive Measurement of Central Vascular Pressures With Arterial Tonometry: Clinical Revival of the Pulse Pressure Waveform," *Mayo Clinic Proceedings*. 2010 May; 85(5): 460-472.
- [28] Grimnes, and O. Martinsen, "Bioimpedance and Bioelectricity Basics," Academic Press, 2008.
- [29] S. Guttke, M. Laukner, and P. Weber, "Cross sensitivity of different electrode types for impedance plethysmography under motion conditions," *Journal of Physics: Conference Series* 434, 2013.
- [30] P. Kauppinen, J. Hyttinen, and J. Malmivuo, "Sensitivity Distribution Visualizations of Impedance Tomography Measurement Strategies," *International Journal of Bioelectromagnetism*, 2006, Vol. 8, No. 1, pp. VII/1 - VII/9.
- [31] C. Canali, "An impedance method for spatial sensing of 3D cell constructs – towards applications in tissue engineering," *Electronic Supplementary Material (ESI) for Analyst*, The Royal Society of Chemistry, 2015.
- [32] O'Rahilly, Müller, Carpenter, and Swenson, "Basic Human Anatomy, Chapter 10: THE FOREARM", *Dartmouth.edu*, 2018, [Online]. Available: https://www.dartmouth.edu/~humananatomy/part_2/chapter_10.html. [Accessed: 10- Dec- 2018].
- [33] S. Gabriel, R.W. Lau, and C. Gabriel, "The dielectric properties of biological tissues: II. Measurements in the frequency range 10 Hz to 20 GHz," *Phys. Med. Biol.* 41, 1996.

Publication III

Pesti, Ksenija; Metshein, Margus; Annus, Paul; Kõiv, Hip; Min, Mart (2021). Electrode Placement Strategies for the Measurement of Radial Artery Bioimpedance: Simulations and Experiments. *IEEE Transactions on Instrumentation and Measurement*, 70, 1–10.

Electrode Placement Strategies for the Measurement of Radial Artery Bioimpedance: Simulations and Experiments

K. Pesti¹, M. Metshein¹, P. Annus¹, *Member, IEEE*, H. Kõiv²,
and M. Min¹, *Life Senior Member, IEEE*

Abstract—Continuous cardiac output is a significant matter that must be considered in monitoring the functioning of cardiovascular system. A noninvasive sensing system that is based on measuring electrical bioimpedance variations of radial artery is proposed to evaluate the physical condition of a patient. To optimize the signal acquisition, different electrode placement strategies are compared with the goal of finding the most suitable ones. The finite-element method (FEM) simulation of sensitivity distribution and experimental measurements on radial artery are performed for experimenting circular and distal electrode placements. Importantly, also the modified electrode placement strategies, guided by the idea of focused impedance method (FIM), are investigated. To reduce the number of electrodes in measurement setup, its novel version is proposed: a five-electrode FIM strategy. The efficiency of the proposed strategy can be seen in the reduced amount of required number of electrodes: the smaller area of electrode–skin contact interface results in smaller influence of uncertainties. Moreover, the reduced number of electrodes contributes to benefit through developing simpler instrumentation having lower energy consumption and cheaper manufacturing costs. The results show the advances of the proposed novel five-electrode FIM strategy for measuring the pulsating volume of blood in radial artery with the goal of determining the central aortic pressure (CAP) of blood.

Index Terms—Electrical bioimpedance (EBI), finite-element analysis, focused impedance, impedance cardiography, pulse wave, sensitivity analysis, wearable sensors.

I. INTRODUCTION

ACCORDING to the World Health Organization, cardiovascular diseases (CVDs) are the leading cause of death globally [1]. Continuous monitoring of cardiac output plays an important role in diagnosing CVDs and providing the treatment of patients in the cardiac intensive care unit, also

used to estimate the state of health or fitness in sport [2]. Among the existing techniques of continuous hemodynamics monitoring, the most common in clinical application is intra-arterial catheters. However, the procedure is invasive and could cause several complications to the patient [3], [4].

For monitoring the hemodynamic parameters—especially the pulse, several other approaches are used [5]–[11]. A well-known technique is optical approach that is based on light transmission or reflection [7], [8]—used widely for heart rate measurement. The main limitation of the method is caused by low penetration ability of light, so the transmission-based method could be applied only on certain thin body areas. In addition, some other limitations of long-term pulse monitoring by the means of optical approach are reported: low accuracy of diastolic blood pressure measurement, movement artifacts affect the result [10].

The common noninvasive alternative for monitoring the CAP of blood is based on placing a pressure sensor on skin over radial artery (applanation tonometry) [5], [6]. The disadvantage of this method is a risk of additional error occurrence due to the tonometry plunger that compresses the artery and possibly leads to the change of shape and properties of pressure wave.

However, the transfer function between the CAP of blood, measured in aortic arch and in peripheral arteries, has been shown to exist in measurements of the electrical bioimpedance (EBI) by our research group [11], [12]. This could be a helpful complimentary part of tonometry or even replace it in future developments [12]. Furthermore, the method provides low complexity in electronic design, and since the EBI is measured noninvasively near the location of radial artery, the device could be integrated into wristband of wearable device [11].

Developing of noninvasive, continuously operating, accurate, and wearable device for blood pressure wave estimation combines several different challenges. The EBI measurement instrumentation is sensitive to noise and, therefore, even small errors in the measured data can be translated into large uncertainties in the results—the risk of artifacts is serious. Different ways have been proposed in the literature to mitigate distortions [13]–[15] where methods for purification of the cardiac signal have been proposed. Still, a supportive approach

Manuscript received June 1, 2020; accepted July 11, 2020. Date of publication July 29, 2020; date of current version December 14, 2020. This work was supported by the Estonian Research Council under Grant EAG34, in part by the European project H2020—Flag-ERA JTC 2016 CONVERGENCE, in part by the Estonian ICT Center of Research Excellence EXCITE under Grant TAR16013, and in part by Mobilitas+ grant Mobera20 for Chist-era JEDAI project (EU Regional Development Fund). The Associate Editor coordinating the review process was Dr. Chao Tan. (*Corresponding author: K. Pesti.*)

The authors are with the Thomas Johann Seebeck Department of Electronics, Tallinn University of Technology (TalTech), 19086 Tallinn, Estonia (e-mail: ksenija.pesti@taltech.ee; margus.metshein@taltech.ee; paul.annus@taltech.ee; hip.koiv@taltech.ee; mart.min@taltech.ee).

Digital Object Identifier 10.1109/TIM.2020.3011784

to signal processing is the development of the electrode placement strategies that result as qualitative and motion artifact free signal of EBI.

To compare the ability of different electrode placement strategies to provide access into the data of cardiovascular system of human, a robust approach of evaluating the amount of time-varying changes in the measured signal of EBI, caused by the pulsating blood, is utilized. The larger the amount of change, the more suitable the strategy is. Similarly, but in reverse, the effect of concurrent movements of the forearm is evaluated by determining the amount of change of the measured signal of EBI—the larger the change, the poorer the result.

The simulation of EBI measuring on a static model of forearm by using different electrode placement strategies is expected to predict the emerging sensitivity distribution. The model was composed, and sensitivity distribution simulated. The expectation is that the more accurately the region of positive sensitivity applies to the source of the change of volume in wrist (expectedly—radial artery), the larger the detected change in the measured signal of EBI. The same applies in the case of the movements of hand, as the volumes in the forearm change due to the tightening of the muscles, moving of the extensor tendons, etc.

Despite the fact that experimental EBI measuring research on radial artery to determine the most suitable electrode placement strategies have been reported before [16]–[19], these are typically not compared to the simulation results in static model. However, other combinations of electrodes and clever techniques have been proposed as well: like FIM [20]. Importantly, by our knowledge FIM method has not been applied for monitoring the pulsating volume of blood in radial artery with the goal of providing input for the estimation of CAP of blood.

Some studies [21]–[23] of sensitivity distribution in different simplified and homogeneous virtual models have been performed for different applications. However, only few reports [2], [16], [24] are available about sensitivity distribution in order to compare different configurations of EBI electrodes placed on radial artery [2] and none of these that would cope with FIM method. The gained data can be used as reference in designing instrumentation and prototypes.

This article is primarily focused on investigation of different electrode placement strategies on forearm with the goal of determining the ones that provide convenient access to the cardiac activity of human. The previous study of FEM simulation of sensitivity distribution of EBI measurement on radial artery was performed only for circular and distal electrode placements relative to forearm [2] which is extended now in this article. This was chosen as traditionally, four-electrode configurations have been used in research and commercial products (e.g., Fitness Tracker UP3 by Jawbone), applied either distally [19] and [25] or circularly [26] relative to forearm.

A 3-D model of human forearm fragment was created in Comsol Multiphysics and sensitivity distribution was investigated. In addition to the traditional in-line four-electrode impedance measurement, the modified four-electrode

placement strategies, and electrode placements, guided by the idea of FIM method are investigated. Measurements of EBI for chosen electrode placement strategies are presented and compared to simulation results.

Novelty of the presented work lies in the reduced number of electrodes in measurement setup—the modified version of six-electrode FIM is proposed as a five-electrode FIM with different electrode locations relative to radial artery. The results are promising, indicating the advance of modifying the FIM method relative to the path of pulsating flow of blood in arteries. The contribution to the further development and adaption of FIM method has been provided through simulations on static model of forearm and relative comparison with practical measurements. The goal of providing novel means for estimating CAP of blood through the measurements of EBI of time-varying changes of pulsating blood in radial artery is targeted.

II. SIMULATION OF SENSITIVITY DISTRIBUTION

This section is primarily focused on investigation of sensitivity distribution of EBI measurement for chosen electrode configurations. The understanding of sensitivity distribution in measured region is essential to link with experimental results with different electrode configurations.

A. Sensitivity

The transfer impedance Z of an object can be approximated as a ratio between the measured voltage E by the pick-up (PU) electrodes and the injected current I by the current-carrying electrodes (CC) [27]

$$Z = \frac{E}{I} \quad (1)$$

where Z [Ohm] is transfer impedance, E [V] is measured voltage, and I [A] is injected current.

The resistivity of the object ρ is defined as a ratio between the voltage E and current density J

$$\rho = \frac{E}{J}. \quad (2)$$

As biological tissue is inhomogeneous, the total measured impedance Z could be expressed as a sum of all local resistivity ρ values of all small sub-volumes of the tissue and can be indicated by the following equation:

$$Z = \iiint \rho \frac{J_{CC} \cdot J_{PU}}{I_{CC} \cdot I_{PU}} dv \quad (3)$$

where Z is impedance, ρ is the resistivity of the volume, J_{CC} is the current density under CC electrodes, and J_{PU} is the current density under PU electrodes [27].

Sensitivity distribution of an EBI measurement gives a notion of the measured impedance that is caused by a given conductivity distribution [28]. The sensitivity S of EBI measurement is a scalar value representing the CC electrode current density lines J_{CC} projection on the PU electrode current density lines J_{PU} [27] (Fig. 1)

$$S = \frac{J_{CC} \cdot J_{PU}}{I_{CC} \cdot I_{PU}}. \quad (4)$$

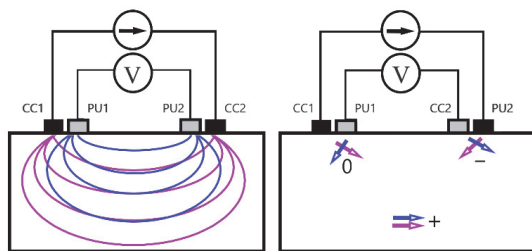


Fig. 1. Sensitivity formation of the four-electrode impedance measurement in homogeneous volume. CC1 and CC2 form current-carrying electrode pair. PU1 and PU2 form voltage pick-up electrode pair [28].

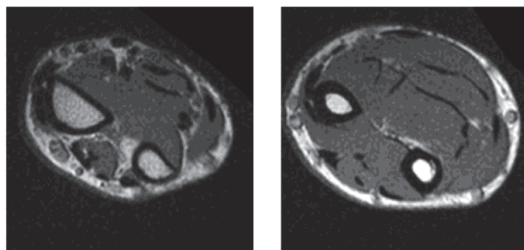


Fig. 2. Cross-sectional MRI of upper extremity anatomy of human [29].

Sensitivity S maintains positive value, if measured Z increases and negative value, if measured Z decreases. This can clearly be seen by drawing the current density vectors of the CC and PU electrode pairs [27].

If current density vectors are in the same direction, then sensitivity S will be positive; if these are in the opposite direction, then sensitivity S will be negative. Sensitivity S will be maximum, if current density vectors are superimposed. Sensitivity S will be zero, if current density vectors are in perpendicular directions [27].

Using FEM-based analysis, the sensitivity S value can be estimated for the contribution of EBI.

B. Forearm Model Description

The object of the study is a human forearm, which consists of matter of different conductivities: skin, fat, muscle, etc. The vascular supply is from the branches of ulnar and radial arteries, which backflow is ensured by veins.

To determine the highest sensitivity applying on radial artery, the sensitivity distribution is researched in this study. The geometry of a simplified 3-D model of human left forearm fragment was created based on cross-sectional magnetic resonance imaging (MRI) of upper extremity anatomy of human (Fig. 2) by using AutoCAD 2018.

The geometry was implemented in COMSOL Multiphysics (version 5.3a) and the electrical conductivity of tissues was set according to Gabriel *et al.* [30].

The model (Fig. 3) was partitioned into mesh elements by using the FEM through increasing the mesh density around the electrodes to have minimal effect on the results.

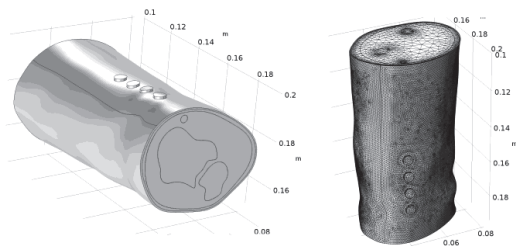


Fig. 3. Consol Multiphysics 3-D model of human forearm fragment with distal four-electrode placement.

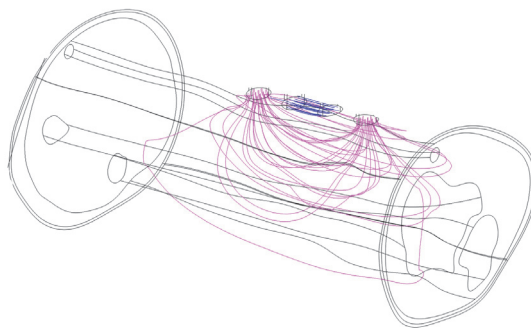


Fig. 4. Current density lines in case of distal four-electrode placement.

The simulation of sensitivity distribution of EBI measurement was performed for several electrode placements listed in Section IV. The electrical properties were set based on the widely used Ag/AgCl electrodes. Modeled electrodes have round shape with radius of 3 mm and are implemented on a boundary level. For optimal response Ag/AgCl electrodes have a conductive gel placed between skin and electrode.

Simulations were originally performed for dry electrodes with direct skin contact. Concurrently, a comparative simulation with conductive gel layer between the electrode–skin contact interface was executed to confirm the validity of simulations with respect to support the experimental results. The thickness of the layer was 1 mm and electrical properties were set according to [31]. As expected, there is equal effect of gel layer presence on all the simulations and conclusions remain unchanged. Simulation results are presented in Section V-A and contain outcome in case of model with conductive gel layer.

Predefined settings of electric currents physics found under the ac/dc branch were used in the model. The physics interface solves a current conservation equation based on ohm's law using the scalar electric potential as the dependent variable [32]. Voltage excitation of 1 V was applied to the electrodes and the frequency domain study steps were used to compute the model for frequency 10 kHz.

As the sensitivity S of an impedance measurement is represented by the CC current density lines J_{CC} projection on the PU current density lines J_{PU} , these current density lines were investigated J'_{cc} (Fig. 4). By using vectors of current density lines, the sensitivity of EBI measurement was calculated and the corresponding sensitivity maps were obtained for the different electrode configuration strategies. The results of simulation are detailed in Section V.

III. MEASUREMENTS

Methods and instrumentation used for experimental measurements of EBI with the goal of experimenting chosen electrode placement strategies are presented in this section.

A. Instrumentation

The EBI measurements were performed by using an adapted USB digital data acquisition (DAQ) module U2531A of Keysight Technologies (Santa Rosa, CA, USA). This device provides a sampling rate of 2 MSa/s in the case of 14-bit resolution per each channel (total of four differential input channels) simultaneously. The time-varying signal of Z ($Z(t)$) in both utilized channels was determined by using reference resistors with the value of 1 k Ω . For this, a circuit on printed circuit board as user interface for electrode connector was implemented and connected to suitable 68-pin Digital and Trigger I/O Terminal Block CB-68LP by using SH68M-68M-EPM cable of National Instruments (Austin, TX, USA). The measurement setup together with the user interface is thoroughly described in [33].

The signal was gathered by custom made LabView program and saved to personal computer. The program allows to visualize and gather the EBI waveforms separately with two measurement channels and with the same applied parameters.

Standard solid gel Ag/AgCl ECG monitoring electrodes of type T709 of Comepa Industries (Albuquerque, NM, USA) were used in the measurement experiments. The dimensions of the electrodes were modified by cutting their width approximately to 10 mm. The modification of dimensions was implemented with the aim of placing the electrodes on top of the location of radial artery more densely.

B. Measurement Method and Setup

The measurement experiments were performed on the forearm of a single volunteer (an author of this article) (healthy adult male, age of 35, height of 183 cm and weight of 71 kg), sitting comfortably on a chair with the arm lying on the armrest.

In measuring experiment, research ethics was followed, and no sensitive data gathered. The measurements on single subject are acceptable as biological objects mainly have active character and the single measurement experiment is enough for gaining reference measurement data for comparison.

The radial artery of the left arm was determined by palpation and electrodes attached according to the desired placement strategies. The leads of measurement device ($L = 200$ mm) were connected to the electrodes by using crocodile clips.

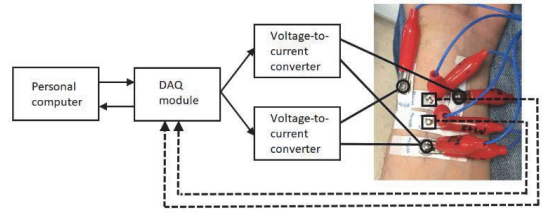


Fig. 5. Visual representation of measurement setup for determination of $\Delta Z(t)$ caused by pulsating volume of blood in radial artery.

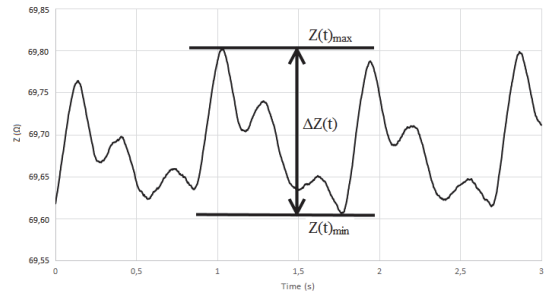


Fig. 6. Determination of $\Delta Z(t)$ in the case of pulse waveform.

The schematic visualization of measurement setup and the electrodes is available in Fig. 5.

The excitation signal of frequency of 10 kHz and amplitude of 1 V was utilized. In the cases of FIM, where applying of two excitation channels is required, the excitation signals of equal parameters were used.

The digital processing of the signals was implemented in LabView by using Savitzky–Golay filter at side points of 25.

To compare the ability of chosen electrode placement strategies to grant access to the pulsating blood in radial artery, the following two parameters were evaluated.

- 1) The amount of change in measured $Z(t)$, caused by the pulsating volume of blood: marked as $\Delta Z(t)_{\text{pulse}}$.
- 2) The amount of change in measured $Z(t)$, caused by the movements of the hand: marked as $\Delta Z(t)_{\text{move}}$.

The minimum $Z(t)_{\text{min}}$ and maximum $Z(t)_{\text{max}}$ points of pulse wave in the measured signal of EBI were determined and $\Delta Z(t)_{\text{pulse}}$ calculated (for visual representation, see Fig. 6).

Similarly, the effect of concurrent movements of the hand was determined by calculating the difference between the minimum and maximum points of the measured signal of EBI. Pulse was not visually identifiable in the gained signal of $Z(t)$ while the movements of hand were implemented.

As the noninvasive connection of electrode to skin surface is highly dependent on several factors like exact placement, external pressure, skin condition, etc., the ratio of $\Delta Z(t)$ from $Z(t)_{\text{max}}$ ($R_{\Delta Z(t)}$) was also calculated in comparability reasons in both and each case according to

$$R_{\Delta Z(t)} = \frac{\Delta Z(t) \cdot 100}{Z(t)_{\text{max}}} \quad (5)$$

and represented by $R_{\Delta Z(t)_{\text{pulse}}}$ and $R_{\Delta Z(t)_{\text{move}}}$, respectively, in the following discussion.

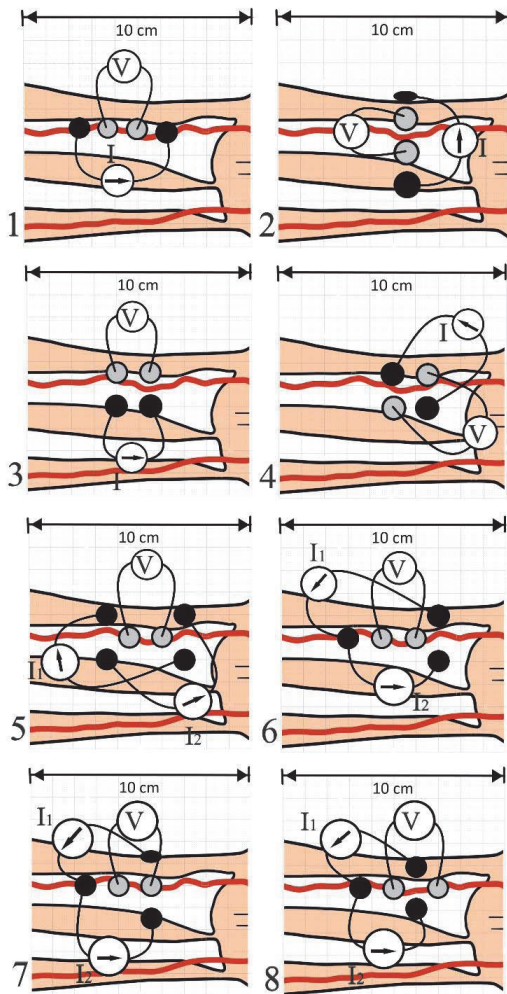


Fig. 7. Electrode configuration strategies that are described in Section IV.

The measurement procedure included two activities, which the volunteer was asked to follow: 1) sit quietly for 20 s and 2) rhythmically clenching the first for 20 s. Altogether eight different electrode placement strategies on top the location of radial artery in left forearm were experimented as listed in Section IV.

The results of measurement are detailed in Section V.

IV. ELECTRODE CONFIGURATION STRATEGIES

FEM simulation of sensitivity distribution and experimental EBI measurements on human forearm were utilized for the following electrode configurations, shown in Fig. 7 as follows.

- 1) Classical in-line four-electrode configuration with distal placement along forearm (radial artery).

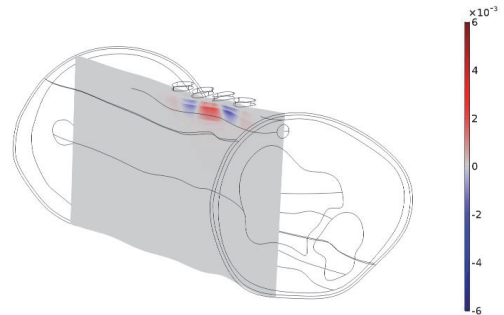


Fig. 8. Sensitivity map obtained for electrode configuration strategy 1.

- 2) Classical in-line four-electrode configuration with circular placement around forearm (radial artery).
- 3) Rectangular four-electrode configuration with the exciting pair on one side and the measuring pair on another side of radial artery.
- 4) Rectangular four-electrode configuration with the location of one exciting and one measuring electrode on either side of the radial artery.
- 5) Six-electrode FIM with measuring electrodes placed along the radial artery.
- 6) Five-electrode FIM (option A) with two exciting electrodes combined into one and measuring electrodes set between the excitation electrodes.
- 7) Five-electrode FIM (option B) with two exciting electrodes combined into one and measuring electrodes set between the excitation electrodes.
- 8) Five-electrode FIM (option C) with two exciting electrodes combined into one and measuring electrodes set between the excitation electrodes.

V. RESULTS

A. Simulation Results

By using vectors of current density lines, the sensitivity of EBI measurement was calculated, and sensitivity color maps were obtained for eight different electrode configuration strategies as listed in Section IV. Scaling of the color map is kept the same within each simulation: positive values are indicated with red color and negative values are indicated with blue color (Figs. 8–15).

Color maps of strategies 1 and 2 are shown in Figs. 8 and 9, respectively, representing the FEM simulations of sensitivity distribution. Previously we have implemented FEM simulations for several different distal and circular electrode configurations, reported in [2]. The disadvantage of the four-electrode impedance measurement strategy is an emerging opposite (negative) sensitivity in the regions between the respective current and potential electrodes [34]. If radial artery is placed in these regions, the measured transfer impedance will decrease due to negative sensitivity impact.

Besides the classical in-line four-electrode configurations, two modified four-electrode placement strategies (3 and 4) were researched (Figs. 10 and 11) with the goal of

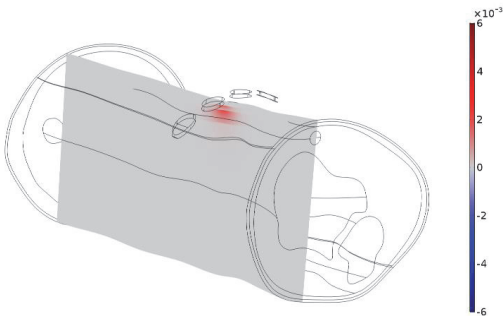


Fig. 9. Sensitivity map obtained for electrode configuration strategy 2.

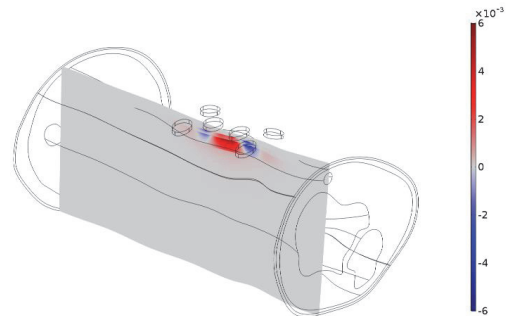


Fig. 12. Sensitivity map obtained for electrode configuration strategy 5.

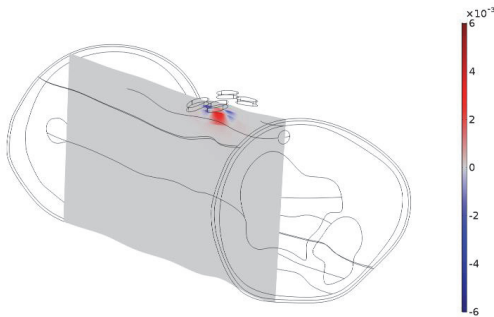


Fig. 10. Sensitivity map obtained for electrode configuration strategy 3.

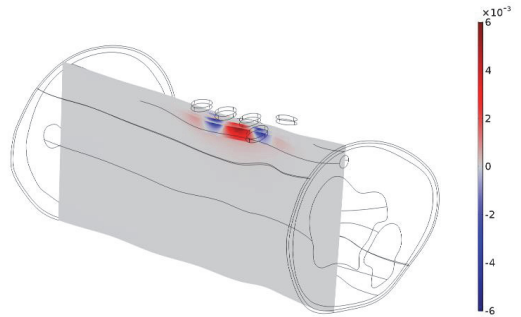


Fig. 13. Sensitivity map obtained for electrode configuration strategy 6.

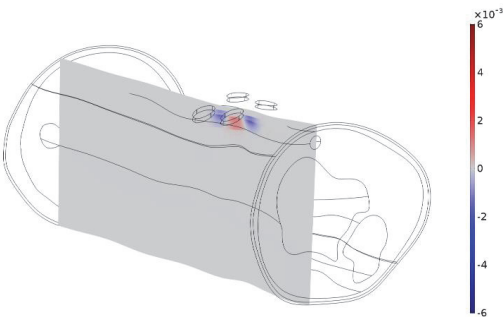


Fig. 11. Sensitivity map obtained for electrode configuration strategy 4.

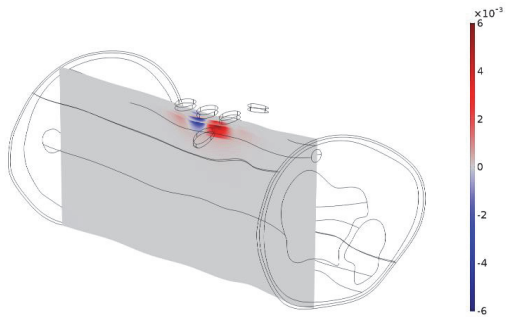


Fig. 14. Sensitivity map obtained for electrode configuration strategy 7.

investigating the effect of misplacement of electrodes on sensitivity distribution.

To reduce the opposite sensitivity impact in the neighboring zones, FIM has been proposed in the literature [20]. FIM is attractive because of its ability to localize a small region in a volume conductor using only few electrodes. The transfer impedances in the two orthogonal directions are merged, so the small negative sensitivity on one side is canceled by a small positive sensitivity [34]. Furthermore, the negative sensitivity becomes insignificant with depth, because of growing predominance of positive focused sensitivity [34].

Four different electrode strategies that are based on FIM approach by using five and six electrodes were simulated—the sensitivity maps are presented in Figs. 12–15.

As the simulation results show that negative sensitivity impact is present, it is important to consider the sensitivity value—the change in the measured signal is the largest [30] with the highest sensitivity. Fig. 16 shows the calculated difference between the absolute values of maximum negative and maximum positive sensitivities in radial artery.

B. Experimental Results

The $Z(t)$ of the forearm was measured by using four-electrode configurations. Single measurement was performed in the case of each electrode placement to gain data for comparison with other electrode placement strategies and the results of simulation. The results represented by the calculated

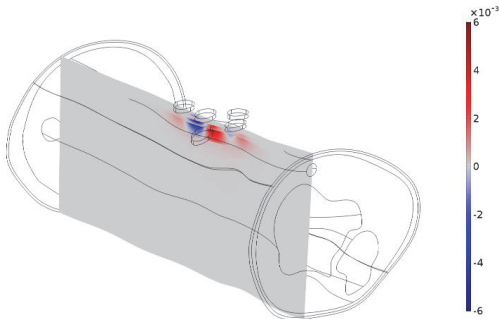


Fig. 15. Sensitivity map obtained for electrode configuration strategy 8.

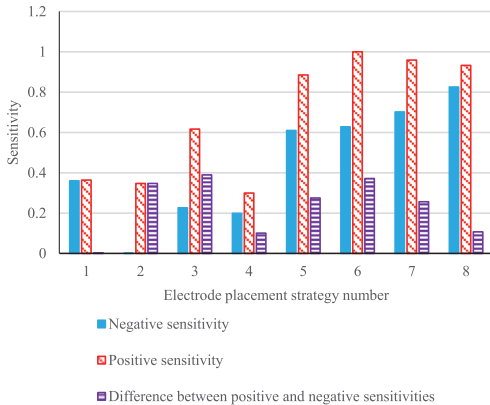


Fig. 16. Maximum negative and maximum positive sensitivities ratio of absolute values and difference between values along the radial artery for electrode configuration strategies described in Section IV.

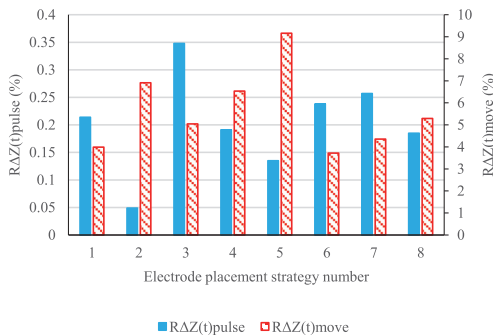


Fig. 17. Comparison of the calculated $R_{\Delta Z(t)pulse}$ and $R_{\Delta Z(t)move}$ in the cases of the chosen electrode placement strategies.

$R_{\Delta Z(t)pulse}$ and $R_{\Delta Z(t)move}$ shown in percentages are visible in Fig. 17.

The presentation of the results by using the calculated $R_{\Delta Z(t)pulse}$ and $R_{\Delta Z(t)move}$ provides opportunity to compare the different electrode placement strategies on the same basis which can be considered as sensitivity of the placement to volume changes in underlying tissues and vessels. The results clearly indicate the difference between the different electrode

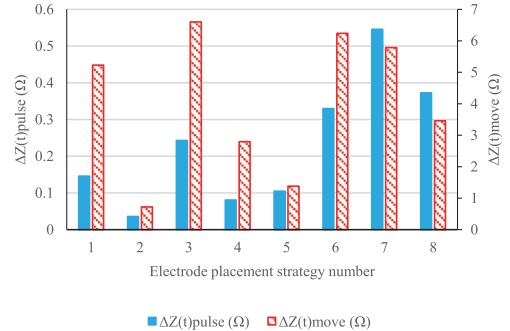


Fig. 18. Comparison of the calculated $\Delta Z(t)pulse$ and $\Delta Z(t)move$ in the cases of the chosen electrode placement strategies.

placement strategies in the sense of both: the amount of pulsating blood in radial artery and the concurrent movements. The results of $\Delta Z(t)pulse$ and $\Delta Z(t)move$ shown in ohms are visible in Fig. 18.

VI. DISCUSSION

As simulation results show, the emergence of negative sensitivity on radial artery appears in all strategies, but not in strategy 2. At the same time, the positive sensitivity value shows to be lowest in strategy 2 compared to other strategies (Figs. 9 and 16). The change in the measured signal is the largest with the highest sensitivity [28].

The worst experimental result in the cases of $R_{\Delta Z(t)pulse}$ and $\Delta Z(t)pulse$ is clearly delivered by the electrode placement strategy 2 (Fig. 7)—confirming the simulation results. Also, similar conclusion has been reported in the literature before [18], related to the suitability of the circular placement of electrodes relative to radial artery [17], [35]. The answer is expected to be hidden in the exact placement and the dimensions of the electrodes—the relatively small diameter of radial artery expects the usage of small electrodes to precisely set the sensitivity region to desired area.

Surprisingly, the best result in the case of experimentally gained $R_{\Delta Z(t)pulse}$ is achieved by using the peculiar approach of electrode placement strategy 3. Also, the simulation confirms the sensitivity electrode placement strategy 3 to be the highest among the four-electrode strategies. This result strongly refers to the long-run discussion of what is the actual physiological source of the $\Delta Z(t)$ in the measured signal of EBI [36], [37]. However, similar electrode placements have been utilized before with satisfactory results, for example with the goal of detecting the pulse pressure velocity in forearm through the measurements of EBI [25].

In the case of experimented FIM strategies, the simulation results also show the presence of negative sensitivity impact. However, the positive sensitivity tends to be higher than negative, so the negative sensitivity becomes less significant. Figs. 10 and 11 confirm that claim, however, the negative sensitivity increases with positive sensitivity. Also, Figs. 12–15 reveal that the utilized FIM electrode placement strategies issue the best outcome, confirming their claimed

TABLE I
PERCENTAGES OF MEASURED $\Delta Z(t)_{\text{pulse}}$ $\Delta Z(t)_{\text{move}}$ IN THE CASES
OF THE CHOSEN ELECTRODE PLACEMENT STRATEGIES

Electrode placement strategy no.	$R_{\Delta Z(t)\text{portion}}$ (%)
1	5.229
2	0.721
3	6.603
4	2.794
5	1.382
6	6.238
7	5.786
8	3.460

focusing property in front of four-electrode approach. Moreover, the proposed novel five-electrode FIM options provide comparably good and evidently better result to six-electrode FIM (Fig. 17). Outcome confirms that the measuring electrodes must remain disclosed by the area, induced by the exciting electrode pairs [option A of five-electrode FIM (Fig. 13)]. In this case the difference between the positive and negative sensitivities is the highest.

When considering the effect of concurrent movements ($R_{\Delta Z(t)\text{move}}$), which is expected to have major impact in the case of incorporation of electrodes into a wearable device, the best result is gained by using the electrode placement strategy 6 (Figs. 13 and 18). The calculated $R_{\Delta Z(t)\text{pulse}}$ in the case of two first five-electrode FIM strategies (Figs. 13 and 14) present here above the average result, while the result in the case of the strategy 8 (Fig. 15) already deteriorates. This confirms the expectation that the measuring electrodes in the case of five-electrode FIM must rest between a triangle of excitation electrodes to operate according to the focusing strategy.

The visualization of absolute values of measured $Z(t)$ (Fig. 18) reveals the sensitivity of chosen strategies to simultaneous movements of hand. Here the clear relationship between the number of electrodes in strategy and calculated $\Delta Z(t)_{\text{move}}$ can be noticed—if there are more electrodes than four, the sensitivity to simultaneous movements of hand increases. The same applies generally on $\Delta Z(t)_{\text{pulse}}$ as well.

In the case of $\Delta Z(t)_{\text{pulse}}$, the efficiency of the proposed five-electrode FIM is evident, while the result in the case of six-electrode FIM belongs among the three worst ones.

Strategy 3 provides top three result for motion artifact-resistance: when finding the percentage of $\Delta Z(t)_{\text{pulse}}$ from $\Delta Z(t)_{\text{move}}$ ($R_{\Delta Z(t)\text{portion}}$) (Table I) by using the simple equation

$$R_{\Delta Z(t)\text{portion}} = \frac{\Delta Z(t)_{\text{pulse}} \cdot 100}{Z(t)_{\text{move}}}. \quad (6)$$

The calculated $R_{\Delta Z(t)\text{portion}}$ reveals the comparable result of the classical distally placed four-electrode placement strategy (strategy 1). The result belongs to the top three of the artifact-resistant placements strategies. However, the proposed novel five-electrode FIM (options A and B) emerged to be the most suitable option for example for smart wearable device as [37].

The results of the practical measurement experiments are confirmed by the simulation models. Some deviations can be explained by the ideality and the static essence of the computer

simulation model when compared to real living and highly dynamic biological object.

The results of the performed measurement experiments are generally in line with the outcome of simulation. The most important concurrency is the generally above average result of the electrode placement strategy 6 (five-electrode FIM). Initially, this modified version of six-electrode FIM was expected to contribute to the development of instrumentation by reducing the number of needed electrodes. However, the result revealed the potential of focusing the highest sensitivity onto the interesting physiological variable—through the proposed five-electrode FIM.

VII. CONCLUSION

The present study investigated the effect of different electrode configurations with the goal of finding the ones that provide the best access to the cardiac activity of human. While the other experimented electrode placement strategies are known, and FIM is researched by using the proposed six-electrodes [38] and modified version of FIM by using five-electrode approach is novel. This method lies in the idea of combining one excitation electrode from both independent measurement channels, constituting a virtual ground. The other two exciting electrodes relative to common ground are forming a “barrier” around the two measuring electrodes that are placed distally on top of the radial artery. In principle, the round located excitation electrodes are expected to result as force in the positive sensitivity region to focus the excitation on the radial artery under the measuring electrodes.

The results of simulation and practical experimentation validated the assumption that the amount of change in the measured EBI signal, caused by the pulsating blood in arteries, is strongly affected by the chosen electrode placement strategy. The results of performed measurement experiments are generally in line with the outcome of simulations with some deviations. The proposed novel five-electrode FIM placement strategy was verified to provide the top two position in the case of motion artifact-resistance depending on the exact positioning of measuring electrodes relative to excitation electrodes. Though, based on the results of experimental measurements, the best determined electrode placement strategy is a simple rectangular placement of four-electrode EBI measuring setup, where the location of radial artery remains between the exciting and measuring pair.

REFERENCES

- [1] World Health Organization (WHO). *Cardiovascular Diseases (CVDs)*. Accessed: May 17, 2017. [Online]. Available: <https://www.who.int/news-room/fact-sheets/detail/cardiovascular-diseases-cvds>
- [2] K. Pesti, H. Koiv, and M. Min, “Simulation of the sensitivity distribution of four-electrode impedance sensing on radial artery,” in *Proc. IEEE Sensors Appl. Symp. (SAS)*, Mar. 2019, pp. 1–6, doi: [10.1109/SAS.2019.8705976](https://doi.org/10.1109/SAS.2019.8705976).
- [3] B. Freeman and J. Berger, “Invasive arterial blood pressure monitoring,” in *Anesthesiology Core Review: Part 2*. Beijing, China: McGraw-Hill, 2016, ch. 1.
- [4] C. M. McEniery, J. R. Cockcroft, M. J. Roman, S. S. Franklin, and I. B. Wilkinson, “Central blood pressure: Current evidence and clinical importance,” *Eur. Heart J.*, vol. 35, no. 26, pp. 1719–1725, Jul. 2014.

- [5] B. Lee, J. Kim, K. Chun, J. Jeong, and B. Kim, "Cantilever arrayed blood pressure sensor for arterial applanation tonometry," *IET Nanobiotechnol.*, vol. 8, no. 1, pp. 37–43, Mar. 2014.
- [6] E. Kaniusas *et al.*, "Method for continuous nondisturbing monitoring of blood pressure by magnetoelastic skin curvature sensor and ECG," *IEEE Sensors J.*, vol. 6, no. 3, pp. 819–828, Jun. 2006.
- [7] Y.-J. Wang, C.-H. Chen, C.-Y. Sue, W.-H. Lu, and Y.-H. Chiou, "Estimation of blood pressure in the radial artery using strain-based pulse wave and photoplethysmography sensors," *Micromachines*, vol. 9, no. 11, p. 556, Oct. 2018.
- [8] H. Lin, W. Xu, N. Guan, D. Ji, Y. Wei, and W. Yi, "Noninvasive and continuous blood pressure monitoring using wearable body sensor networks," *IEEE Intell. Syst.*, vol. 30, no. 6, pp. 38–48, Nov. 2015.
- [9] M. K. Chaithanya, K. V. K. Kishore, and A. Srinivasulu, "Continuous blood pressure measurement and data logging device with SMS alert," *Int. J. Multimedia Ubiquitous Eng.*, vol. 9, no. 8, pp. 25–38, Aug. 2014.
- [10] M. Raghunath, V. Kiran, and S. Aravapalli, "Design of Na optical blood pressure sensor for noninvasive monitoring of blood pressure," *Int. J. Sci. Eng. Adv. Technol.*, vol. 3, no. 2, pp. 1112–1117, 2015.
- [11] H. Kõiv, M. Rist, and M. Min, "Development of bioimpedance sensing device for wearable monitoring of the aortic blood pressure curve," *Technisches Messen*, vol. 85, no. 5, pp. 366–377, May 2018.
- [12] M. Min, P. Annus, H. Kõiv, A. Krivosei, T. Uuetoa, and J. Lamp, "Bioimpedance sensing—a viable alternative for tonometry in non-invasive assessment of central aortic pressure," in *Proc. IEEE Int. Symp. Med. Meas. Appl. (MeMeA)*, May 2017, pp. 373–378.
- [13] P. Augustyniak, "Separating cardiac and muscular ECG components using adaptive modelling in time-frequency domain," in *Proc. WACBE World Congr. Bioeng.*, 2007, pp. 1–4.
- [14] P. S. Hamilton and M. G. Curley, "Adaptive removal of motion artifact," in *Proc. IEEE 19th Annu. Conf. (EMBS)*, vol. 1, Nov. 1997, pp. 297–299.
- [15] B.-H. Ko *et al.*, "Motion artifact reduction in electrocardiogram using adaptive filtering based on half cell potential monitoring," in *Proc. Annu. Int. Conf. IEEE Eng. Med. Biol. Soc.*, Aug. 2012, pp. 1590–1593.
- [16] M.-C. Cho, J.-Y. Kim, and S. H. Cho, "A bio-impedance measurement system for portable monitoring of heart rate and pulse wave velocity using small body area," in *Proc. IEEE Int. Symp. Circuits Syst.*, May 2009, pp. 3106–3109.
- [17] S.-H. Liu, D.-C. Cheng, and C.-H. Su, "A cuffless blood pressure measurement based on the impedance plethysmography technique," *Sensors*, vol. 17, no. 5, p. 1176, 2017.
- [18] M. Metshein, "Wearable solutions for monitoring cardiorespiratory activity," Ph.D. dissertation, Thomas Johann Seebeck Dept. Electron., Tallinn Univ. Technology, Tallinn, Estonia, 2018.
- [19] T. Huynh, R. Jafari, and W.-Y. Chung, "An accurate bioimpedance measurement system for blood pressure monitoring," *Sensors*, vol. 18, no. 7, p. 2095, Jun. 2018.
- [20] K. S. Rabbani, M. Sarker, M. H. R. Akond, and T. Akter, "Focused impedance measurement (FIM): A new technique with improved zone localization," *Ann. New York Acad. Sci.*, vol. 873, no. 1, pp. 208–220, Apr. 1999.
- [21] F. J. Pettersen, H. Ferdous, H. Kalvøy, Ø. G. Martinsen, and J. O. Høgetveit, "Comparison of four different FIM configurations—A simulation study," *Physiol. Meas.*, vol. 35, no. 6, pp. 1067–1082, Jun. 2014.
- [22] S. P. Ahmed, M. A. Kadir, G. D. A. Quaderi, R. Rahman, and K. S. E. Rabbani, "Improved understanding of the sensitivity of linear tetrapolar impedance measurement (TPIM) and 8-Electrode focused impedance method (FIM) in a volume conductor," *Bangladesh J. Med. Phys.*, vol. 8, no. 1, pp. 22–31, Sep. 2017.
- [23] O. I. Shuvo and M. N. Islam, "Sensitivity analysis of the tetrapolar electrical impedance measurement systems using COMSOL multiphysics for the non-uniform and inhomogeneous medium," *Dhaka Univ. J. Sci.*, vol. 64, no. 1, pp. 7–13, Jun. 2016.
- [24] I. Jivet, "Wrist pulse monitoring by electrical impedance using a 3D model of the arm," in *Proc. ISETC*, Nov. 2014, pp. 1–4.
- [25] M. Moderhak, M. Madej, J. Wtorek, and B. Truyen, "Pulse pressure velocity measurement—A wearable sensor," in *Proc. Federated Conf. Comput. Sci. Inf. Syst. (FedCSIS)*, Szczecin, Poland, Sep. 2011, pp. 411–416.
- [26] M. Metshein, P. Annus, R. Land, M. Min, and A. Aabloo, "Availability and variations of cardiac activity in the case of measuring the bioimpedance of wrist," in *Proc. IEEE Int. Instrum. Meas. Technol. Conf. (I2MTC)*, May 2018, pp. 51–147.
- [27] C. Canali, "An impedance method for spatial sensing of 3D cell constructs—towards applications in tissue engineering," *Analyst*, vol. 140, pp. 6079–6088, 2015.
- [28] P. Kauppinen, J. Hyttinen, and J. Malmivuo, "Sensitivity distribution visualizations of impedance tomography measurement strategies," *Int. J. Bioelectromagn.*, vol. 8, no. 1, pp. 1–9, 2006.
- [29] (IMAIOS). *Arm, Forearm, and Hand: MRI of Anatomy*. Accessed: Dec. 10, 2018. [Online]. Available: <https://www.imaios.com/en/e-Anatomy/Limbs/Upper-extremity-MRI>
- [30] S. Gabriel, R. W. Lau, and C. Gabriel, "The dielectric properties of biological tissues: II. Measurements in the frequency range 10 Hz to 20 GHz," *Phys. Med. Biol.*, vol. 41, no. 11, p. 2252, 1996.
- [31] A. R. Ward, "Electrode coupling media for transcutaneous electrical nerve stimulation," *Austral. J. Physiotherapy*, vol. 30, no. 3, pp. 82–85, 1984.
- [32] *AC/DC Module User's Guide, COMSOL Multiphysics V. 5.3*, COMSOL AB, Stockholm, Sweden, 2019.
- [33] T. Palo, "Synchronous two-channel electric bioimpedance measurement system for detecting pulse wave from radial artery," B.Sc. thesis, Thomas Johann Seebeck Dept. Electron., Tallinn Univ. Technol., Tallinn, Estonia, 2019.
- [34] A. R. Abir and K. S. E. Rabbani, "Sensitivity study for a 4-electrode focused impedance method (FIM) using finite element method analysis," *Bangladesh J. Med. Phys.*, vol. 7, no. 1, pp. 1–7, Oct. 2015.
- [35] J. Xu *et al.*, "Wrist-worn heartbeat monitoring system based on bio-impedance analysis," in *Proc. 38th Annu. Int. Conf. IEEE Eng. Med. Biol. Soc. (EMBC)*, Aug. 2016, pp. 6294–6299.
- [36] R. P. Patterson, "Impedance cardiography: What is the source of the signal?" *J. Phys., Conf. Ser.*, vol. 224, Apr. 2010, Art. no. 012118.
- [37] M. Metshein, H. Kõiv, P. Annus, and M. Min, "Electrode optimization for bioimpedance based central aortic blood pressure estimation," in *Proc. World Congr. Med. Phys. Biomed. Eng. (IFMBE)*, vol. 68/2, L. Lhotska, L. Sukupova, I. Lacković, and G. Ibbott, Eds. Singapore: Springer, 2019, doi: 10.1007/978-981-10-9038-7_92.
- [38] K. S. Rabbani, "Focused impedance method (FIM) and pigeon hole imaging (PHI) as two potentially low cost and simple modalities for different diagnostic applications," in *Proc. 7th Int. Conf. Appropriate Healthcare Technol. Developing Countries*, London, U.K., 2012, p. 12.



K. Pesti was born in Kunda, Estonia, in 1985. She received the B.S. degree in electronics and bionics and the M.Sc. degree in electronics and biomedical engineering from TalTech, Tallinn, Estonia, in 2006 and 2009, respectively, where she is currently pursuing the Ph.D. degree with the Thomas Johann Seebeck Department of Electronics.

Her current research interests are covering the fields of bioimpedance measurement, biomedical sensors, and simulation toward the medical sensor solutions.



M. Metshein was born in Kuressaare, Estonia, in 1983. He received the B.S and M.S degrees in electronics and bionics and the Ph.D. degree in information and communication technology from the Tallinn University of Technology (TUT), Tallinn, Estonia, in 2006, 2010, and 2018, respectively.

From 2016 to 2018, he was an Early Stage Researcher with Thomas Johann Seebeck Department, TUT. In 2018, he joined the Mud Products Development Laboratory Expert-Specialist, Centre of Excellence in Health Promotion and Rehabilitation, Haapsalu College of Tallinn University, Haapsalu, Estonia. Since 2019, he has been a Research Scientist with the Thomas Johann Seebeck Department of Electronics, TUT. He has authored more than 15 articles and one invention. His research interests are covering the fields of bioimpedance measurement, biomedical signal acquisition, and related instrumentation toward the medical sensor solutions.

Dr. Metshein was a recipient of the IEEE I2MTC2020 International Instrumentation and Measurement Technology Conference Best Paper Award in 2020.



P. Annus (Member, IEEE) was born in Tallinn, Estonia, in 1962. He received the diploma engineer's degree in electrical engineering from BME, Budapest, Hungary, in 1987, and the Ph.D. degree in electronics from the Tallinn University of Technology (TUT), Tallinn, in 2010.

He is currently a Senior Research Scientist and a Lecturer with the Thomas Johann Seebeck Department of Electronics, TUT. He has authored or coauthored more than 100 publications and ten inventions. His interests are related to bioelectromagnetism and embeddable sensorics.



H. Kõiv was born in Kanepi, Estonia, in 1990. She received the B.S. degree in electronics and bionics and the M.S. degree in electronics and communication from the Tallinn University of Technology (TalTech), Tallinn, Estonia, in 2013 and 2015, respectively, where she is currently pursuing the Ph.D. degree with the Thomas Johann Seebeck Department of Electronics.

Her current research interests include the bioimpedance study, aortic blood pressure measurements, and the materials for developing biological phantoms.



M. Min (Life Senior Member, IEEE) received the diploma engineer's degree in electronics and the Ph.D. degree in measurement science from Kiev Polytechnic, Kiev, Ukraine, in 1984.

He has been a Full Professor and a Leading Scientist with the Thomas Johann Seebeck Department of Electronics, Tallinn University of Technology, Tallinn, Estonia, since 1992. From 1992 to 1993, he was a Scientist and a Guest Professor with Technical University and Bundeswehr University, Munich, Germany. From 2007 to 2010, he was with the

Institute of Bioprocessing and Analytical Measurement Technique, Heilbad Heiligenstadt, Germany. He has authored more than 200 articles and holds 40 patents. He is interested in measurement and signal processing with implementations in medical industry, including developing of pacemakers for the companies St. Jude Medical/Abbot (USA/Sweden) and Guidant/Boston Scientific (USA).

Dr. Min is with the both Instrumentation and Measurement Society and Engineering in Medicine and Biology Society. He is a member of the International Committee for Promotion of Research in Bio-Impedance (ICPRBI) and a Professor Emeritus since 2016.

Publication IV

Metshein, Margus; Pesti, Ksenija; Min, Mart, Annus. Paul; Märtens, Olev (2020). Feasibility of Utilizing Air Gapped Toroidal Magnetic Cores for Detecting Pulse Wave in Radial Artery. 2020 17th Biennial Baltic Electronics Conference (BEC), Tallinn, Estonia, IEEE, 1–5.

Feasibility of Utilizing Air Gapped Toroidal Magnetic Cores for Detecting Pulse Wave in Radial Artery

Margus Metshein, Ksenija Pesti, Mart Min, Paul Annus, Olev Märtens
Thomas Johann Seebeck Department of Electronics
Tallinn University of Technology
Tallinn, Estonia
margus.metshein@taltech.ee

Abstract—The feasibility study of utilization of air gapped toroidal magnetic cores for monitoring changing volume of pulsating blood in artery is shown in this paper. The changing impedance of conductive path of blood is represented by a single solid core copper wire, connected to a closed circuit with potentiometer. Commercially available toroidal magnetic cores with two different shapes of custom implemented air gaps and desired number of windings were used to induce current in copper wire. The theoretical expectation of the possibility to focus most of the reluctance of emerging magnetic field into the air gap was experimented. The location of conductive path relative to the implemented air gap was determined to be critical and the best outcome was gained when the copper wire was passing through the center of toroidal core instead of the gap itself. Also, the shape of the air gap was determined to acquire important role related to the location of the conductive path – as the flux fringing is appearing not to significantly affect the magnitude of induced current. The potentiality of monitoring pulse wave by positioning the air gap of toroidal core noninvasively onto the location of radial artery in forearm was concluded not to be feasible with the used setup. The results of on-desk measurements were validated with finite element method simulation of magnetic flux density distribution.

Keywords—air gap, flux fringing, magnetic induction sensing, toroidal magnetic core, magnetic flux density.

I. INTRODUCTION

Monitoring the circulatory system parameters of a man is of high interest, especially in the light of World Health Organization data, where the cardiovascular diseases (CVDs) are reported to be the no. 1 cause of deaths globally [1]. The changing nature of physical work to operate machines with computers fosters the sedentary lifestyle despite the continuous information of its health risks. The sedentary lifestyle, among others, is one of the reasons of overweight and obesity, having direct causing effect on the raised blood pressure and, due to that, emergence of CVDs. The effect of CVDs can be alleviated with daily monitoring of circulatory system and effective medical care in primary care facilities.

To evaluate the condition of circulatory system, novel means and methods are needed in both modalities: personal everyday health monitoring and clinical apparatus in primary care facilities. The development of devices for determination of variations in circulatory system parameters is key topic in providing means for preventing and treating CVDs. However, the interest of gaining more elaborated data by finding correlations with known parameters (blood pressure, pulse rate etc.) and data provided by emerging solutions, is actual.

For estimating the central aortic pressure (CAP) of blood, the measuring of electrical bioimpedance (EBI) of forearm has

been reported as promising solution [2]. EBI measurement is suitable method for determining volume changes in biological organisms as it comprises variety of data in its complex essence and is already in clinical validation [2]. Currently the effort has been put on developing approaches based on the principles of focused impedance measurements [3] and on studying the effect of applying external pressure on artery [4].

Besides EBI, other solutions such as electrocardiography (ECG), photoplethysmography (PPG), ballistocardiography etc. are known for decades for detecting heart rate and finding, for example, the pulse wave velocity. However, motion artifact, which is not a problem in the case of a patients in coma, appears immediately when the object starts to move.

A solution may lie in magnetic induction sensing which is a known method for detecting material imperfections and the proximity of objects but also flow of conductive matter in tube. For example, the usage of giant magnetic resistance sensors which principle relies on the effect where electrical resistance of ferro- and non-magnetic materials vary when placed into magnetic field [5]. Also, coils can be used to determine pulse wave by causing the electromagnetic field to induce eddy currents in artery and detecting the emerging secondary alternating electromagnetic field [6].

Blood flow can be monitored by using electromagnetic flow meters, relying on the conductive properties of blood. In the case of such flow meter, blood is considered as a conductor which is excited externally by using alternating electromagnetic field while the responsive voltage is measured with electrodes in direct contact. Such monitoring is done during the surgery when the sensor is attached around the exposed artery after the anesthetization [7,8].

The usage of such flow meters assumes the placement of toroid around the interesting matter, which in the case of forearm is its whole composition with its ever-moving tendons and contracting muscles. This has large effect on conductivity, burying the desired signal of pulse. Motion artifact is expected to be a key problem also in air gapped toroidal magnetic cores-based solutions as tolerates no shift relative to artery.

Similar approach has been used in [9], where the evaluation of electrical properties of liquids has been implemented by using a pair of toroidal magnetic cores – one for excitation and second for measuring. However, the cores are not air gapped and surrounded by liquid, i.e. the induced current has possibility find its path of flow freely, not in single wire or complex composition of forearm.

In current paper, the research on possible usage of commercially available toroidal magnetic cores of different configurations for monitoring the pulse wave in radial artery

is presented. The results of performed laboratory on-desk experiments on copper wire are introduced. With the goal of verifying the practical measurements, the simulations in Comsol Multiphysics were implemented by using the finite element method (FEM) on the models of toroidal magnetic cores of comparable dimensions and magnetic properties.

The novelty of current paper stands in the utilization of commercially available toroidal cores with implemented gap, where, according to the theory, the reluctance of emerging magnetic field is expected to be focused. By placing the pulsating volume of blood in largest contribution of reluctance, its effect on magnetic field can be expected to be the largest. The simulation models reveal the best possible location of radial artery relative to the gap. The focusing of the gap of toroidal core noninvasively on radial artery in forearm expectedly grants the access to the signal of pulse wave.

II. METHOD

The proposed magnetic induction sensing technique incorporates the utilization of toroidal magnetic cores. The interesting property of toroidal magnetic cores is that the strength of magnetic field flux density B (T) is focused inside the core and is close to zero outside the core, given by:

$$B = \frac{\mu_0 N I}{2\pi R}, \quad (1)$$

where μ_0 is the absolute magnetic permeability of a vacuum (H / m), N is the number of windings of wire around the toroidal magnetic core, I is the current in the wire (A) and R is the radius of the toroidal core (m). Magnetic flux Φ inside the toroidal core can be stated as:

$$\Phi = BS = \frac{\mu_0 I N A_{core}}{l}, \quad (2)$$

where S is the area of the surface (m²) and l is the average length of the coil wire (m).

The approach bases on the idea, known already more than 75 years [7] – the mounting of toroidal magnetic core around the blood vessel with the goal of measuring the blood flow by using the knowledge from Faraday's Law of Electromagnetic Induction. It is shown that the magnetic field inside the toroidal magnetic core is not uniform, varying inversely with the distance r from the central axis of the toroidal core.

The approach relies on the fact that most of the reluctance in magnetic field of toroidal core, and, thereby also the energy, is expected to be possible to focus on restrained volume by implementing an air gap. The expectation is that when placing the air gap on top of the location of radial artery in wrist, the contribution of pulsating blood to emerging magnetic field is enough to induce modulated alternating signal (current) in the coil. Air gap can be designed in variety of shapes, also considering the possible effect of flux fringing that can be expected to cause the magnetic flux to spread into radial artery even more. Flux fringing is phenomena, where, due to the increased reluctance, the magnetic flux in magnetic core spreads out in air in the vicinity of air gap. For assessing the effect of emerging flux fringing, the fringing flux factor F_{FF} can be calculated based on:

$$F_{FF} = 1 + \frac{l_{gap}}{\sqrt{A_{core}}} \ln \left(\frac{2W}{l_{gap}} \right), \quad (3)$$

where l_{gap} is length of the gap (m), A_{core} is cross-section area of the core (m²) and d is the inner diameter of the core (m). The expectation is that the flux fringing effect can be used for

excitation, when modifying the air gap accordingly with the goal of targeting it to the location of radial artery.

The choice of the magnetic core material was dictated by the desire of gaining the highest possible magnetic field strength – the higher the permeability μ of the material the stronger the induced magnetic field. For the experiments, the epoxy coated manganese-zinc (MnZn) ferrite (T38) toroidal core of type B64290L0038X038 TDK (Tokyo, Japan) was chosen, possessing the μ of 10000. Outer diameter of the core is 10 mm, inner diameter is 6 mm, and height is 4 mm.

The proposed method relies on the idea that the blood (which conductivity is reported to be 0.703 S/m at the frequency of 100 kHz [12]) is a relatively good electrical conductor and can carry flow of electric current. In focusing on the non-invasive domain, one cannot wound artery around the core, instead the number of windings of the wire should be suitable enough to force enough current into the blood. The relationship between the number of windings (n), current and voltage can be presented by the following equation:

$$n = \frac{N_1}{N_2} = \frac{U_1}{U_2} = \frac{I_2}{I_1}, \quad (4)$$

where N_1 and N_2 are the number of windings in primary coil and secondary coils respectively, U_1 and U_2 are voltages on primary and secondary coils respectively, I_1 and I_2 are currents in primary and secondary coil, respectively. One can realize that by increasing the N_1 , the I_2 can be increased together with the density of magnetic flux. This is the reason of using the highest possible number of windings on the toroidal cores in the consequent experimentation.

III. MEASUREMENT SETUP AND USED DEVICES

Three configurations of toroidal cores were prepared for the experimentation: without air gap (Fig. 1a); with 180° cut air gap (width of 1.2 mm) (Fig. 1b); with 0° cut air gap (width of 4 mm) (Fig. 1c).

Varnished copper wire (with the solid core diameter of 0.4 mm) was wound circularly on each toroidal core with the number of 50 turns. Varnish performs the wire to have dielectric coating so that it does not cause short circuits when wound onto the toroidal core. The measured electrical parameters of the wound coils at excitation signals of 100 mV and 10 V in the case of 100 kHz can be seen in Table I.

Experiments were performed in the case of single insulated solid core copper wire (core diameter of 0.5 mm, insulation thickness of 0.2 mm) that constitutes conductive path. The conductive path, representing blood in radial artery

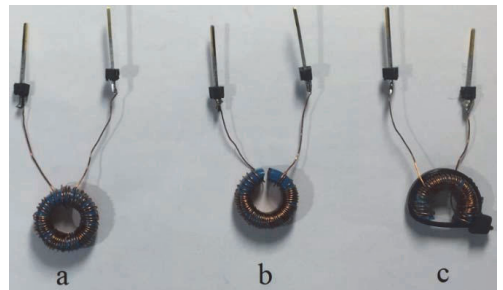


Fig. 1. Configurations of toroidal cores that were used in the experiments: (a) without air gap; (b) with straight (with the angle of 180°) cut air gap; (c) with horizontally (with the angle of 0°) cut air gap.

TABLE I. MEASURED ELECTRICAL PARAMETERS OF THE COILS WINDING ($N = 50$) ON THE SELECTED SETUPS OF TOROIDAL CORES

Toroidal core	Z at 100 mV (Ω)	L at 100 mV (mH)	Z at 10 V (Ω)	L at 10 V (mH)
a	7371	11.15	1657	2.475
b	65.0	0.103	80.1	0.128
c	30.9	0.049	34.4	0.044

constituted a closed loop, containing resistors with values of 10Ω (R_2 in Fig. 2) and 1Ω (R_3 in Fig. 2) and 100Ω valued potentiometer (TR in Fig. 2) in series with the copper wire. The choice of the sum of resistances was guided by the desire of representing the impedance of skin in the case of noninvasive monitoring. The choice of copper wire to imitate blood in artery is explained by the desire to utilize a rough electronic components-based solution, which resistance can be changed manually with a potentiometer. In literature, however, pulsating flow of saline solution, imitating pulse wave [4, 10, 11], either in rigid [10] and flexible [4] tubes have been used to study the properties of blood flow, but typically not for evaluating inductive sensors.

The coil was excited with sine wave signal of amplitude of $140 V_{pp}$ and frequency of 100 kHz , which was converted to alternating current with $100 \text{ k}\Omega$ resistor (R_1 in Fig. 2). The voltage amplitude was measured by using the oscilloscope of type DSO8104A of Keysight Technologies (Santa Rosa, CA, US).

IV. MEASUREMENT RESULTS

The results of measurements by using toroidal cores of different configurations to determine the changing impedance of electronic circuit with copper wire are presented subsequently. The ability of chosen toroidal core configurations to induce current in copper wire was evaluated. The copper wire was placed in three positions relative to toroidal core and air gap.

1. Copper wire placed in the center of the core.
2. Copper wire placed in the center of the air gap.
3. Copper wire placed outside of the toroidal core about 1 mm above the gap.

The voltage amplitude was measured on resistor R_2 in closed circuit with copper wire (V_1 in Fig. 2). Two measurements were performed with the goal of determining the effect of varying resistance of potentiometer (TR in Fig. 2) into both extremes (0Ω and 100Ω) onto the amplitude of detected sine wave. The amplitude of the measured voltage was detected and compared. The results can be seen in Table II.

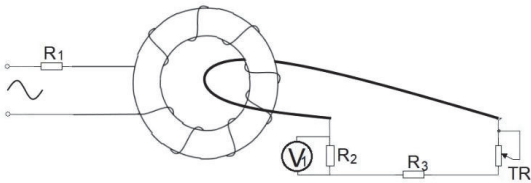


Fig. 2. Measurement configuration in the experiments where the imitation of conductive path of blood is represented by single insulated copper wire.

TABLE II. MEASURED VOLTAGE AMPLITUDES IN THE CASE OF IMITATING THE CONDUCTIVE PATH OF BLOOD IN RADIAL ARTERY WITH COPPER WIRE BY USING DIFFERENT TOROIDAL CORE CONFIGURATIONS

Setup no.	Air gap	Toroidal core configuration	ΔV_{ppV1} (OR $\rightarrow 100R$) (mV)
A1	Uncut	Center of toroidal core	273.40
B1	Cut 180°	Center of toroidal core	2.4
B2	Cut 180°	Center of air gap	1.73
B3	Cut 180°	Outside of air gap	0.68
C1	Cut 0°	Center of toroidal core	0.58
C2	Cut 0°	Center of air gap	0.04
C3	Cut 0°	Outside of air gap	0.01

V. SIMULATION OF MAGNETIC FLUX DENSITY IN THE CASES OF DIFFERENT GAPS IN TOROIDAL MAGNETIC CORES

To validate the results of measurements in the case of imitating blood in radial artery with copper wire, FEM simulations of magnetic flux density distribution were performed. The geometries of toroidal cores were implemented and simulations performed in COMSOL Multiphysics (version 5.3a) Magnetic Field physics under AC/DC section. The dimensions and magnetic properties of the composed toroidal cores were the same in both modalities.

The simulations were performed by using identical setups, i.e. the locations of wire that represent the conductive path of blood relative to toroidal core were the same. The voltage, induced by the emerging flux of magnetic field, applying onto the wire, was calculated, and compared (Table III).

The placing of radial artery, which lies underneath the skin, inside the air gap, is not feasible in noninvasive utilization of the proposed approach. In best case and small thickness of body fat layer, the air gap can be placed only in close vicinity of radial artery. However, the visual representation of emergence of magnetic flux density distribution in FEM model (Fig. 4-8) is shown for all the setups with the implemented air gap. In the case of simulation results, the setup without air gap is not shown.

TABLE III. DETECTED VOLTAGES IN COPPER WIRE IN SIMULATION MODEL IN THE CASES OF DIFFERENT TOROIDAL CORE CONFIGURATIONS

Setup no.	Air gap	Toroidal core configuration	V_{sim} (V)
A1	Uncut	Center of toroidal core	2.40
B1	Cut 180°	Center of toroidal core	2.03
B2	Cut 180°	Center of air gap	0.93
B3	Cut 180°	Outside of air gap	0.19
C1	Cut 0°	Center of toroidal core	0.73
C2	Cut 0°	Center of air gap	0.7
C3	Cut 0°	Outside of air gap	0.54

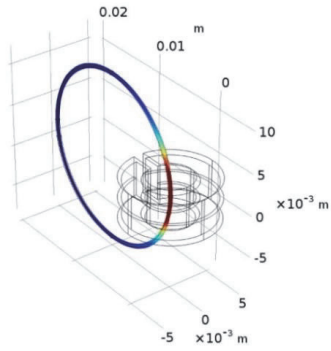


Fig. 3. Simulation result of magnetic flux density in copper wire in the case of setup B1.

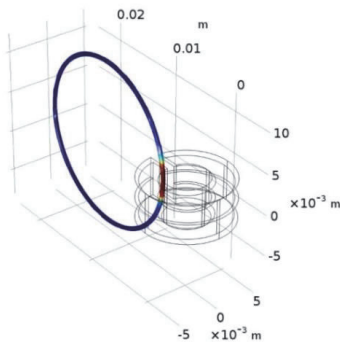


Fig. 4. Simulation result of magnetic flux density in copper wire in the case of setup B2.

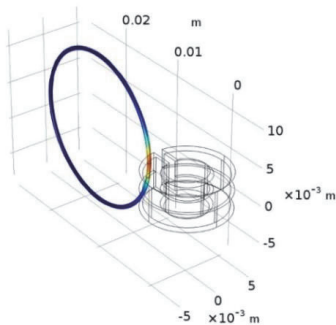


Fig. 5. Simulation result of magnetic flux density in copper wire in the case of setup B3.

VI. DISCUSSION

Results show the decrease of strength of the induced magnetic field inside the exciting toroidal magnetic core when air gap is presented. In the case of utilization of air gapped toroid for excitation, the induced current in copper wire for both extremes of TR remain below 1 mA. In the case of toroidal core without air gap, the induced current in closed circuit with copper wire for the value of 0Ω of TR comprises about 10 mA and is about 10 times smaller at 100Ω .

This is a noticeable difference that gives notion that the utilization of toroidal core with air gap for excitation, by using currently selected configuration does not provide reproducible

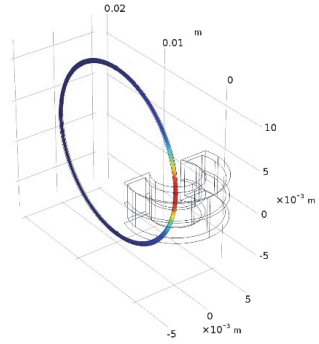


Fig. 6. Simulation result of magnetic flux density in copper wire in the case of setup C1.

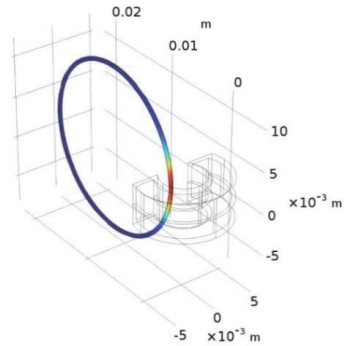


Fig. 7. Simulation result of magnetic flux density in copper wire in the case of setup C2.

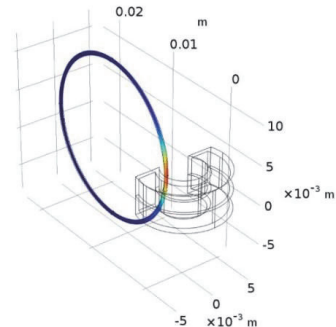


Fig. 8. Simulation result of magnetic flux density in copper wire in the case of setup C3.

results. The validating experiments with toroidal cores of higher value of μ are needed as the introduction of more windings increases the unnecessary robustness of the device. This is probably a reason, why also in existing solutions the excitation is done by using toroidal cores without air gaps [8].

As known, most expensive part of a toroidal core is the air gap – the narrower it is, the higher the reluctance in the gap. In this sense, the produced gaps in used toroidal cores are, due to technological reasons, relatively large. However, when considering the diameter of the radial artery which is reported for right forearm to be 2.09 mm (± 0.35 mm) [13] and the desire to set the artery near (and hopefully partially inside) the gap, the 1.2 mm gap is not too large.

One can see that the results of simulation in the case of toroidal core without air gap is more than 100 times lower than in the case of on-desk measurements. The difference comes from the implementation of custom geometry of toroidal core and its application in Comsol Multiphysics simulations.

The idea of modifying the shape of gap shows that the 180° cut (B1-3) provides the induction of highest current in the copper wire that imitates blood in artery. The 0° cut (C1-3) shows the decrease in induced current in all three locations of copper wire of closed circuit about three times. The outcome reveals that the expectation of focusing the reluctance of magnetic field into the air gap of toroidal core does not result as highest value of induced current in copper wire. In the case of excitation coil setup B1, the emerging voltage amplitude is almost 1.5 times higher than for the setup B2, where the wire passes through the air gap. The location of wire outside of the air gap lowers the measured signal amplitude already significantly.

The setups of toroidal cores with 0° cut air gap (C1-3) demonstrates even worse results. The expected emergence of fringing flux does not contribute to magnetic flux density for inducing desired value of current. So, the original idea of placing the cut side of the toroidal magnetic core setup C on top of the location of radial artery on the surface of skin with the goal of inducing current in relatively good conductive blood, will not result as enough magnitude of emerging voltage. A possibility could be the placement of toroidal core setup C along the location of radial artery to increase the presence of blood in vicinity, however, the influence is expectedly low.

The results of simulation of the same setup confirm the outcome of on-desk measurements. The fall into the same range of measured V_{sim} of setup A1 to setup B1 in simulation model can be explained by the properties of model. It must be noticed that the experiment in simulation model does not mimic fully the performed on-desk measurements. In practical measurements, the change of voltage on copper wire (and respective electronic circuitry (Fig. 2)) between the two chosen resistance values of potentiometer is determined and presented. While in simulation model, the emerging static voltage on copper wire is determined and presented. However, the results in both cases are comparable in magnitude, being a direct reflection of the density of induced magnetic flux.

When considering the proposed method for noninvasive detection of pulsating blood flow in radial artery, only the setups with air gaps suit. Even in very optimistic approach, the pressing of radial artery into the air gap is not feasible. So, realistically, only the setups B3 and C3 can be used in such wearable device. However, the results of measurements and simulation show the worst possible outcome.

CONCLUSIONS

The study of using toroidal magnetic cores for determining variable impedance of copper wire with electronic circuitry was implemented with the goal of assessing the possibility of the method for detecting pulse wave in radial artery.

Results showed the capability of the magnetic core without air gap of inducing a larger current in copper wire than all the toroidal cores with variety of air gaps and setups. Expectation of focusing the reluctance of emerging magnetic field into air gap and, throughout, inducing higher currents in conductive matter in it, resulted negatively. The best result in the case of

the air gapped toroidal core was achieved, when placing the copper wire through the center of the core.

The presented theoretical work and performed preliminary experimentation by using copper wire was expected to provide input for implementing a solution the monitoring of pulse wave in radial artery. The utilization of large toroidal core around forearm could be considered. It is expected that some amount of change in magnetic field is contributed also by the pulsating amount of blood in artery. By using either the non-invasive electrodes on top of the radial artery or second magnetic core, the induced current will be picked up, expectedly modulated by the pulsating blood. Through the frames of non-invasive monitoring, the placement of specially designed toroidal core in the composition of wearable device around the wrist is forming an acceptable solution.

ACKNOWLEDGMENT

This research has been supported by Estonian Centre of Excellence in ICT Research EXCITE (TAR16013) and Mobilitas+ grant Mobera20 for Chist-era JEDAI project, supported by EU Regional Development Fund. Support have also been gained from European project H2020 Flag-ERA JTC 2016 CONVERGENCE and EAG34 grant of Estonian Research Council.

REFERENCES

- [1] "Global Hearts Initiative Infographic (Flyer)." [Online]. Available: http://www.who.int/cardiovascular_diseases/globalhearts/HEARTS_Infographic_rev1.pdf?ua=1.
- [2] M. Min, P. Annus, H. Kõiv, A. Krivošei, T. Uuetoa, and J. Lamp, "Bioimpedance sensing – a viable alternative for tonometry in noninvasive assessment of central aortic pressure," IEEE Int. Symp. on Med. Meas. and Appl. (MeMeA), pp. 373-8, May 2017.
- [3] K. Pesti, M. Metshein, P. Annus, H. Kõiv, and M. Min, "Electrode placement strategies for the measurement of radial artery bioimpedance: Simulations and experiments," IEEE Trans. Instrum. Meas., to be published.
- [4] M. Metshein, P. Annus, R. Land, M. Rist, M. Min, and O. Märtnens, "Correlation between electrical bioimpedance and pressure waveform in radial artery and in mechanical pulsating pipe system," in Proc. 2020 IEEE I2MTC, Dubrovnik, Croatia, pp. 1-6, May 2020.
- [5] C. T. Phua, "Novel method of blood pulse and flow measurement using the disturbance created by blood flowing through a localized magnetic field," PhD Thesis, Université Paris-Est, France, 2012.
- [6] D. Teichmann, J. Foussier, D. Löschecke, S. Leonhardt, and M. Walter, "MonitoRing – magnetic induction measurement at your fingertip," J. Phys.: Conf. Ser. 434 012084, pp. 1-4, April 2013.
- [7] A. Kolin, "An electromagnetic flowmeter: principle of method and its application to blood flow measurements," Proc. Soc. Exper. Biol. and Med. Vol. 35, Iss. 1, pp. 53-6, Oct. 1936.
- [8] J. D. Folts, "The electromagnetic flowmeter and its use in the operating room," J. of ExtraCorporeal Technology, Vol. 6, 1974, pp. 127-36.
- [9] H. Wakamatsu, "A Dielectric spectrometer for liquid using the electromagnetic induction method", Hewlett-Packard Journal, Vol. 48, No. 4, 2017, pp. 37-44.
- [10] R. L. Gaw, B. H. Cornish, and B. J. Thomas, "Time frequency analysis of the experimental electrical impedance of pulsatile blood flowing through rigid tubes," IFMBE Proc., vol. 25/7, pp. 255-8, Sept. 2009.
- [11] T. Xie, S. C. Tjin, Q. Yang, and S. L. Ng, "Effect of blood's velocity on blood resistivity," IEEE Trans. Instrum. Meas. vol. 47, issue. 5, pp. 1197-200, Oct. 1998.
- [12] D. Andreuccetti, R. Fossi, and C. Petrucci, "An internet resource for the calculation of the dielectric properties of body tissues in the frequency range 10 Hz - 100 GHz," [(accessed on 6 May 2020)]; Available online: <http://niremf.ifac.cnr.it/tissprop/>.
- [13] E. Shao, H. Vaghadia, N. Ramsay, R. Tang, and A. Sawka, "Evaluation of two novel techniques for increasing radial artery size: a pilot study utilizing volunteers," Canadian J. Anesth/J Can Anesth, Vol. 64, Iss. 7, 2017, pp. 786-787.

Publication V

Priidel, Eiko; Pesti, Ksenija; Min, Mart; Ojarand, Jaan; Märtnens, Olev (2021). FPGA-based 16-bit 20MHz device for the inductive measurement of electrical bio-impedance. International Instrumentation and Measurement Technology Conference (IEEE I2MTC2021), Glasgow, Scotland, May 17-20, 2021 (accepted for publication), 1–5.

FPGA-based 16-bit 20 MHz device for the inductive measurement of electrical bio-impedance

Eiko Priidel, Ksenija Pesti, Mart Min, *Life Senior Member, IEEE*,
Jaan Ojarand, *Senior Member, IEEE*, Olev Martens, *Senior Member, IEEE*
T J Seebeck Department of Electronics
Tallinn University of Technology,
Ehitajate tee 5, Tallinn, 19086, Estonia
Email: eiko.priidel@taltech.ee

Abstract—A novel FPGA based 16-bit 20 MHz real-time electrical impedance measurement device has been developed. While such device can have several applications, then one of the purposes is to measure and monitor the human cardio-respiratory activity signals by inductive magnetic induction based coupling, where a fine resolution in relatively high frequency range is needed. As such a small form-factor device with affordable price and low power consumption is not commercially available, for wearable personal healthcare, the first prototype of such instrumentation device was developed. The solution uses the Altera Max10 FPGA and the external fast operating 16-bit analog-to-digital and digital-to-analog converters (ADC and DAC) with complementary analog components for signal generation, conditioning and handling. The WiFi data communication is based on a separate ESP8285 chip. The overall solution was tested in the frequency range of analog signals up to 20 MHz, getting 4000 measurement results during every second, what is certainly enough for the real-time presenting of impedance waveforms of such physiological processes as breathing and heart beating.

I. INTRODUCTION

Electrical impedance characterizes the properties of different materials, structures and processes as composition of metals, structures of materials, electro-chemical reactions as corrosion etc. [1]. Electrical bio-impedance (EBI) is the electrical impedance of biological matter, describing living biological materials (cells, tissues, organs) and such the physiological processes as breathing, heart beating, flowing of blood and tissue oxygenation. In summary, electrical bio-impedance allows to measure and analyze the cardiopulmonary and vascular dynamics, which are the most necessary physiological processes for medical diagnosing of human health [2]. To avoid serious electrode problems and reduce artefacts, the non-contact sensing methods are of interest [3] by using both capacitive and inductive coupling.

An important application of the impedance is monitoring of the hemodynamics of the person. One specific application could be impedance cardiography (ICG[4]), but more generally, monitoring of cardiac and respiratory data [5].

Impedance of the chest and head can be measured not only by electrically conductive electrodes placed on the body,

but also by using inductive (magnetic induction) coupling [6], enabling not only cardiovascular but also respiratory monitoring [7]. For inductive sensing, it is preferable to use higher frequencies (e.g. 10 MHz instead of 100 kHz) because human tissues and blood have low electrical conductivity in comparison with metals, for example, therefore the higher frequencies can give a more reasonable penetration depth of the generated electromagnetic field in the body. The similar problems arise in inductive measurements of metal structures [8] if we need to sense very thin layers (coatings, detection of corrosion etc.). High frequency measurements are similarly preferable in many other cases and the developed instrumentation given in Fig. 1 is required more widely than in the bio-impedance measurement cases described above.

A. Existing solutions for impedance measurement

Well-known are the impedance measurement solutions based on using the single-chip integrated circuit AD5933 of Analog Devices Inc [9]. Such the solutions have both limited bandwidth (100 kHz) and also limited resolution because of only 12-bit analog-to-digital converter (ADC) in the input of it digital processing part. Though some DSP-based solutions for multifrequency impedance measurement devices have been developed [10], [11] in participation of authors of the present paper, these are not suitable for wearable devices by size, resolution, frequency range and cost limitations. There exist also high-resolution inductive impedance converter chips [12] of Texas Instruments, which can be considered for some applications, but their frequency instabilities (due to analog self-oscillating LC-generator inside) make them impossible for using for precise measurements. Several bulky desktop impedance analyzers are available from Wayne Kerr [13] and Agilent and similar, for example, which are not applicable due to their cost and size, but mostly because of inability for real-time measurements.

II. PROPOSED SOLUTION

The block diagram in Fig. 1 depicts the proposed solution based on using the digital signal processing and synthesis

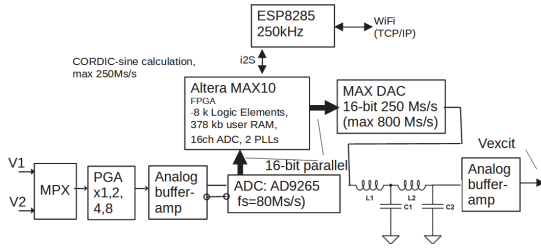


Fig. 1. Block diagram of the proposed solution

by the aid of field programmable gate array (FPGA) Altera MAX10. Analog signals are digitized by the aid of the 16-bit analog-to-digital converter (ADC) AD9265 from Analog Devices, and generated (synthesized) by using the 16-bit digital-to-analog converter MAX DAC. Input and output analog interfaces contain amplifiers, filters and a multiplexor at the input. A special integrated circuit ESP (8226) serves for wireless data communication (WiFi) with a standard computer.

A. Key components

The device includes the following electronic components:

- FPGA - Altera MAX 10 (*MAX10M16SAU169*), featured by the dual configuration flash memory, analog blocks (not used in the current project), DSP-blocks (including 18x18 bit multipliers), complex control management, single-core voltage support, user flash memory;
- Analog-to-digital converter (ADC) - AD 9265, featured by 16-Bit resolution, up to 125 MSPS sample-rate (utilized at 80 Ms/s in the current project);
- MUX: AD8184 (*700 MHz, 5 mA 4-to-1 Video Multiplexer*);
- PGA: THS7001 (*70-MHz High-Speed Programmable-Gain Amplifier, with max gain 20 dB*);
- AD8130, an ADC input driver buffer (*Low Cost 270 MHz Differential Receiver Amplifier*);
- Digital-to-analog converter (DAC): MAX5891, 16-Bit resolution, up to 600 MSPS sample-rate (utilized at 80 Ms/s in the current project);
- THS3215, DAC output driver buffer (*DC to 650-MHz, Differential-to-Single-Ended, DAC Output Amplifier*);
- The ESP8285 is a low-cost Wi-Fi microchip, with a full TCP/IP stack.

The ADC and DAC are connected to the FPGA by separate synchronous parallel 16-bit buses, giving the 80Ms/s data rates. The ESP8285 chip connected to the main FPGA by the I²S bus.

B. Algorithms used

Generation of sine/cosine waves (as excitation signal and as reference waveforms) for the Discrete Fourier Transform (DFT) is done by using of the CORDIC algorithm (COordinate

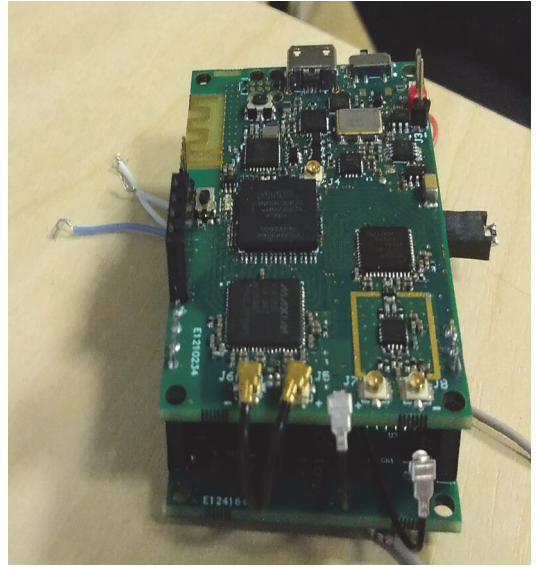


Fig. 2. Photo of the prototyped device

Rotation Digital Computer), known also as Volder's or "shift-and-add" algorithm [14].

C. Overall algorithm description

The overall impedance measurement consists of the following steps:

- The FPGA generates the excitation sinewave 2 V peak-to-peak amplitude and frequency from 100 kHz to 20 MHz;
- The excitation signal passes the circuit of series connected resistor $R=1K\Omega$ and unknown complex impedance $\tilde{Z}x$;
- Beside the sine wave, the chirp waveform signals can be synthesized for both, excitation and reference waveforms for performing Fourier analysis as proposed in the patented solution [15]. As a result, the spectral analysis of unknown impedances becomes possible.

III. APPLICATION EXAMPLE

In Fig. 3 it is given a schematic diagram for evaluation of functioning of human cardiopulmonary through simultaneous measurement of impedance variation of lungs, heart and vascular system of hand. The magnetic method is used for generating the induced measurement current ii in the wrist by a generator G, incorporated in the prototyped measurement device (see Fig. 1 and 2) as a DAC based synthesizer of a magnetizing electrical current i_m . The induced current flow ii passes through the hand and conductive belt and closes through both heart and lungs.

Fig. 3 and 4 demonstrate the work of inductive sensor in more detail. Magnetizing current $i_m = 10$ mA flows through

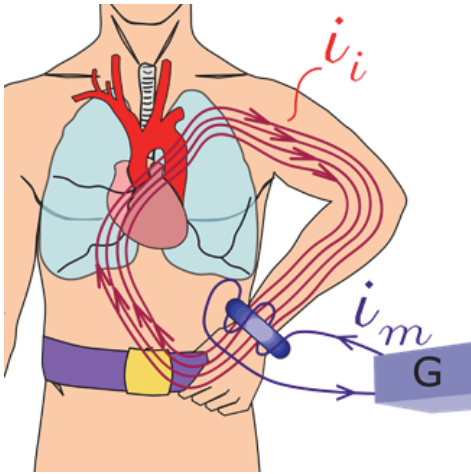


Fig. 3. Experimental evaluation of cardiopulmonary system

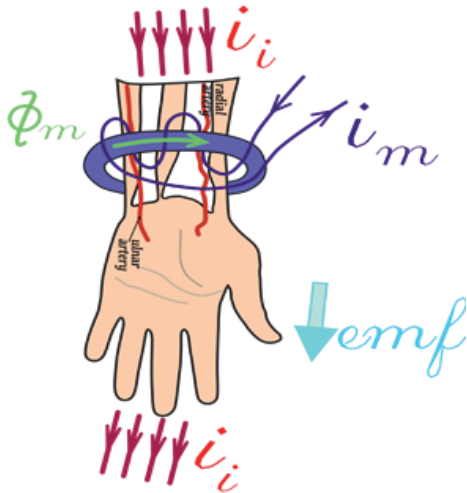


Fig. 4. Current density lines in case of distal four-electrode placement

the coil winding ($N = 10$ turns) of a toroidal magnetic ring (flexible material, $\mu = 20$) and creates a magnetic induction Φ_m inside the magnetic ring. In turn, the the magnetic induction Φ_m induces an electromagnetic force emf , which generates the inductive i_i , the level of which depends inversely on the impedance Z of the closed current circuit.

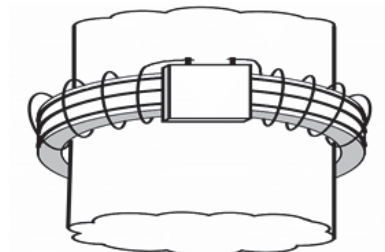
Construction of the toroidal magnetic coil is given in Fig. 5.

Breathing and heart beating together with blood flow modulate the impedance Z . Impedance modulation results in the output voltage of the device as illustrated in Fig. 6.

The acquired waveform of breathing satisfies the best

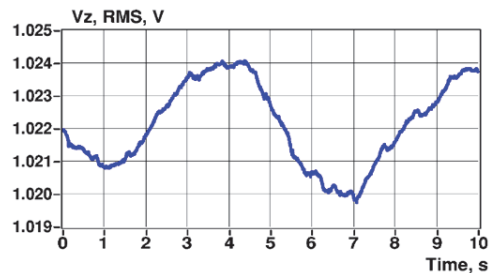


(a)

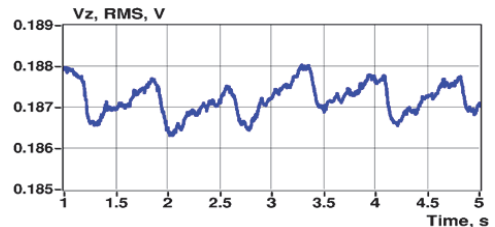


(b)

Fig. 5. Construction of the toroidal magnetic coil: a prototype (a) and principles of the design (b)



(a)



(b)

Fig. 6. Impedance caused demodulated waveforms of breathing (a) and heart beating (b) acquired with the prototyped device

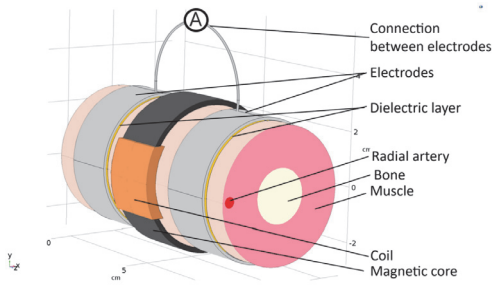


Fig. 7. Schematics of the sensor for sensing cardiac activities

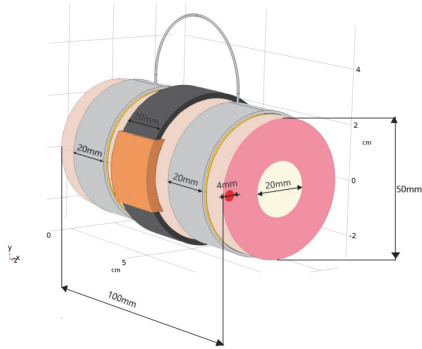


Fig. 8. Geometric data of the sensor model given in the previous figure

expectations, but heart-beating response in composite waveform remains too low and contains disturbances.

To overcome the problems, the following sensor schemes were proposed in Fig. 7 and 8 for sensor solutions.

In Fig. 7, the sensor model is supplemented with two capacitive electrodes connected with each other through a wire connection directly, not via body. Fig. 8 gives us the geometric data of the sensor. This enables us to measure the blood pulsation in the wrist area without taking into account other part of the body. Moreover, the capacitances of supplemented electrodes and inductance of the coil were tuned to have a serial resonance at the frequency of 10 MHz to measure the loss resistance directly.

The results show the modulation due to heart-beating $\Delta Z(t)$ in around of acceptable value 0.3% of basal value Z . Simulations using COMSOL Multiphysics software were carried out. The results in the form of magnet flux density and induced current density are given in the Fig. 9 and 10. The effect of electromagnetic induction penetrates about up to 5 mm into the wrist tissue (Fig. 9). There it induces the electromotive force emf (Fig. 4), which generates the induced current ii , inversely proportional to the tissue impedance Z . Distribution of the density of induced current ii shows clear

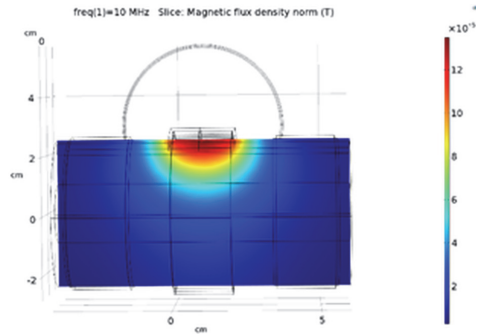


Fig. 9. Simulation results: distribution of the magnetic flux density

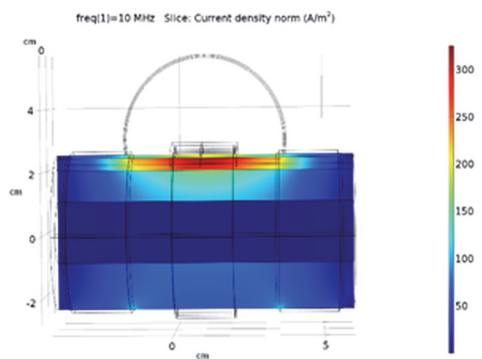


Fig. 10. Simulation results: distribution of the induced current density

concentration into the radial artery because of a concentration of the electromotive force in this area, but mostly due to the fact that the electrical conductivity of blood is about three time higher than of surrounding tissues.

IV. RESULTS

The developed FPGA based impedance measurement electronics works, as expected. The evaluation showed the following results:

- resolution of the final impedance - better than 0.01%;
- full analog bandwidth of the system 60MHz;
- analog bandwidth for precise measurement to 30 MHz;
- signal-to-noise ratio: 80 dB (total measurement tract);
- noise level 40 μV in the whole bandwidth.

For evaluation, the purity of the output sinewave (generated by CORDIC algorithm) was tested at 1MHz, where the distortion and noise level is around 10 μV -better than 0.01% of the fullscale (Fig. 11). Also, the full (DAC - ADC) channel was independently tested (Fig. 12), showing still some nonlinearity on the 0.01% to 0.1% level, which is very reasonable result, as the harmonics are not giving any direct measurement error (except if multiple frequencies used simultaneously and the measurement frequencies are badly selected).

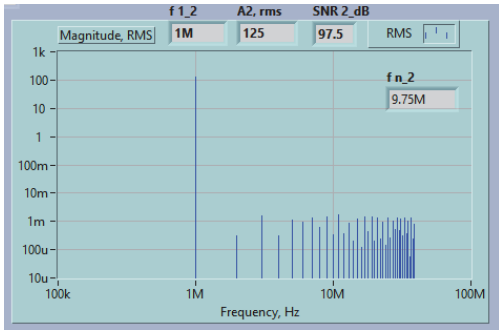


Fig. 11. Spectra of the output sinewave (showing harmonics and noise)

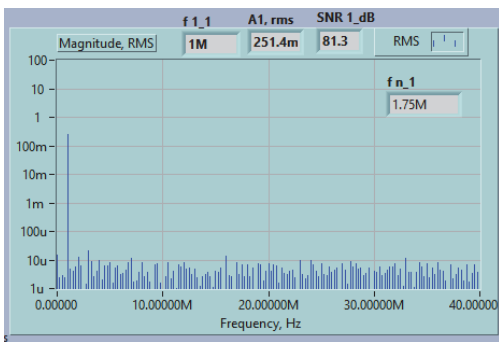


Fig. 12. Spectra of the input sinewave (total channel, showing harmonics and noise)

V. CONCLUSION AND FUTURE WORK

The dedicated device for inductive measurements of the conductivity and its changes and variation has been developed. Evaluation of the prototyped device fulfills the expected requirements in all aspects - by form factor, relatively simple construction and reasonable price of components. The future work involves further miniaturization of the present solution, careful tuning of the analog design and layout (to minimize noise and disturbances) and implementation of the multifrequency approach to get the impedance spectra simultaneously. While the simplest approach is to use a sum of two or more sinewaves for the excitation (and similar waveforms for the Discrete Fourier Analysis), interesting solution could be the usage of the chirp signals in both roles, as for excitation as well as for reference waveforms for Fourier analysis, as proposed in the patent description [15].

The proposed solution can be beneficially used in the wide range of bio-medical applications, like e.g. in bio-electrical impedance analysis (BIA), electrical impedance cardiography (ICG), electrical impedance tomography (EIT), electrical impedance spectroscopy (EIS), and magnetic induction tomography (MIT) [16].

ACKNOWLEDGMENT

Current work has been supported by grant EAG34 of Estonian Research Council, by Estonian Centre of Excellence in ICT Research EXCITE (TAR16013, EU Regional Development Fund) and Chist-ERA JEDAI (Mobilitas+ project *Mobera20*, EU Regional Development Fund) and finally by Estonian ICT programme "IT Academy" (EU European Social Fund). The authors would like to thank also colleagues from TalTech impedance measurement group for their technical help.

REFERENCES

- [1] Y. Barsukov and J. Macdonald, *Impedance Spectroscopy: Theory, Experiment, and Applications*, 2nd Edn., 01 2005.
- [2] S. Grimnes and O. Martinen, *Bioimpedance and Bioelectricity Basics*, 01 2008.
- [3] H.Sanier, S.E.J. Knobel, N. Shuetz, and T. Nef, "Contact-free signals as a new digital biomarker for cardiovascular disease: chances and challenges," *European Heart Journal – Digital Health*, vol. 1, no. 1, pp. 30–39, 2020.
- [4] W. Kubicek, R. Patterson, and D. Witsoe, "Impedance cardiography as a noninvasive method of monitoring cardiac function and other parameters of the cardiovascular system," *Annals of the New York Academy of Sciences*, vol. 170, pp. 724 – 732, 12 2006, First Published 1970.
- [5] D. Naranjo, J. Reina-Tosina, and M. Min, "Fundamentals, recent advances, and future challenges in bioimpedance devices for healthcare applications," *Journal of Sensors*, vol. 2019, pp. 1–42, 07 2019.
- [6] P. P. Tarjan and R. McFee, "Electrodeless measurements of the effective resistivity of the human torso and head by magnetic induction," *IEEE Transactions on Biomedical Engineering*, vol. BME-15, no. 4, pp. 266–278, 1968.
- [7] D. Teichmann, J. Foussier, and S. Leonhardt, "Respiration monitoring based on magnetic induction using a single coil," in *2010 Biomedical Circuits and Systems Conference (BioCAS)*, 2010, pp. 37–40.
- [8] J. García-Martín, J. Gómez-Gil, and E. Vázquez-Sánchez, "Non-destructive techniques based on eddy current testing," *Sensors*, vol. 11, no. 3, pp. 2525–2565, 2011.
- [9] *AD5933 1-MSPS, 12-Bit Impedance Converter, Network Analyzer: Datasheet*, Analog Devices, 2017, rev. F.
- [10] O. Martens, M. Min, R. Land, and P. Annus, "Multi-frequency and multi-channel bio-impedance measurement solution," in *Proceedings of the 7th Nordic Signal Processing Symposium - NORSIG 2006*, June 2006, pp. 178–181.
- [11] M. Rist, M. Reidla, M. Min, T. Parve, O. Martens, and R. Land, "Tms320f28069-based impedance spectroscopy with binary excitation," in *2012 5th European DSP Education and Research Conference (EDERC)*, Sep. 2012, pp. 217–220.
- [12] *Application Report: Optimizing L Measurement Resolution for the LDC161x and LDC1101*, Texas Instruments Inc, 2016, SNOA944.
- [13] *Technical Datasheet: Precision Impedance Analyzers*, Wayne Kerr Electronics, 2018, rev. E.
- [14] J. E. Volder, "The cordic trigonometric computing technique," *IRE Transactions on Electronic Computers*, vol. EC-8, no. 3, pp. 330–334, 1959.
- [15] O. Märtens, M. Min, R. Land, P. Annus, T. Saar, and M. Reidla, "Method and device for frequency response measurement," U.S. Patent 8,854,030, April, 20, 2010.
- [16] G. Singh, S. Anand, B. Lall, A. Srivastava, and V. Singh, "A technical review of various bioelectric impedance methods for health monitoring," in *2018 IEEE Long Island Systems, Applications and Technology Conference (LISAT)*, 2018, pp. 1–6.

Appendix 2

Experimental results

Priidel, Eiko; Ojarand, Jaan; Min, Mart; Pesti, Ksenija (2021).

Experimental results

To verify the results of simulations some experiments were carried out using the experimentation set-up given in Figure A1.1. The set-up contains electronic unit in a white box attached to the arm together with a power supply battery. The electronic unit is for generating of electrical current (controllable from 1 to 50 mA) in the frequency range of 10 kHz to 10 MHz, detect and demodulate the variations introduced by the body and make a WiFi data communication available with a standard computing device. In the present set-up, this unit generates the excitation current of 4.2 MHz into an inductive coil with a closed magnetic core under its black textile wrist-strap (see Figure A1.1). The core is manufactured on the bases of flexible ferrite tape TDK Flex IRL 02 with double thickness (2+2 mm) of it. The induction coil has $N = 10$ windings (copper wire 0.6 mm in diameter) concentrated into a 12 mm long sector on the radial artery region.

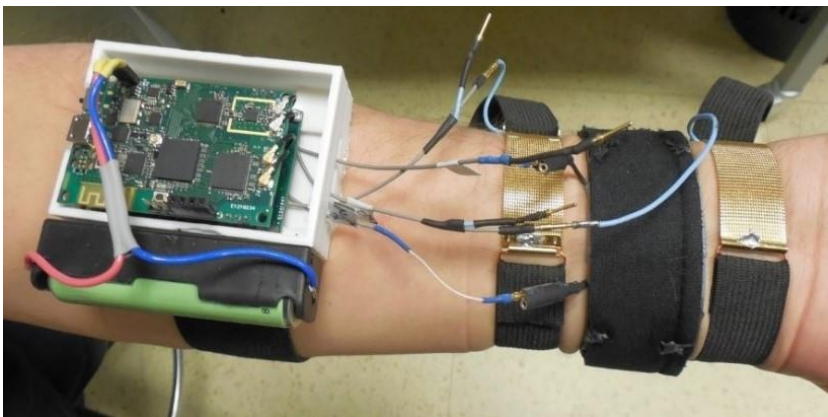


Figure A1.1. Experimental set-up.

Two gold-covered metallic electrodes (soft and flexible metallic watchbands) are used to pick-up the induced current from the wrist area. The electronic unit measures the current (about 1 mA RMS or less in accordance with safety standards) and demodulates the variations in it, caused by blood pulsation (Figure A1.2).

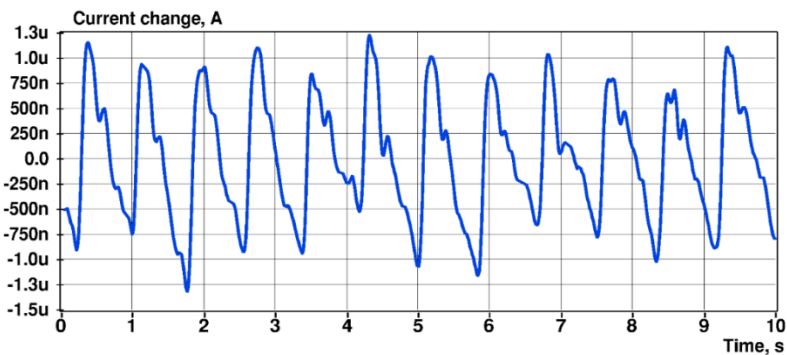


Figure A1.2. Current pulsation due to heart beating and breathing (lungs modulate heart work mechanically, slowly and slightly). Peak-to-peak value extends to $2.6 \mu\text{A}$ around the average RMS value of $850 \mu\text{A}$ given as a zero-level line in the present figure.

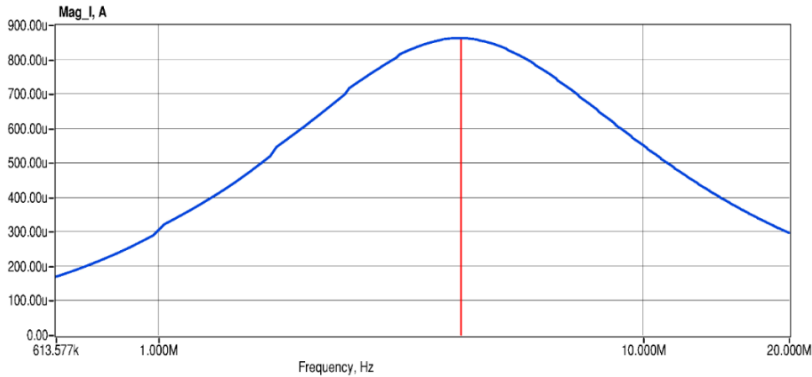


Figure A1.3. The resonance tuned to the frequency $f_r = 4.2$ MHz, $I = 850 \mu\text{A}$.

Mean value of the induced current through metal electrodes received in our experiments a value of $850 \mu\text{A}$ (see Figure A1.3). The peak-to-peak variation of this current is about $2.6 \mu\text{A}$ (see Figure A1.2). In other words, the variations in the current amount to 0.3%. In the majority, these variations are mostly due to beating of the heart, the respiration caused part reaches only to about some tenths of that.

Current in the coil was set to 20 mA for obtaining the induced current near to 1mA, more exactly, $I = 0.85 \text{ mA}$ was achieved. Current transfer $k_i = 0.85\text{mA}/20\text{mA} = 0.0425$ from the excitation to induced current was obtained.

Resonance at the frequency of $f_r = 4.2$ MHz has been achieved by adding a coil with inductance L to compensate the capacitive impedance X_C appearing between the gold covered electrodes and skin due to existing of double layer. **Equivalent model:** Serially connected two capacitances of 1200 pF (effective capacitance $C = 600 \text{ pF}$) and added inductance $L = 2.2 \mu\text{H}$. Equation for calculating the resonant frequency $f_r = (1/2\pi) \times (LC)^{-1/2}$. Resistance of blood and another resistive part of tissue and artery is $R \approx 50 \Omega$. Quality factor of the resonance is low ($Q \approx 1$).

The model for performing simulations is given in Figure A1.4 and the simulation results are depicted in Figures A1.5a and A1.5b.

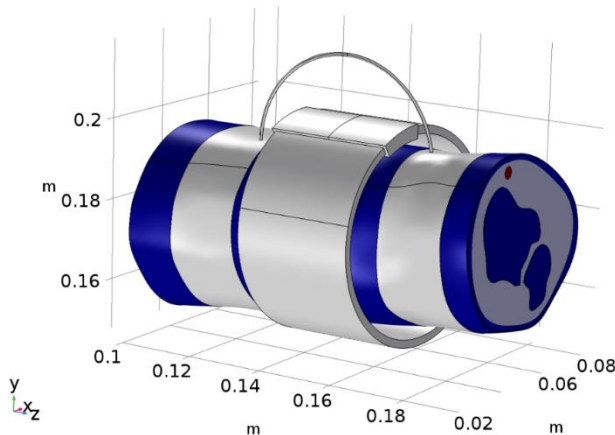


Figure A1.5. Model of the wrist section of the forearm with a magnetic coil and metal electrodes shorted by metal wire to each other.

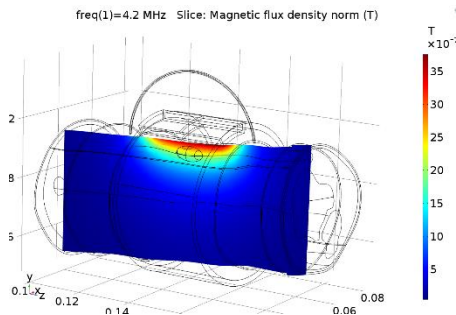


Figure A1.5a. Simulation results: distribution of the induced magnetic flux.

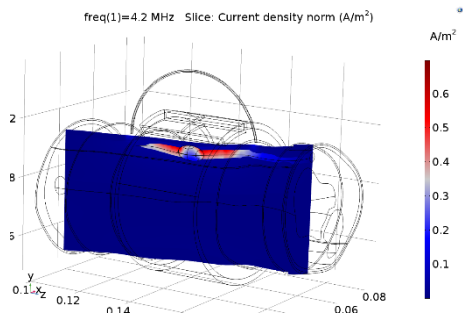


Figure A1.5b. Simulation results: distribution of the induced current density.

Remarks on the using of opened magnetic core: To compare the effectiveness of the closed magnetic core with respect to the open one, our experiments were repeated with the largely opened magnetic system, see Figure A1.6. Cross section of the TDK Flex IRL 02 core is of 60 mm^2 and its length is only 70 mm. The coil with 10 concentrated windings (width 12 mm) from 0.6 mm wire is placed onto its center.

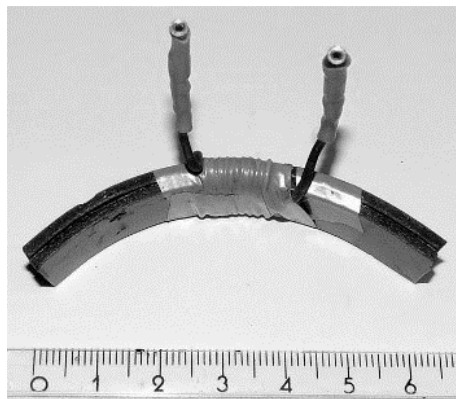


Figure A1.6. An opened double ferrite magnetic core shortened to only 7 cm.

It is remarkable that the physical processes differ only slightly in both quality and quantity from the case with closed magnet. This is understandable, because the magnetic flux penetrates into the body only a few millimeters deep, even when the magnet was closed, see Figure A1.6a. According to this, almost no electric current is induced in the depth of the wrist section (Figure A1.6b) and the results of both tests turned to be nearly the same.

Reference: Priidel, Eiko; Min, Mart; Pesti, Ksenija; Ojarand, Jaan; Märtens, Olev (2021). FPGA-based 16-bit 20MHz device for the inductive measurement of electrical bio-impedance. International Instrumentation and Measurement Technology Conference (IEEE I2MTC2021), Glasgow, Scotland, May 25-27, 2021 (accepted), 1-5.

Clinical experiments permission was provided by Medical Research Ethics Committee of the National Institute for Health Development (TAIEK nr. 395, 14.07.2020).

Curriculum vitae

Personal data

Name: Ksenija Pesti
Date of birth: 30 October 1985
Place of birth: Estonia
Citizenship: Estonian

Contact data

E-mail: ksenija.pesti@gmail.com

Education

2012–2020 Tallinn University of Technology – PhD, Electronics and Telecommunication
2006–2009 Tallinn University of Technology – MSC, Electronics and Bionics
2003–2006 Tallinn University of Technology – BSC, Electronics and Bionics
1999–2003 Rakvere Vene Gümnaasium – High school

Language competence

Estonian Native
Russian Native
English Fluent

Elulookirjeldus

Isikuandmed

Nimi: Ksenija Pesti
Sünniaeg: 30. oktoober 1985
Sünnikoht: Rakvere, Eesti
Kodakondsus: Eesti

Kontaktandmed

E-post: ksenija.pesti@gmail.com

Hariduskäik

2012–2020 Tallinna Tehnikaülikool – PhD, Elektroonika ja telekommunikatsioon
2006–2009 Tallinna Tehnikaülikool – MSC, Elektroonika ja bioonika
2003–2006 Tallinna Tehnikaülikool – BSC, Elektroonika ja bioonika
1999–2003 Rakvere Vene Gümnaasium – Keskkharidus

Keelteoskus

Vene keel Emakeel
Eesti keel Kõrgtase
Inglise keel Kõrgtase

ISSN 2585-6901 (PDF)
ISBN 978-9949-83-717-5 (PDF)